In situ X-ray photoelectron spectroscopy investigation of lithium-solid electrolyte interphases

Yi LIANG

Linacre College

University of Oxford

A thesis submitted for the degree of

Doctor of Philosophy

Trinity 2025

Acknowledgements

At the very beginning, I would like to express my sincere gratitude to my supervisor, Professor Mauro Pasta, for his invaluable support throughout my DPhil journey.

Most importantly, I would like to express my deepest gratitude to my parents Pengbin and Qiaoyun) for their unwavering support and understanding throughout these years. I am also profoundly thankful to my grandparents, Fange and Youcai, whose encouragement carried me through moments of emotional difficulty. I love them always, always.

My heartfelt appreciation extends to my dear friends, whose companionship has brightened my darkest days and whose encouragement has lifted me in times of doubt.

I would like to express my heartfelt gratitude to Minyi Zhang, my very first and best friend in Oxford. It was her unwavering support that helped me through the most challenging phase of my PhD journey, allowing me to grow into a renewed version of myself. I am also deeply grateful to Xinya Niu, my room mate for two years and one of my closest friends in Oxford. I truly cherish all the wonderful moments we shared together as a trio.

Equally, I am grateful to my lab mates for the joy, assistance, and support they have provided. I truly cherish the time spent with each of you—Brigita, Max, Shobhan, Giulia, Yvonne, Lorenz, Liwei, and Poyuan, Soochan—as your friendship and camaraderie have made my PhD journey all the more vibrant and unforgettable.

I would also like to thank all my friends from the badminton team—Yuying, Tianshu, Huimin, Ziwei, and Lily—for the joy and companionship you brought into my life. I truly cherished the time we spent together, both on and off the court. My sincere thanks go to my undergraduate classmate, Haolin, who first introduced me to badminton. Without that encouragement, I would not have had the opportunity to meet so many wonderful people through the team. Thanks to all of you, my PhD life was not just about work and home, but was also filled with laughter, friendship, and movement.

I would also like to thank Johannes Ihli for his guidance and support on my project, as well as for his care and encouragement during times when I was feeling low. His kindness gave me the confidence and strength to keep moving forward. I sincerely wish him all the best and a smooth journey in the future.

I would like to thank Matthew Burton for the invaluable support he provided throughout my DPhil journey, both academically and personally. His guidance, encouragement, and thoughtful insights helped me navigate challenges, enrich my research, and stay motivated. I am truly grateful for his kindness and generosity every step of the way.

I would also like to thank Stephen Turrell for his valuable support in preparing the LiPON samples and for his thoughtful review of the LiPON work we published together.

Additionally, I would like to extend my gratitude to Sudarshan for his support during my second year, particularly for training me on XPS. His guidance and patience were instrumental in helping me develop essential skills and confidence in this area.

It is because of all these incredible people that I have found the strength, resilience, and confidence to complete my doctoral journey. I could not have done it without them.

List of Publication

1. Yi Liang, Matthew Burton, Ben Jagger, Hua Guo, Johannes Ihli, Mauro Pasta. "*In situ* XPS investigation of the SEI formed on LGPS and LAGP with metallic lithium". In: *Chemical Communications* 60.86 (2024),pp. 1259712600.
2. Stephen J Turrell, Yi Liang, Tiancheng Cai, Ben Jagger, Mauro Pasta. "Origin of Stability in the Solid Electrolyte Interphase formed between Lithium and Lithium Phosphorus Oxynitride", In: *Chemistry of Materials* (Apr. 2025)
3. Matthew Burton, Ben Jagger, Yi Liang, Joshua S Gibson, Jack Aspinall, Jack EN Swallow, Robert S Weatherup, Mauro Pasta. "The role of phosphorous in the solid electrolyte interphase of argyrodite solid electrolytes", Manuscript submitted
4. Souhardh Kotakadi, Jack Aspinall; Matthew Burton, Yi Liang, Yuichi Aihara, Mauro Pasta. "Impact of metallic interlayers at the lithium-Li6PS5Cl solid electrolyte interface", Manuscript submitted
5. Hua Guo, Junhao Li, Matthew Burton, John Cattermull, Yi Liang, Yvonne Chart, Gregory J. Rees, Jack Aspinall, Mauro Pasta. "High-entropy sulfide argyrodite electrolytes for all-solid-state lithium-sulfur batteries", In: *Cell Reports Physical Science* 5.10 (Oct. 2024), p. 102228.

Abstract

Lithium batteries are among the most crucial energy storage technologies, and further enhancing their performance, particularly in energy density, is essential to meet the growing demands of modern applications. For example, in electric vehicles, increasing battery energy density—defined as the energy stored per unit mass or volume—is crucial for extending driving range, a primary concern for consumers. Although battery packs are usually priced per kilowatt-hour of capacity, higher cell-level energy density allows the same capacity to be delivered with reduced mass and volume. Reducing battery mass within the vehicle in turn lowers energy consumption for a given driving distance. Together, these effects show higher energy density indirectly yet appreciably extends driving range.

Solid-state electrolytes (SSEs) are considered one of the most promising advancements for next-generation energy storage. By enabling the use of lithium metal anodes, SSEs offer significantly higher energy densities while enhancing safety through their mechanical suppression of dendrites and intrinsic non-flammability. However, the highly reactive nature of lithium metal and the limited electrochemical stability of SSEs present significant challenges, particularly in the formation and evolution of the solid electrolyte interphase (SEI). This interfacial layer critically influences ionic transport and overall battery stability, yet its formation mechanisms and long-term behaviour remain poorly understood.

To address these challenges, this work utilises *in situ* X-ray photoelectron spectroscopy (XPS) to investigate SEI formation at the interfaces between lithium metal and several promising SSEs. The SEI characteristics of $Li_{10}GeP_2S_{12}$ (LGPS) and $Li_{1.5}Al_{0.5}Ge_{1.5}(PO_4)_3$ (LAGP) were compared, revealing that LAGP forms a more passivating SEI with fewer conductive phases. Further investigation on Li_6PS_5Cl suggests that its SEI continues to evolve due to the progressive delithiation of phosphorus-containing species, which explains the variation of reported SEI thickness. Lastly, a graded SEI structure was proposed for LiPON, providing insights into its exceptional stability against lithium metal.

These findings demonstrate the power of *in situ* XPS in capturing the chemical evolution of the SEI, offering valuable insights into its formation and degradation. When combined with complementary characterisation techniques, this approach enables a more comprehensive understanding of SEI behaviour, aiding the development of more stable and high-performance SSE-based lithium batteries.

Contents

Appendices

List of Abbreviations

ASSB	All-solid-state battery
B.E. or BE	Binding Energy
ALD	Atomic layer deposition
BSE	Backscattered electrons
CEI	Cathode electrolyte interface
CTTA	Coulometric titration time analysis
CVD	Chemical vapour deposition
ECM	Equivalent circuits model
EDX	Energy dispersive X-ray spectroscopy
EELS	Electron energy loss spectroscopy
EIS	Electrochemical impedance spectroscopy
ESW	Electrochemical stability window
HOMO	Highest occupied molecular orbital
ICE	Internal combustion engine
IMFP	Inelastic Mean Free Path
LAGP	$Li_{1.5}Al_{0.5}Ge_{1.5}(PO_4)_3$
LCO	$LiCoO_2$
LGPS	$Li_{10}GeP_2S_{12}$
LIB	Lithium-ion batteries
LIPON	Lithium Phosphorus Oxynitride electrolyte
LiTFSI	Lithium bis(trifluoromethanesulfonyl)imide
LMA	Lithium metal anode
LMB	Lithium metal batteries
LPSCl	Argyrodite Li_6PS_5Cl electrolyte
LUMO	Lowest unoccupied molecular orbital

FWHM	Full Width Half Maximum
OCV	Open circuit voltage
PAN	Polyacrylonitrile
PEIS	Potentiostatic electrochemical impedance spectroscopy
PEC	Poly(ethylene carbonate)
PEO	Poly(ethylene oxide)
PVDF	Poly(vinylidene fluoride)
PVD	Physical vapour deposition
RF	Radio frequency
SEI	Solid electrolyte interface
SEM	Scanning electron microscopy
SHE	Standard hydrogen electrode
SSB	Solid-state battery
SSE	Solid-state electrolyte
SPE	Solid polymer electrolyte
SXI	Scanning X-ray Induced secondary electron image
STM	Scanning Tunnelling Microscope
VEP-XPS	Virtual Electrode Plating X-ray Photoelectron Spectroscopy
XRD	X-ray diffraction
XPS	X-ray Photoelectron Spectroscopy

1

Introduction

Contents

1.1 General background of battery research

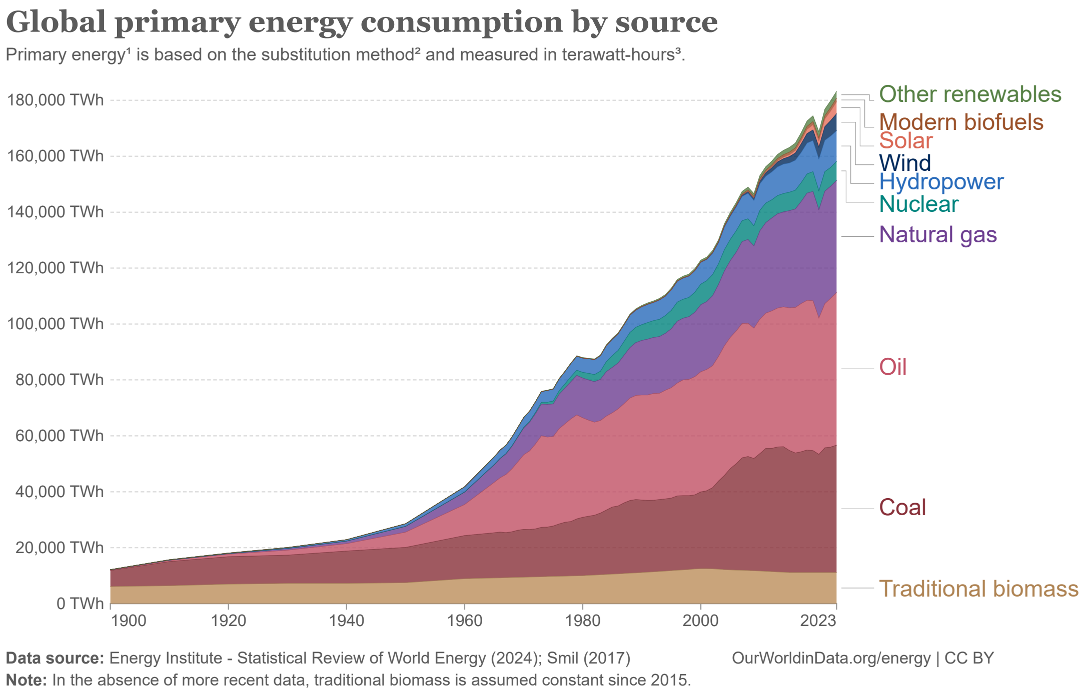

Data source: Energy Institute - Statistical Review of World Energy (2024); Smil (2017)
Note: In the absence of more recent data, traditional biomass is assumed constant since 2015.

Figure 1.1: Global consumption of energy by source. Reprinted from [1]

The population growth and the rising demand for higher living standards have increased carbon dioxide emissions beyond what the ecosystem can absorb[2]. Figure 1.1 illustrates that the primary sources of energy consumption are fossil fuel-based (oil, coal, natural gas), which significantly contribute to air pollution and greenhouse gas emissions, and are also finite (non-renewable). Solar, wind, and hydroelectric power provide low-carbon, renewable alternatives, yet their full life-cycle footprints are not negligible. Large dams inundate ecosystems and consume vast quantities of concrete and steel, whereas photovoltaic and wind installations rely on high-purity silicon, silver, aluminium, and rare-earth magnets, all of which require energy- and resource-intensive extraction and processing[3–6]. These realities underscore the need for material-efficient designs, robust end-of-life recovery pathways, and, critically, high-performance energy-storage systems capable of buffering the inherent intermittency of renewables at grid and utility scale. Chemical energy storage in advanced batteries therefore becomes indispensable for matching fluctuating generation with steady demand and for accelerating the transition to a truly sustainable energy infrastructure[7, 8].

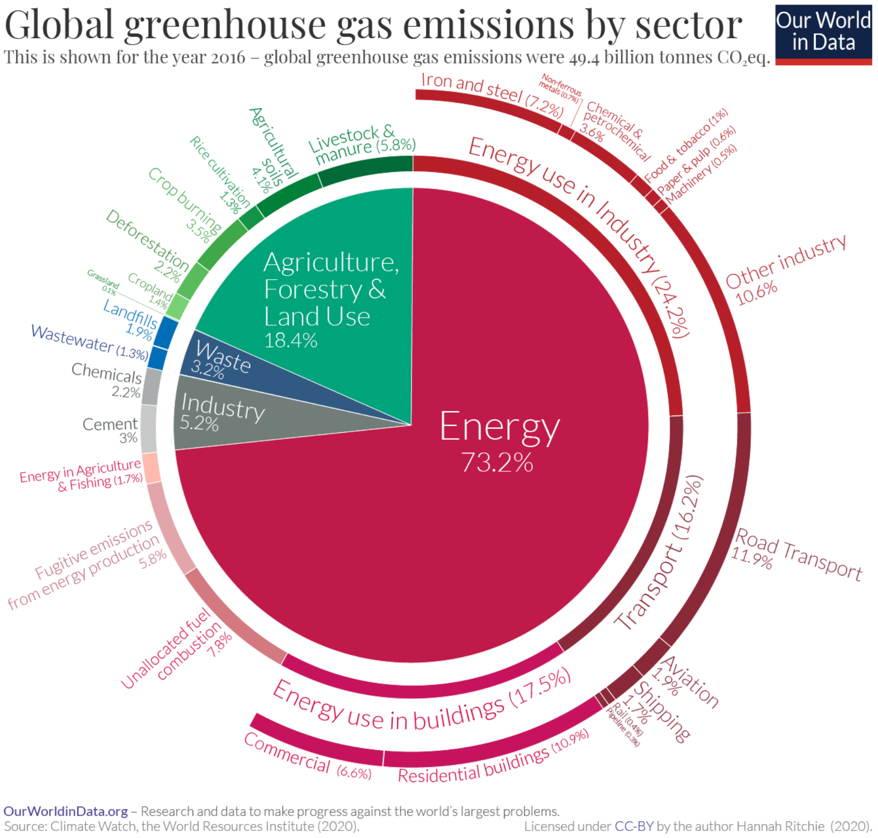

Figure 1.2: Global greenhouse emission by sector (2020). Reprinted from [1]

Greenhouse gas emissions from the energy sector, which account for over 70% of total emissions as shown in Figure 1.2, must be significantly reduced. Since the majority of energy is still derived from fossil fuels, transitioning to clean energy sources is essential, with electrification being one of the key strategies for decarbonisation[9–11]. In addition to adopting more renewable energy sources for electricity generation, the electrification of heating and transportation is critical. As vehicles are the primary consumers of fossil fuels in the transport sector, transitioning to electric vehicles (EVs) and electrified transportation systems is vital for achieving decarbonisation goals[12, 13]. However, to compete with traditional internal combustion engine (ICE) vehicles and to increase market share without relying on legislation, EVs must advance in several key areas, particularly in battery technology. The ongoing electrification of transportation requires battery-powered vehicles to offer extended driving ranges and fast-charging capabilities[14–16].

Lithium-ion batteries (LIBs) offer significant advantages, including high specific capacity, low self-discharge rate, negligible memory effect, and robust long-term cycling performance compared to lead-acid and nickel-metal hydride batteries[17, 18]. As shown in Figure 1.3, LIBs outperform other battery technologies in energy density, along with other merits making them the key technology driving the success of EV development[19–21]. Furthermore, LIBs are increasingly integral to portable electronics, medical devices, and even space exploration, where reliable and efficient energy storage is crucial[22, 23].

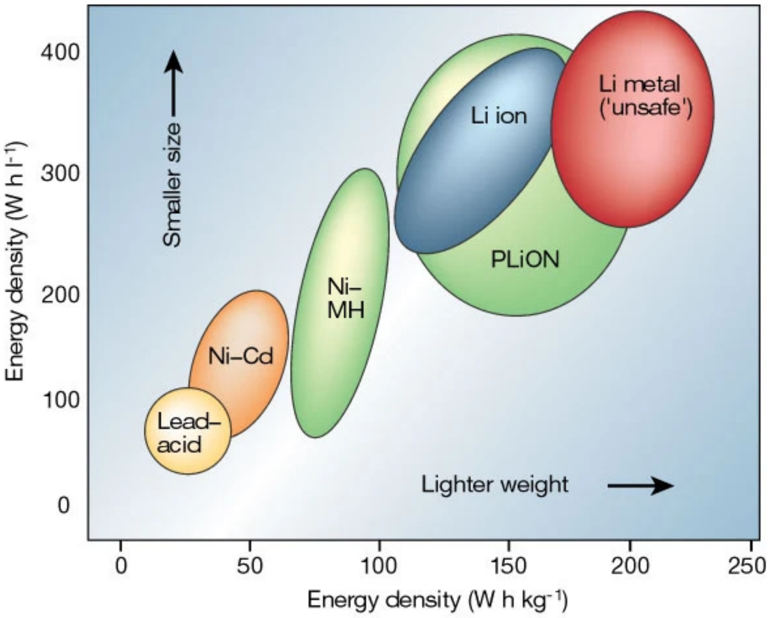

Figure 1.3: Comparison of energy density among different battery technologies, Reprinted with permission from [23], Copyright 2001 Springer Nature

With the ever-increasing demand for improved battery performance, researchers are exploring advanced materials and innovative designs to push the boundaries of current technology. The primary focus is on enhancing energy density, which extends the driving range of EVs, and optimizing charging rates to significantly reduce recharging times[17]. Greater energy density allows the same usable capacity to be packaged in a smaller volume and lower mass, enabling manufacturers to install more energy within the limited envelope of an EV while reducing curb weight in the process. A lighter curb requires less power for propulsion, thereby decreasing the energy consumption per kilometre and further extending the practical driving range[24]. Next-generation lithium batteries may incorporate novel anode materials, such as silicon or lithium metal, which offer much higher capacities than traditional graphite. Moreover, advancements in solid-state electrolytes (SSEs) are expected to improve safety by eliminating flammable liquid components, potentially further solidifying the dominance of LIBs in the battery market[22].

1.2 Lithium-ion batteries

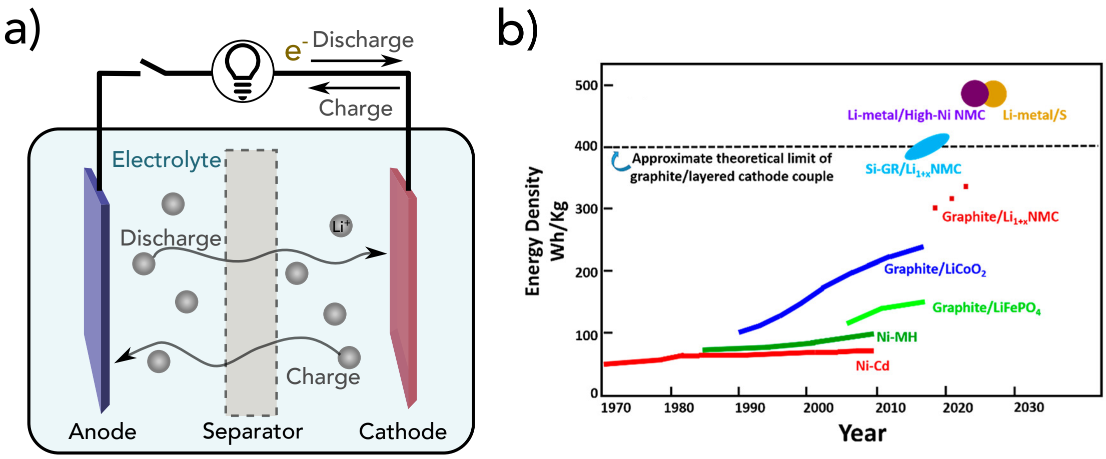

Figure 1.4: (a) A schematic of conventional LIB; (b) Evolution of energy densities of batteries with different chemistries, Reprinted with permission from [25], Copyright 2018 American Chemical Society

Figure 1.4a presents a schematic of a typical LIB, comprising an anode, a cathode, a liquid electrolyte, and a porous separator. In LIBs, a liquid-electrolyte-permeable separator, usually made from porous polymeric materials, is employed to prevent direct contact between the electrodes[26, 27]. During charging, electrons move from the cathode to the anode through the external circuit, facilitating reduction, while Li^+ ions are extracted from the cathode's host structure and migrate through the electrolyte and separator to be inserted into the anode, typically graphite. Upon discharging, this process reverses, with the difference in redox potentials between the anode and cathode as the driving force. The separator and liquid electrolyte composite must be ionically conductive for efficient Li^+ transport and electrically insulating to prevent internal short circuits.

An LIB with a carbon-based anode and a $LiCoO_2$ (LCO) cathode was first commercialised by SONY in 1991[28]. Reactions that happen inside the system during discharging are represented by Equations 1.1 and 1.2.

$$Anode : Li_xC_6 \rightarrow C_6 + xe^- + xLi^+ \tag{1.1}$$

$$Cathode : Li_{1-x}CoO_2 + xe^- + xLi^+ \rightarrow LiCoO_2 \tag{1.2}$$

LIBs have become the dominant energy storage system, and the energy density has increased from 80 Wh kg^{-1} in 1991 to about 280 Wh kg^{-1} by 2025, driven by advancements in high-performance materials and battery design[29–34]. Despite the advantages of LIBs, concerns about their battery capacity persist due to space and weight constraints in products. Through extensive development and optimisation, LIBs have achieved significant progress in both manufacturing and performance[28, 35].

In the automotive market, driving range and charging time remain significant concerns for customers choosing between ICE vehicles and EVs[14]. ICE vehicles typically offer a driving range of approximately 400 to 800 km per refuelling, depending on fuel efficiency and tank size. In contrast, the average driving range for EVs is 200 to 350 km on a single charge, depending on the battery pack. However, some EVs, such as the Tesla Model S and Volkswagen ID Hatch, achieve significantly higher driving ranges exceeding 500 km[36–41]. Although the energy density of LIBs is approaching its theoretical limit, it remains significantly lower than that of gasoline[42–44]. Furthermore, recharging of most EVs takes hours to finish, because the charging rates commonly employed range from roughly 0.12 C to 0.8 C—substantially slower than the few minutes required for the refuelling time for ICE vehicles[45–48]. This highlights the need to improve the fast-charging capabilities of batteries, which are primarily governed by the Li^+ ion intercalation and diffusion properties within the system. The charging/discharging rate, also referred to as the C-rate, defines the rate at which a battery is charged or discharged relative to its maximum capacity. For example, a 1C rate corresponds to a current that can fully charges or discharges the battery in one hour. According to Deng *et al.*, LIBs with an energy density exceeding 350 Wh kg^{-1} and a 4C charging rate are necessary, prompting the development of new battery technologies[14, 43, 44]. In LIBs, these properties are determined by cell chemistry and material characteristics. For example, in graphite anodes, the lithiation onset potential (approximately 0.05 V vs. Li^+/Li) is close to that of metallic lithium. At high charging rates, the increased overpotential and sluggish Li^+ ion intercalation kinetics can lead to lithium plating on the anode surface instead of proper intercalation. This unwanted lithium deposition can result in the formation of dendrites, which pose significant safety risks. If these lithium dendrites penetrate the separator and reach the cathode, they can cause an internal short circuit, potentially leading to thermal runaway, cell failure, or even fire hazards.[14, 25, 41, 49, 50]. Current expectations demand LIBs to provide longer driving ranges and shorter charging times, presenting substantial challenges to existing battery technology[51].

Alongside the growing need for higher energy density, reports of battery fires and explosions have intensified safety concerns. These concerns are largely due to the chemistry of LIBs, which involves the use of flammable organic liquid electrolytes[19, 52]. This underscores the necessity for innovation in battery technologies that offer higher energy densities and require a deeper understanding of the electrochemical behaviour occurring within the battery system, spurring research into new chemistry and novel materials capable of exceeding the limitations of traditional LIBs.

1.3 Battery performance metrics

So far, a few key battery performance metrics such as energy density and C-rate have been mentioned. Their definition and physical meaning along with other important metrics will be included in this section, as understanding these metrics is essential for evaluating and optimising battery performance.

The energy density of a battery is the amount of energy stored in a battery per unit mass (gravimetric energy density, Wh kg^{-1}) or per unit volume (volumetric energy density, Wh l^{-1}).

$$Energy\ density = \frac{nominal\ voltage\ (V) \times capacity\ (Ah)}{Battery\ mass\ (kg)\ or\ volume\ (l)} \tag{1.3}$$

Here, the nominal voltage is the battery operating voltage, which is determined by the battery chemistry and working conditions. The capacity is the overall charge the battery can deliver over a specific time.

The battery capacity can be measured by recording the current and time during the discharge process and can be calculated using Equation 1.4.

$$Q\ (capacity) = \int I dt \tag{1.4}$$

Apart from battery capacity, the theoretical capacity of electrode materials is often considered when selecting suitable materials for battery applications. The theoretical capacity (Q_{th}) of an electrode material can be calculated using Faraday's law shown in Equation 1.5, which relates the charge stored per unit mass of the material.

$$Q_{th} = \frac{nF}{3.6\ M}\ (mAh\ g^{-1}) \tag{1.5}$$

Here, n refers to the number of electrons transferred per formula unit during the reaction, F is Faraday's constant (96485 C mol^{-1}), and M is the molar mass of the active materials (g mol^{-1}). Taking a lithium metal anode (LMA) as an example, the electrochemical reaction involved is $Li \rightleftharpoons Li^{+} + e^{-}$, where n=1 and the molar mass of lithium is 6.94 g mol^{-1}. Thus the theoretical capacity of the LMA is calculated as below:

$$Q_{th} = \frac{1 \times 96485\ C\ mol^{-1}}{3.6 \times 6.94\ g\ mol^{-1}} \approx 3860\ mAh\ g^{-1} \tag{1.6}$$

The charge storage capacity of a cell/battery is largely determined by the capacities of the electrode materials, while the overall battery design also influences the capacity at the device level. Coulombic efficiency (CE) measures the ratio of charge extracted during discharge to the charge input during the preceding charge cycle, as shown in Equation 1.7.

$$CE = \frac{discharge\ capacity}{charge\ capacity} \times 100\% \tag{1.7}$$

Ideally, the CE of 100% would indicate that all the charge input during charging is fully recovered during discharge. However, in practical applications, CE is typically less than 100% due to various inefficiencies and side reactions occurring within the battery system. Over extended cycling, a consistently low CE can lead to capacity fade and reduced battery lifespan, making it a critical metric for assessing battery performance and stability. Notably, most commercial LIBs have a CE approaching 100%[53, 54]. Another important metric is capacity retention, which is defined as the ratio of the discharge capacity at a given cycle to the initial discharge capacity. It serves as an indicator of the battery's long-term stability and durability. In practical applications, a battery is typically considered to have reached its end of life (EoL) when its capacity retention falls to 80% of its original capacity.

1.4 Lithium metal batteries (LMBs)

The increasing demand for high-energy-density battery systems at an affordable price prompts a shift from conventional LIBs to batteries based on lithium metal. The LMA, which possesses the highest theoretical capacity (3860 mAh g^{-1}, with calculation process shown in Equation 1.6) and the lowest redox potential (-3.04 V vs standard hydrogen electrode (SHE)), is considered the 'holy grail' for high-energy-density batteries. However, integrating lithium metal into LIB systems faces several challenges. The high reactivity and low potential of lithium metal lead to reactions with the electrolytes and the formation of an interphase layer. More importantly, persistent issues such as volume changes and dendrite formation and penetration further complicate its integration[23, 55, 56].

As shown in Figure 1.5a, under open circuit voltage (OCV) conditions, the LIB cell system is thermodynamically stable, with two adjacent phases in equilibrium. The equilibria between these phases can be described by the following equations:
Phase α'|A: $\mu_{e-}^{\alpha'} = \mu_{e-}^{A}$
Phase A|E: $\mu_{Li}^{A} = \mu_{e-}^{A} + \mu_{Li^+}^{E}$
Phase E|C: $\mu_{Li}^{C} = \mu_{e-}^{C} + \mu_{Li^+}^{E}$
Phase C|α'': $\mu_{e-}^{\alpha''} = \mu_{e-}^{A}$

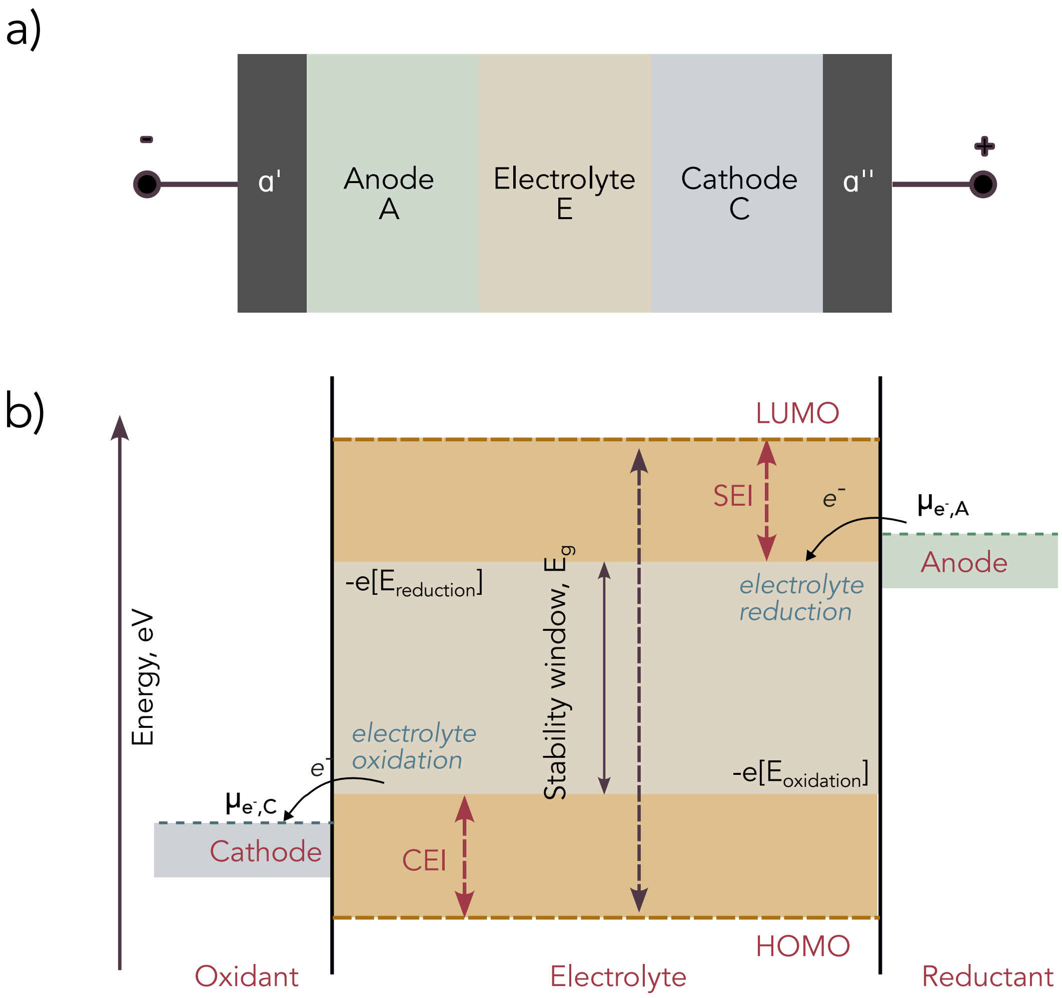

Figure 1.5: (a) The Galvani representation of the LIB system includes different phases: α' and α" represent the external metallic contacts, the anode, the electrolyte, and the cathode; (b) Schematic illustration of the electrochemical window of electrolytes estimated using the bandgap approach: energy level diagram of an electrochemical cell where LUMO is the Lowest Unoccupied Molecular Orbital, HOMO is the Highest Occupied Molecular Orbital, $\mu_{\mathrm{e}^-,\ \mathrm{A}}$ is the electrochemical potential of the anode, $\mu_{\mathrm{e}^-,\ \mathrm{C}}$ is the electrochemical potential of the cathode. The gap between the LUMO and HOMO is the 'electrochemical window'. An interphase layer is formed when $\mu_{\mathrm{e}^-,\ \mathrm{A}}$ >LUMO or $\mu_{\mathrm{e}^-,\ \mathrm{C}}$<HOMO. Reproduced with permission from [57]

The OCV can be calculated using $OCV = V_A - V_C = \frac{\mu_{e-}^A - \mu_{e-}^C}{F}$.

Here, A represents the anode, C represents the cathode and μ refers to the electrochemical potential of different species in the system, measured in joules per mole (J mol^{-1}), and F is the Faraday's constant[58].

Side reactions between the electrolyte and electrode occur when the electrochemical potentials of the electrodes fall outside the electrochemical stability window (ESW) of the electrolyte materials. The ESW is defined as the energy gap (E_g) between the Highest Occupied Molecular Orbital (HOMO, also valence band maximum) and the Lowest Unoccupied Molecular Orbital (LUMO, also conduction band minimum), as illustrated in Figure 1.5b[59].

When μ_A exceeds the LUMO, the electrolyte is reduced by the anode, resulting in the formation of solid electrolyte interphase (SEI); similarly, when μ_c falls below the HOMO, the cathode oxidises the electrolyte, leading to the formation of cathode electrolyte interphase (CEI). To ensure the thermodynamic stability of the battery system, the following condition must be met: see Equation 1.8[59, 60].

$$eV_{oc} = (\mu_A - \mu_c) \leq E_g \tag{1.8}$$

Here, e denotes the magnitude of the electric charge carried by a single electron and μ represents the electrochemical potential of the anode or cathode, measured in electronvolts (eV).

Notably, the formed SEI and CEI play a crucial role in preventing further anodic reduction and cathodic oxidation of the electrolyte at the electrode interfaces.

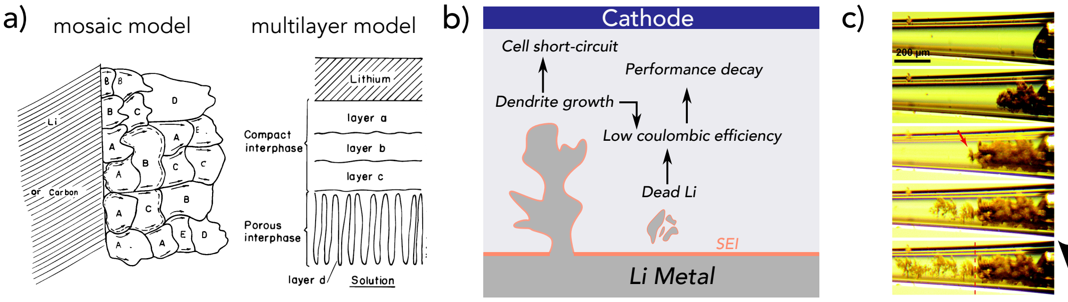

Figure 1.6: (a) Schematic of the mosaic and multilayer SEI model, Reprinted with permission from [61], Copyright 1997 IOP Publishing, and [62], Copyright 1996 American Chemical Society; (b) Schematic of lithium dendrite formation and related problem; (c) Snapshots illustrating the growth of lithium dendrite during *in situ* lithium electrodeposition in a liquid electrolyte, the red arrow labelled the emergence of lithium dendrite. Reprinted with permission from [63].

The SEI formed as the result of the reaction between metal and electrolyte solution was first proposed by Peled in 1979[64]. The SEI plays a critical role in determining battery performance, including irreversible capacity loss, coulombic efficiency, cycle life, and shelf life. It acts as a protective layer that separates the anode and the electrolyte, preventing direct contact, while selectively allowing Li^+ transport through the layer.

To achieve high performance with LMA, the formed SEI must be both chemically and electrochemically stable against both lithium metal and the electrolyte. Additionally, mechanical stability also plays a critical role. Several models of the SEI structure have been proposed, including the mosaic model and the multilayer model, as illustrated in Figure 1.6a. These models suggest that highly reduced inorganic phases are in close contact with the anode, while partially reduced phases with less dense structure are positioned closer to the electrolyte[61, 62, 64, 65]. The exploration and initial investigation of SEI in liquid systems has provided valuable insights into the composition, morphology, and effects on cycling performance, highlighting its critical role in determining battery performance.

The unevenness and pre-existing defects on the lithium surface, along with the heterogeneous SEI layer formed atop, lead to uneven current distribution and localised hotspots for lithium deposition and dissolution. This ultimately causes the formation of lithium dendrites and dead lithium, as illustrated in Figure 1.6b and 1.6c. Additionally, the volumetric changes in the LMA during cycling tend to fracture the SEI, continuously exposing fresh lithium surfaces to the electrolyte, further promoting SEI growth. This results in increased internal resistance, a loss of active lithium in the system, and eventually the failure of the battery. To address these challenges, the use of a three-dimensional host structure has been proposed to mitigate the degradation caused by volumetric changes[66]. The compatibility of LMA in LIB systems can also be improved through electrolyte formulation, including the optimisation of lithium salts, solvents, and other additives, as well as surface treatment of the LMA prior to cell assembly to form a robust and stable SEI[67]. In liquid electrolyte systems, the SEI requirements are particularly stringent: it must be electrochemically stable in relation to LMA and possess robust mechanical properties to inhibit further SEI growth and dendrite formation.

Furthermore, the use of SSEs is becoming an attractive strategy for enabling LMA due to their higher mechanical strength, which can potentially suppress lithium dendrite penetration[68–71]. Some SSEs have been shown to form a stable SEI against LMAs and allow for the use of high-voltage cathodes[67, 72]. In addition, the safety of the battery system is improved as electrolyte leakage and flammability are avoided. As a result, the development of solid-state batteries (SSBs) shows great potential for achieving higher energy density and enhanced safety. However, further investigation is required to address interfacial challenges, which will be discussed in the following section.

1.5 All-solid-state batteries

1.5.1 Background

Since the discovery of solid ionic conductors, SSEs have been intensively researched and developed, with several key materials and technologies summarised in Figure 1.7[73]. Advances in the synthesis of SSEs exhibiting high ionic conductivities (up to 10^{-2} S cm^{-1}) have significantly enhanced their potential for application in energy storage systems[74–77].

SSEs can serve dual roles as both ionic conductors and separators between the anode and cathode, effectively replacing liquid electrolytes and separators in LIB systems to create SSBs. Mostly, SSEs are single-ion conductors due to their rigid anion framework, making their lithium transfer number near unity[41, 78]. SSEs can also provide higher mechanical rigidity compared to the polymeric separators used in LIBs, so the lithium dendrite formation is largely suppressed[68, 77]. Unlike traditional LIBs, the integration of SSEs into lithium battery systems is expected to enable the direct use of lithium metal as the anode. This is crucial for significantly improving energy density, given that the LMA possess the highest theoretical capacity. The solid-state configuration also facilitates novel geometric designs, which shows potential for improving packing efficiency [43]. Additionally, replacing flammable liquid electrolytes with solid ones enhances the safety of SSB systems by eliminating the risks of liquid electrolyte leakage and thermal runaway[52]. Notably,

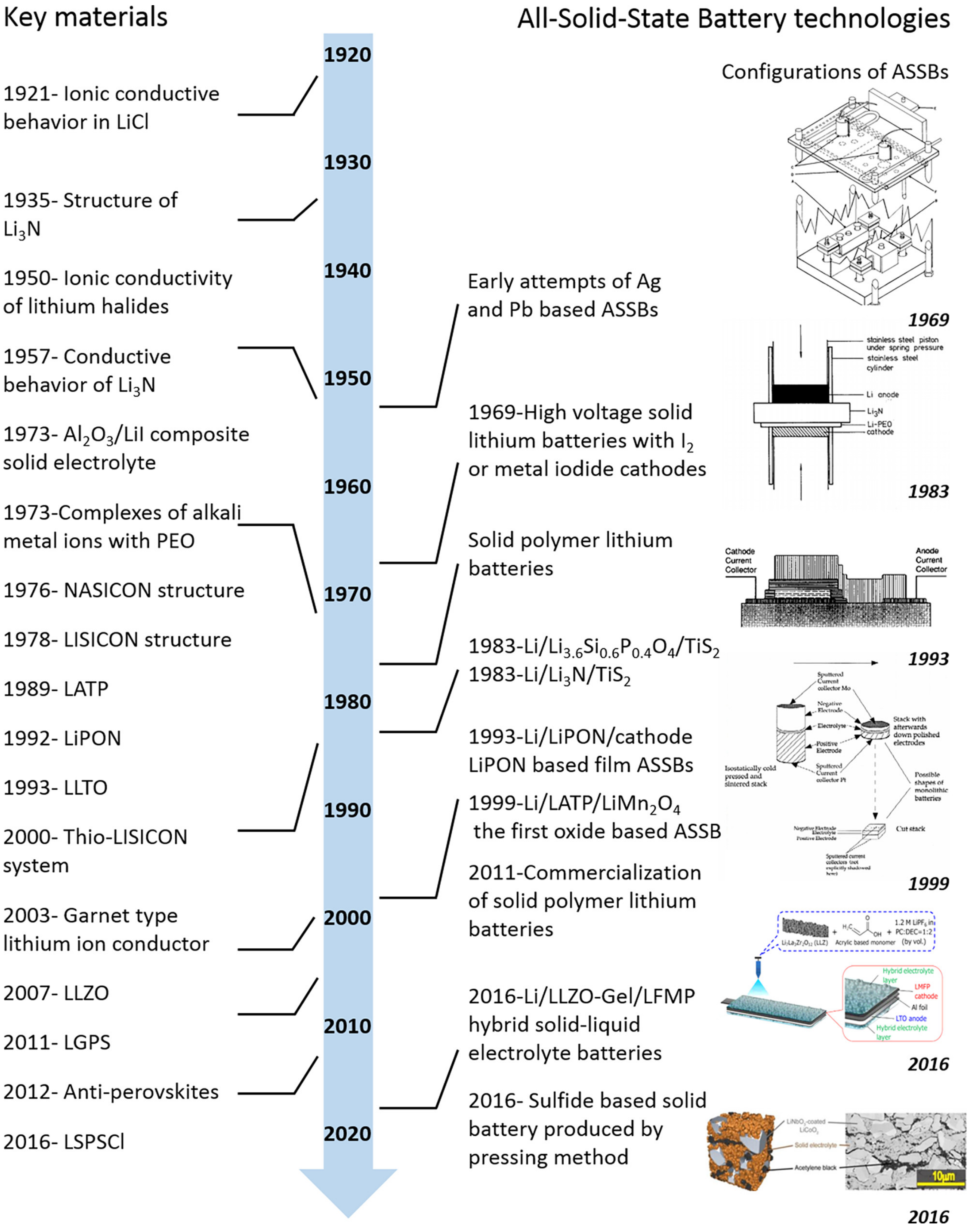

Figure 1.7: Development history of solid-state electrolyte materials and technologies of all-solid-state batteries (ASSBs), Reprinted with permission from [73], Copyright 2019 American Chemical Society

the stiffness and fracture strength of SSEs further reduce the likelihood of dendrite penetration and short circuits[68, 70, 71]. Consequently, the development and commercialisation of SSBs is regarded as one of the most promising avenues for next-generation energy systems as illustrated in Figure 1.8, with ASSB energy density surpassing 500 Wh kg^{-1} .

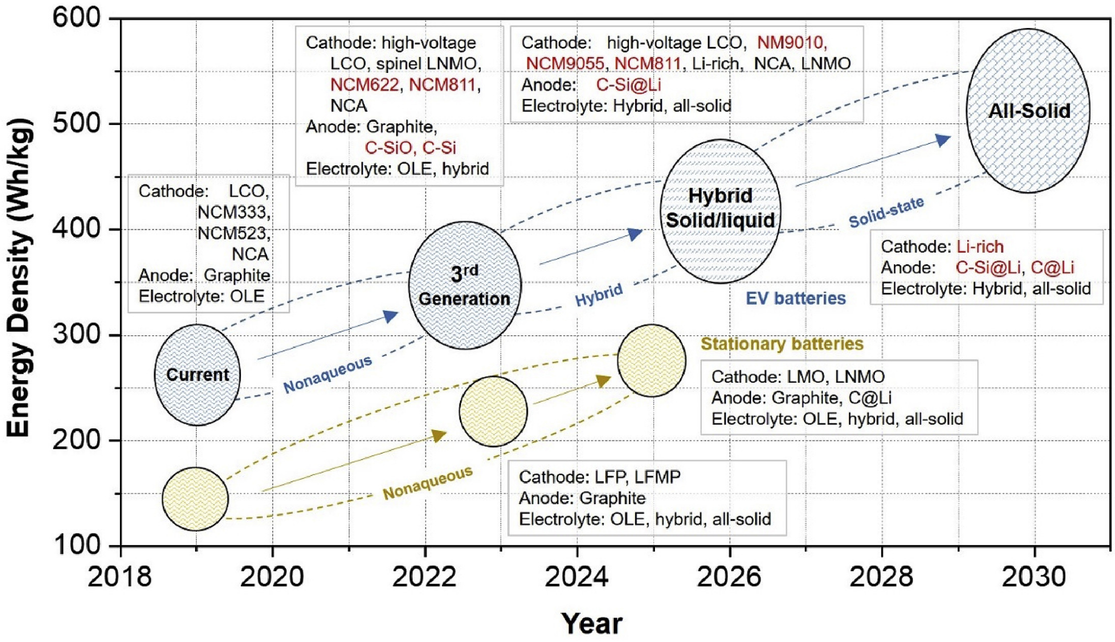

Figure 1.8: Development history of key materials and technologies of ASSBs, Reprinted with permission from [79], Copyright 2019 Elsevier

1.5.2 Solid-state Electrolytes

As a crucial component of the SSB system, the properties of the SSE play a vital role in determining battery performance. Due to the rigid structure of the anion framework in the SSE, many SSEs exhibit lower ionic conductivity compared to liquid electrolytes. Consequently, considerable effort has been devoted to the design and synthesis of SSEs with high ionic conductivity over the past decades. As summarised in Figure 1.9, many SSEs have been developed with significantly improved ionic conductivity, some of which have even surpassed that of liquid electrolytes.

1.5.2.1 Solid polymer electrolyte

Solid polymer electrolytes (SPEs) can be defined as the solid solution of alkali metal salts in a polymer host, without liquid organic solvents existing in the system[81]. SPEs offer benefits in terms of interfacial contact, which are attributed to the soft

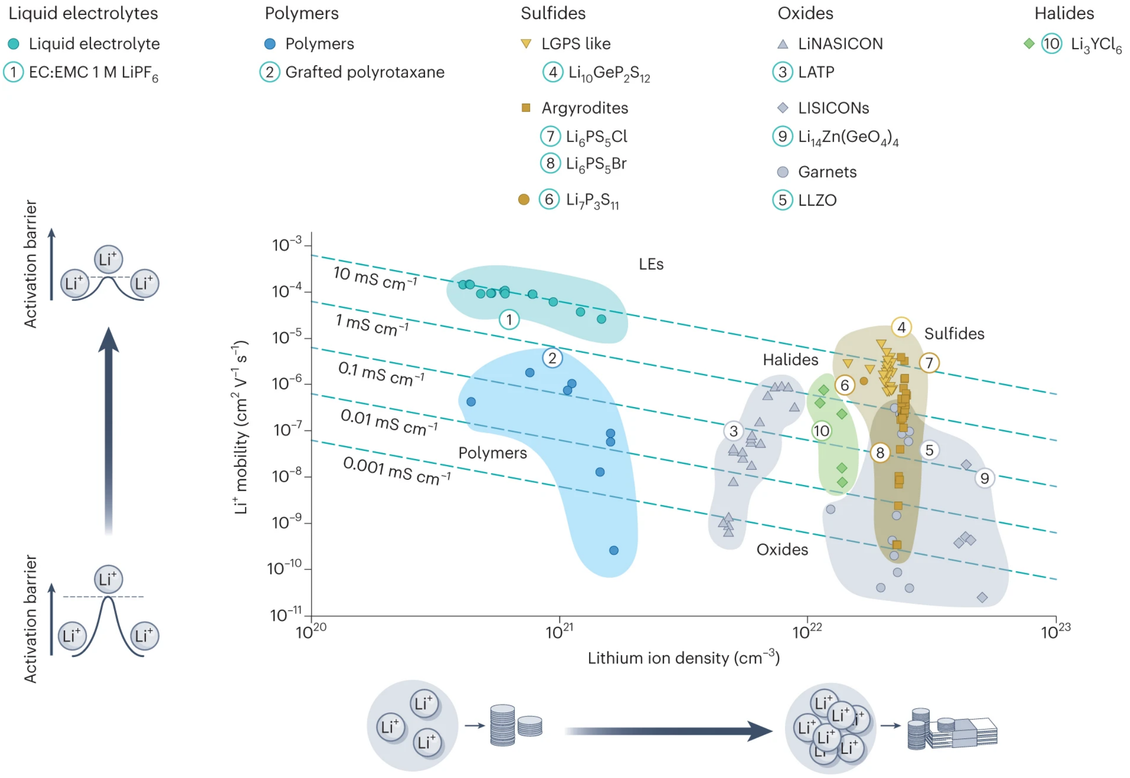

Figure 1.9: Summary of different groups of solid electrolytes; SSEs with equal conductivity lie on dotted conductivity lines. The diffuse clouds indicate different groups of SSEs. Reprinted with permission from [80], Copyright 2019 Springer Nature

nature of SPEs compared to their inorganic counterparts. The most frequently used polymer matrices include polyacrylonitrile (PAN), poly(vinylidene fluoride)(PVDF), poly(ethylene oxide) (PEO), poly(ethylene carbonate) (PEC), etc[72, 82–84]. The implementation of lithium salts, such as lithium tetrafluoroborate ($LiBF_4$), lithium bis(trifluoromethanesulfonyl)imide (LiTFSI), lithium perchlorate ($LiClO_4$), etc, is mainly to improve the ionic conductivity, whilst modifying the mechanical and thermal properties of the composite electrolyte[85–87]. Some other fillers can be incorporated into the structure to improve its mechanical and thermal properties. Compared to conventional liquid electrolytes, the application of SPEs can address the challenges associated with electrolyte leakage and flammability. However, since the matrix often contains a significant amount of carbon in the structure, it remains inherently flammable, necessitating improvements in flame retardance[72].

1.5.2.2 Inorganic SSEs

Inorganic SSEs are mainly composed of oxide SSEs, sulphide SSEs, and halide SSEs according to their composition.

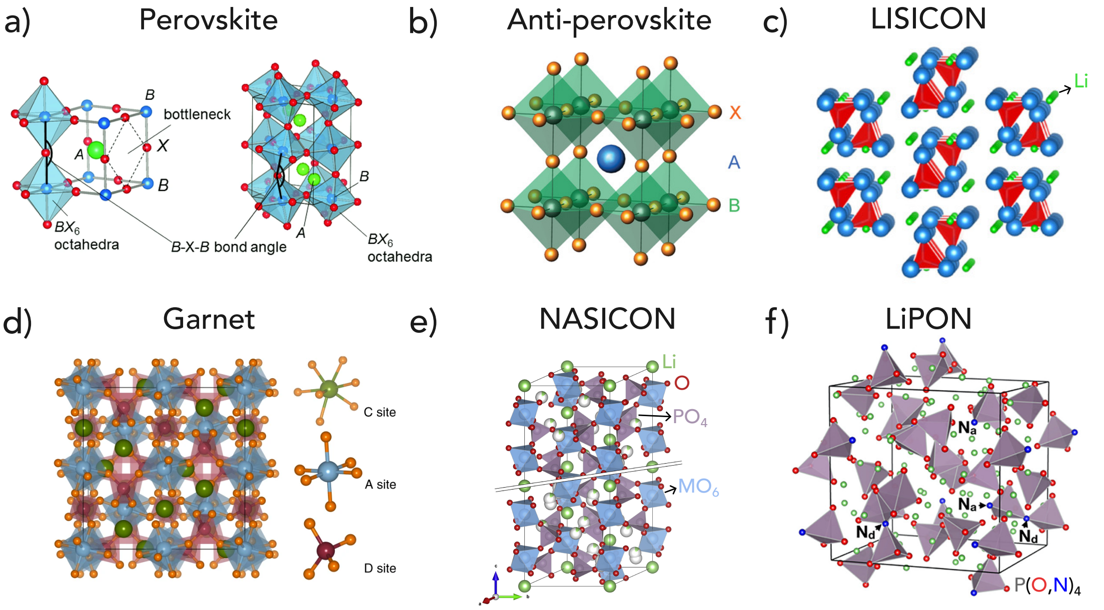

Figure 1.10: Schematic of crystal structure of oxide solid electrolytes: a) Perovskite, Reprinted with permission from [88], Copyright 2021 Springer Nature; b) Antiperovskite, Reprinted with permission from [89], Copyright 2019 John Wiley and Sons; c) LISICON, Reprinted with permission from [90], Copyright 2022 American Chemical Society; d) Garnet, Reprinted with permission from [91], Copyright 2018 Springer Nature; e) NASICON-type electrolyte, Reprinted with permission from [92], Copyright 2018 Elsevier; f) Simulated amorphous LiPON structure with the composition of $Li_{2.94}PO_{3.50}N_{0.31}$, Reprinted with permission from [93], Copyright 2018 American Chemical Society

Oxide SSEs typically exhibit a rigid ceramic nature and good thermal stability, which reduce the risk of combustion and restrain lithium dendrite penetration. Additionally, oxides generally show better air stability compared to sulphides and halides. A few examples include perovskite-type, antiperovskite-type, NASICON-type and garnet-type oxides, each showing different structures respectively[72].

The general formula of perovskite-type SSEs is ABO_3 (A=Li, La, Sr; B=Ti, Zr, Hf, Sn, Ta, etc), where A sites are in 12-fold coordination and B sites are in 6-fold coordination as schematically shown in Figure 1.10a. One of the representative SSE is $La_{2/3\text{-}x}Li_xTiO_3$ (LLTO), of which the ionic conductivity is related to the bottleneck size and site percolation. However, its application with LMA is limited by the reduction of B^{x+} upon contact[88, 94–97]. Antiperovskite-type SSEs have a similar formula, X_3BA, where 'A' stands for halide ions (Cl^-, Br^-, I^-), 'B' represents O^{2-}, and 'X' denotes Li^+, with the anion and cation position inverted compared to perovskite structure. Though it has been reported to exhibit good stability against lithium metal, these materials have limited room temperature ionic conductivity and require a dry condition during the synthesis process due to their moisture sensitivity. Additionally, their oxidation stability needs improvement[98]. NASICON-type with the formula of $AM_2(PO_4)_3$ (M=Ti, Ge, Zr) is one promising SSE; by doping with various elements, its ionic conductivity can be further improved. The partial substitution of tetravalent metal ions in the structure with trivalent cations, such as Al^{3+}, Fe^{3+}, etc., is a promising method to improve the Li^+ concentration in the structure and the ionic conductivity. Typical examples include $Li_{1+x}Al_xTi_{2-x}(PO_4)_3$ and $Li_{1-x}Al_xGe_{2-x}(PO_4)_3$, with ionic conductivity of $\sim 10^{-4}$ S cm^{-1}[92, 99, 100]. Lithium super ionic conductors (LISICONs) have a similar crystal structure to that of γ-Li_3PO_4; some examples include $Li_{14}Zn(GeO_4)_4$, $Li_{3+x}Ge_xV_{1-x}O_4$ ($0<x<1$)[101] and $Li_{4-x}Si_{1-x}P_xO_4$ ($0<x<1$)[102]. Though the ionic conductivity of electrolytes within this type can be improved by substituting O^{2-} with Cl^- or substituting Si^{4+} with P (or Al, Ge), the application of these of electrolytes is limited by their low ionic conductivity, which is usually below 10^{-5} S cm^{-1} at room temperature. Garnet-type electrolytes with a general formula of $A_3B_2(XO_4)_3$, where A=Ca, Mg, Y, La, etc; B= Al, Fe, Ga, Ge, Mn, Ni, or V; X= Si, Ge, Al, have also been considered as promising solid electrolytes with their wide electrochemical stability windows. One typical example is the $Li_7La_3Zr_2O_{12}$ (LLZO) electrolyte with high ionic conductivity of $\sim 10^{-4}$ S cm^{-1} and high reduction stability against lithium metal[72, 103, 104].

In practice, the oxide SSEs are facing many challenges including their brittleness, unfavourable mechanical properties, and poor interfacial contact. These all require further investigation and solutions to achieve commercialisation[105].

A notable example that demonstrates good mechanical properties/dendrite resistance is lithium phosphorus oxynitride, commonly referred to as LiPON, which was first fabricated by Oak Ridge National Laboratory using radio-frequency (RF) magnetron sputtering for use as solid electrolyte[106]. LiPON is typically produced as an amorphous thin film (with a thickness of approximately $\sim 1\mu m$) to compensate for its limited lithium ionic conductivity (10^{-6} S cm^{-1}). It offers advantages such as superior stability against both the LMA and high-voltage cathodes, excellent long-term cycling stability, and the ability to enable flexible cell geometry designs, which will be discussed in detail in Chapter 5[107–109].

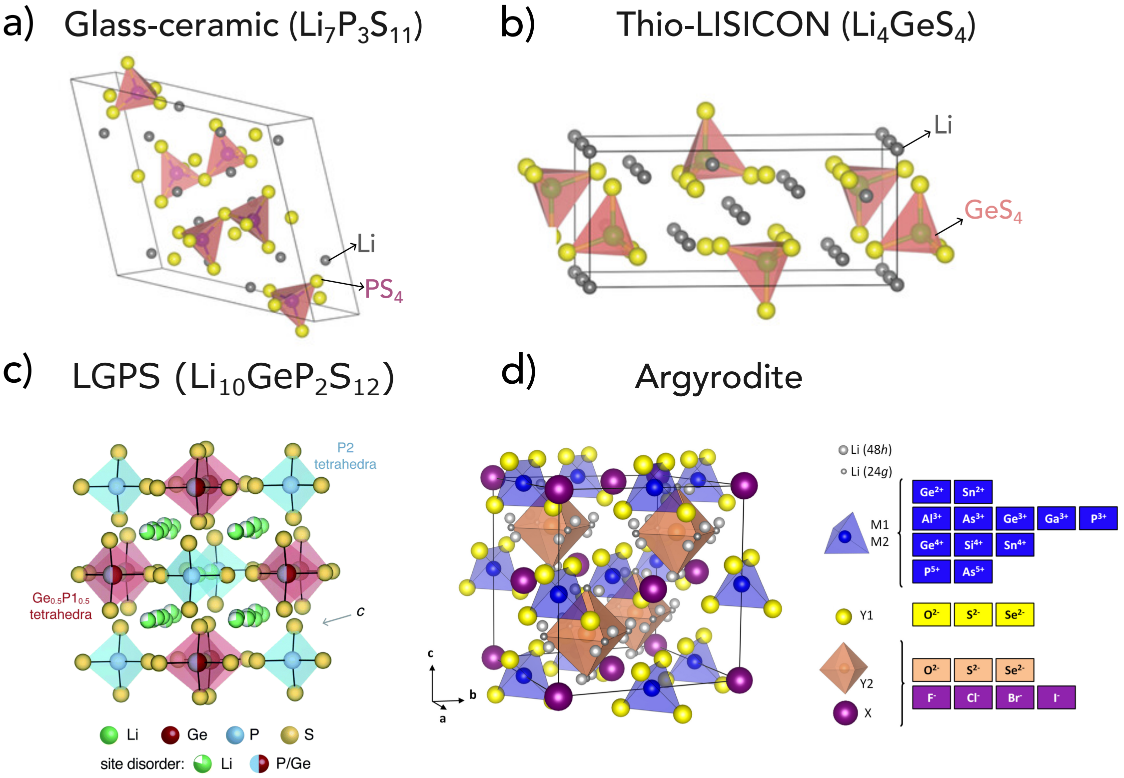

Figure 1.11: Schematic of crystal structure of four sulphide solid electrolytes: a) Glass-ceramic electrolyte with $Li_7P_3S_{11}$ as a typical example[110]; b) Thio-LISICON electrolyte, with Li_4GeS_4 as a typical example, Reprinted with permission from [110], Copyright 2023 John Wiley and Sons; c) LGPS-type electrolyte, Reprinted with permission from [111], Copyright 2020 Royal Society of Chemistry d) Argyrodite-type electrolyte, Reprinted with permission from [112], Copyright 2022 Elsevier

Sulphide SSEs are generally mechanically softer and possess higher ionic conductivity compared to oxide-SSEs. The investigation of sulphide solid electrolytes began with glass-type multicomponent systems, such as Li_2S-SiS_2, Li_2S-GeS_2 and Li_2S-P_2S_5

(shown in Figure 1.11a)[110, 113]. Subsequently, the development of thio-LISICON type SSEs, whose anion arrangements are similar to the LISICON-type γ-Li_3PO_4 electrolyte, led to advancements in electrolyte formulas. These SSEs have a general formula of $Li_{4\text{-}x}M_{1\text{-}y}M'_yS_4$ (where M = Si, Ge; M' = P, Al, Zn, Ga). Figure 1.11b illustrates the crystal structure of Li_4GeS_4 as an example, showing a monoclinic unit cell composed of GeS_4 tetrahedral building blocks charge balanced by Li^+[110, 114]. LGPS-type electrolytes with a general formula of $Li_{11\text{-}x}M_{2\text{-}X}P_{1+x}S_{12}$ (where M = Ge, Sn, or Si) have been reported with superior ionic conductivity, significantly boosting the development and investigation of sulphide-type solids. Although this group of SSEs may share the same elemental composition as some thio-LISICON type SSEs, LGPS SSEs feature a different crystal structure with a tetragonal unit cell. Depicted in Figure 1.11c is a typical LGPS-type electrolyte with the composition $Li_{10}Ge_2P_2S_{12}$, comprising PS_4 tetrahedra, LiS_4 tetrahedra, LiS_6 octahedra, and $(Ge_{0.5}P_{0.5})S_4$ tetrahedra[74]. Its practical application in LMBs is hindered by the high cost of Ge raw materials and the formation of a mixed-conductive interphase (which will be introduced in the next section) against lithium metal. Substituting Ge with lower-cost elements, such as Sn and Si, is an effective way to reduce costs but results in reduced ionic conductivity[115–117]. Argyrodite-type electrolytes, inspired by the high Ag^+ conductivity of Ag_8GeS_6, were developed, displaying promising ionic conductivity at the 10^{-2} S cm^{-1} level[118]. With a general formula of Li_6PS_5X (where X = Cl, Br, or I), argyrodite electrolytes can be synthesised using inexpensive precursors. Their ionic conductivity is related to the S^{2-}/X^- disorder in the structure, and with the goal of improving ionic conductivity, halide-rich argyrodite electrolytes have also been synthesised and investigated[119].

Some of the sulphide SSEs are derived from the parent structures of oxide SSEs. By comparison, S^{2-} has a larger ionic radius and lower electronegativity compared to O^{2-}, which results in weaker bonding with Li^+ and enlarged Li^+ conduction channels. This leads to generally higher ionic conductivity compared to oxide electrolytes as shown in Figure 1.9[74].

Although sulphide SSEs exhibit significantly improved Li^+ conductivity, they face challenges related to a limited electrochemical stability window (ESW), as schematically illustrated in Figure 1.13. Consequently, the formation of a stable SEI upon contact with an LMA is essential for achieving high cycling performance. Furthermore, sulphide SSEs are more prone to reacting with air, producing harmful H_2S gas and causing performance degradation[120].

Further research and exploration are necessary to understand the interfacial reaction mechanisms between sulphides and LMAs, as well as to develop effective interfacial modifications.

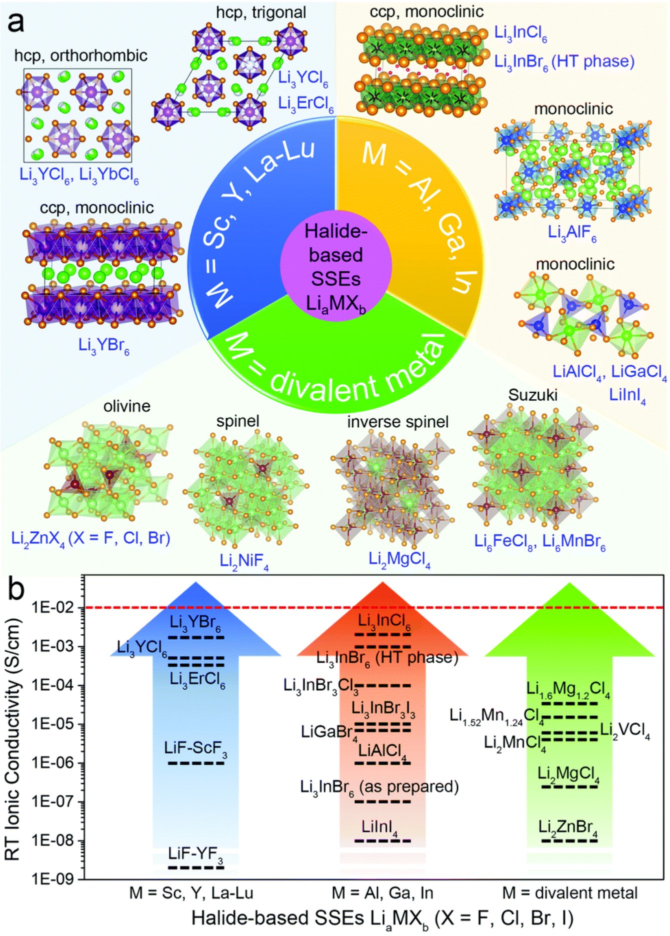

Figure 1.12: a) summary of different halide SSEs; b) summary of the ionic conductivities of some halide SSEs, Reprinted with permission from [121]

Halide SSEs , with the general formula Li_aMX_b (X = F, Cl, Br, I), can be divided into three categories based on the M elements (referring to metal elements):

M = group 3 elements, such as Sc, Y, and La to Lu; M = group 13 elements, such as Al, Ga, and In; and M = divalent metal elements, such as Ti, Fe, Zn, Cu, and Co. Some examples are listed in Figure 1.12, along with their corresponding ionic conductivities. One limitation of halide SSEs is their restricted ionic conductivity at room temperature, with only a few exceeding 10^{-3} S cm^{-1}, such as Li_3YBr_6 and Li_3InCl_6[122–124]. Additionally, halides exhibit poor stability against lithium metal, which is largely determined by the non-lithium cations in the structure. As depicted in Figure 1.13a, fluoride-based halide SSEs have higher oxidation onset voltages compared to other halides but at the cost of reduced ionic conductivity, owing to the small radius of F^-. Some recent reports attempt to apply halide SSEs as cathode active materials due to their oxidation stability at high potentials or sandwiched between other SSEs[121, 125, 126].

1.5.3 Challenges faced by all-solid-state batteries

Achieving high ionic conductivity has been a research focus for the last two decades, and today, the reported ionic conductivity for solid electrolytes at room temperature is on the order of 10^{-2} S/cm, comparable to ionic conductivity of liquid electrolytes and thus meets the targets for practical battery use[74, 127]. However, the practical application of SSBs still faces the following main challenges:

- Manufacturing process: The production of solid-state battery components must be scalable, cost-effective, and environmentally friendly. More importantly, the quality of the products must be ensured.

- Materials compatibility and interface stability: The electrolyte materials should be chemically and electrochemically stable against the electrode (both anode and cathode), as the unwanted reactions will consume the lithium source and lead to increased resistance and capacity fading.

- Mechanical properties: To ensure good physical contact, external pressure is usually applied, which needs to be restricted below $\sim$ 1MPa for practical application[80]. The mechanical properties of each component need to be compatible and capable of withstanding the pressures applied during the production and assembly processes, as well as the stress and strain generated during lithium ion insertion and extraction in the electrodes[128].

Interface-related phenomena, both electrochemical stability and mechanical stability, are now regarded as the greatest barriers to achieving the predicted high performance of SSBs.

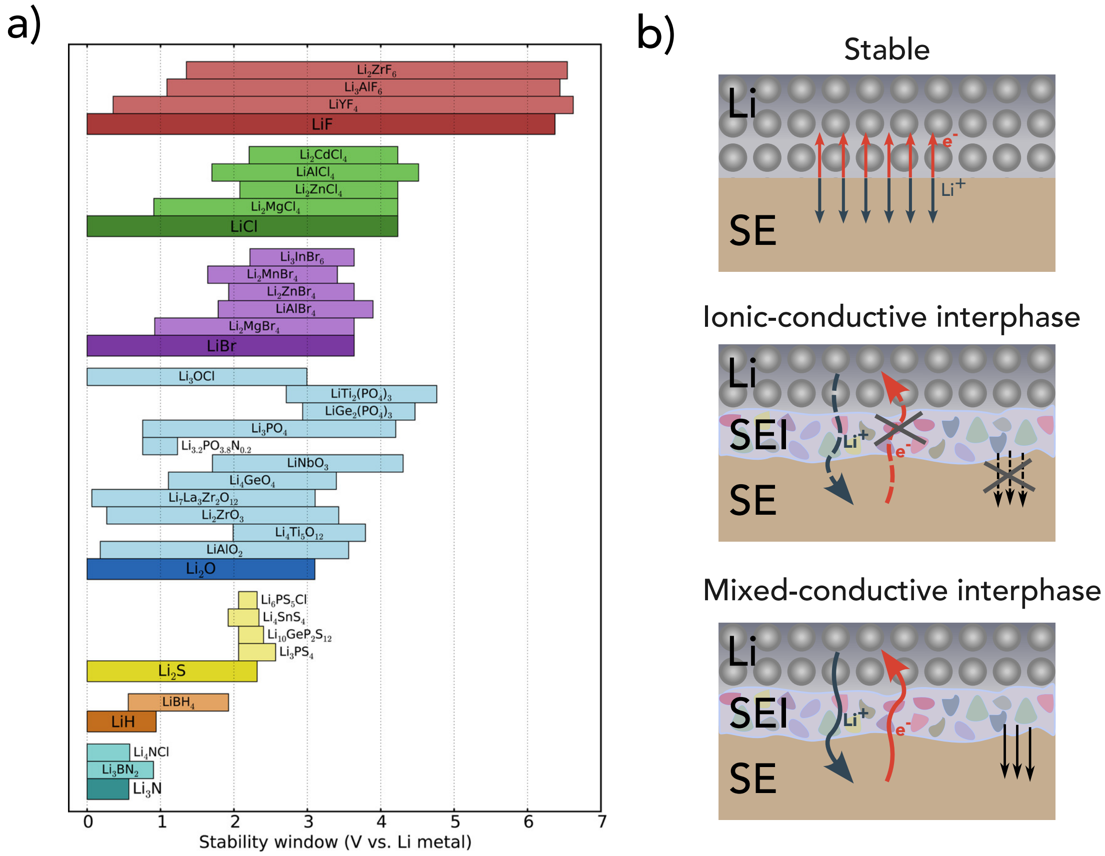

Figure 1.13: (a) Calculated electrochemical stability window of different SSEs grouped by anion in their structure, Reprinted with permission from [129], Copyright 2015 American Chemical Society; (b) Schematic of the three types of interface between SSE and lithium metal based on their electronic and ionic conductivities, Reproduced with permission from [130], Copyright 2015 Elsevier

1.5.3.1 Electrochemical stability and interfacial chemistry

Reactions occurring at the SSE-electrode interface are driven by the thermodynamics of creating stable phases, recognised as the interphase. To make it clear, the 'interface' is usually defined as the general two-dimensional contact area between two phases, and the ‘interphase’ is the reaction layer formed between electrolyte and electrode phases[131, 132].

Figure 1.13a summarises the ESW of some electrolytes categorised by the anion in their structure, all of which exhibit a limited stability window, particularly the sulphide electrolytes. Reactions between the electrolyte and electrode are expected upon contact or under cycling conditions, resulting in the formation of an ‘interphase’ composed of the different reaction products. This is denoted as the solid electrolyte interphase (SEI) at the anode side of the SSE and the cathode electrolyte interphase (CEI) at the cathode side of the SSE.

Clearly, most SSEs cannot maintain complete stability against lithium metal due to its low electrochemical potential, significantly limiting the performance of LMBs and hindering their commercialisation. Various strategies including surface treatments and SSE modifications have been extensively employed to address these interfacial challenges[133, 134]. Consequently, investigating the composition and behaviour of the formed interphases has become one of the most critical directions in SSB-related research[135].

According to Wenzel *et al.*’s work, the interface between the SSE and anode can be categorised into three types based on its electronic and ionic conductive properties as shown in Figure 1.13b[130].

- Thermodynamically stable interface: The SSE is stable when in contact with lithium metal; no SSE decomposition happens in this case. For example, lithium binary compounds such as Li_2O and LiCl are stable against lithium but have very limited ionic conductivities[136].

- Thermodynamically unstable but kinetically stable interphase: The formed interphase is ionically conductive but not electronically conductive, or it presents ultra-low electronic conductivity, thereby prohibiting the growth of the interphase. This type of interphase is typically referred to as the solid electrolyte interphase (SEI). In such cases, the formed SEI can function as a protective layer between the SSE and the LMA[64].

- Thermodynamically and kinetically unstable interphase, also referred to as a mixed-conductive interphase (MCI): This type of interphase contains both ionically and electronically conductive phases. This dual conductivity provide both ionic and electronic pathways throughout the formed interphase, which in turn drives the sustained decomposition of the SSE. As a result, the interphase continues to grow over time, potentially leading to short circuits and eventual cell failure. Furthermore, the ongoing reactions deplete the LMA, compromising cell performance and longevity. The electronic conductive phases are normally metals or lithium alloys which originate from the reduction of metal cations in the SSE structure. A representative example is the LGPS SSE, in which the interphase contains elemental germanium metal formed through reduction reactions with lithium metal.

As a result, a multi-component SEI, which usually possesses distinct properties from the bulk electrolyte, forms due to the electrochemical decomposition happening between SSEs and the LMA. This SEI layer would continue to grow until it blocks the electron leakage. These considerations highlight the importance of investigating the reaction pathways between SSEs and lithium metal, as well as the composition of the formed SEI. Additionally, the impact of the interfacial layer on battery performance is influenced by several factors, including its composition, nanostructure, and spatial distribution. As the SEI is a buried layer in conventional cell designs, its characterisation requires advanced techniques. These characteristics pose significant challenges for interface research, as the mechanisms underlying its degradation are still not fully understood.

1.5.3.2 Mechanical and morphological-related factors

Other than the chemical and electrochemical properties of different cell components, including electrolyte, electrode and the formed SEI, the volume change and the mechanical- and morphological-associated phenomena during repeated charge-discharge cycles also play an important role in determining the battery performance, as summarised in Figure 1.14.

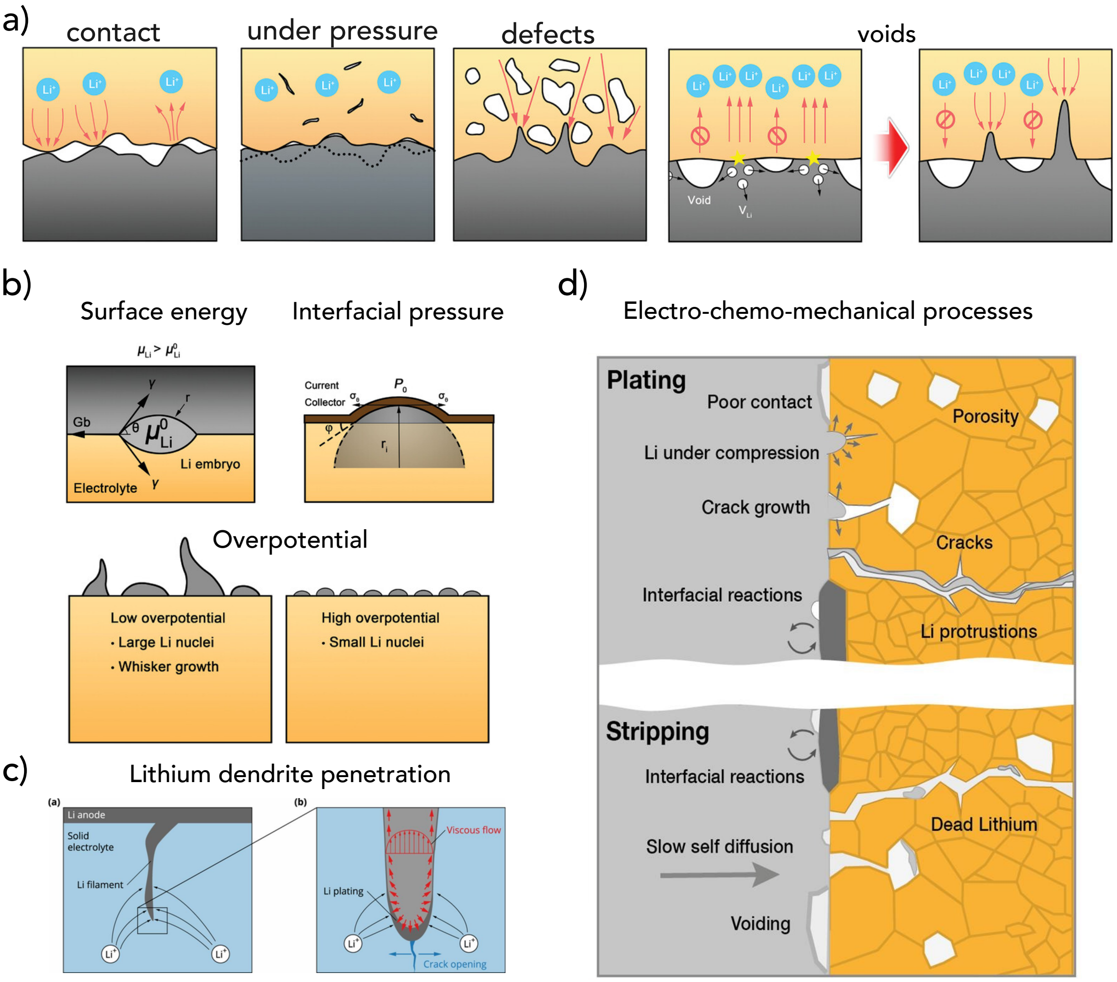

Figure 1.14: (a) Interfacial morphology related factors that affect the battery performance; (b) Schematic of lithium nucleation mechanism and its related factors, (a and b) Reproduced with permission from [137], Copyright 2021 John Wiley and Sons; (c) Schematic of lithium dendrite penetration through SE, Reprinted with permission from [138], Copyright 2019 Journal of The Electrochemical Society; (d) Summary of electro-chemo-mechanical processes occurring at Li/SE interface, Reprinted with permission from [139], Copyright 2022 Elsevier

In LIBs, liquid electrolytes can infiltrate the electrode structure, facilitating good contact between the electrolyte and the electrodes, providing an Li^+ pathway. By contrast, in SSBs the Li^+ pathway and the charge transfer process heavily rely on good physical contact between individual particles (including both electrolyte and electrode materials). Pre-existing defects and inadequate contact can lead to inhomogeneous current distribution, increased impedance and formation of lithium dendrites as shown in Figure 1.14. In most published works, an external pressure is applied to ensure intimate solid-solid contact inside the SSBs, thus achieving good cycling performance. However, practical applications usually require a low stack pressure, typically less than 1 MPa[140–143].

According to the Monroe-Newman model, when the shear modulus of SSEs exceeds twice that of lithium metal (4.8 GPa at room temperature), the formation and growth of lithium dendrites should, in principle, be inhibited[68]. However, lithium dendrite-induced cell failure has been observed in solid electrolytes such as LLZO and LPS, despite their shear moduli being higher than this threshold[131, 144–146], suggesting a more complex mechanism for lithium dendrite growth. In summary, mechanical properties is not the sole factor influencing the formation and penetration of dendrites; other factors including chemical, physical and cycling conditions, also contribute to dendrite growth[137]. The existence of grain boundaries and surface defects can provide preferential sites for lithium plating. Additionally, the volume changes during the charge-discharge cycle result in void formation and contact loss, which facilitate the growth of lithium dendrites due to a non-uniform distribution of current[128].

1.5.3.3 The importance of studying SEIs

The above discussion introduces the main issues related to the interface between SSEs and the LMA, including side reactions, physical contact and the formation of lithium dendrites. To achieve high performance in SSBs an ideal SEI is required, which can be realised through SSE modification or surface engineering. An ideal SEI should possess the following properties:

- stability against lithium metal and SSEs,
- mechanical flexibility to withstand volume changes and dendrite propagation,
- good ionic conductivity and poor electronic conductivity to prevent continuous SEI growth while avoiding high impedance,
- morphologically thin, dense and uniform structure to promote uniform lithium plating/stripping and minimise interfacial resistance.

The formed SEI layer serves as a physical barrier between the SSE and the LMA, preventing further decomposition of the SSE and electrode corrosion. Beyond its transport properties, the mechanical properties and chemical stability of this layer significantly affect battery performance.[147] Indeed, obtaining precise information about interface evolution poses challenges as it is buried underneath the electrode and is not readily accessible by the majority of characterisation techniques. Meanwhile, the complex structure of the nanometre-thick SEI layer brings difficulties for its investigation. Still, after being investigated for more than two decades, the SEI has been regarded as "the most important but the least understood" part due to its complexity[148, 149].

The following section will introduce some characterisation techniques that have been applied to investigate interfaces and interphases in SSB systems.

1.6 Characterisation of interface/interphase in SSBs

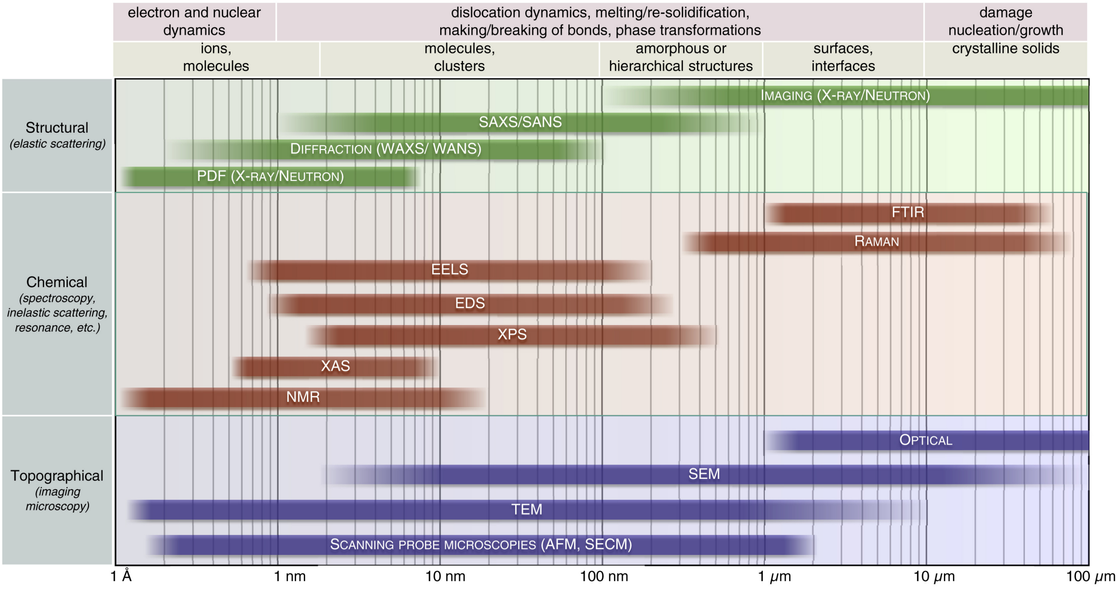

Figure 1.15: Summary of different characterisation techniques applied in the battery field, with lateral and depth resolution and information obtained included, Reprinted with permission from [150], Copyright 2021 Elsevier

1.6.1 Different interfacial characterisation techniques

Different microscopic and spectroscopic techniques capable of providing information from different scales and aspects have been employed to investigate interfacial behaviour; some of the commonly used techniques are listed below.

Microscopic techniques, including optical, electron, and scanning probe microscopy, can provide high-resolution information across various scales and are capable of probing a sample's chemical, electrical, magnetic, and topological properties.

Scanning electron microscopy (SEM) is capable of providing detailed morphological observations of the interface between the electrolyte and electrode and also the lithium plating morphology. Meanwhile, when coupled with energy dispersive X-ray analysis (EDX), it can also provide insights into elemental composition and distribution by collecting emitted characteristic X-rays[151].

Transmission electron microscopy (TEM) is a powerful technique for characterising nanoscale features such as crystal structure, morphology, and grain boundaries with resolution down to the $\sim$Å level. Additionally, performing electron energy loss spectroscopy (EELS) can help to determine the type and quantity of atoms present in the materials, and also their chemical state. However, sample preparation can be challenging as it sometimes requires using a focused ion beam (FIB) to prepare the electron-transparent thin samples, during which the pristine sample may be distorted or damaged. Similarly, the irradiation of high-energy electrons during the imaging process can cause radiation damage, altering the sample information. Consequently, cryo-TEM—where the sample is maintained at a low temperature—is often preferred, especially for sulphide solid electrolytes, to minimise beam damage. Thus, TEM characterisation is typically time-consuming and costly[152].

Atomic Force Microscopy (AFM) operates by scanning a fine probe tip (typically with a radius of a few nanometres) across the sample surface. When different tips and scanning modes are applied, AFM yields information about the sample's morphological, mechanical, and physical properties, such as surface roughness, electronic conductivity, surface potential, and Young's modulus. AFM generally requires a relatively flat surface, as the cantilever has a limited movement and deflection range, and also has limited temporal resolution[153].

Spectroscopic techniques measure the interaction of materials with electromagnetic radiation. Incident radiation of varying frequencies or energies interacts with the sample, resulting in reflection, transmission, and emission. By collecting the resulting radiation, detailed information about the sample's chemical composition, valence state, crystal structure, vibrational modes, defects, and other properties can be investigated.

X-ray diffraction (XRD) has its advantages in probing crystalline materials but is limited to probing relatively thicker SEIs, due to the incident angle, unless grazing angle XRD is applied. However, key information may be missing when amorphous phases are present in the SEI[151].

Raman spectroscopy (RS) applies a monochromatic laser of known wavelength to illuminate the sample while the scattered light is collected, processed and analysed. The frequency difference between the incident probing light and the scattered light is referred to as the Raman shift, which corresponds to the vibrational energy levels of the characterised systems. By plotting the intensity of the scattered light as a function of its frequency, RS measurements show advantages in probing the molecular structure and chemical information of electrodes and SSEs, thus helping to understand the failure mechanisms of batteries [154]. RS has its limitations when metal phases and laser-sensitive materials are evolved in the system.

X-ray photoelectron spectroscopy (XPS) is based on the photoelectric effect by using a monochromatic X-ray source of known energy. The emitted photoelectrons are collected by the hemispherical detector and a plot of intensity against binding energy (BE) is produced. It is a surface-sensitive technique determined by the limited escape depth of emitted photoelectrons, which is about 10 nm. The value of the BE helps identify the element and its chemical state, as well as its electronic and bonding environment, and the relative composition can be calculated from the peak intensity, making it a superior technique for the investigation of SEI chemistry. Its sample preparation is also relatively easy, and it is a non-destructive technique. The Ar-ion sputtering depth profile enables the investigation of SEI evolution over thickness, but sample damage-induced changes must be considered when processing the collected data[139].

1.6.2 The necessity of *in situ*/*operando* analysis

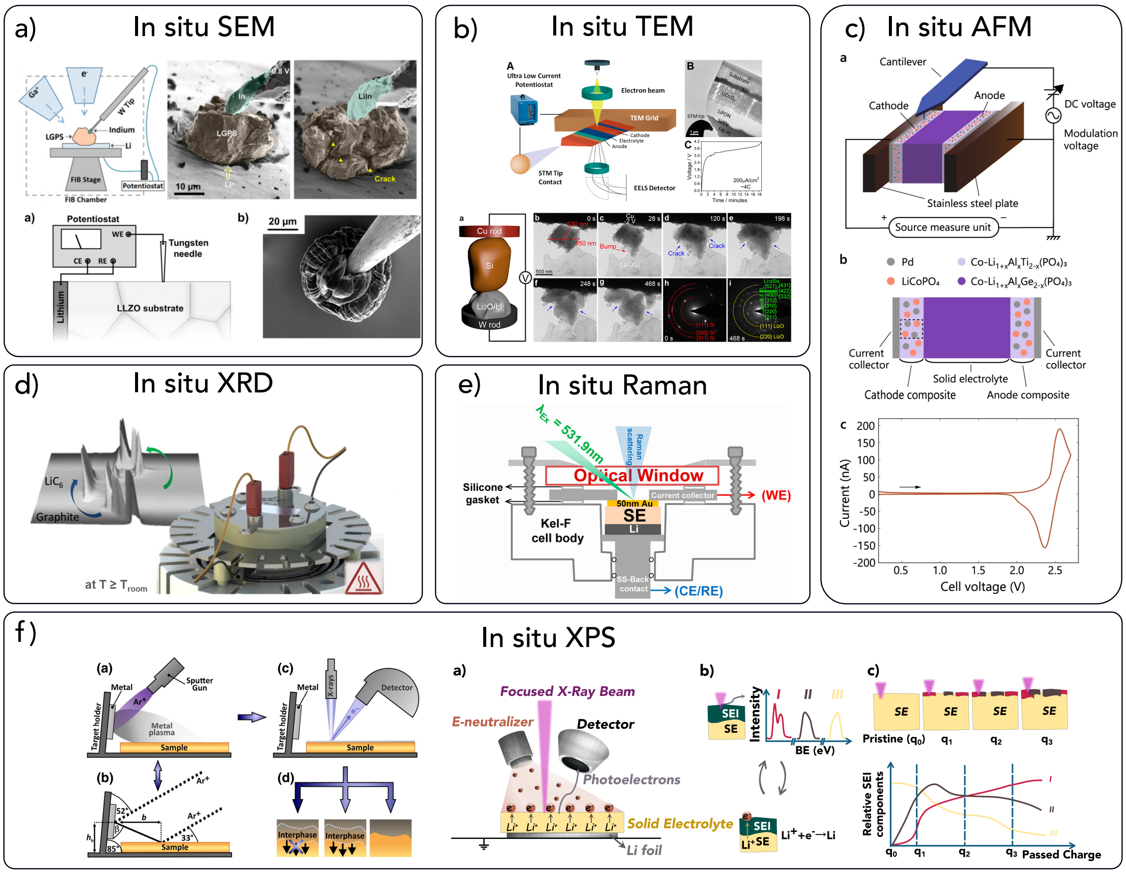

Figure 1.16: Summary of *in situ/operando* characterisation techniques: a) *In situ* SEM for the investigation of morphological evolution and lithium plating behaviour, Reprinted with permission from [155], Copyright 2022 American Chemical Society and [156], Copyright 2020 John Wiley and Sons; b) *In situ* TEM characterisation using a specially designed TEM holder, Reprinted with permission from [157], Copyright 2016 American Chemical Society and [158], Copyright 2016 Springer Nature; c) *In situ* AFM schematic for dynamic visualisation of potential evolution during cell cycling, Reprinted with permission from [159], Copyright 2019 Springer Nature; d) *In situ* XRD cell setup, Reprinted with permission from [160], Copyright 2017 Elsevier; e) *In situ* Raman setup, Reprinted with permission from [161], Copyright 2017 American Chemical Society; f) *In situ* XPS technique for SEI investigation, Reprinted with permission from [130], Copyright 2015 Elsevier, and [162]

The conventional process of accessing the is SEI referred to as '*ex situ*' analysis, and involves removing the cell from its original testing setup after electrochemical cycling, at which point the materials' evolution is halted. This process includes steps such as cell disassembly after reaching a specified state, sample washing (in cases of liquid electrolyte), sample cutting, and sample transfer. All these procedures must be performed in an inert environment, as most materials are sensitive to oxygen and moisture. However, these steps pose the risk of losing or damaging sample information, potentially compromising the reliability of the results[162].

In response to these challenges, scientists are actively exploring *in situ* or *operando* techniques to acquire real-time information about SEI evolution, thereby overcoming the limitations associated with traditional sample handling procedures, including the potential loss or alteration of information during sample preparation and loading. '*In situ*' refers to conditions where materials are retained in their original electrochemical testing environments during characterisation, whereas '*operando*' denotes that characterisation is conducted during the electrochemical cycling process. In this work, the term '*in situ*' is primarily used because it encompasses '*operando*' in most cases.

Many *in situ* investigations have been conducted for various purposes, not only to study SEI evolution but also to explore failure mechanisms, such as the formation and penetration of lithium dendrites, stress and strain evolution, and crack propagation. To conduct these *in situ* experiments, sample conformation and cell design are often compromised to load the sample safely into the characterisation system and ensure efficient data collection[150], as illustrated in Figure 1.16. Although the conditions of the devices or cell conformations used in *in situ* characterisation differ from those used in practical applications, combining various characterisation techniques can offer valuable insights into the changes occurring within the battery during cycling from different perspectives. These approaches effectively aid our understanding of the mechanisms behind battery failure, thus helping to improve battery performance further.

1.7 Aims and objectives of this work

The previous discussion has highlighted the significant impact of the SEI on battery performance. Characterising and analysing the SEI and its evolution during the electrochemical cycling process is a crucial aspect of battery research since it holds the potential to improve understanding of the degradation mechanism. Among these investigations, examining the reactions between the electrolyte and lithium metal and their reaction products, particularly the composition of the interfacial layer, is of paramount importance. Understanding the interfacial layer composition can reveal critical information about its conductivity and stability, providing vital insights for electrolyte design and interface engineering.

XPS, characterised by its surface sensitivity and element specificity, is an ideal technique for investigating surface chemistry. It is also well-suited for studying the bonding environment in amorphous phases, which are often present in SEIs. In addition, the recently developed *in situ*/operando XPS techniques (which will be discussed in detail in Section 2.1.2) allow electrochemical reactions to occur within the XPS chamber, enabling the formation of the SEI *in situ* on the top surface of SSE pellets. These techniques are highly effective in providing insights into the electrochemical evolution during lithium deposition and in revealing the reaction pathways of different SSEs with the LMA[130, 163–165].

Chapter 3 compares SEI formation between two promising SSE candidates, LGPS and LAGP, demonstrating that LAGP can form a more stable SEI compared to LGPS. This is primarily attributed to the presence of a less conductive phase in the SEI structure. This study constitutes the first application of the *in situ* XPS characterisation technique to investigate SEI formation on LAGP. Additionally, this work provides a potential new method for probing SEI evolution kinetics; however, it requires a ultra-high vacuum (UHV) condition, ideally at a pressure level of 10^{-9} Pa or lower.

Chapter 4 investigates the properties of the SEI formed between LPSCl and lithium metal, as LPSCl is considered one of the most promising candidates among sulphide-based SSEs. While previous studies using electrochemical methods have reported that SEI formation follows a linear relationship with the square root of time, this work employed *in situ* XPS to assess the stability of the resulting SEI. The results revealed that the SEI continues to evolve, particularly through transformations involving phosphorus-containing species. Furthermore, when combined with the CTTA results, it becomes evident that SEI growth deviates from the expected linear trend—especially during the initial stages of formation.

Chapter 5 systematically studied the SEI formation on LiPON SSEs, including both thin-film and bulk LiPON samples. This is the first time that *in situ* XPS, which employs the electron beam to drive the Li^+ migration, has been applied to study the SEI evolution on the LiPON sample. The result reveals the structural breakdown process with continuous lithium plating, and the formed SEI displays a graded structure with the most reduced lithium binary phases closest to the lithium side.

2

Experimental techniques

Contents

This chapter introduces the experimental techniques used in this work, covering both sample preparation and characterisation methods. More detailed information on sample preparation and specific experimental conditions is provided in the respective chapters.

2.1 X-ray photoelectron spectroscopy (XPS)

2.1.1 Theory of XPS

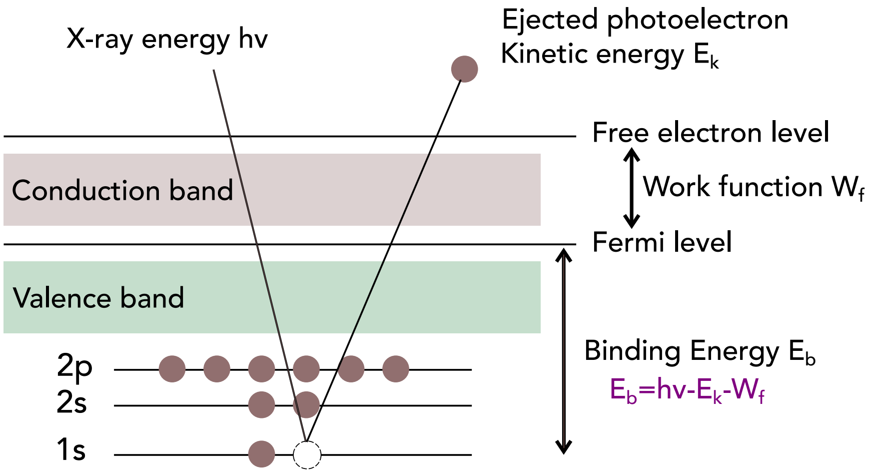

Figure 2.1: Schematic of the Working Principle of X-ray Photoelectron Spectroscopy (XPS) Measurement

2.1.1.1 Working mechanism

The working mechanism of XPS is based on X-ray radiation and the photoelectric effect as illustrated in Figure2.1. The sample is exposed to X-rays, which eject photoelectrons from various energy levels of surface atoms. Subsequently, these ejected photoelectrons are collected and analysed by a hemispherical analyser, which measures the kinetic energy and intensity of the photoelectrons. The binding energy $\mathrm{E_b}$ of the electron is calculated by Equation 2.1

$$E_b = h\nu - E_k - W_f \tag{2.1}$$

where, hν is the photon energy, E_k is the kinetic energy of the ejected photoelectron, and W_f is the work function of the spectrometer. The energy of these photo-emitted core-level electrons provides a wealth of information, including chemical composition, the valence states of different elements, and electronic structures.

2.1.1.2 X-ray sources

Table 2.1: Characteristics of some commonly used X-ray sources [166]

Anode materials (X-ray line)	Energy (eV)	Linewidth (eV)
Mg Kα	1253.6	0.70
Al Kα	1486.6	0.85
Ag Lα	2984.4	2.6
Ti Kα	4510.0	2.0
Cr Kα	5417.0	2.1

Lab-based X-ray sources are generated by bombarding a metallic anode, such as Mg or Al, with high-energy electrons via fluorescence. The electron beam is typically produced by a hot filament cathode, often LaB_6. A list of some available anode materials is provided in Table 2.1[166]. The energy of the X-ray source determines the transitions that can be probed and the probing depth, while the linewidth largely determines the resolution of the measurement. During the fluorescence process, other characteristic X-ray lines, background radiation, and satellite X-rays are also generated, which can degrade the quality of the collected XPS data. Consequently, a monochromator system is employed to select a single X-ray line while blocking other emissions from the anode.

2.1.1.3 Monochromatic system and hemisphere analyser

The monochromator (quartz crystal) is positioned at a specific angle to allow only the Al Kα X-rays (the X-ray source used in this work) to diffract and then reach the sample surface as shown in Figure 2.2a, which significantly improves the data quality[166].

The emitted photoelectrons are collected and analysed by the hemisphere analyser, where the inner hemisphere maintains a more positive potential than

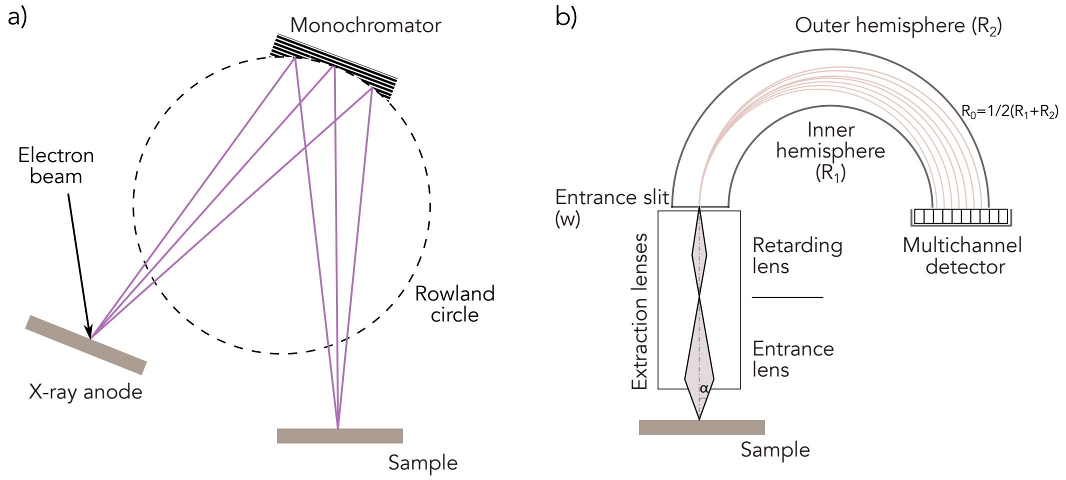

Figure 2.2: Schematic of (a) the monochromator; (b) the photoelectron collecting system, Reproduced with permission from [166], Copyright 2020 American Vacuum Society

the outer hemisphere. Before entering the hemisphere analyser, photoelectrons are initially collected and manipulated by the extraction lenses, which control the acceptance angle and sampling area. Additionally, the retarding lens reduces the energy of the photoelectrons to a fixed value, known as the pass energy E_p (defined by Equation 2.2).

$$E_p = \frac{e\Delta V}{R_2/R_1 - R_1/R_2} \tag{2.2}$$

Here, ΔV represents the potential difference between the inner and outer hemispheres, while R_1 and R_2 denote the radii of the inner and outer hemispheres, respectively.

As the photoelectrons travel through the hemisphere they are deflected, and only those with specific energies reach the multichannel detector. Equation 2.3 defines the energy resolution (ΔE).

$$\frac{\Delta E}{E_p} = \frac{w}{2R_0} + 2\alpha^2 \tag{2.3}$$

Here, w is the entrance slit width, R_0 is the analyser radius and α is the angular spread of incident electrons. Lower pass energy will give a higher resolution but at the cost of total signal intensity[167]. The energy step size, which is the range over which the channel detects photoelectrons, correlates with the pass energy;

typically, the larger the pass energy, the wider the energy step size, allowing more photoelectrons to be detected. Therefore, a survey scan is typically performed at a higher pass energy (approximately 100 eV) to identify the elements present in the system. This is followed by high-resolution scans at lower pass energies to analyse the chemical states and bonding environments, as well as to enable quantitative analysis.

2.1.1.4 Surface sensitivity of XPS

Typically, the penetration depth of X-rays (approximately 1-3 keV) in solid materials is at the micrometre level and varies significantly depending on the energy of the incident X-rays, the nature of the materials, and the incident angle[168]. The surface sensitivity of XPS arises from the limited escape depth of X-ray ejected photoelectrons. As photoelectrons travel through a solid, they experience inelastic scattering, which significantly attenuates those originating from deeper regions. Consequently, only photoelectrons emitted from the uppermost surface layers can escape without energy loss. This renders XPS highly surface-sensitive and particularly well-suited for investigating surface chemistry and interfacial phenomena. To be collected by the detector with its original energy information retained, the ejected electrons must travel through the solid and escape the surface without undergoing energy loss[169].

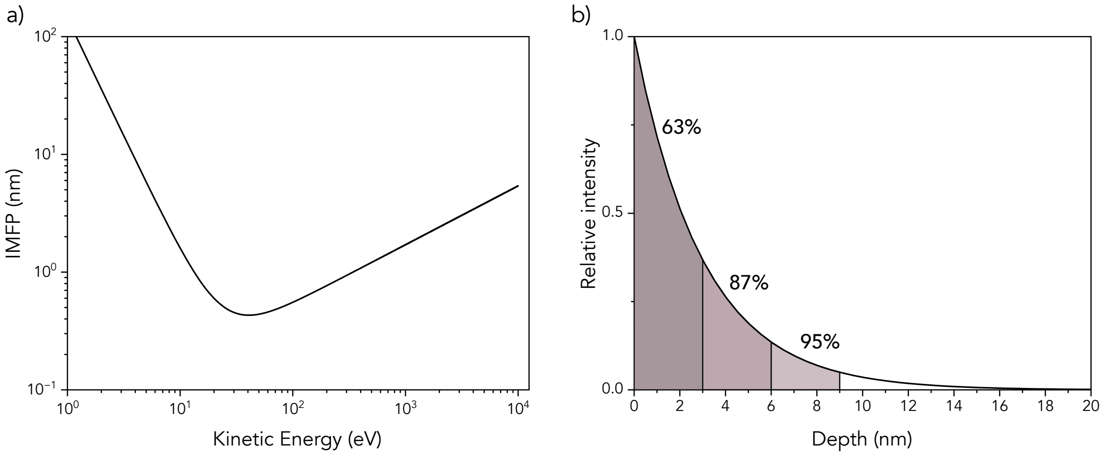

Figure 2.3: (a) Schematic of the universal curve for the electron inelastic mean free path (IMFP) based on equation $\lambda= \frac{143}{E^2}+0.054\sqrt{E}$, where E is the kinetic energy of ejected photoelectrons [170]; (b) Intensity attenuation curve based on Beer-Lambert law assuming λ=3 nm

Therefore, it is essential to introduce the concept of inelastic mean free path (IMFP, λ), which defines how far an electron can travel through the solid before losing energy. As shown in Figure 2.3a is the universal curve for λ; the value of λ depends on the energy of the photoelectron (affected by the light source) and the characteristics of the characterised materials.

$$\lambda_{IMFP} = \frac{a}{(E_k)^2} + b \times (E_k)^{\frac{1}{2}} \tag{2.4}$$

Here, a and b are material-dependent constants and E_k is the kinetic energy of ejected photoelectrons. In another way, IMFP refers to the average distance that electrons of a given energy can travel without undergoing inelastic collisions, which result in energy loss. The scattering process can occur in all phases—solid, liquid, and gas. Due to this, most XPS measurements are performed under high vacuum conditions, aside from ambient pressure XPS which will not be discussed here.

The intensity of the photoelectrons attenuates exponentially and can be calculated according to the Beer-Lambert law (Equation 2.5).

$$I_s = I_0 \times e^{\frac{-x}{\lambda}} \tag{2.5}$$

Here, I_0 is the intensity of the emitted photoelectron at a depth x below the surface and I_s is the intensity as the photoelectron reaches the surface. This is schematically shown in Figure 2.3b, assuming λ equals 3 nm. The detection depth of XPS is typically considered to be 3λ, within which approximately 95% of the detected signal originates. As a result, photoelectrons generated deep within the sample lose all their energy during inelastic collisions before escaping the sample surface. Photoelectrons generated near the surface may escape after a few collision events; however, these electrons lose part of their energy, contributing to the spectral background and Auger peaks. Only photoelectrons emitted from the surface escape without energy loss, contributing to the characteristic peaks in the XPS spectra[166].

The sampling depth for most materials used in battery applications ranges from 5 to 10 nm; however, this depth can be extended for materials containing light elements. For example, a Li 1s core-level photoelectron with a binding energy of

54 eV, ejected by Al Kα x-rays, has an λ_{IMFP} of 5.36 nm (through lithium metal), resulting in a sampling depth of about 16 nm[171]. The limited escape depth of the photoelectrons confirms that XPS is a surface-sensitive technique that allows the characterisation of surface information.

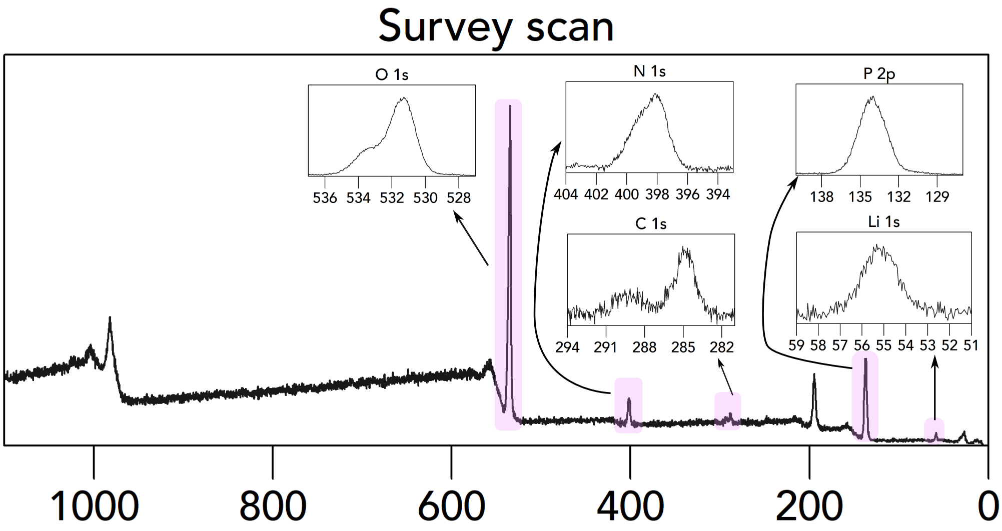

Figure 2.4: Example of XPS survey scan and high-resolution scans taken from a LiPON sample surface, detailed fitting will be discussed in Chapter 5

2.1.1.5 Calibration of XPS spectra and its fitting

Samples with low electronic conductivity, such as insulators and semiconductors, are susceptible to surface charging during XPS measurements, owing to the accumulation of positive charge resulting from photoelectron emission. Since the identification of elements and their chemical states in XPS relies on BE values, accurate BE calibration is essential for reliable analysis. The C 1s peak from adventitious carbon contamination is commonly used for charge calibration when it is the only carbon species present in the sample. This peak, attributed to C-C/C-H bonding, is typically referenced at 284.8 eV, though values around 285.0 eV are also reported in some cases[172, 173]. Alternatively, internal references can be used for charge calibration in specific systems. For instance, in studies of SEI formation on argyrodite-based SSEs, the Cl 2p core-level signal is often employed, as its binding energy remains stable during interfacial evolution[174–176].

When fitting the spectra, the background signal—primarily arising from photoelectrons that have lost energy through inelastic scattering during their escape from the sample—must be subtracted for accurate fitting and quantification. Three commonly used background subtraction methods include linear, Tougaard and Shirley backgrounds. The linear background assumes a straight-line relationship between two points selected on either side of the region of interest. The Tougaard type background accounts for the continuous distribution of energy losses due to inelastic scattering events, providing a more physically accurate representation of the background compared to simpler models. However, its implementation involves more complex mathematical treatment and computational effort. The Shirley type background is an S-shaped background based on the assumption that the background intensity at a specific BE is proportional to the integrated signal intensity at higher BE values. It is commonly used for fitting spectra that exhibit step-like changes over the energy range of interest[177, 178].

The core-level spectra of photoelectrons—emitted from different atomic orbitals—exhibit a variety of peak shapes, which are influenced by both the fundamental physics of the photoemission process and instrumental factors involved in electron detection and energy analysis. Ideally, these spectral peaks display a lineshape that combines a Gaussian profile with a Lorentzian component. The Lorentzian shape reflects intrinsic lifetime broadening of the core hole, governed by the uncertainty principle, while the Gaussian contribution arises from phonon interactions and instrumental broadening effects[177, 179, 180].

In summary, different elements and their chemical states can be identified by measuring the binding energies of core lines as shown in Figure 2.4, while quantitative compositional information can be derived from the peak areas. Changes in binding energy, known as “chemical shifts” are influenced by the properties of surrounding atoms, including electronegativity, polarizability, and bonding length.

As discussed in Chapter 1, the interface between the electrode and the electrolyte plays a pivotal role in battery performance. XPS has been widely employed in interface studies to elucidate electrochemical reaction mechanisms and interphase components. Post-cycling changes in composition can be investigated by comparing spectra to their pristine state, while variations in composition with depth can be analysed through ion-gun sputtering. Understanding the formation and behaviour of the SEI is crucial for developing high-performance batteries, as it impacts ionic conductivity, electronic insulation, and overall cell stability. The application of *in situ* XPS techniques provides a powerful means to probe these interfacial phenomena under more realistic operating conditions, guiding the design of more efficient and durable energy storage systems.

The following section introduces relatively new *in situ* XPS techniques developed for SEI investigation. These include methods such as *in situ* lithium sputtering and virtual electrode plating XPS (VEP-XPS), which enable time- and condition-resolved characterisation of SEI formation and evolution without destructive sample preparation. In this work, VEP-XPS and *in situ* lithium plating are used interchangeably to convey the same meaning. For instance, VEP-XPS replicates the lithium plating process within the XPS chamber, facilitating a detailed analysis of SEI dynamics. These advancements have been instrumental in studying the SEI formed between lithium metal and various solid electrolytes, offering valuable insights into the composition, stability, and electrochemical properties of the interphase.

2.1.2 *In situ* XPS characterisation techniques

Currently, the majority of XPS studies on SEIs are performed *ex situ*, which involves disassembling the cell after electrochemical testing, exposing the surface of interest and transferring the sample from the glovebox to the XPS chamber. This is because of the buried nature of the SEI, especially in the SSB systems. These procedures can cause irreversible alteration of the surface characteristics. Such alterations may result not only from damage incurred during the peeling of the electrode to access the interface between the electrolyte and electrode but also from environmental reactions that occur upon surface exposures due to the existence of residual gases (including H_2O, CO_2, O_2, etc) in the glovebox[186–188].

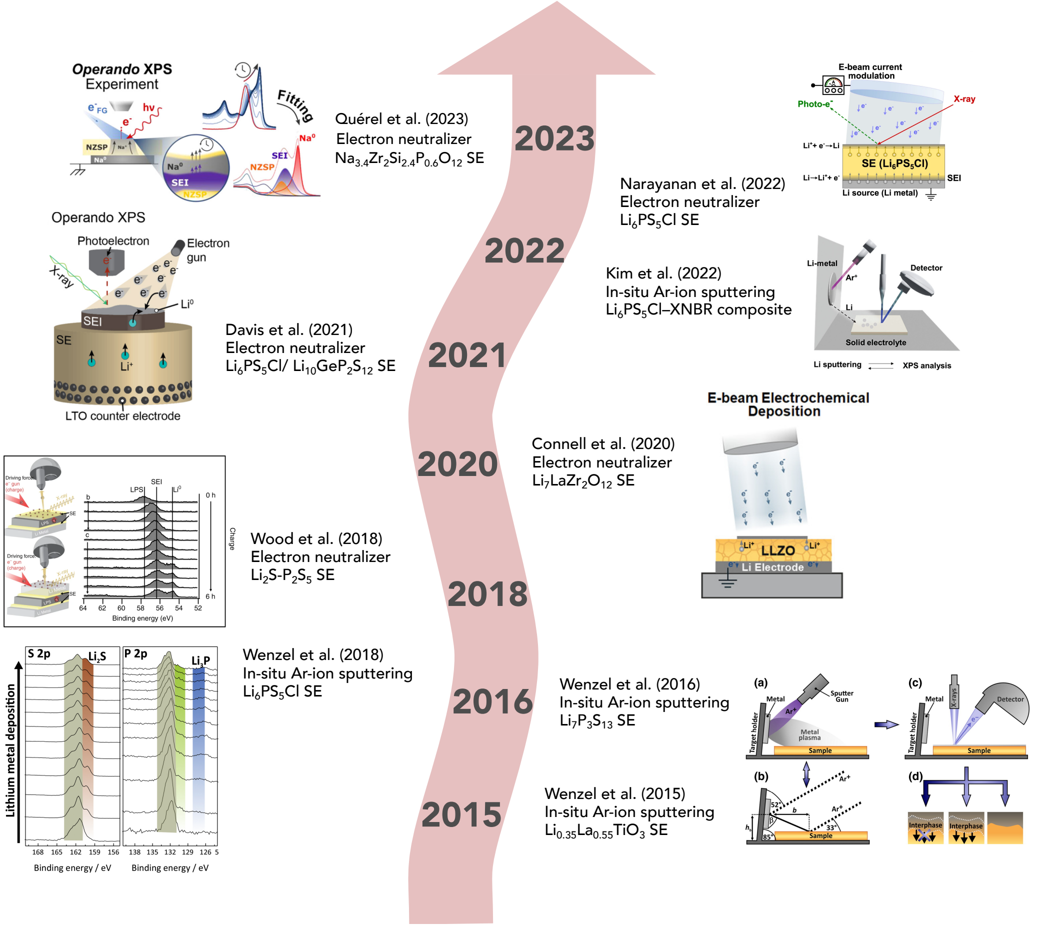

Figure 2.5: The development of *in situ* XPS in the field of solid-state battery interphase characterisation. Reproduced with permission from [181], Copyright 2023 American Chemical Society; [174], Copyright 2022 Springer Nature; [182] 2022 American Chemical Society; [183], Copyright 2021 IOP Publishing; [184], Copyright 2020 American Chemical Society; [185], Copyright 2018 Springer Nature; [176], Copyright 2018 Elsevier; [130], Copyright 2015 Elsevier

These limitations also apply to other characterisation techniques. Consequently, significant efforts have been invested in developing the *in situ* or ‘*operando*’ characterisation techniques, aiming to probe the authentic degradation processes. Figure 2.5 displays the development of the *in situ* XPS characterisation techniques and the SSEs that have been studied using them.

2.1.2.1 *In situ* Ar^+ ion Sputtering

In a series of studies between 2013 and 2016, the Janek research group developed a new *in situ* lithium deposition XPS technique to investigate the stabilities of interfaces between solid electrolytes and lithium metal[130, 163–165]. The technique involves the sputter deposition of lithium metal onto the solid electrolyte surface from an adjacent lithium foil using the built-in argon ion gun of the XPS system as shown in Figure2.6a. The orientation of the sample stage may require adjustment to align with the position and azimuth of the argon ion gun, thereby ensuring that the target material faces the incident argon ion beam directly. Sputter deposition—typically 5 to 15 minutes per sputtering step—and acquisition of XPS spectra are performed alternately to track the chemical changes at the sample surface with minimal perturbation from the atmosphere.

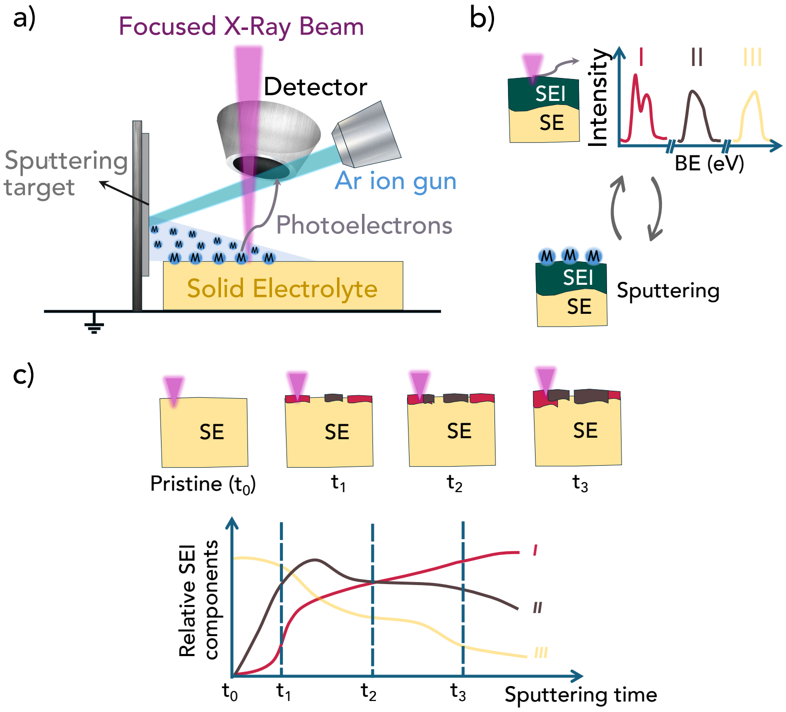

Figure 2.6: Schematic diagrams outlining the operating principles of the *in situ* sputtering XPS technique used in this investigation: a) *in situ* lithium sputtering. The target material was deposited onto the sample surface from the adjacent target using the Ar ion gun of the XPS instrument. The target material deposition was carried out for a predetermined time and then paused while XPS characterisation was performed; b) Experiment workflow: XPS measurements and *in situ* sputtering are periodically alternated; c) Illustration of SEI growth and composition as a function of sputtering time; chemical phases are determined from deconvoluted XPS spectra

After applying this technique to a variety of Li^+-conducting solid electrolytes including $Li_7P_3S_{13}$ (LPS), $Li_{0.35}La_{0.55}TiO_3$ (LLTO), Li_6PS_5Cl (LPSCl), and $Li_{10}GeP_2S_{12}$

(LGPS), different types of interface, as depicted in Figure 1.13, were identified according to the chemical evolutions and stability against lithium metal[130, 162, 174, 176, 183, 185]. The stability of the SEI is typically assessed using the Li 1s core-level spectra, where the presence of a metallic lithium peak usually signifies a more stable SEI.

Additionally, by replacing the lithium sputtering target with other materials, this technique can be used to probe interfacial reactions between various SSEs and alternative interlayers. Some of these interlayers are often employed to mitigate the reactivity of LMA, promote uniform lithium deposition, or serve other functional purposes. Further discussion of this application is provided in Chapter 4.

2.1.2.2 Thickness estimation by XPS measurements

The sputtering rate can be estimated based on the signal attenuating through the top layer. The calculation is shown in Equation 2.6 to 2.9.

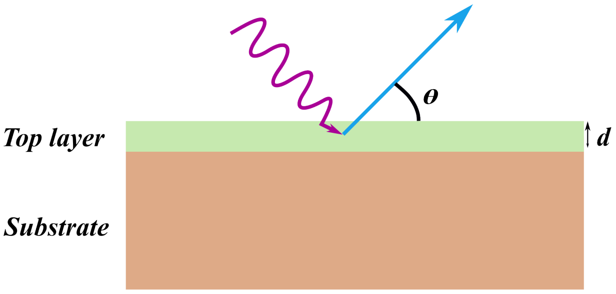

Figure 2.7: Schematic of the thickness estimation working mechanism

$$I_{clean} = k \times n_{sub} \times \sigma \times \lambda_{sub} \times T \tag{2.6}$$

$$I_{covered} = k \times n_{sub} \times \sigma \times \lambda_{sub} \times T \times e^{-\frac{d}{\lambda_{top}}} \tag{2.7}$$

$$\frac{I_{covered}}{I_{clean}} = e^{-\frac{d}{\lambda_{top}}} \tag{2.8}$$

$$d = -\lambda_{top} ln \frac{I_{covered}}{I_{clean}} \tag{2.9}$$

Here, I_{clean} refers to the intensity of a core-level spectrum from the clean substrate surface, $I_{covered}$ refers to the intensity of the core-level spectrum after the sputtering process, n_{sub} is the atomic density, λ_{top} is the IMFP of photoelectrons from the core-level orbital of the substrate in the sputtered top layer, k is the instrumental factors, T is the transmission function and σ is the ionisation cross-section. During the derivation, the factors k, T, and σ cancel out; consequently, the thickness of the deposited layer can be extracted by comparing the intensities of the selected core-level spectra recorded before and after deposition.[189].

For example, a circular copper mesh with pores comparable in size to the X-ray beam size and whose outer diameter matches that of the sample pellet can be placed and pressed onto the top of the sample pellet (assuming the target material is lithium metal). The mean free path (λ) is determined by the photoelectrons of certain kinetic energy from the Cu 2p orbital through the lithium layer. The attenuation rate of the Cu 2p signal (the rate of decrease of the peak area) allows the thickness of the sputtered lithium layer to be calculated according to Equation 2.9. The measuring point established on the copper mesh should be positioned near the probing location on the sample surface, as the sputtering rate may vary with the distance from the target. Since the sputtered material (typically metal) may alloy with Cu, alternative reference materials may be employed in such cases. Additionally, photoelectrons emitted from the substrate material can also be used to estimate the thickness; however, this approach is qualitative and assumes that the layer is uniform and homogeneous.

This approach provides invaluable insights into the dynamic processes occurring at the interface between the electrolyte and the sputtered material, such as the formation of different chemical compounds and the changes in electronic structure. This helps to gain a deeper understanding of the mechanisms that govern SEI formation and stability, leading to improved battery materials and technologies.

2.1.2.3 Virtual Electrode Plating-XPS (VEP-XPS)

Shortly thereafter, another *in situ* XPS technique capable of simulating the first charge of an “anode-free” cell was developed. This technique, first reported by Wood *et al.*, used the electron beam generated by the built-in electron flood gun of the XPS system to plate lithium electrochemically on the SSE surface of Li|SSE

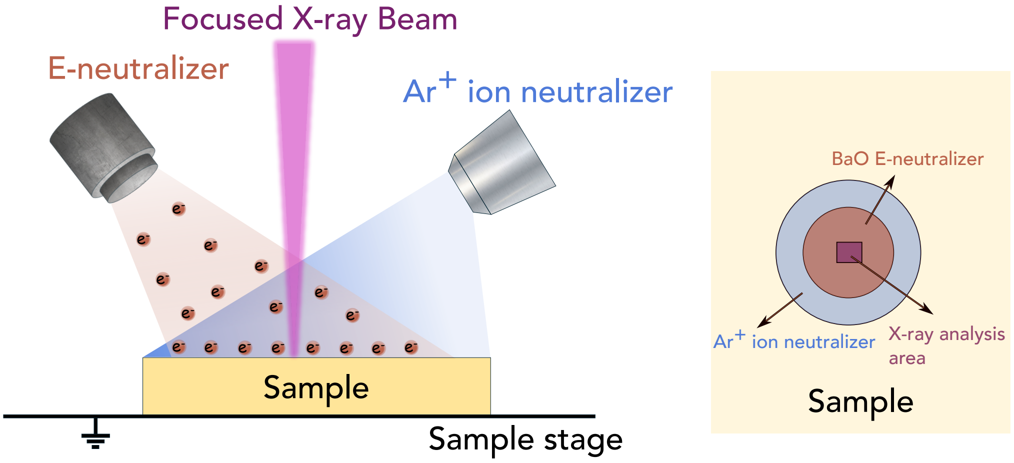

Figure 2.8: Schematic of the Physical Electronics Inc. (PHI) XPS dual beam neutraliser system

bilayer samples[185]. It has been used to study interphase formation on Li_2S-P_2S_5, $Li_7La_3Zr_2O_{12}$ (LLZO), LGPS and LPSCl solid electrolytes[174, 183, 184, 190]. This method provides the advantage of probing the chemical composition and its evolution under conditions closely resembling battery operating environments, with the current density limited to 0.15 mA cm^{-2} for a 5 mm-diameter pellet, except that real cells are generally subject to pressure.

As depicted in Figure 2.8, the XPS system used in this work was equipped with Physical Electronics Inc. (PHI)'s patented dual-beam charge neutraliser system[173, 191]. The electron neutraliser is utilised to compensate for the positive charge accumulated on the sample surface after the ejection of photoelectrons, with the purpose of improving the accuracy of collected information. In the PHI Versaprobe III XPS system, a beam of low-energy (~1 eV) electrons 5 mm in diameter is provided by the BaO cold cathode electron flood source. The beam current is adjustable from a few μA up to 30 μA, which enables investigation of the effect of current density on SEI formation[174].

As depicted in Figure 2.9, the XPS instrument's integrated electron neutraliser gun, acting as a "virtual electrode", provides a constant flux of electrons to the surface of the SSE pellets, driving Li^+ migration upward through the Li|SSE bilayer sample. The combination of migrated Li^+ ions and electrons at the SSE's top surface

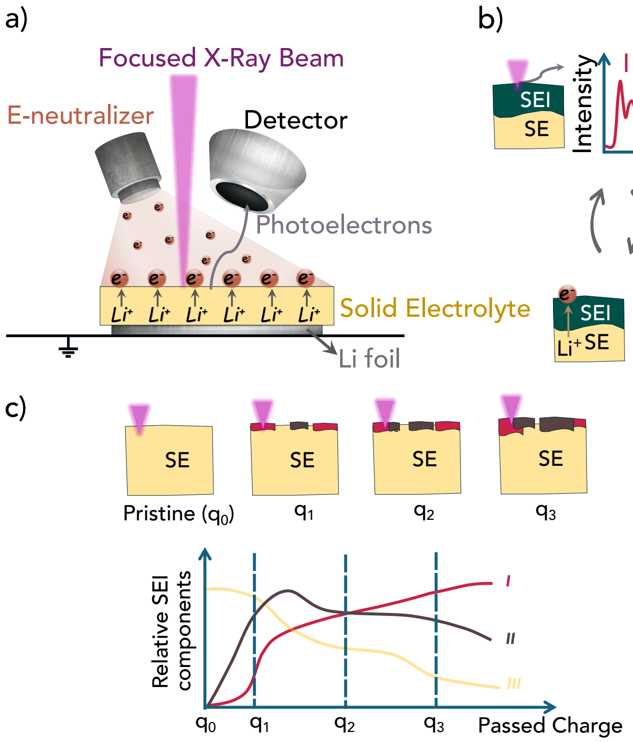

Figure 2.9: Schematic diagrams outlining the operating principles of the *in situ* plating XPS technique used in this investigation: a) *in situ* lithium plating. The electron neutraliser provides an electron beam and generates a bias across the sample stack which facilitates Li-ion migration towards the top surface; b) Experiment workflow: XPS measurements and *in situ* plating are periodically alternated; c) Illustration of SEI growth and composition as a function of passed charge; chemical phases are determined from deconvoluted XPS spectra

results in the gradual formation of SSE decomposition species and lithium metal (depending on the stability of SSE and the formed SEI). By alternating between XPS measurements and VEP, the electrochemical evolution of the surface can be effectively probed.

Additionally, this technique holds the potential to probe the evolution kinetics of the formed SEI, either against lithium metal or the SSE. In the first scenario, continuous XPS measurements of the sample surface with metallic lithium plated atop can monitor the chemical evolution of various species. In the second scenario, a specific amount of lithium metal can be plated onto the SSE pellet using the VEP method until fully lithiated decomposition species are formed. Through continuous XPS measurements, the stability of these decomposition species against the SSE can also be investigated.

2.1.2.4 Effective current density and sample resistance

The applied current density can be calculated from the electron flood gun current and exposed sample area. The calculated current density is generally a close approximation of the true value, as in most cases this technique is applied to investigate SSEs with high ionic conductivities ranging from 10^{-3} to 10^{-2} S/cm; under these conditions, the ohmic voltage drop across the sample is sufficient to sustain the predicted current density[139, 162, 183, 185].

In theory, on applying a constant current (I_{gun}), of 30 μA, the potential difference (V_{sample}), across the sample will rise to a value given by Equation 2.10.

$$V_{sample} = I_{gun} \times R_i \tag{2.10}$$

Here, R_i is the ionic resistance of the sample. This transition cannot occur instantaneously, as a portion of the applied current initially flows into the circuit branch containing the geometric capacitance, denoted as $\mathrm{CPE_{geom}}$. As the potential difference increases, the current into this capacitance decreases and eventually ceases once it reaches V_{sample}. Physically, this corresponds to the accumulation of electrons on the SSE surface until the potential difference is sufficient to drive the full applied current (30 μA) through R_i, thereby establishing the condition $I_{sample} = I_{gun}$. Although the $\mathrm{CPE_{geom}}$ values can be extracted from impedance spectra, they are typically negligible.

Since the energy of the electrons is about 1 eV, this implies that the applied voltage across the sample has an upper limit. Assuming the applied current density is 0.15 mA cm^{-2}, which is the maximum that can be applied for a sample of 5 mm in diameter, the resistance of the sample R_i is calculated as 3.33×10^4 Ω when the ohmic drop across the sample stack is 1 V. If the sample resistance is higher, the applied electron beam is insufficient to drive the current density of 0.15 mA cm^{-2} through the sample. In this case, although a 30 μA beam is directed to the sample surface, the extra electrons must have been deflected to ground due to the surface charge. Therefore, there is a dependence of the lithium plating rate on the sample's ionic conductivity and thickness, which will be discussed in more detail in Chapter 5.

In summary, these two techniques involve alternating between XPS measurements and lithium deposition (either sputtering or plating) under UHV conditions within the XPS chamber, which helps to preserve the pristine SEI information as much as possible. Additionally, the *in situ* XPS techniques provide the capability to isolate the electrochemical degradation process from other factors that would affect the interfacial information, including pressure. The collected results are able to provide valuable information about the SEI composition, SEI thickness, and SEI stability, which will be discussed in result chapters.

2.2 Radio frequency (RF) magnetron sputtering

Radio frequency (RF) magnetron sputtering, as schematically illustrated in Figure 2.10, is a type of physical vapour deposition (PVD) process that can be applied to sputter both conductive metals and electronically insulating compounds. The sputtering process is achieved by ionic sputtering, where the atoms on the target surface are knocked off by high-energy ions.

As shown in Figure 2.10, a target is placed on a circular magnetron source with a substrate attached to the rotating holder using Kapton tape. It is worth noting that the distance between the substrate and the target will affect the uniformity of the resulting thin film and the deposition rate; usually they are separated by a few centimetres. Prior to the sputtering, the chamber is evacuated to a pressure below 10^{-6} mbar to eliminate potential volatile contamination species left in the chamber, such as oxygen and water. Thereafter, a gas that can be easily ionised (nitrogen or argon) is fed into the chamber to raise the pressure to 10^{-3} to 10^{-2} mbar.

An RF power supply, typically operating at 13.56 MHz, applies an alternating electric field between the target (cathode) and the chamber (anode). A negative potential is generated on the target surface because electrons, having higher mobility, respond instantaneously to the fluctuating electric field. The alternating electric field ionizes the N_2 gas (taking N_2 gas as example), generating a plasma composed

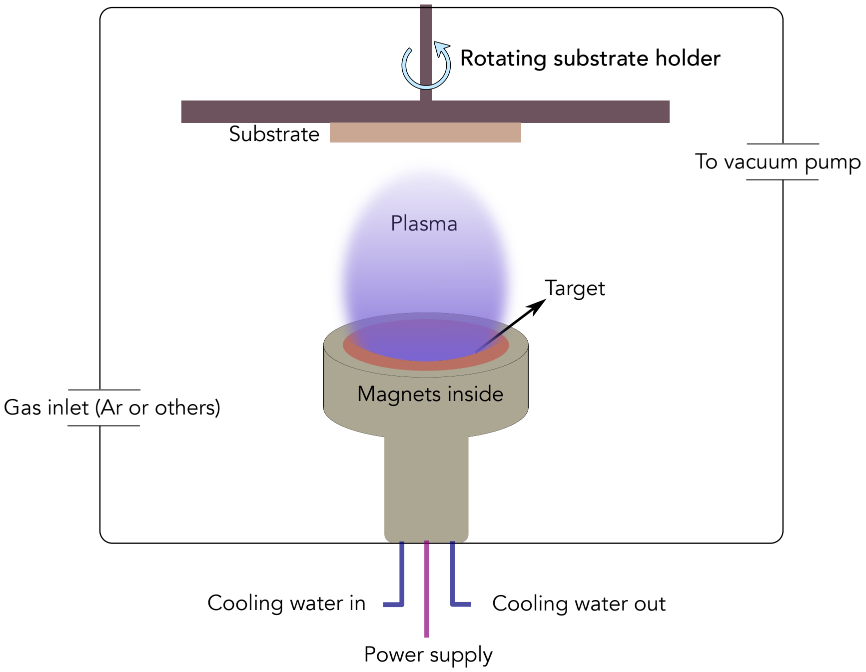

Figure 2.10: Schematic of the RF magnetron sputtering

of positive N^+ ions and free electrons. N^+ ions are accelerated by the electric field toward the target; on colliding, they eject atoms from the target surface (note: N_2 gas was used for LiPON SSE deposition). The deposition of other targets was performed using argon gas. The magnetic field produced by the magnet beneath the target traps electrons in a region close to the cathode, increasing the likelihood of ionization collisions. This significantly enhances ionization efficiency and, consequently, the sputtering rate. Since a substantial portion of the incoming ions' energy is transferred to the target as heat, an effective cooling system is essential to maintain system stability and prevent overheating.

The N_2 gas flow rate is usually reduced after ignition to decrease collisions between sputtered atoms and gas ions, which increases the deposition rate. A shutter is employed to control the initiation and termination of the sputtering process. Once the shutter is opened, the substrate is exposed to the plasma, allowing the ejected atoms to be deposited onto the substrate, forming a thin film.

The RF magnetron sputtering processes and lithium evaporation in this work were performed using a PVD system (MBEVAP, MBraun) integrated into an argon glovebox (O_2<0.1 ppm and H_2O<0.1 ppm). The RF magnetron sputter deposition of the thin-film LiPON samples used in this work was conducted by Dr Stephen Turrell.

2.3 Scanning electron microscopy (SEM)

Scanning electron microscopy (SEM) is a widely applied technique for characterising the microstructure and morphology of various samples using an electron beam. Different signals are generated by the primary incident electron beam, including secondary electrons, backscattered electrons, and X-rays, as shown in Figure 2.11.

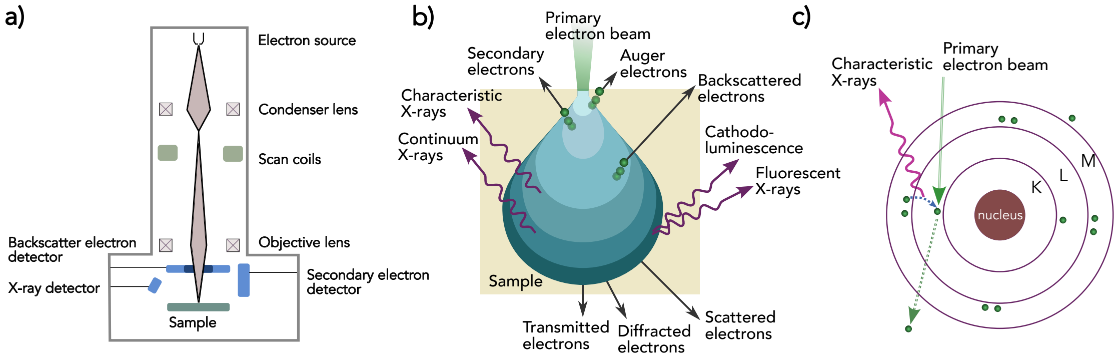

Figure 2.11: (a) Schematic of an SEM system, Reproduced with permission from [192], Copyright 2021 Elsevier; (b) Schematic of the interaction volume of incident primary electrons with the sample, Reproduced from web [193], Image credit: Wikipedia user Ponor, distributed under CC BY-SA 4.0; (c) Schematic of the mechanism of the generated characteristic X-ray signals, Reproduced from web [194]

Secondary electrons originate from the outer shells of atoms, ejected by primary electrons, and are capable of providing topographical information about the sample surface. Backscattered electrons (BSEs), on the other hand, refer to primary electrons that undergo elastic interactions with surface atoms. The likelihood of an electron being elastically scattered is influenced by the atomic number of the atoms present on the surface; the higher the atomic number, the greater the probability of elastic scattering. This property gives BSEs an atomic number contrast (Z-contrast), making them valuable for identifying different elements on the surface.

Characteristic X-rays, generated during the SEM process, can be collected and analysed using an energy-dispersive spectroscopy (EDS) detector, which is available in many SEM systems. The mechanism of X-ray emission in this process is similar to that of XPS but not identical as illustrated in Figure 2.11c. When a primary electron interacts with an electron from a core-level orbital in an atom, a vacancy is created as the core-level electron is excited to an outer orbital with higher energy. During relaxation, this vacancy is filled by another electron from a higher energy state, accompanied by the emission of a characteristic X-ray photon. The energy of the emitted X-ray photon is element-specific, making the collected EDS data instrumental in identifying surface elements and determining their spatial distribution.

SEM characterisations in this work about the LiPON samples were performed with a Zeiss Merlin SEM with an Oxford Instruments EDS detector (Ultim Max 170 X-ray detector). Samples were transferred from gloveboxes to the SEM using an air-tight transfer holder (Gatan, Inc.). The SEM images in this work were collected by Dr Stephen Turrell.

2.4 X-ray diffraction (XRD)

X-ray diffraction (XRD) measurements were carried out using a Rigaku MiniFlex instrument located inside a glovebox under N_2 atmosphere. Similar to the X-rays used for XPS, the X-rays used for XRD were also generated by bombarding a metal anode (copper) with electrons. A monochromator is used to select the most intense Cu Kα1 radiation, with a 1.5406 Å wavelength. The Cu Kβ radiation can be absorbed by adding a nickel monochromator, and the Cu Kα2 radiation can be removed by a germanium monochromator. The source, sample holder and X-ray detector are precisely positioned in a circular geometry. The source and detector are on the circumference and the sample is at the centre of the diffractometer axis.

The peaks in a diffraction pattern come from the constructive interference of the monochromated X-rays with the sample when Bragg's law (Equation 2.11) is satisfied.

$$2dsin\theta = n\lambda \tag{2.11}$$

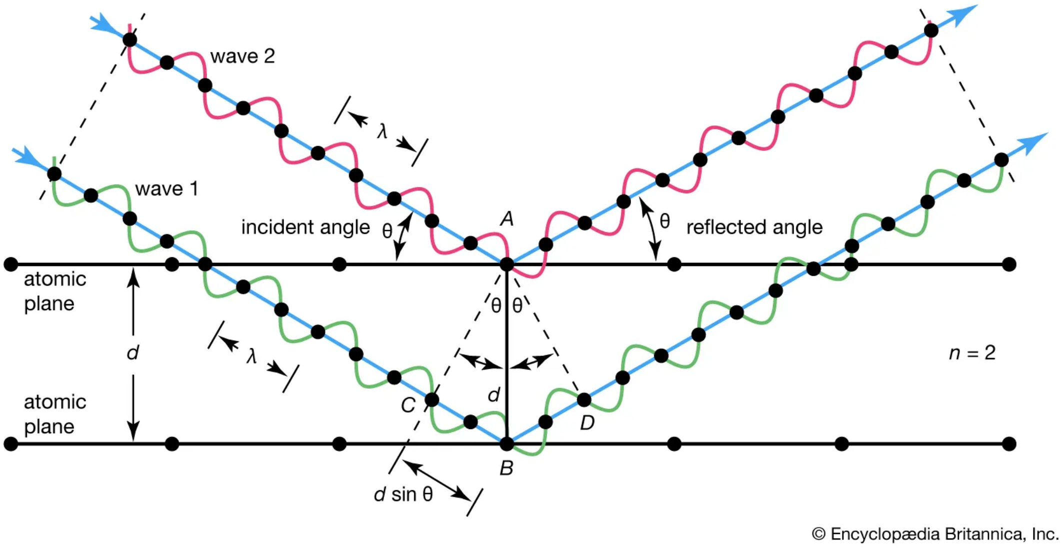

Figure 2.12: Schematic of X-ray diffracted on atomic planes following the Bragg's law, Reprinted from web [195], *Encyclopædia Britannica, Inc.*

here, λ is the wavelength, d is the inter-planar spacing, θ is the incident angle, and n is an integer. The detector collects the reflected X-rays and yields a diffraction pattern with peak intensity plotted against the peak position; this is determined by the sample's crystal structure. Each peak corresponds to the X-rays diffracted from a certain set of planes in the sample. Thus, the XRD diffraction pattern can help to identify the crystallinity of the sample and its crystal structure[196].

2.5 Sintering

High-temperature sintering is commonly employed to densify ceramic materials, particularly oxide solid electrolytes in this context. As illustrated in Figure 2.13a, the thermodynamic driving force for the sintering process is the reduction of the surface energy, where the total surface energy of the system can be defined by the following equation:

$$\Delta(\gamma^{sg}S) = \Delta\gamma^{sg\to ss}S + \gamma^{sg}\Delta S \tag{2.12}$$

here, the γ^{sg} is the interfacial energy between solid/gas interface, $\Delta\gamma^{sg\to ss}$ is the change in interfacial energy during sintering caused by the formation of grain boundaries, and $\Delta\gamma^{sg\to ss}$ can be calculated by $\gamma^{ss} - \gamma^{sg}$ (γ^{ss} is the interfacial energy

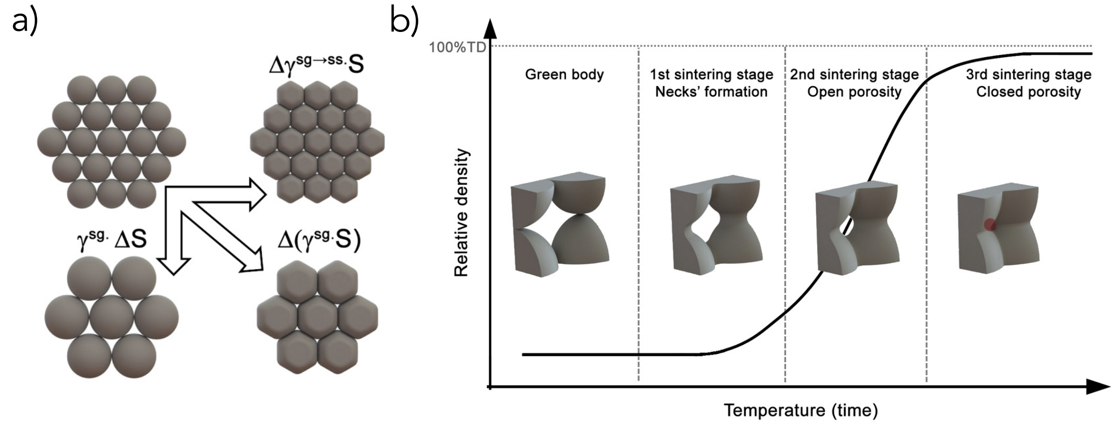

Figure 2.13: (a) Schematic of the change in surface energy during the sintering process, (b) Schematic of three stages during the sintering process, Reprinted with permission from [197], Copyright 2014 Elsevier

of solid/solid interfaces), S is the surface area of the powder and ΔS is the change in surface energy introduced by particle coarsening processes.

As depicted in Figure 2.13b, the sintering process can be broadly divided into three stages. Initially, necks form between particles, a stage characterized by surface diffusion. Subsequently, continuous pore channels develop, accompanied by significant pore shrinkage and overall volume reduction. Finally, the residual pores become isolated from the outer surface. Ultimately, the sintered body typically exhibits higher mechanical strength and a denser structure[197].

2.6 Coulometric titration time analysis (CTTA)

The CTTA operates by applying a series of coulometric titration steps, each followed by a relaxation period, as illustrated in Figure 2.14. During each titration step, a small amount of lithium is deposited onto the current collector at a predetermined current, while side reactions simultaneously occur. During lithium deposition, the cell voltage initially drops to a negative value. Then after the lithium titration step, the open-circuit voltage (OCV) of the cell is continuously monitored. The cell voltage recovers to approximately 0 V as both electrodes reach equilibrium at the lithium metal potential. Once all deposited lithium has been consumed during side reactions, the OCV gradually deviates from 0 V. The OCV period is

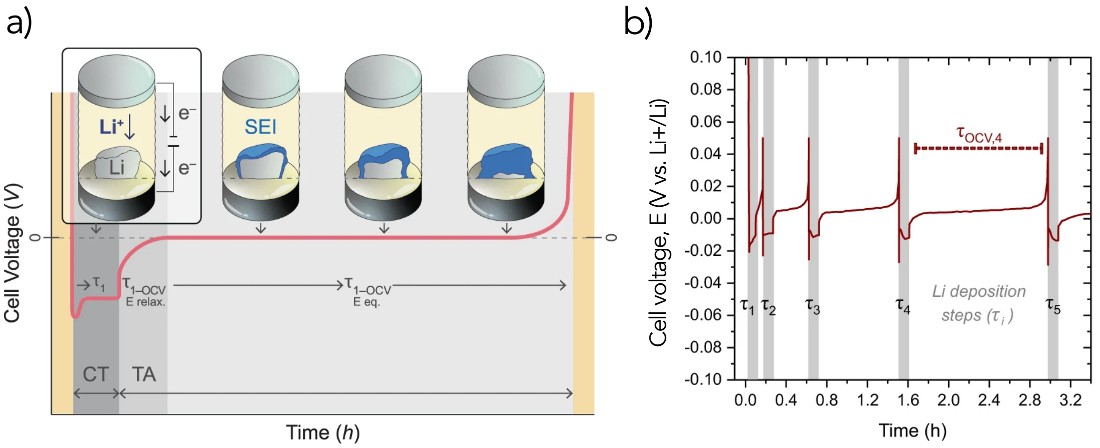

Figure 2.14: Illustration of the coulometric titration time analysis (CTTA) method: (a) Schematic representation of the CTTA setup, detailing the lithium deposition and subsequent open-circuit voltage (OCV) monitoring process; (b) CTTA results obtained from a stainless steel current collector|Li$_6$PS$_5$Cl|Li cell, operated at a current of 10 μA (15.6 $\mu A\ cm^{-2}$) for 0.1 hours per titration step. The increasing OCV period with successive titration steps indicates progressive SEI passivation. Reproduced with permission from [198], Copyright 2013 Springer Nature

considered complete when the cell voltage surpasses 50 mV vs Li$^+$/Li, triggering the initiation of the next titration step. The lithium titration and OCV measurements are repeated iteratively for as many cycles as needed to capture the SEI evolution.

The OCV period tracks the time required to fully consume the same amount of deposited lithium during each titration step, serving as an indicator of the stability of the formed SEI. As schematically illustrated in Figure 2.14b, the lithium consumption time progressively increases with each successive titration step, suggesting that the SEI becomes more passivating over time. The SEI growth over time can then be quantified by analysing the changes in the duration required to consume the deposited lithium, in conjunction with the amount of lithium plated during each titration step. This provides a direct measure of the passivation behaviour of the SEI and its impact on interfacial stability.

2.7 Electrochemical Impedance Spectroscopy (EIS)

Electrochemical reactions at the electrode-electrolyte interface involve multiple processes, including mass transport and charge transfer, each occurring at different time scales. EIS or ac impedance operates by applying a small sinusoidal signal over a predefined frequency range, typically spanning nine orders of magnitude from the millihertz (mHz) to megahertz (MHz) range, while monitoring the system's response. This technique provides valuable kinetic insights into electrochemical processes, including SEI formation and evolution. Additionally, EIS is a non-destructive characterisation method that can be performed *in situ*, making it particularly useful for the real-time analysis of interfacial dynamics.

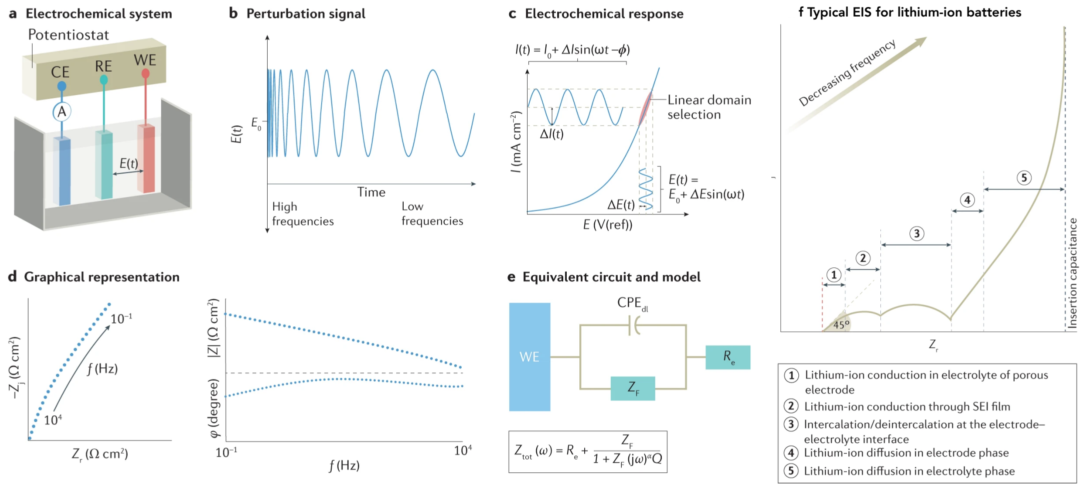

Figure 2.15: (a) Schematic representation of an electrochemical system used for EIS measurements, consisting of a working electrode (WE), reference electrode (RE), and counter electrode (CE). (b) Illustration of the sinusoidal voltage input signal applied during EIS measurements. (c) The corresponding sinusoidal current response. (d) Two commonly used graphical representations of EIS results, including the Nyquist plot (which plots the imaginary impedance vs. real impedance) and the Bode plot (which displays impedance magnitude and phase angle as a function of frequency). (e) An example equivalent circuit model (ECM) used to interpret the collected impedance data by representing different electrochemical processes using electrical components. (f) A typical EIS response for LIBs, showing the corresponding physical processes such as charge transfer resistance and ion diffusion. Reprinted with permission from [199], Copyright 2021 Springer Nature.

In a typical potentiostatic EIS (PEIS) measurement, a small sinusoidal voltage $E_{(t)} = E_0 + \Delta Esin(wt)$ with specific amplitude (ΔE) and frequency (w represents the angular frequency) is applied to the system. The output current shares the frequency, but the amplitude and phase may differ and can be represented with $I_{(t)} = I_0 + \Delta Isin(wt - \phi)$. Since both $\mathrm{E}_{(\mathrm{t})}$ and $\mathrm{I}_{(\mathrm{t})}$ contain magnitude and phase information, they can be expressed as complex numbers. Consequently, the impedance $Z_{(w)}$ can also be represented as the complex ratio potential and current as shown in Equation 2.13.

$$\begin{aligned} Z_w &= \frac{\tilde{E}_{(w)}}{\tilde{I}_{(w)}} = |Z|e^{j\phi} \\ &= |Z|(cos(\phi) + jsin(\phi)) \\ &= Z' + jZ'' \end{aligned} \tag{2.13}$$

where Z' is the real part corresponding to a frequency-dependent resistance, and Z" is the imaginary part corresponding to the frequency-dependent reactance part.

The EIS results are usually displayed in a Nyquist plot, where the imaginary part of the impedance is plotted on the y-axis and the real part on the x-axis, as shown in Figure 2.15. Each point on the plot corresponds to a data point collected at a specific frequency, with high-frequency data generally appearing on the left and low-frequency data on the right. The shape of the Nyquist plot provides insight into different electrochemical processes, such as charge transfer resistance, diffusion behaviour, and SEI properties, allowing for a detailed analysis of interfacial kinetics, with an example included in Figure 2.15f.

The equivalent circuit model (ECM) is usually employed to interpret EIS data by representing different electrochemical processes using electrical components. A commonly used electrical element includes the resistor (R), which can represent an ohmic resistance, charge transfer resistance, or the ionic resistance of the electrolyte; the capacitor (C), which can be used to model the electrochemical double-layer capacitance at the electrode-electrolyte interface and the charge accumulation/depletion at the SSE/electrode interface; and the inductor (L), which represents the non-ohmic contributions from the electrical connections in the system. Some other elements are also frequently used, such as the constant phase element (CPE), as the surface inhomogeneity and roughness can cause non-ideal capacitive behaviour, and the Warburg Element (W) is used to represent diffusion impedance in the system. The impedance responses of different passive circuit elements are given by Equation 2.14 to Equation 2.16:

$$Z_{resistor} = R \tag{2.14}$$

$$Z_{capacitor} = \frac{1}{j\omega C} \tag{2.15}$$

$$Z_{inductor} = j\omega L \tag{2.16}$$

When these elements are connected in series, the total impedance is calculated as:

$$Z_{total} = \sum Z_i \tag{2.17}$$

For elements connected in parallel, the total impedance follows:

$$\frac{1}{Z_{total}} = \sum \frac{1}{Z_i} \tag{2.18}$$

These relationships form the foundation for constructing ECMs, allowing the extraction of electrochemical properties such as charge transfer resistance, interfacial capacitance, and diffusion characteristics from EIS data.

The temperature-dependent resistances can be obtained by performing EIS measurements at different temperatures, allowing for the determination of the ionic conductivity of the sample using Equation 2.19:

$$\sigma = \frac{l}{RA} \tag{2.19}$$

where R is the resistance obtained from the EIS measurement, l is the sample thickness, and A is the cross-sectional area.

The temperature dependence of ionic conductivity follows the Arrhenius equation:

$$\sigma = \sigma_0 e^{-E_a/RT} \tag{2.20}$$

where σ_0 is the pre-exponential factor, E_a represents the activation energy (J mol^{-1}), R is the universal gas constant (8.314 J mol^{-1} K^{-1}), and T is the absolute temperature in Kelvin (K). By plotting the Arrhenius plot of $\ln \sigma$ versus $1/T$, the activation energy (E_a) for ionic conduction can be extracted from the slope, providing insights into the energy barrier associated with lithium-ion transport within the solid electrolyte.

3

In situ XPS investigation of the interphases formed on LGPS and LAGP with metallic lithium

Contents

The major part of the work in this chapter was first reported in the following published research article: Liang, Y.; Burton, M.; Jagger, B.; Guo, H.; Ihli, J.; Pasta, M. *In situ* XPS investigation of the SEI formed on LGPS and LAGP with metallic lithium. Chemical Communications 2024[162].

3.1 Introduction

SSBs comprising SSE and LMA are widely regarded as the ‘holy grail’ of energy storage, attributed to their potential for enhanced safety and higher energy density compared to conventional LIBs[200–202]. The compatibility of SSEs with lithium metal is critical for achieving stable, high-energy-density lithium metal SSBs[51] Since most SSEs have limited electrochemical stability windows, an SEI will form as a result of interfacial reactions. This formed nanocomposite, which may comprise of both crystalline and amorphous reaction products, directly influences battery performance by impacting interfacial stability, ionic conductivity, and electronic insulation.

A well formed SEI is supposed to be ionically conductive to facilitate Li^+ transport while being electronic insulating to suppress continuous decomposition of the SSE[130, 203, 204]. Investigating the reaction pathways, composition and spatial extent of the formed SEI has become a key focus in the development and optimisation of SSBs.[129, 205, 206]. While research on SSEs with high ionic conductivity has expanded significantly over the past two decades, the characterisation of the SEIs has remained challenging due to their ultra-thin thickness and compositional heterogeneity[80, 127, 151, 204, 207, 208].

As introduced in Section 2.1, XPS is a powerful technique for probing the chemistry information of the SEI. Understanding the SEI’s composition is crucial, as its properties significantly influence the battery performance. Currently, the majority of XPS experiments are conducted *ex situ*, requiring the disassembly of the cell after electrochemical testing, followed by sample treatment and preparation for the XPS analysis[153, 209, 210]. However, these procedures can potentially alter the pristine surface characteristics. Such alterations may arise from mechanical damage incurred during the peeling of the electrode to access the interface between the electrolyte and electrode, as well as from exposure to ambient contaminants. It has been demonstrated that even under UHV conditions, trace amounts of oxygen, water, and carbon dioxide persist, which can react with the SSE and the formed SEI, altering its composition. This also suggests that samples will be more susceptible to contamination during handling in gloveboxes[175]. These factors highlight the importance of employing *in situ* or operando XPS techniques, which allow for minimising the impact of sample handling and environmental contamination.

As introduced in Section 2.1.2, VEP-XPS is an emerging technique that enables time- and operational condition-resolved characterisation of the SEI formed during the first charge in an “anode-free” cell configuration. By employing an electron beam, this method replicates the lithium plating process directly inside the XPS chamber, while allowing analysis of SEI formation dynamics. Similarly, the *in situ* lithium sputtering technique facilitates the investigation of SEI composition upon direct contact between SSEs and lithium metal. The use of these two techniques enables SEI characterisation while avoiding the need for destructive or invasive sample preparation in many cases[157, 211–213]. By employing these two techniques (illustrated in Figure 2.9 and Figure 2.6, respectively), a thin layer of lithium is gradually deposited onto the surface of an SSE pellet under UHV conditions. Sequential XPS measurements following each lithium deposition step allow for a detailed investigation of SEI formation and its evolution as the deposited lithium interacts with the SSE.[163, 174, 176, 183].

In this work, the composition, chemical stability, electrochemical stability and evolution of the interphase formed between lithium metal and two types of SSEs: $Li_{10}GeP_2S_{12}$ (LGPS) and NASICON-type $Li_{1.5}Al_{0.5}Ge_{1.5}(PO_4)_3$ (LAGP) were investigated using both techniques. LGPS has been proposed as a promising sulphide SSE due to its high ionic conductivity of up to 12 mS cm^{-1}, which surpasses that of many other SSEs[74]. However, its practical implementation has been hindered by its instability against lithium metal and the unstable SEI growth during battery operation[163, 214]. A previous study investigated the SEI formed between LGPS SSE and lithium metal using a similar VEP setup, which helps to validate the result obtained in this study and serves as a benchmark for assessing SEI stability[183]. LAGP has also been extensively investigated as an SSE due to its promising ionic conductivity and good stability in ambient conditions[215–219]. However, SEI growth remains a major limitation to its application, and the underlaying mechanisms have not been well understood[220]. This work applied the *in situ* XPS technique to investigate SEI formation on LAGP SSE for the first time, thus aiding in the understanding of its decomposition mechanism. Additionally, the pristine structures of both SSEs contain Ge^{4+}, which is susceptible to reduction to Ge^0 when in contact with the lithium metal[163, 183, 216, 221]. Ge^0 is an undesirable electronically conductive phase within the SEI; however, its impact on SEI stability depends on the concurrent evolution of other SEI components, necessitating a study of the overall degradation process.

The results collected in this work reveal that the LAGP SSE exhibits slower reaction kinetics against lithium metal compared to the sulphide-based LGPS SSE. The SEI formed between LGPS and lithium metal consists of both electronically and ionically conductive phases, namely Ge(Li) and Li_3P, which contribute to continuous SEI growth[174, 222]. In contrast, the SEI formed atop LAGP SSE demonstrates improved stability against lithium metal compared to LGPS SEI. This is attributed to the lower volume fraction of conductive phases (Ge^0 in this case), which do not form a continuous conduction pathway. These findings indicate that the stability of the naturally formed SEI, resulting from electrochemical reactions, is not solely determined by its composition but also by the proportion and distribution of its conductive phases. Additionally, this work introduces a potential approach for quantifying SEI evolution kinetics by continuously monitoring the sample surface with XPS measurement after metallic lithium has been plated *in situ* by the neutraliser provided electron beam. This method can be applied to different SSE systems, providing a more comprehensive understanding of interfacial stability and degradation mechanisms.

3.2 Experimental

3.2.1 Materials and synthesis procedure

$Li_{1.5}Al_{0.5}Ge_{1.5}(PO_4)_3$ SSE power (99.99% pure, D_{50}=500 nm) was purchased from Ampcera^{TM} via MSE Supplies LLC. Lithium ribbon (99.9% pure) was obtained from Sigma-Aldrich. The $Li_{10}GeP_2S_{12}$ SSE powder was synthesised via a combination of ball milling and heat treatment. The precursors—Li_2S (99.98%, Merck), GeS_2 (MP Biomedicals), and P_2S_5 (99%, Merck)—were weighed in the stoichiometric ratio, along with an additional 2 wt% sulphur (sublimed, Alfa Aesar). The mixture was mechanically milled at 700 rpm for 5 hours in sealed ball-milling jars. The resulting mixture was pelletized and annealed at 550 °C for 8 hours in an argon-filled glovebox ($[H_2O]$ and $[O_2] < 0.1$ ppm). After natural cooling to room temperature, the pellet was ground, and the final product, $Li_{10}GeP_2S_{12}$ powder, was collected.

3.2.2 XPS sample preparation

LAGP pellets were prepared by cold-pressing 150 mg of LAGP powder under a pressure of 150 MPa using a 10 mm stainless steel die. The resulting pellets were sintered in a box furnace at 900 °C for 10 hours in air with a temperature ramping rate of 2 °C min^{-1}. To compensate for lithium loss during sintering, the pellets were placed on a bed of LAGP powder. After sintering, both sides of the pellets were polished using sandpaper with grit sizes ranging from 800 to 4000, producing a smooth surface. The final sintered pellets measured approximately 850 μm in thickness and 8.38 mm in diameter. LGPS pellets were prepared by cold pressing 150 mg powder at 400 MPa for 5 minutes using an 8 mm stainless steel die.

The lithium ribbons were brushed using a toothbrush to remove surface contaminants, followed by calendering to produce lithium metal foils approximately 500 μm thick. Circular lithium metal electrodes, approximately 8 mm in diameter, were then punched out from these foils.

For the VEP-XPS sample, the SSE pellet was pressed onto the pre-punched 8 mm lithium disk, which had been affixed to a thin copper disk under a lower pressure of 40 MPa. The assembled sample stack was then mounted onto the XPS stage using carbon tape, with the lithium-foil-free surface facing upward. To avoid ambient air exposure, the sample was transferred from the glovebox to the XPS intro chamber using an air-tight transfer vessel. For the *in situ* sputtering experiment, the pressed SSE pellet was directly mounted onto the sample stage without any additional treatments. The lithium foil was attached to the target wall using conductive carbon tape.

3.2.3 XPS measurements and the settings

XPS experiments were conducted using the PHI VersaProbe III with an Al Kα X-ray (hν = 1486.6 eV) source. The pressure inside the XPS chamber was maintained at the 10^{-7} Pa level during all measurements.

During the VEP-XPS experiment, the integrated electron neutraliser gun of the XPS instrument—functioning as a virtual electrode—supplied a constant flux of electrons to the surface of the SSE pellet, thereby driving the upward migration of Li^+ ions through the pellet. The combination of migrated Li^+ ions and electrons supplied by the neutraliser at the top surface of the SSE led to the gradual formation of metallic lithium. The measurement point was aligned to the centre of the pellet using scanning X-ray-induced secondary electron imaging (SXI), ensuring precise positioning of the electron beam, which was also focused at the pellet centre. The applied beam current was 20 μA for both LGPS and LAGP SSEs, corresponding to current densities of 0.0398 mA cm^{-2} and 0.0361 mA cm^{-2}, respectively (see calculation process in section A.1.2). The slight difference in current density arises from their different pellet diameters, because sintering causes the LAGP pellet to shrink. The lithium plating rate was calculated based on the total charge passed, yielding deposition rates of approximately 3.24 nm min^{-1} for LGPS SSE and 2.94 nm min^{-1} for LAGP SSE. Electron beam plating and XPS acquisition were alternated to track SEI evolution, enabling detailed investigation of the interfacial reactions between lithium metal and SSEs.

For the *in situ* sputtering experiment, the ion gun beam voltage was set to 4 kV, and the lithium metal target was positioned directly facing the Ar^+ ion gun during the sputtering process. The sputtering rate was estimated to be approximately 0.14 nm min^{-1}, based on the attenuation rate of the Cu signal (a copper mesh was used as a reference-further details are provided in Section 2.1.2.2), as reported by Narayanan *et al.*, using the same experimental setup[174]. The lithium metal sputtering and XPS measurements were conducted alternately to track the evolution of surface chemistry.

The XPS sampling area was set as 500 μm × 500 μm, and all measurements were conducted with the neutraliser turned off. The pass energy was set to 224 eV for the survey scan and 55 eV for the high-resolution scans. The collected spectra were processed using CasaXPS software and calibrated based on the C 1s peak at 284.8 eV, unless otherwise specified[223].

3.3 Results and Discussion

3.3.1 SEI formation and evolution by VEP-XPS

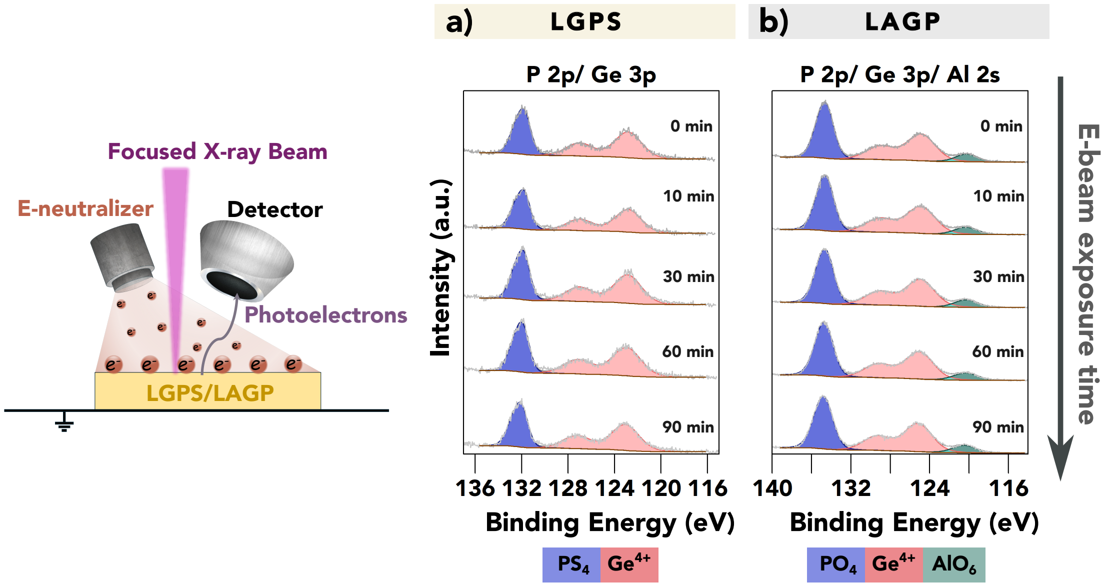

Figure 3.1: XPS spectra near the P 2p region for VEP-XPS experiment of LGPS (a) and LAGP (b) SSEs without lithium source underneath the pellet, the electron beam exposure time is labelled in both panels. The peak intensity is normalised to show the deconvoluted results. Note: charge calibrated based on C 1s to 284.8 eV. Reprinted from Liang *et al.*[162]

Among various characterisation techniques, such as TEM, Raman, SEM, and XPS, beam damage is always a concern. To address this, VEP experiments were conducted on both LGPS and LAGP SSEs without a lithium source provided (plain pellet samples mounted on carbon tape), with the setup schematically illustrated in Figure 3.1. The collected spectra near the P 2p region, which includes the most relevant chemical information, showed no significant changes over time. Additional core-level spectra for both LGPS and LAGP SSEs are provided in Figure 3.2. With increasing electron beam exposure time, no peak shifts or shape variations were observed, apart from a slight shift in the pristine spectra (labelled as 0 min), which is likely attributed to charge calibration or surface effects. This confirms that both samples are stable under the applied electron and X-ray beams.

It is also worth noting that the electron neutraliser was designed to mitigate surface charging by applying a low-energy electron beam. The accelerating voltage for the electron beam was 1 V, which is substantially lower than the typical accelerating voltage used for TEM characterisation, which is usually in the range of 200 to 300 kV[224, 225]. This significantly reduces the likelihood of beam-induced damage, further ensuring the reliability of the VEP-XPS technique for probing SEI formation and evolution.

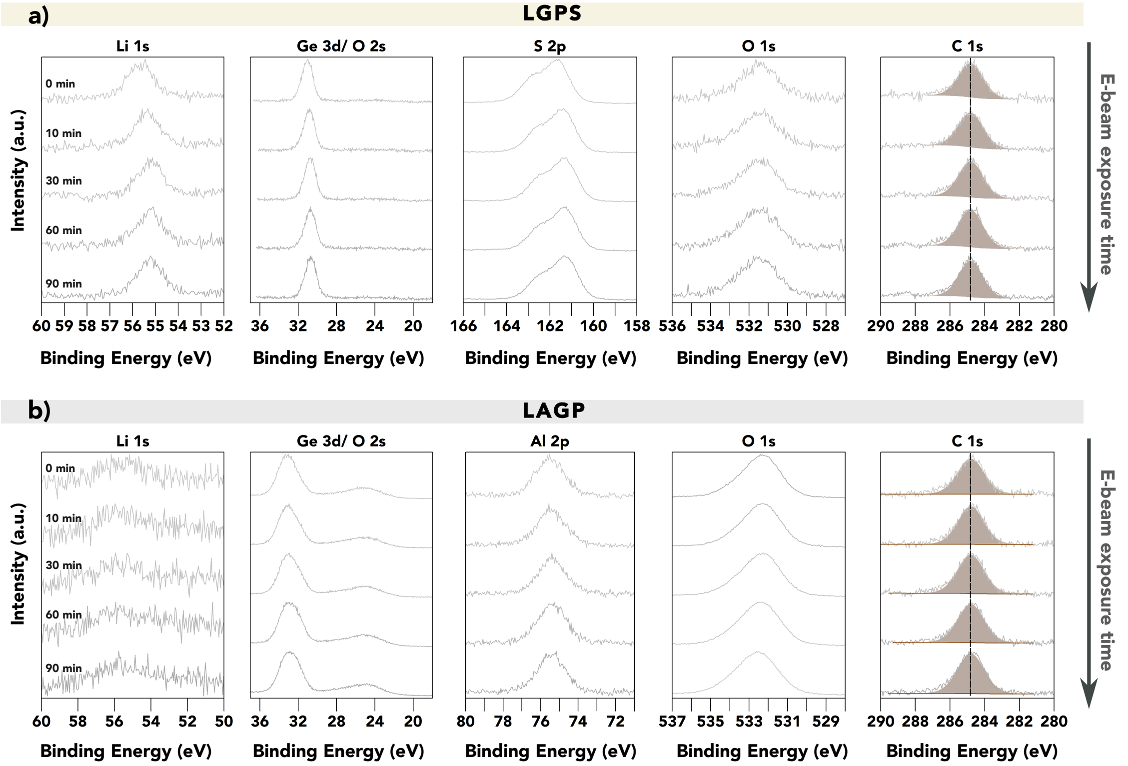

Figure 3.2: XPS spectra for VEP-XPS experiment of LGPS (a) and LAGP (b) SSEs without lithium source underneath the pellet, the electron beam exposure time is labelled in both panels. The peak intensity is normalised. Note: charge calibrated based on C 1s to 284.8 eV, indicated by the dashed line. Peak fitting is not performed here as it is to show the stability of SSEs under electron beam and X-ray beam.

The above discussion confirms that the changes observed during the VEP-XPS experiment, with the lithium source provided, are due to the reaction between the SSE and lithium metal. Figure 3.3 compares the XPS spectra collected for (a) LGPS and (b) LAGP during the VEP experiment. The evolution of the core-level spectra for the main elements (Li, Ge, P, and S/Al, respectively, from left to right) is shown as a function of lithium plating time (also electron beam exposure time), with the corresponding amount of plated lithium (q_A : μAh cm^{-2}) indicated in the last column.

A single Li 1s spectrum centred at 55.4 eV and 55.5 eV was observed for pristine LGPS and LAGP SSEs, respectively, summarising all bonding environments of lithium atoms in the structure. Similarly, a single Ge 3d peak corresponding to GeS_4 was observed at 30.5 eV for LGPS SSE. In contrast, the Ge 3d peak for LAGP SSE appears at a higher binding energy (32.5 eV), attributed to the Ge atoms being bonded to six more electronegative oxygen atoms, forming a GeO_6 octahedron. The BE values observed in this work are consistent with previous reports by He *et al.* and Yu *et al.*[221, 226]. In the P 2p region, peaks corresponding to PS_4^{3-} in LGPS SSE and PO_4^{3-} in LAGP SSE were observed. The S 2p and Al 2p and S 2p spectra further reveal the bonding environments of PS_4^{3-} units in LGPS and AlO_6 octahedra in LAGP, respectively. The crystal structures of LGPS and LAGP SSEs are schematically illustrated in Figure 1.11c and Figure 1.10e , respectively[92, 111].

After completing the XPS measurement on the pristine surface, the electron beam was applied to drive lithium plating on the surface, leading to the formation of the SEI. The pellet was exposed to the electron beam for 5-minute intervals before each subsequent XPS measurement, during which the neutraliser was turned off. As shown in Figure 3.3, new peaks corresponding to SEI components became visible after 5 minutes of lithium plating.

In the Li 1s region, a secondary peak at the lower BE side, labelled as “Li-SEI” was observed. The Ge 3d spectra revealed the formation of a secondary Ge environment with a reduced oxidation state—corresponding to the electronically conductive Ge metal phase—appearing in both LGPS and LAGP SSEs at approximately 28

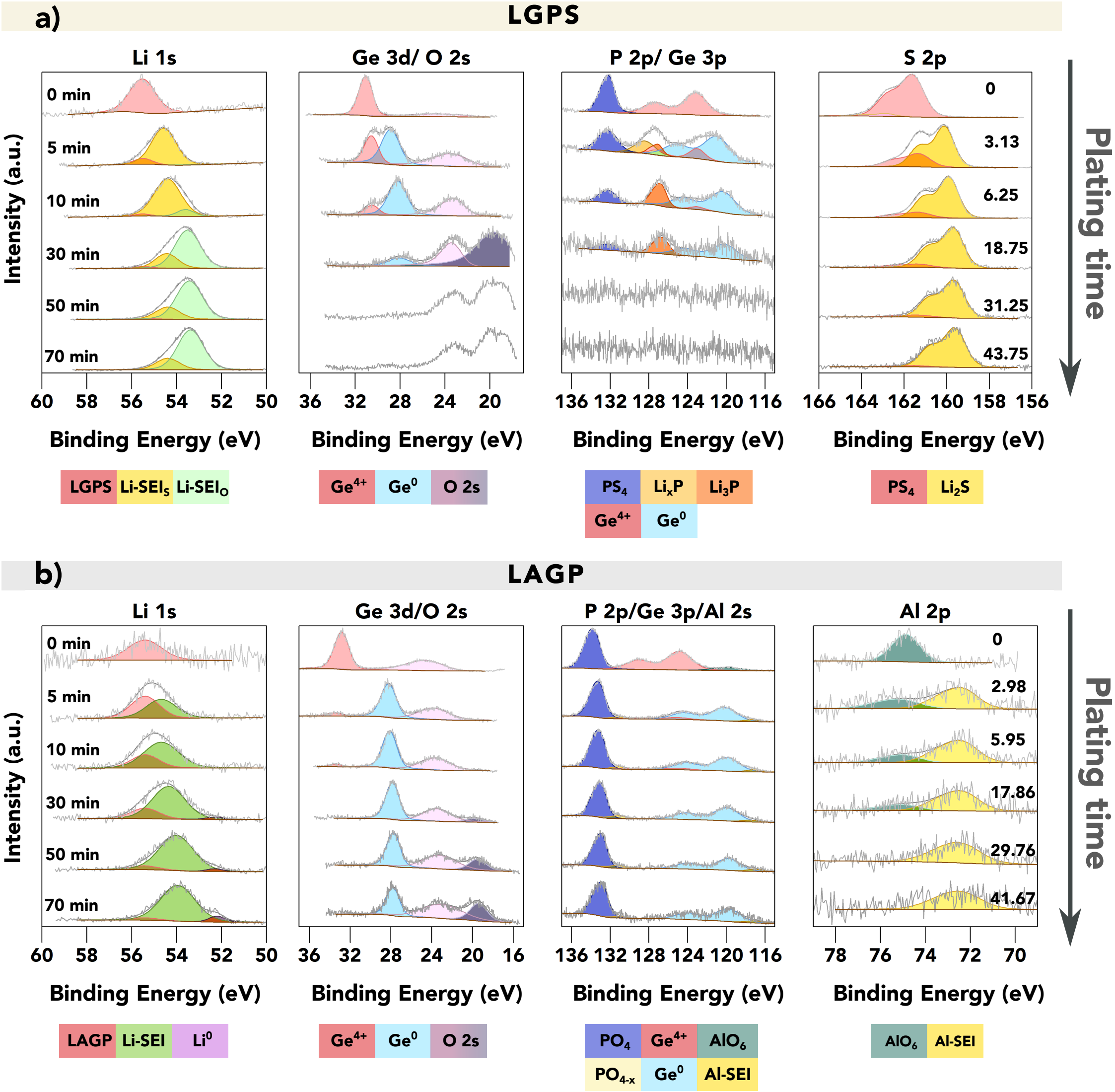

Figure 3.3: VEP-XPS investigations of LGPS and LAGP. The plots show a time series of XPS core spectra acquired during VEP-XPS experiments examining the SEI formation on top of (a) LGPS and (b) LAGP. The total Li plating time (electron beam exposure time) is given in the first column, whilst the passed charge q_A (μAh cm^{-2}), normalised by area, is labelled in the last column. Acquired spectra (grey) are shown along with linear combination fitting results. The individual spectral components are coloured; a key is provided below each group of spectra. For LGPS SE, two Li 1s SEI peaks are labelled in two colours with the subscripts donating the main non-Li contributing element, as their close BE values make it difficult to deconvolute the peaks accurately. The peak intensities were normalised for each acquired core spectrum to improve the visibility of minor spectral contributions; the raw peak intensity variations are provided in the A.1. The applied beam current was 20 μA for both samples. Reprinted from Liang *et al.* [162].

eV, highlighted in blue. This reduction of Ge suggests that the SEI formed on both SSEs contains electronically conductive species, which can influence the interfacial stability and lithium transport properties.

The differences in SEI composition formed on top of LGPS and LAGP SSEs are primarily observed in the S 2p (LGPS), Al 2p (LAGP), and P 2p spectral regions. Correlated with the reduction of Ge in the LGPS structure, the Ge-S framework in LGPS SSE underwent significant degradation, evidenced by the substantial formation of Li_2S. Furthermore, P-S bonds were disrupted during the reactions, leading to the formation of reduced phosphide species, including Li_xP ($x<3$) and Li_3P. These findings align with previous reports on SEI formation in LGPS[163, 183].

For LAGP SSE, the formation of a new Al-containing component at the interphase is evidenced by the BE shift of the Al 2p peak from 74.5 eV to 72.3 eV. This decrease in BE indicates a change in the Al bonding environment, transitioning from the original AlO_6 octahedra, where the Al atom is coordinated to six oxygen atoms, to a new bonding configuration. Zhu *et al.* evaluated the electrochemical stability of LAGP SSE against lithium metal using density functional theory (DFT) calculations, which predicted the formation of a Li-Al alloy under phase equilibrium with lithium metal[136]. Additionally, Chung *et al.* reported the formation of an $AlPO_4$ phase when LAGP SSE reacted with molten lithium at high temperatures[227]. To further investigate the chemical state of Al atoms in this new environment, XPS measurements were performed on a piece of aluminium foil. The results, presented in Figure 3.4, show that the Al 2p peak for metallic Al appears at 71.6 eV, approximately 0.7 eV lower than the BE of the Al-SEI peak. Additionally, Al in Al_2O_3, which adopts an AlO_6 octahedral structure, exhibits a BE of approximately 74.5 eV. This value closely matches the BE of Al in LAGP SSE, as both share an AlO_6 bonding environment.

This suggests that the Al atoms in the Al-SEI phase are likely bonded to fewer oxygen atoms, potentially forming $LiAlO_2$, where the Al atom is bonded to four O atoms in an AlO_4 tetrahedral structure. This structure is recognized for its promising stability against lithium metal[136, 228, 229]. Further investigations are required to confirm the identity of this Al-containing decomposition product. High-resolution TEM with careful sample preparation, Raman spectroscopy and solid-state nuclear magnetic resonance (NMR) can provide complementary structural and composition

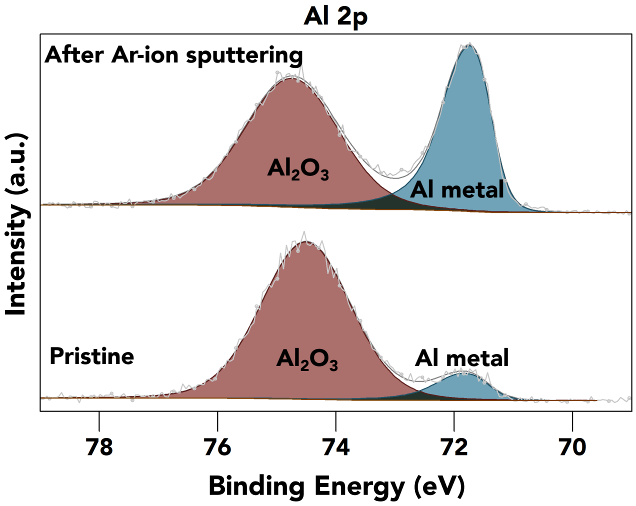

Figure 3.4: XPS measurement of aluminium foil, Ar-ion sputtering was performed to remove the surface oxide layer, charge calibration based on C 1s to 284.8 eV, Reprinted from Liang *et al.* [162]

information for its identification[230–232]. Meanwhile, the low peak intensity of Al 2p, as shown more clearly in the non-normalised spectra in Figure A.1, indicates a low atomic concentration of the Al-SEI phase in the SEI. The atomic concentration of Al-SEI after 50 minutes of electron beam plated was calculated to be approximately 1.14 at%, with Al-SEI being the only detectable component in the Al 2p spectrum.

The peak in the P 2p spectra of LAGP remains relatively stable at around 133.2 eV up to this point and continues to be detectable during further lithium plating, suggesting that the P atoms preserve their PO_4 tetrahedral coordination environment[226, 233]. The strong bonding strength of P-O bonds supports the retention of the PO_4 tetrahedral structure throughout the lithium plating process. Although continued lithium plating would typically reduce the phosphorus species to Li_3P[136], such reduction is notably absent in the case of LAGP SSE. This observation suggests that PO_4^{3-}-containing phases constitute a significant portion of the SEI structure in LAGP, contrasting with the SEI formed in LGPS, where Li_2S is the predominant component. SEI growth continues on both electrolyte materials as more lithium is plated.

Derived from the collected XPS data, the decomposition reactions occurring at the interface between the SSE and lithium metal at the very beginning are summarised in Equations 3.1 and 3.2[136, 163].

$$Li_{1.5}Al_{0.5}Ge_{1.5}(PO_4)_3 + 6Li \rightarrow 0.5LiAlO_2 + Li_4P_2O_7 + Li_3PO_4 + 1.5Ge \quad (3.1)$$

$$Li_{10}GeP_2S_{12} + 20Li \rightarrow 12Li_2S + 2Li_3P + Ge \quad (3.2)$$

3.3.2 Stability of the formed SEI

With continuous *in situ* lithium plating, the surface chemistry within the XPS probing depth is progressively replaced by SEI-associated phases. After 30 minutes of lithium plating, the probed volume consists predominantly of SEI components. Notably, the Li 1s-Li^0 peak, corresponding to metallic lithium, was observed only for LAGP SSE, indicating that the SEI layer formed on LAGP is more passivating than that on LGPS SSE.

As lithium plating continues up to 70 minutes, differences in the stabilities of the SEIs formed on LGPS and LAGP become more pronounced. These differences are most evident in the Li 1s and Ge 3d spectral regions in two key aspects.
Firstly, while the SEI of LAGP consistently retains a significant fraction of the electronically conductive Ge^0 phase throughout the plating process, the fraction of this phase in the LGPS SEI decreases over time. This trend aligns with a previous report[183], suggesting that the SEI formed on LGPS undergoes continuous chemical evolution. Additionally, as shown in the Li 1s spectra in Figure 3.3a, the fraction of oxide species progressively increases, which will be discussed in detail later.
Secondly, in both cases, the Li-SEI peak shifts toward the lower BE side as lithium plating time increases. The emergence of the Li^0 peak on the LAGP SSE surface indicates that the reaction rate between the plated lithium and the underlying SEI layer is slower than the duration of the XPS measurement cycle, which is approximately 30 minutes. In contrast, the absence of a Li^0 peak in the LGPS system suggests that the plated lithium continues to react rapidly with the underlying SSE, at a rate exceeding the measurement time. This observation implies that the SEI formed on LAGP is more passivating, effectively limiting further reaction with lithium metal and stabilising the interphase.

Previous *ex situ* studies and electrochemical tests have identified the presence of a mixed conductive interphase between LAGP and lithium metal[227]. However, the VEP-XPS experiments conducted in this work were performed in an "anode-free" configuration under zero stack pressure, allowing for the characterisation of the intrinsic reactions occurring between the SSE and lithium metal without external mechanical influences. This setup effectively isolates other contributing factors, particularly applied pressure, which is known to affect interfacial reactions in conventional battery configurations[140]. By eliminating these variables, this study provides a more fundamental understanding of interphase formation and stability at the LAGP-lithium metal interface.

The Janek group suggested that the SEI growth relies on the availability of both electrons and ions in the SEI and is therefore limited by the slowest of either ionic or electronic transport as shown in Equation 3.3 [176, 234].

$$d = \sqrt{\frac{2}{F^2 \times \rho_{SEI} \times x} \times \frac{M_{SEI} \times \sigma_{el} \times \sigma_{ion}}{\sigma_{el} + \sigma_{ion}} \times \mu_{Li}^0} \times \sqrt{t} \tag{3.3}$$

Here, d represents SEI thickness, F is the Faraday constant (96485 C mol^{-1}), ρ_{SEI} is the mean density of SEI. The parameter x denotes the number of moles of lithium metal required for the stoichiometric decomposition reaction (the stoichiometric number of lithium metal), while $\mathrm{M_{SEI}}$ is the mean molar mass of the SEI. The mean electronic and ionic conductivities of the SEI are represented by σ_{el} and σ_{ion}, respectively. μ_{Li}^0 is the chemical potential of lithium metal (8.35 kJ mol^{-1}), and t is the reaction time. From Equation 3.3, it can be inferred that the growth of the SEI is linked to its composition and physical properties; these determine the rate and extent of SEI formation.

Although the SEIs formed on both LGPS and LAGP contain electronically conductive phases, their stability varies significantly. This difference can be attributed to variations in the fraction of conductive phases within the naturally formed SEI. According to percolation theory, the formation of a continuous conduction pathway requires the conductive phase to occupy at least 15 vol% of the structure, as schematically illustrated in Figure 3.5[235]. If the volume fraction of the conductive phase surpasses this threshold, percolating network of both electronic and ionic pathways forms, enabling continuous electron and ion transport and thereby promoting sustained SEI growth. Conversely, a lower fraction of conductive phases limits percolation, leading to a more passivating SEI.

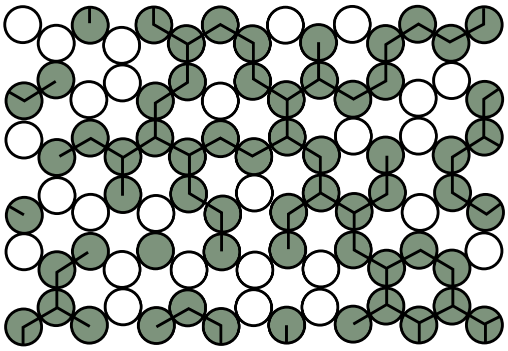

Figure 3.5: Percolation on a two-dimensional honeycomb lattice. Coloured circles indicate filled sites, open circles indicate empty sites and linked clusters are shown connected by heavy lines, Reproduced with permission from [235], Copyright 1970 AIP Publishing

From the above information, the volume fraction of the conductive phases within the SEI layer can be calculated as illustrated below (density information obtained from Materials Project is included in Table A.1):

- Calculation of volume ratio of conductive Ge phase in the LAGP SEI:

  volume of $LiAlO_2 = 0.5mol \times 65.92\ g/mol \div 2.64\ g/cm^3 = 12.48\ cm^3$

  volume of $Li_4P_2O_7 = 1mol \times 201.71\ g/mol \div 2.38\ g/cm^3 = 84.75\ cm^3$

  volume of $Li_3PO_4 = 1mol \times 115.7944\ g/mol \div 2.54\ g/cm^3 = 45.59\ cm^3$

  volume of Ge$= 1.5mol \times 72.64\ g/mol \div 5.28\ g/cm^3 = 21.46\ cm^3$

  volume ratio of Ge = 10.8 %

- Calculation of volume ratio of Ge and Li_3P phases in the LGPS SEI:

  volume of $Li_2S = 12mol \times 45.95\ g/mol \div 1.67\ g/cm^3 = 330.18\ cm^3$

  volume of $Li_3P = 2mol \times 51.79\ g/mol \div 1.48\ g/cm^3 = 69.99\ cm^3$

  volume of Ge$= 1mol \times 72.64\ g/mol \div 5.28\ g/cm^3 = 13.76\ cm^3$

  volume ratio of Ge and Li_3P = 20.2 %

For the SEI initially formed on LGPS SSE, the conductive phases—Li_3P and Ge—constitute more than 20 vol% of the interphase. This high fraction facilitates the formation of a continuous electronic and ionic conduction pathway, ensuring that the SEI electrochemical potential remains equal to that of the sample surface when the electron beam is applied. Consequently, the LGPS SSE continues to degrade, leading to progressive SEI thickening toward the lithium source beneath. In contrast, the SEI formed on LAGP SSE contains a lower fraction of conductive phases, estimated to be less than 11 vol%. This insufficient fraction prevents the formation of a continuous electronic percolation network, effectively limiting electron transport and restraining further reaction kinetics. As a result, the SEI on LAGP acts as a more passivating layer, offering improved interfacial stability against lithium metal compared to LGPS.

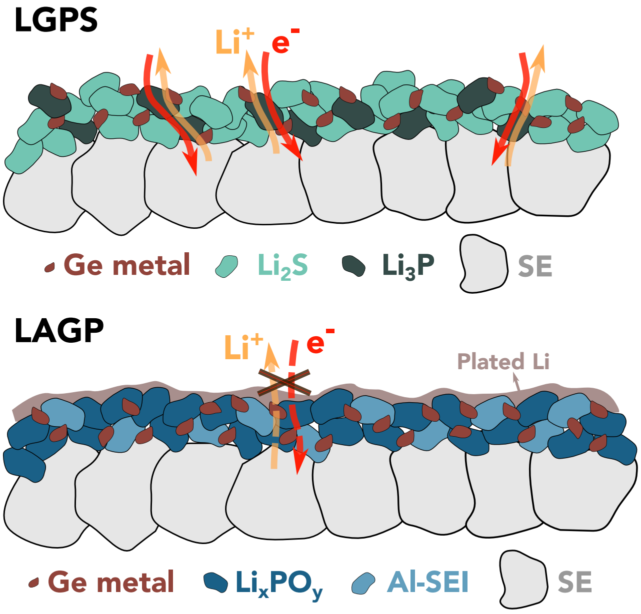

Figure 3.6: Schematic of the multi-component SEI layer formed on top of LGPS and LAGP SEs. Reprinted from Liang *et al.* [162]

This concept is schematically illustrated in Figure 3.6. Further investigations into the nanostructure and precise composition of the SEI are necessary to determine whether its growth is primarily limited by electron transport or lithium-ion diffusion.

3.3.3 Explanation of diminishing Ge and P signal for LGPS surface during VEP experiment

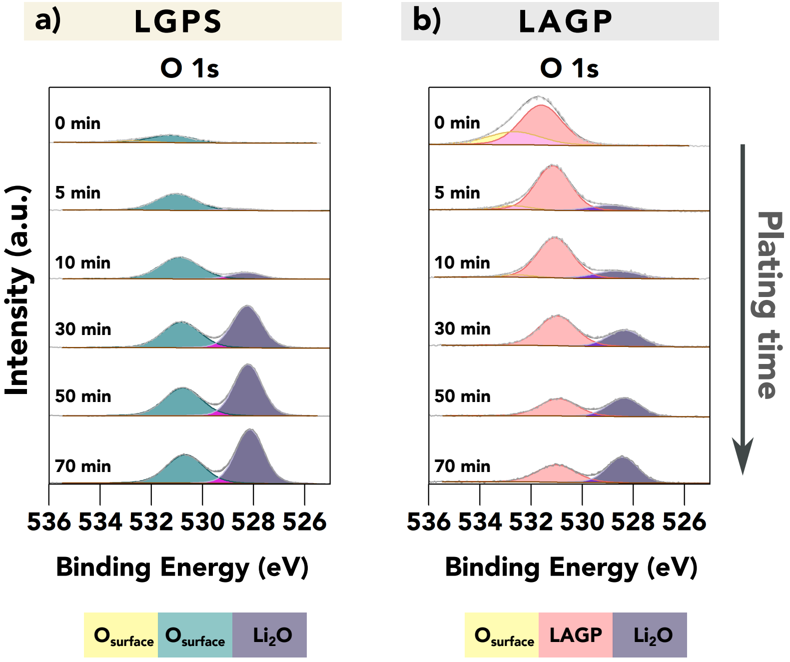

Figure 3.7: XPS spectra (O 1s region) for VEP-XPS experiment of LGPS (a) and LAGP (b) SSEs without lithium source underneath the pellet, the E-beam exposure time is labelled in both panels. The peak intensity is non-normalised. Note: charge calibrated based on C 1s to 284.8 eV. Reprinted from Liang *et al.* [162]

Notably, the LGPS system inherently lacks oxygen in its structure. However, an accumulation of oxide species is evident in the Li 1s spectra (Figure 3.3a), and the corresponding O 1s spectra (Figure 3.7a) confirm the formation of Li_2O on the surface. The fraction of Li_2O relative to the Li 1s signal continues to increase as the P 2p and Ge 3d signals become attenuated, leaving Li_2S as the dominant component in the surface region. This suggests that Li_2S may undergo reaction with residual contaminants in the chamber environment, leading to its conversion into Li_2O over time.

To evaluate the stability of Li_2S during XPS measurements, a cold-pressed Li_2S pellet was prepared and loaded into the XPS chamber. The pristine Li_2S powder (99.98% trace metal basis) was purchased from Sigma-Aldrich and subsequently pelletized under 500 MPa. Figure 3.8b displays the deconvoluted S 2p core-level spectrum, which reveals the presence of polysulfides and oxidation products in the as-received powder. To further assess its stability, the pelletized Li_2S sample underwent continuous XPS measurements inside the chamber with the electron neutraliser activated, allowing real-time tracking of spectral changes over time. A progressive formation of Li_2O on the surface is evidenced by the increasing intensity of the Li_2O peak, as shown in Figure 3.8a. Figure 3.8c illustrates a steady rise in the atomic concentration of oxygen within the probing area (top surface) over time, while the lithium concentration remains relatively stable. Additionally, Figure 3.8d presents the ratio of Li_2O to the total Li_2S and Li_2O content, further confirming the continuous oxidation of Li_2S. These observations indicate that Li_2S progressively reacts with residual contaminants inside the XPS chamber, leading to the continuous formation of Li_2O throughout the measurement process. This explains the persistent formation of Li_2O on the surface of LGPS SSE during the *in situ* XPS experiment, as its SEI contains a substantial fraction of Li_2S. Over time, Li_2S undergoes oxidation due to exposure to trace contaminants in the XPS chamber, gradually converting into Li_2O. By extension, this also accounts for the formation of Li_2O on the surface of other sulphide-based SSEs that inherently lack oxygen in their composition. During *in situ* XPS experiments, Li_2O formation is often observed before the detection of a Li^0 peak, as reported for the argyrodite Li_6PS_5Cl[174]. This suggests that the reaction between Li_2S and trace environmental contaminants is a common phenomenon in *in situ* XPS studies of sulphide SSEs. Thus, when analysing SEI formation and stability, it is essential to consider these oxidation effects to accurately interpret the results. A higher vacuum level (lower pressure) is preferred to provide a cleaner environment during XPS measurements, and samples should be prepared with particular care inside gloveboxes.

3.3.4 SEI evolution kinetics

As mentioned earlier, previous studies have reported an unstable SEI at the LAGP-lithium interface when the cell was cycled in a confined setup, where strain build-up and mechanical degradation could facilitate SSE decomposition[217,

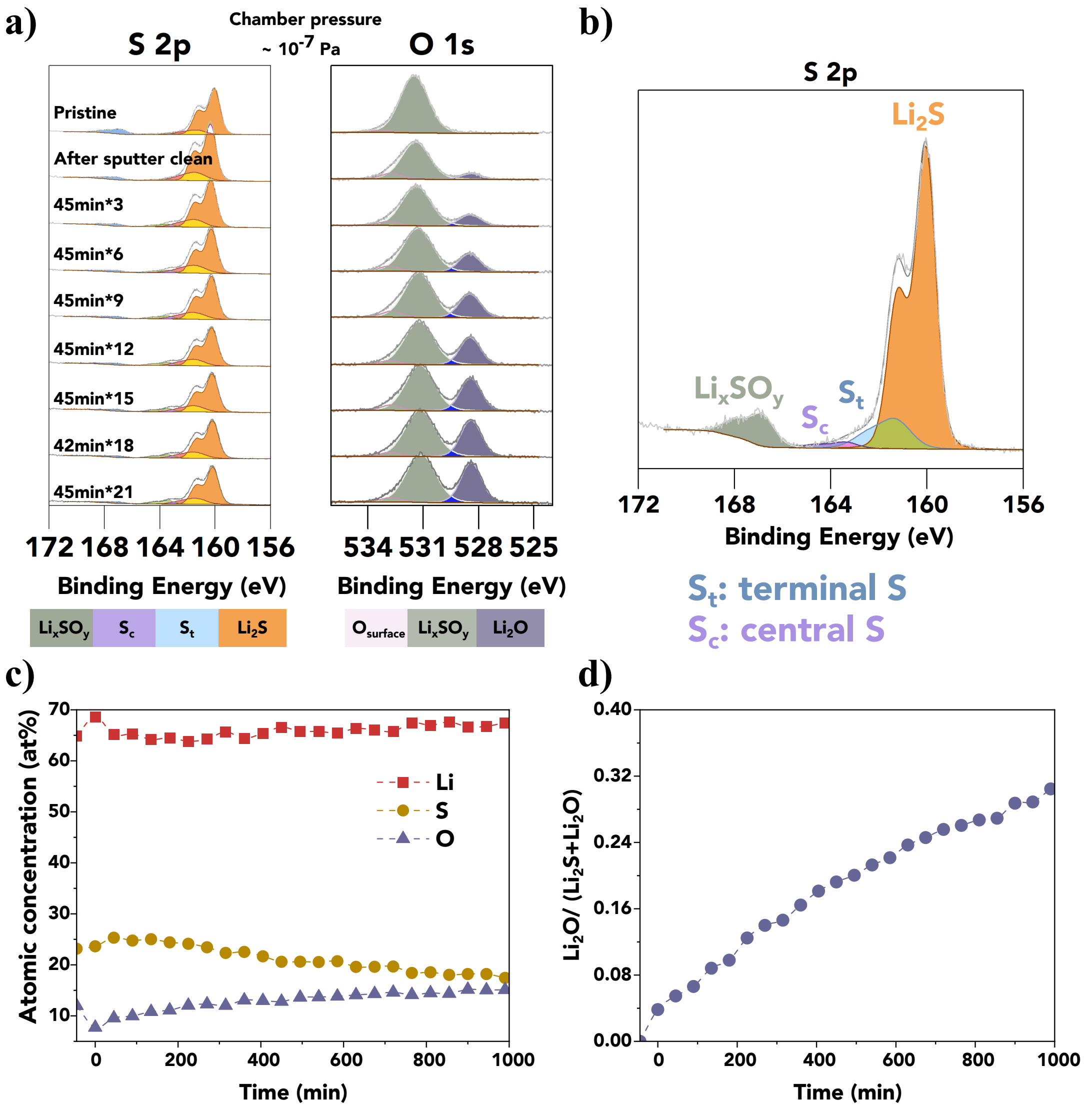

Figure 3.8: XPS measurement of Li_2S sample inside the XPS chamber over time: **(a)** O 1s and S 2p core-level spectra. In the sequence of XPS spectra presented here, the progression from top to bottom reflects the information of the pristine surface, followed by the surface after gentle Ar-ion sputter cleaning, and subsequently, the changes observed on the sample surface over time. Each sequence of XPS measurement was conducted over a duration of 45 minutes (labelled in the first column); **(b)** Enlarged XPS S 2p spectrum of the pristine surface showing detailed fitting results; **(c)** The evolution of Li, S and O atomic concentration over time; **(d)** Evolution of the ratio of Li_2S/ (Li_2S+Li_2O), Reprinted from Liang *et al.* [162]

236]. In contrast, the experimental setup used in this work eliminates pressure effects, allowing the SEI's chemical properties to be examined in isolation. By decoupling mechanical factors from chemical reactivity, this approach provides a clearer understanding of degradation mechanisms. Therefore, further investigations into SEI stability in this system are necessary to assess its intrinsic stability and long-term performance.

By continuously monitoring the LAGP SSE surface after lithium metal is plated, SEI kinetics information can, in principle, be extracted from the attenuation rate of the Li 1s-Li^0 peak and the increasing intensity of other peaks corresponding to SEI components (practical limitations are discussed below). In the case of LAGP SSE, the Ge, P, and O spectra serve as key indicators for this quantification process. This approach enables the assessment of SEI stability and growth dynamics, offering insights into the evolution of interfacial reactions over time.

As shown in Figure 3.9, the Li 1s-Li^0 peak gradually diminishes over the resting period, indicating the consumption or transformation of plated lithium. Meanwhile, Ge remains in its metallic state, as evidenced by both Ge 3d and Ge 3p spectra. The BE of the P 2p-PO_4 peak remains stable, suggesting that the PO_4 structure is resistant to reduction by lithium metal. Both Ge and P signals show a slight decrease in peak intensity over time. Notably, the ratio of O 1s-PO_4 to O 1s-Li_2O appears to increase over time, which may be attributed to ongoing reactions between the plated lithium metal and the underlying SEI layers. This suggests a gradual evolution of the interphase, where lithium continues to participate in secondary reactions, potentially leading to further structural and compositional modifications within the SEI.

The oxidation of metallic lithium in the XPS chamber must be considered in this case, as there are two possible pathways for the plated lithium metal on the surface:

(1) Reaction with the underlying SEI layer: The plated lithium metal may continue to react with the SEI components beneath it, leading to the formation of additional decomposition products. This reaction pathway would result in a gradual decrease in the Li^0 peak intensity while simultaneously increasing the intensity of peaks corresponding to SEI-related species.

(2) Oxidation by residual contaminants in the XPS chamber: The metallic lithium at the top surface may undergo oxidation due to trace contaminants in the XPS chamber, primarily residual O_2 or H_2O, even under UHV conditions[237]. This

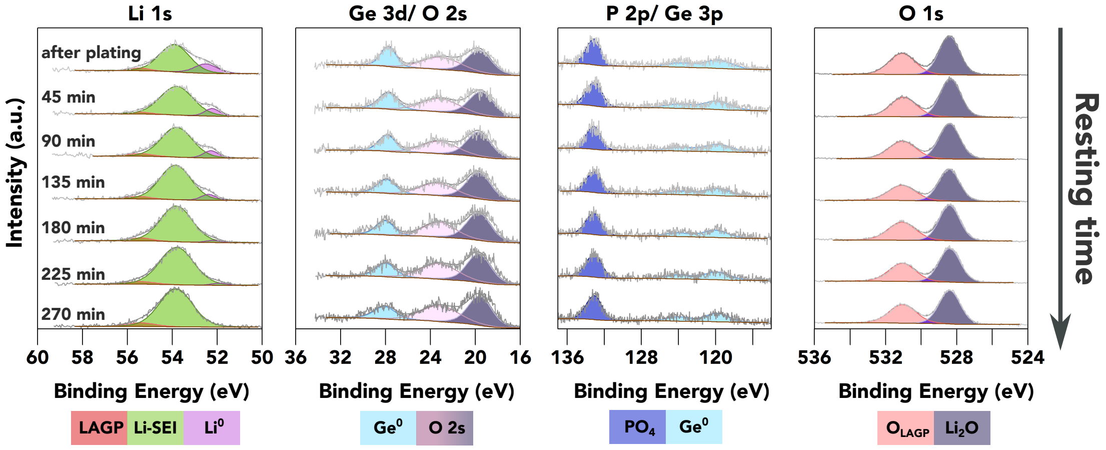

Figure 3.9: XPS investigation of the further reaction of plated lithium metal with the underneath layer. The plots show a time series of XPS core spectra acquired after a strong Li^0 peak was observed on top of LAGP. The peak intensity is non-normalised. The resting time is given in the first column. Reprinted from Liang *et al.* [162]

would lead to the formation of Li_2O or LiOH on the lithium surface, which can be misinterpreted as part of the SEI evolution rather than an environmental effect.

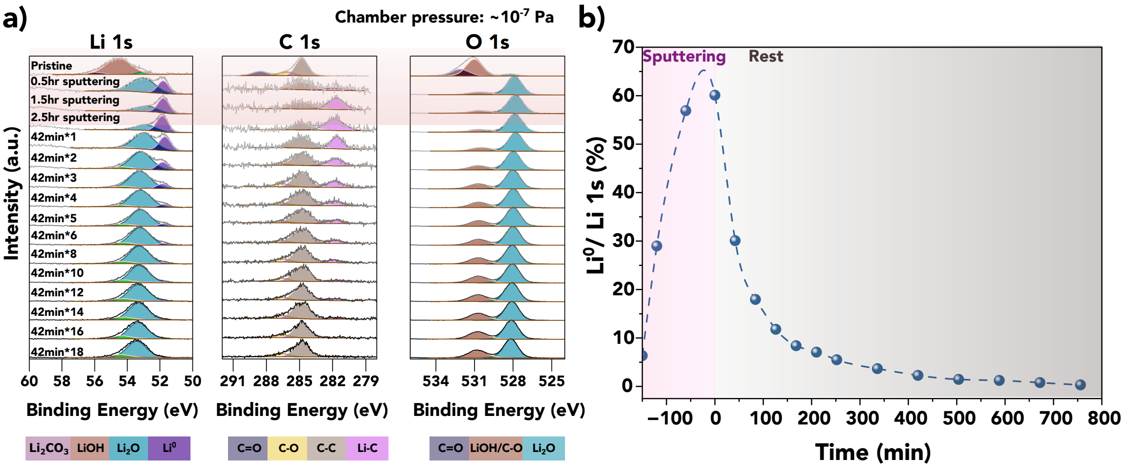

Figure 3.10: XPS measurement of lithium metal sample inside the XPS chamber over time: **(a)** Li 1s, C 1s and O 1s core-level spectra. In the sequence of XPS spectra presented here, the progression from top to bottom reflects the information of the pristine surface, followed by the surface after Ar-ion sputter cleaning, and subsequently, the changes observed on the sample surface over time. Each sequence of XPS measurement was conducted over a duration of 42 minutes (labelled in the first column);**(b)** Evolution of the compositional fraction of Li^0/ Li 1s, Reprinted from Liang *et al.* [162]

Distinguishing between these two pathways is crucial for accurately interpreting SEI evolution kinetics. The oxidation rate study conducted on metallic lithium in the XPS chamber (Figure 3.10) serves as a reference for determining whether the observed lithium consumption results from reactions with the underlying layer or oxidation due to exposure to residual gases in the chamber.

The oxidation rate of metallic lithium inside the XPS chamber was investigated through continuous XPS measurements on a piece of sputter-cleaned lithium foil. Before being loaded into the XPS chamber, the lithium foil was mechanically brushed and scraped to remove surface contamination. As depicted in Figure 3.10a, the top surface of the pristine lithium foil, despite appearing shiny, primarily consists of oxide species or contaminants. This suggests that even after surface preparation, a thin oxide or hydroxide layer persists on the lithium surface, likely due to unavoidable exposure to trace contaminants during sample handling and transfer.

Following this, Ar-ion sputtering was performed to remove the passivation layer and expose the fresh metallic lithium surface. The formation of lithium carbide was observed post-sputtering, likely due to the reaction between lithium and lithium carbonate or other surface contaminants during the sputtering process[187].

Subsequently, continuous XPS measurements were conducted on the sputter-cleaned lithium surface without further treatment to assess its oxidation rate inside the XPS chamber. As shown in Figure 3.10a, the freshly exposed lithium surface underwent continuous oxidation, evidenced by the increasing peak intensity of Li_2O. Figure 3.10b tracks the compositional evolution of metallic lithium (Li^0) in the Li 1s spectra, illustrating a gradual decline in the Li^0 fraction. After approximately 400 minutes of measurement, a relatively thick oxide layer had formed, with the Li^0 fraction approaching zero. This progression highlights the dynamic chemical changes occurring in metallic lithium under XPS experimental conditions in a UHV environment.

During this experiment, the O 1s peak corresponding to LiOH (with a BE of approximately 530.7 eV) is less than 0.4 eV away from the O 1s-PO_4 peak. This close proximity introduces potential errors in the quantification process, thereby reducing the accuracy of reaction kinetics estimations. Given that these two peaks correspond to different possible reaction pathways, their spectral overlap makes it difficult to reliably distinguish their individual contributions. Consequently, precise quantification of the reaction kinetics could not be performed due to uncertainties arising from this spectral interference.

This work introduces a novel approach for quantifying the stability of the formed SEI and its evolution kinetics using the *in situ* XPS technique. However, the accuracy of the information extracted from the LAGP surface is constrained by lithium oxidation and peak overlapping. Ideally, this technique requires a significantly higher vacuum level in the chamber, specifically below 10^{-7} Pa, to minimise oxidation-related artifacts. Some XPS systems are capable of achieving such high vacuum levels, and baking out the chamber helps remove residual gas molecules, thereby further improving vacuum conditions[238–242]. For other SSEs, such as Li_6PS_5Cl, where core-level spectra do not overlap with oxide species, continuous XPS monitoring provides a more reliable means of studying SEI evolution. In such systems, SEI compositional changes can be tracked with higher precision, enabling a clearer understanding of interfacial stability and reaction mechanisms over time. These aspects will be further explored in Chapter 4.

3.3.5 *In situ* sputtering investigation of the SEI

In this work, SEI investigation was also conducted using *in situ* Ar^+ ion sputtering, in which lithium was sputtered from a lithium target and subsequently deposited onto the SSE surface. The SEI then formed as a result of the reaction between the deposited lithium and the SSE. By continuously monitoring the XPS spectra after each lithium deposition step, insights into the composition, structure, and stability of the SEI can be obtained, providing valuable information on interfacial reactions in solid-state battery systems. A detailed explanation of this technique is provided in Section 2.1.2.1.

As shown in Figure 3.11, the formation of Li_2S, Li_3P, and Ge^0 was consistently observed, confirming the interfacial reactions between LGPS SSE and lithium. The absence of a metallic lithium peak further indicates that the SEI at the LGPS-lithium interface remains unstable, continuously growing due to its mixed

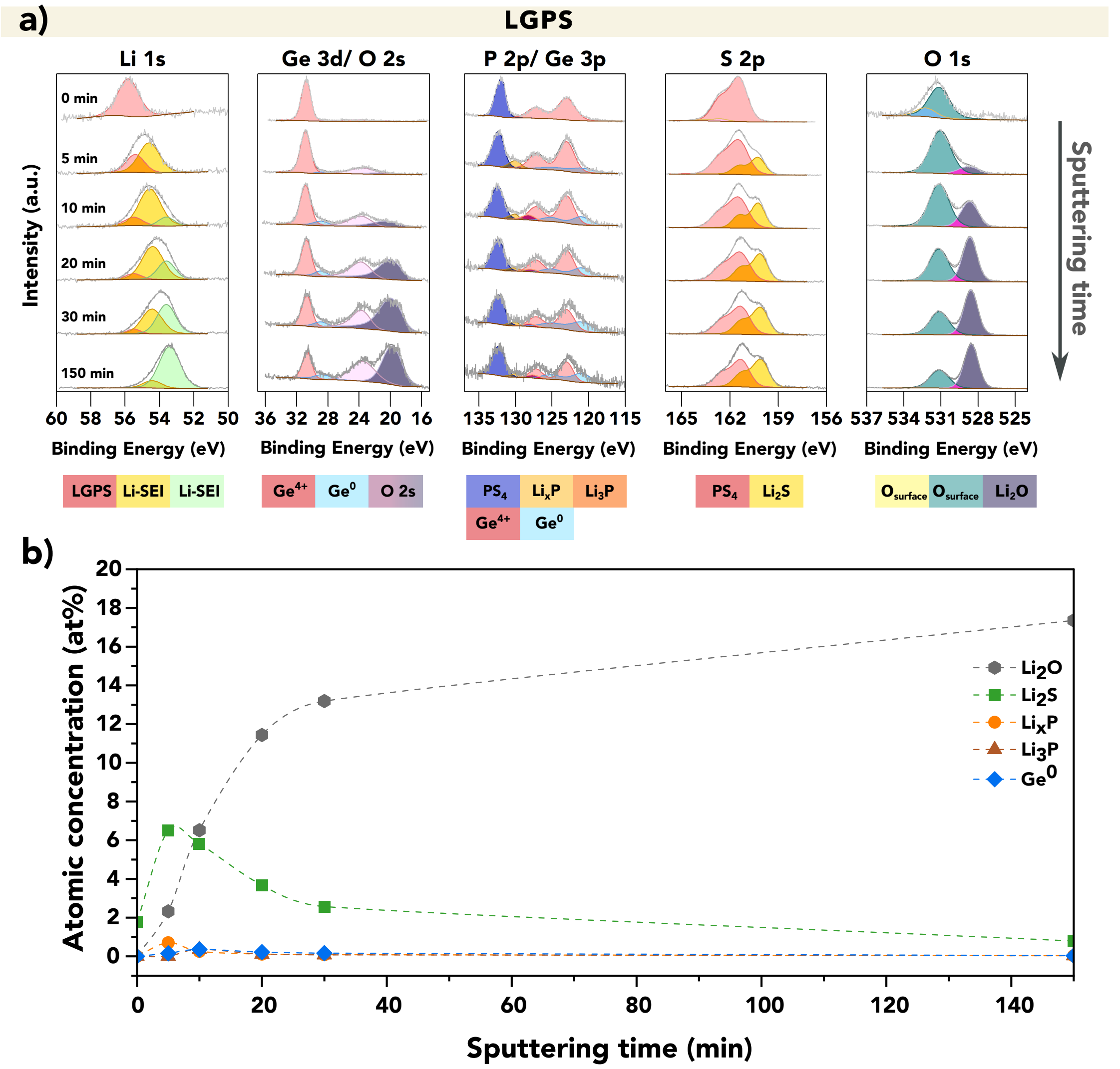

Figure 3.11: XPS core spectra evolution of in situ sputtering experiments of LGPS SSE (a). The total lithium sputtering time is given in the first column. Acquired spectra (grey) are shown along with linear combination fitting results. The individual spectral components are coloured; a key is provided below each group of spectra. The peak intensities were normalised for each acquired core spectrum to improve the visibility of minor spectral contributions; The applied voltage for the sputtering was 4 kV; (b) The atomic concentration variation with sputtering time. Reprinted from Liang *et al.* [162]

conductive nature. The decomposition of LGPS SSE during the *in situ* sputtering experiment follows a similar trend to that observed in the VEP-XPS experiment. These consistent findings reinforce the validity of using both techniques for studying SEI formation and evolution, as the fundamental decomposition reactions and their resulting interphases remain comparable. This further suggests that the instability of the SEI in LGPS is an inherent material property rather than a consequence of specific experimental conditions. The agreement between the VEP-XPS and *in situ* sputtering experiments highlights that regardless of the lithium deposition method, the formation of a mixed conductive interphase in LGPS persists, leading to continuous SEI growth.

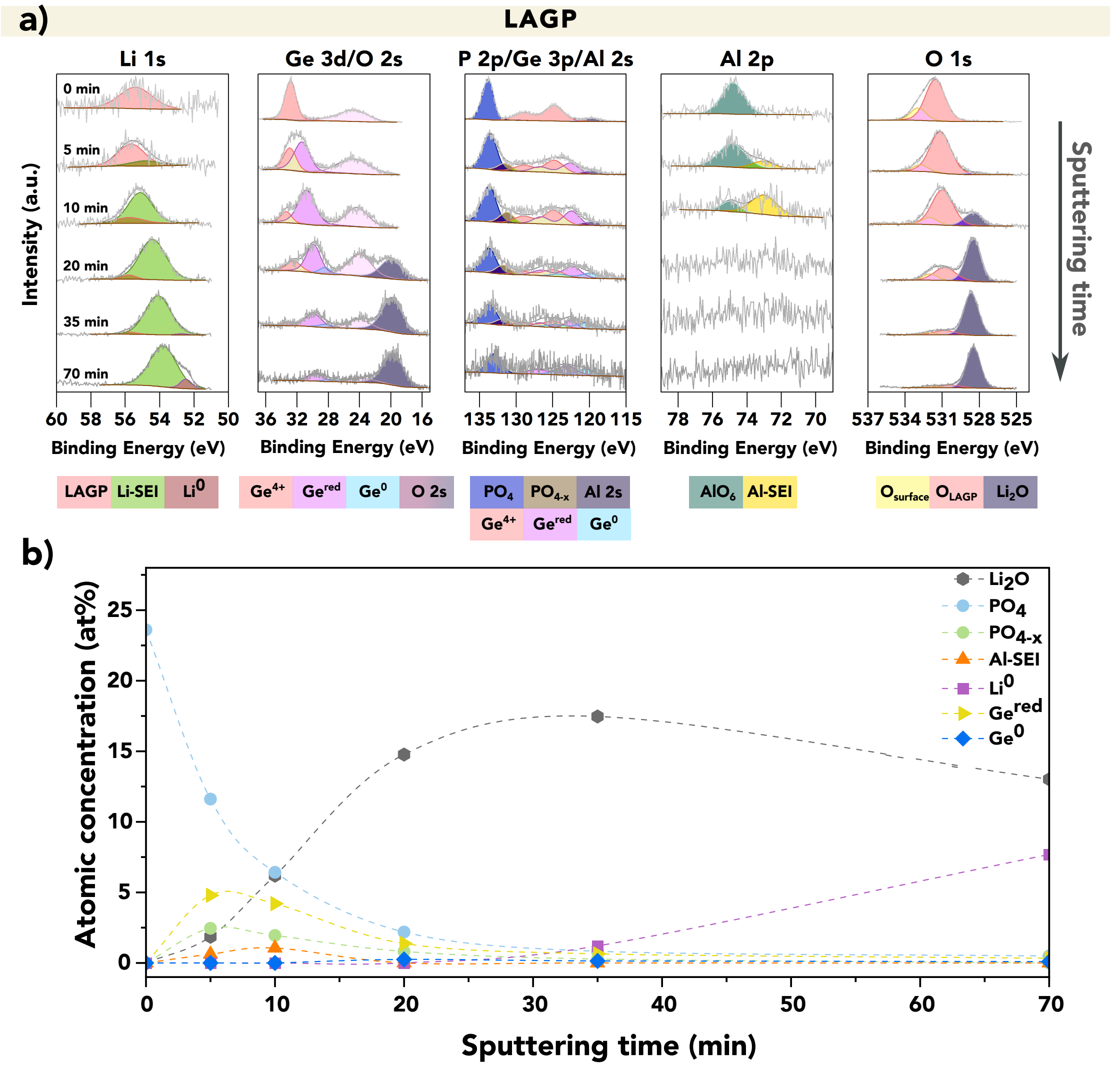

Figure 3.12: XPS core spectra evolution of in situ sputtering experiments of LAGP SSE **(a)**. The total lithium sputtering time is given in the first column. Acquired spectra (grey) are shown along with linear combination fitting results. The individual spectral components are coloured; a key is provided below each group of spectra. The peak intensities were normalised for each acquired core spectrum to improve the visibility of minor spectral contributions; The applied voltage for the sputtering was 4 kV; **(b)** The atomic concentration variation with sputtering time. Charge calibration is carried out based on the P 2p peak for PO_4. Reprinted from Liang *et al.* [162]

For LAGP SSE, in comparison to the results presented in Figure 3.3b, an additional Ge 3d component corresponding to reduced valence state, denoted as Ge^{red}, is observed prior to the appearance of metallic Ge peak. This indicates a stepwise reduction process rather than a direct transition as previously observed in Figure3.3[164, 216, 243, 244]. Such behaviour may be attributed to kinetic limitations in the lithiation process or the transient formation of intermediate species, both of which could impede the immediate and complete reduction of Ge.

Notably, after approximately 35 minutes of lithium sputtering, the Li^0 peak emerges, further illustrating the formation of a more passivating SEI compared to LGPS SSE. This suggests that, while interfacial reactions occur between LAGP and lithium metal, the SEI formed on LAGP is more resistant to continuous lithium diffusion and reaction, thereby limiting further SSE decomposition. These observations align with previous findings that the SEI on LAGP contains a lower fraction of electronically conductive phases, preventing the formation of a continuous mixed conductive pathway that would otherwise facilitate SEI thickening.

Additionally, when comparing the O 1s spectra shown in Figure 3.7b and Figure 3.12, the ratio of Li_2O/O 1s (if normalised by the the amount of deposited lithium) appears to be substantially higher in the sputtering experiment. This suggests that more Li_2O is formed during sputtering, likely due to oxidation processes occurring as lithium atoms travel from the target to the pellet surface. The differences in oxygen incorporation between the sputtering and VEP-XPS experiments may be attributed to variations in lithium deposition methods, exposure to residual gases in the chamber, or reaction pathways influenced by the different kinetic conditions of each technique.

The decomposition of LGPS SSE during the *in situ* sputtering experiment follows a similar trend to that observed in the VEP-XPS experiment. Overall, the results from both techniques are in good agreement regarding the identified decomposition products and their relative stability. However, some notable differences are observed between the two methods, which are likely due to the combined influence of several contributing factors rather than any single variable. These factors include:

- Lithium deposition method: In the VEP-XPS experiment, lithium is electrochemically plated from a lithium source beneath the SSE pellet, driven by the negative potential provided by the low-energy electron beam. This process mimics a realistic battery operation, where lithium ions migrate through the electrolyte and deposit on the surface. In contrast, during the *in situ* sputtering experiment, lithium atoms are physically deposited onto the SSE surface. This process may introduce different nucleation and growth mechanisms, as lithium arrives in atomic form rather than as Li^+ ions. The kinetic energy of the sputtered lithium atoms, along with possible surface reactions before reaching the substrate, could result in distinct SEI structures compared to electrochemical plating[50, 175].

- Lithium deposition rate: In this work, the lithium deposition rate for VEP-XPS is calculated as 3.24 nm min^{-1} (for an 8 mm LGPS pellet under a 20 μA beam current). In contrast, the deposition rate during the *in situ* sputtering experiment is estimated to be approximately 0.2 nm min^{-1}. This significant difference means that within the same time frame, substantially more lithium is deposited during VEP-XPS experiments compared to sputtering. The higher deposition rate in VEP-XPS—more representative of actual battery operation conditions—could lead to faster SEI formation and different interphase properties, potentially influencing the observed stability, thickness, and composition of the SEI.

- Oxidation effects: The oxidation of lithium metal by the residual contaminants in the chamber may differ between the two methods. In the sputtering process, lithium atoms may interact with background gases before reaching the SSE substrate and absorbed oxidative species on the sample surface, whereas VEP-XPS allows lithium to plate directly from the bulk, minimising oxidation. These would affect the reactivity of the deposited “lithium” against SSEs.

Overall, these factors may contribute to the observed differences between VEP-XPS and *in situ* lithium sputtering results. Further investigations are required to elucidate the underlying mechanisms. By adjusting the current density during VEP experiments and the Ar-ion sputtering rate, SEI formation can potentially be studied under comparable lithium deposition rates, thereby providing insights into SEI formation when lithium is deposited by different methods. Despite these variations, the fundamental decomposition products and SEI formation trends remain comparable, reinforcing the reliability of both techniques for investigating interfacial stability in solid-state battery systems.

3.4 Summary

Virtual electrode plating and *in situ* lithium sputtering XPS experiments on LGPS and LAGP SSEs yielded consistent results regarding SEI composition and growth. LAGP exhibited slower reaction kinetics, as indicated by the emergence of a Li^0 peak, whereas LGPS consumes the deposited lithium at a faster rate to form an interphase, preventing metallic lithium plating under the same applied current.

The absence of applied pressure in VEP-XPS experiments allows these observations to be attributed to SEI composition, distribution, and the physical properties of secondary decomposition products. Notably, the presence of mixed ion-electron conductive Li_3P in LGPS—but not in LAGP—plays a crucial role in SEI stability. The interfacial reactions in LGPS result in an interphase with a continuous conductive pathway, facilitating ongoing interphase thickening. In contrast, SEI growth on LAGP SSE is relatively limited, forming a more passivating interphase.

Furthermore, *in situ* XPS enables the investigation of SEI formation kinetics by continuously monitoring surface evolution after the emergence of Li^0. However, to accurately quantify reaction kinetics, an ultra-high vacuum level (significantly lower than 10^{-7} Pa) is necessary to minimise unwanted reactions between lithium metal and residual gases inside the chamber. These side reactions not only deplete lithium metal but also introduce peak overlapping issues, complicating spectral interpretation.

These findings underscore the dynamic chemical transformations of metallic lithium under XPS experimental conditions. The results provide valuable insights into lithium oxidation kinetics, emphasising the importance of accounting for oxidation effects when analysing XPS data in lithium-based battery studies.

4

Evolution of interphase formed between Li_6PS_5Cl and lithium metal

Contents

The major part of the work in this chapter was first reported in the following research article: Burton M, Jagger B, Liang Y, Gibson JS, Aspinall J, Swallow JEN, *et al.* The Role of Phosphorus in the Solid Electrolyte Interphase of Argyrodite Solid Electrolytes. ChemRxiv. 2025; doi:10.26434/chemrxiv-2024-1727n-v2

4.1 Introduction

As briefly introduced in Chapter 1, sulphide argyrodite SSEs are a class of materials with compositions close to Li_6PS_5X (X = Cl, Br, I). These electrolytes exhibit structures related to the mineral argyrodite (Ag_8GeS_6) and demonstrate high ionic conductivities in the range of 10^{-3} to 10^{-2} S cm^{-1}[118]. Li_6PS_5Cl is one of the most widely studied and applied sulphide SSEs, with extensive literature detailing its synthesis methods, structural characteristics, properties, and electrochemical performance[127, 245]. Like most sulphide-based SSEs, Li_6PS_5Cl has a relatively narrow electrochemical stability window, with a theoretical reduction potential of 1.71 V vs Li^+/Li[136]. Consequently, it readily reacts with lithium metal upon contact, leading to the formation of a SEI, which critically impacts its long-term stability and performance.

Unlike the LGPS SSE discussed in Chapter 3, which forms conductive interphase due to the presence of Li_3P and Ge phases, Li_6PS_5Cl demonstrates better stability against lithium metal by forming a more passivating SEI[125]. If the formed SEI is ionically conductive, electrically insulating, and chemically stable against lithium metal, it can effectively block further decomposition of the SSEs and prevent the loss of lithium resources. Both computational and experimental work have been conducted to uncover the decomposition reaction between Li_6PS_5Cl and lithium metal. The formed SEI is generally agreed to be composed of lithium binary phases including Li_2S, LiCl and Li_3P that are stable against lithium metal[129]. Recent XPS studies also reveal the existence of partially reduced Li_xP ($x<3$) phases in the SEI[174, 183].

Additionally, the reported thickness of the SEI formed between Li_6PS_5Cl and lithium metal ranges from a few nanometres to several hundred nanometres, with variations in composition depending on operating conditions[174, 176, 198, 246]. This raises questions about the stability and growth mechanism of the formed SEI. Recent work by the Janek group has shown that the SEI may continuously grow through an diffusion process[198], which could potentially explain the differences in the probed SEI thickness. Investigating the diffusion mechanism behind this growth could help identify potential strategies to prevent it.

In Chapter 3, continuous XPS measurements were performed on the LAGP SSE surface with metallic lithium plated using the VEP method to quantify SEI evolution kinetics. However, the analysis was constrained by lithium metal oxidation in the chamber and peak overlapping. This method is expected to be more effective for sulphide SSEs, where these limitations are significantly reduced. Consequently, it was applied to investigate SEI evolution on the Li_6PS_5Cl SSE, revealing distinct changes in chemical composition. When combined with electrochemical test results, the findings indicate that the SEI formed between Li_6PS_5Cl and lithium metal continues to grow via lithium diffusion through lithiated phosphorus species as long as a lithium source is available to sustain the reaction. Therefore, to achieve a truly passivating layer at the $Li_6PS_5Cl|Li$ interface, an artificial layer that can stop this diffusion process is essential.

4.2 Experimental

4.2.1 Sample preparation

The sample for XPS measurement was prepared by cold pressing 30 mg of Li_6PS_5Cl (Ampcera 10 μm) under 500 MPa for 5 minutes using a 5 mm stainless steel die set. Then the pellet was placed on top of a 4.76 mm diameter lithium foil (prepared using same method as described in section 3.2.1, which was then placed on top of a copper foil. This stack was pressed at ∼50 MPa for about a minute to ensure good contact. The sample stack was grounded to the XPS sample stage using conductive carbon tape. The sample stage was then transferred from the Ar glovebox to the XPS system (PHI VersaProbe III) using a vacuum transfer vessel (MOD 07-111K, ULVAC-PHI, Inc.) to avoid air contamination.

The sample for CTTA measurement was prepared using a polyetheretherketone (PEEK) cylinder with the internal diameter of 10 mm. The setup is schematically shown in Figure 4.1. The PEEK cylinder used for making the pellet was cut in half perpendicular to the internal 10 mm hole and the two parts were held together

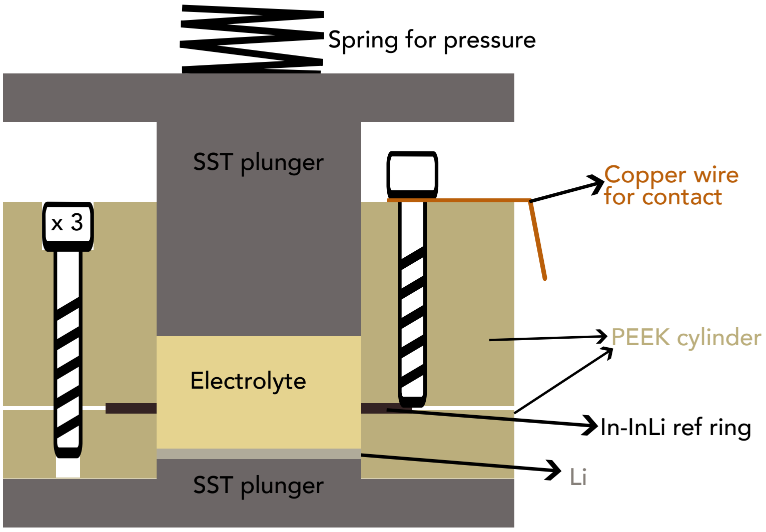

Figure 4.1: Schematic of the three-electrode cell setup for the modified CTTA test

using 3 screws. An In-InLi alloy ring with a 10 mm hole was used as reference electrode and was placed and aligned using the stainless steel plunger. Another screw (connected with the copper wire) was used to make electrical contact of the In-InLi ring with the potentiostat. And the cut was positioned so that the middle of the Li_6PS_5Cl pellet was touching the the In-InLi ring. Then 150 mg Li_6PS_5Cl (Ampcera 10 μm) was put inside the PEEK cylinder and cold pressed under 370 MPa for 5 minutes using stainless steel plungers. Lithium counter electrodes were prepared by brushing away the surface contaminants of the lithium metal followed by calendering to $\sim 200\ \mu m$. Then 10 mm lithium disc was punched out from the calendered lithium foil and pressed onto one side of the pressed Li_6PS_5Cl pellet under 80 MPa for 30 s. The PEEK cell was then placed into a sealed container filled with argon, and a constant pressure of 13 MPa was applied using springs. The cell was then placed inside an environmental chamber maintained at 30 °C for at least 10 hours to ensure temperature stabilisation before measurement.

A phosphorus chunk (Sigma Aldrich, 99.99% trace metals basis) measuring approximately 5 mm × 6 mm with a flat surface was selected as the sputtering target and affixed to the target holder using carbon tape for the *in situ* phosphorus sputtering experiment.

4.2.2 XPS measurements

The X-ray source was Al Kα (hυ = 1486.8 eV), with the vacuum level maintained below 10^{-6} Pa throughout the experiment. The pass energy was set to 224 eV the survey scans and 55 eV for high-resolution scans.

For the VEP experiment mimicking the conditions of the CTTA test, the pellet was exposed to a ~5 mm electron beam, generated by the electron neutraliser, for 1 hour within the XPS system to induce lithium-ion migration through the pellet following the acquisition of XPS data from the pristine surface. The applied electron beam current was set to 2.5 μA, corresponding to a current density of 12.74 μA cm^{-2}. High-resolution XPS scans were continuously performed following the VEP step, with each scan sequence following the order: P 2*p*, Li 1*s*, S 2*p*, O 1*s*, Cl 2*p*, and C 1*s*. Each complete measurement cycle took approximately 53 minutes.

For the phosphorus sputtering experiment, the ion gun accelerating voltage was set to 4 kV, with the phosphorus target positioned directly opposite the ion gun during the sputtering step. Following sputtering, the sample surface was exposed to a 30 μA electron beam. By alternating between VEP and XPS measurements, the evolution of the surface chemistry was continuously monitored. Once fully reduced Li_3P and lithium metal were detected in the XPS spectra, the VEP steps were halted. Subsequent XPS measurements were conducted continuously at intervals of approximately 27 minutes to track further surface evolution.

All collected data were processed using CasaXPS software[223] and calibrated to the Cl 2$p_{3/2}$ peak at 198.5 eV.

4.2.3 Modified CTTA measurement

CTTA measurements were conducted using a VMP3 BioLogic potentiostat. Lithium titration steps were performed by applying a current of -12.25 μA for 6 minutes per step, with a total of 32 titration steps conducted, resulting in the deposition of 1.56 μA h cm^{-2} of lithium per step. PEIS was performed over a frequency range of 400 kHz to 10 Hz, with 10 points per decade measured on a logarithmic scale and two measurements taken per frequency. The amplitude of the applied sinusoidal

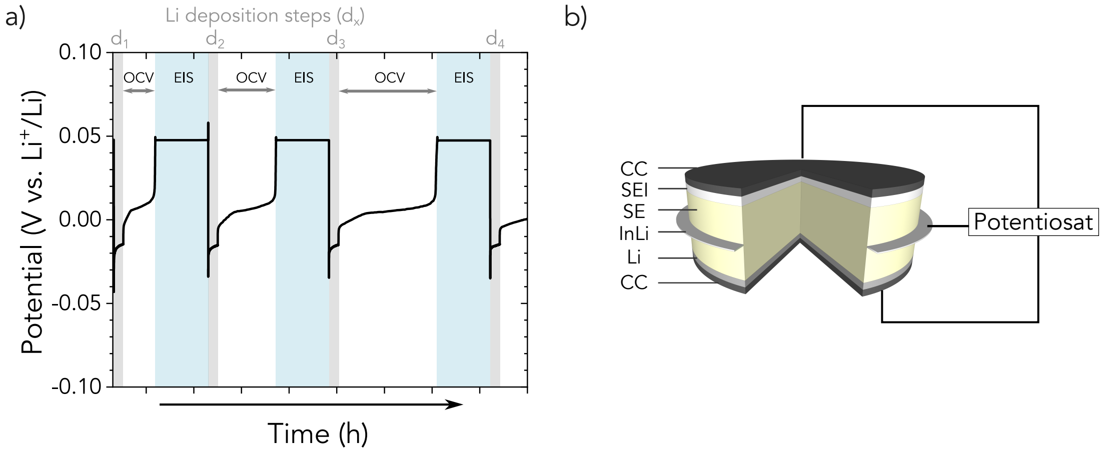

Figure 4.2: a) Schematic of the modified CTTA test with PEIS conducted after the cut-off voltage (50 mV) was reached, and b) is the schematic of the sample used in the three-electrode cell for the experiment. Reproduced from [247]

voltage was 10 mV. A 0.1 s wait period was introduced before each frequency measurement, and drift correction was applied. The collected impedance spectra were fitted using the inbuilt Z-fit function in EC-lab software.

4.3 Results and discussion

4.3.1 Diffusion-limited SEI growth and coulometric titration time analysis (CTTA)

As previously discussed in Section 1.5.3, interfaces between SSE and anode can be classified into three categories—stable interface, SEI and MCI—based on their conductivity properties. Wenzel *et al.* applied the Wagner model to estimate the diffusion-limited growth of the interphase layer, offering a theoretical framework for understanding SEI formation kinetics[147, 165, 248]:

$$j_{Li} \approx \frac{\sigma_{el}\ \sigma_{Li^+}}{F^2(\sigma_{el}+\sigma_{Li^+})}\frac{\mu^0_{Li}}{d_{SEI}} \tag{4.1}$$

Where j_{Li} represents the lithium flux across the SEI layer, σ_{el} and σ_{Li^+} denote the mean electronic and ionic conductivities of the SEI, μ^0_{Li} is the chemical potential of lithium, and d_{SEI} is the SEI thickness. This equation indicates that the lithium flux across the layer is governed by the transport of the minority charge carriers, which limits the overall rate of SEI growth. As a result, the SEI growth follows a diffusion-limited mechanism, where the growth rate progressively decreases as the SEI becomes thicker.

The growth of the SEI thickness over time could be determined by the amount of charge passing through the layer, which can be described by Equation 4.2:

$$\frac{d(d_{SEI})}{dt} = \frac{j_{Li} \times M_{SEI}}{x \times \rho_{SEI}} \tag{4.2}$$

Where M_{SEI} represents the mean molar mass of the SEI, ρ_{SEI} is the SEI density, and x corresponds to the amount of lithium consumed in the reaction. According to Equation 4.2, the SEI growth rate is related to the resulting SEI thickness.

By substituting Equation 4.2 into Equation 4.1, the temporal evolution of SEI thickness (d) can be described using the following Equation4.3 [176]:

$$d = \left(\frac{2M_{SEI}\ \sigma_{el}\ \sigma_{ion}\ \mu^0_{Li}}{F^2\ \rho_{SEI}\ x\ (\sigma_{el} + \sigma_{ion})} \right)^{\frac{1}{2}} (t)^{\frac{1}{2}} = k\ t^{\frac{1}{2}} \tag{4.3}$$

Where M_{SEI} represents the mean molar mass of the SEI, ρ_{SEI} is the SEI density, σ_{el} and σ_{Li^+} denote the mean electronic and ionic conductivities of the SEI, x corresponds to the amount of lithium consumed in the reaction, F is the Faraday constant, μ^0_{Li} is the chemical potential of lithium, k represent the parabolic rate constant and t denotes the SEI grow time.

The resistance of a cylindrical sample can be calculated using Equation 4.4:

$$R = \rho \frac{l}{A} \tag{4.4}$$

Where ρ is the sample resistivity, l is the sample length and A is the cross-sectional area.

By combing Equations 4.3 and 4.4, the time-dependent growth of SEI resistance can be expressed as[176]:

$$R = \frac{1}{A\ \sigma_{SEI}} \left(\frac{2M_{SEI}\ \sigma_{el}\ \sigma_{ion}\ \mu^0_{Li}}{F^2\ \rho_{SEI}\ x\ (\sigma_{el} + \sigma_{ion})} \right)^{\frac{1}{2}} (t)^{\frac{1}{2}} = k'\ t^{\frac{1}{2}} \tag{4.5}$$

Where σ_{SEI} represents the overall conductivity of the SEI, and k' is the modified parabolic rate constant.

Consequently, the SEI growth could be estimated when its compositional information is known, provided that a few necessary assumptions are met: (1) transport occurs in a one-dimensional manner; (2) the transport process is driven by chemical potential gradients; (3) the boundaries are maintained at constant chemical potentials; (4) the solids involved are homogenous; (5) the interfacial contacts are ideal; and (6) there are no phase transfer barriers[234, 249].

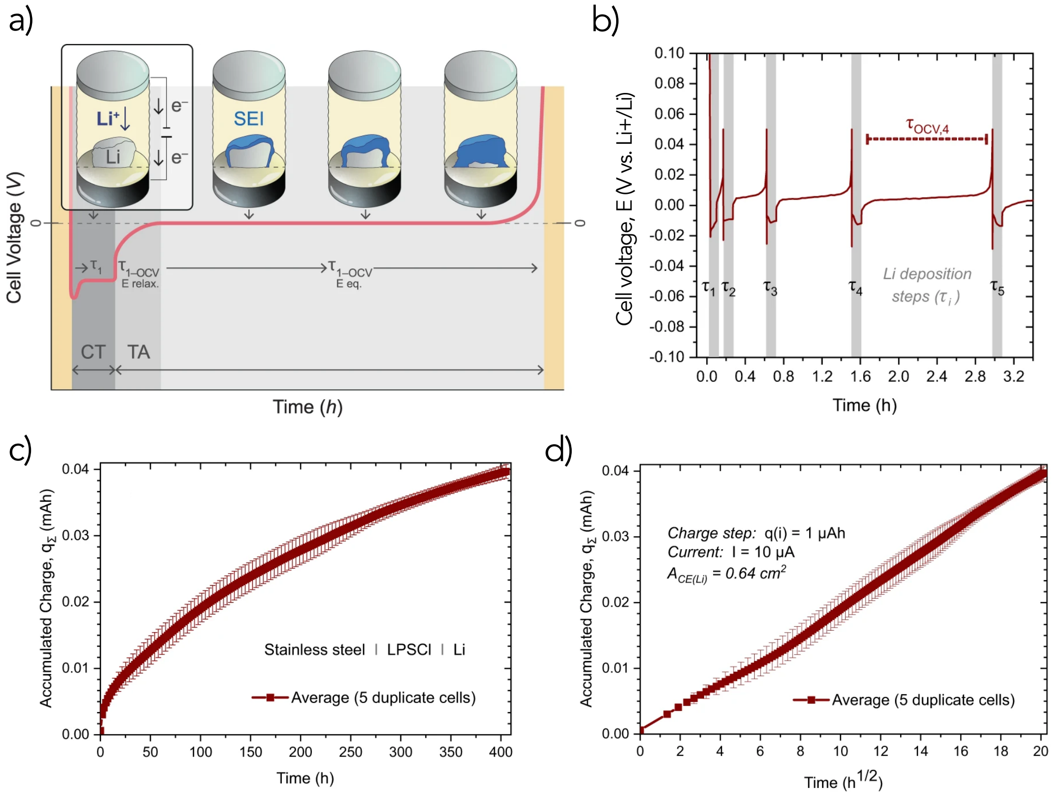

Figure 4.3: Illustration of the coulometric titration time analysis (CTTA) method: (a) Schematic representation of the CTTA setup, detailing the lithium deposition and subsequent open-circuit voltage (OCV) monitoring process. (b) CTTA results obtained from a stainless steel current collector|Li$_6$PS$_5$Cl|Li cell, operated at a current of 10 μA (15.6 $\mu A\ cm^{-2}$) for 0.1 hours per titration step. The increasing OCV period with successive titration steps indicates progressive SEI passivation. (c) The cumulative charge consumed in side reactions as a function of experimental time, illustrating the continuous SEI growth and its influence on interfacial stability; d) The cumulative charge consumed in side reactions as a function of square root of time. Reproduced with permission from [198], Copyright 2013 Springer Nature

As reported by Aktekin *et al.*, the CTTA technique provides a quantitative method for evaluating side reactions between various SSEs and lithium metal[198].

The experimental setup and results are presented in Figure 4.3. During each titration step, 1.56 $\mu A\ h\ cm^{-2}$ of lithium was deposited onto the current collector at a constant current of 10 μA (15.6 $\mu A\ cm^{-2}$) for 0.1 hours. The progressively increasing OCV duration observed in successive titration steps suggests that the SEI is becoming increasingly passivating. Furthermore, as shown in Figure 4.3c, the cumulative charge consumed in side reactions continues to rise, offering a quantitative measure of SEI growth over time. This trend indicates that, while interfacial reactions between lithium and the Li_6PS_5Cl SSE are gradually suppressed, the continuous accumulation of SEI components persists. In this case, the SEI growth exhibits a linear relationship with the square root of time, consistent with Equation 4.3, under the assumption that the formed SEI is uniform in both morphology and composition. However, the long-term stability of the SEI at the $Li_6PS_5Cl|Li$ interface requires further investigation, which will be discussed in the following section.

4.3.2 The stability of SEI between Li_6PS_5Cl SSE and lithium metal

According to Aktekin *et al.*, the growth of the SEI exhibits a linear relationship with the square root of time[198]. However, several factors must be considered when discussing the SEI growth between Li_6PS_5Cl and lithium metal. For Li_6PS_5Cl SSE, it is widely accepted that its reaction pathway with lithium metal follows Equation 4.6[147, 174, 176, 203, 234]:

$$Li_6PS_5Cl + 8Li^0 \rightarrow 5Li_2S + LiCl + Li_3P \tag{4.6}$$

The lithium binary compounds formed at the interface are thermodynamically stable in contact with lithium metal, and their presence could, in principle, prevent further decomposition of the Li_6PS_5Cl SSE once a continuous SEI layer is formed[136]. Several studies have proposed that a kinetically stable SEI forms between Li_6PS_5Cl and lithium metal[147, 174, 203]. However, recent investigations suggest that the Li_3P phase exhibits high electronic and ionic conductivity, as previously discussed in Chapter 3, which could facilitate the formation of a percolation pathway for both electrons and lithium ions[162, 222, 234, 250, 251]. Given its potential influence on interfacial stability, it is important to assess the role of Li_3P in determining SEI stability between Li_6PS_5Cl SSE and lithium metal.

Table 4.1: Volume fractions of different phases if phosphorus species are fully lithiated

Species	Molar Volume ($cm^3\ mol^{-1}$)	Molar Ratio	Volume Fraction (%)
Li_2S	27.5	5	80.4
LiCl	20.5	1	12.0
Li_3P	36.2	1	18.6

The volume fraction of different phases within the SEI, calculated based on Equation 4.6 under the assumption that the SEI is uniform, pore-free, and that all phosphorus species are fully reduced to Li_3P, is presented in Table 4.1. In this case, the conductive Li_3P phase constitutes 18.6 vol% of the SEI layer, exceeding the 15 vol% threshold required for the formation of a continuous electronic pathway according to 3D percolation theory[235]. This suggests that the SEI would be inherently unstable, promoting continuous growth rather than passivation. However, sulphide-based argyrodite electrolytes with compositions close to Li_6PS_5Cl have demonstrated greater stability by forming a more passivating SEI compared to other sulphide electrolytes[162, 183, 252]. This suggests that additional factors beyond the presence of a conductive phase influence the passivation behaviour of the SEI.

According to the first-principles calculations conducted by Zhu *et al.* on the stability of various SSEs, the Li_6PS_5Cl SSE is thermodynamically susceptible to reduction, leading to the formation of elemental phosphorus (P) within the SEI, shown in Equation 4.7.

$$Li_6PS_5Cl + 5Li^0 \rightarrow 5Li_2S + LiCl + P \tag{4.7}$$

The reaction pathway, assuming that P remains in its non-lithiated state, is illustrated in Equation 4.7. Under these conditions, the volume fraction of the P phase in the SEI is approximately 7.6 vol%, as shown in Table 4.2. This fraction is below the percolation threshold, meaning that it would not form a continuous electronically conductive pathway within the SEI. Nevertheless, phosphorus exhibits significantly

Table 4.2: Volume fractions of different phases if phosphorus is not lithiated

Species	Molar Volume ($cm^3\ mol^{-1}$)	Molar Ratio	Volume Fraction (%)
Li_2S	27.5	5	70.8
LiCl	20.5	1	10.6
P	13.0	1	7.6

lower electronic conductivity[253, 254]. Consequently, the presence of non-lithiated phosphorus could contribute to the passivating nature of the SEI, effectively limiting further interfacial reactions and stabilising the Li|Li_6PS_5Cl interface.

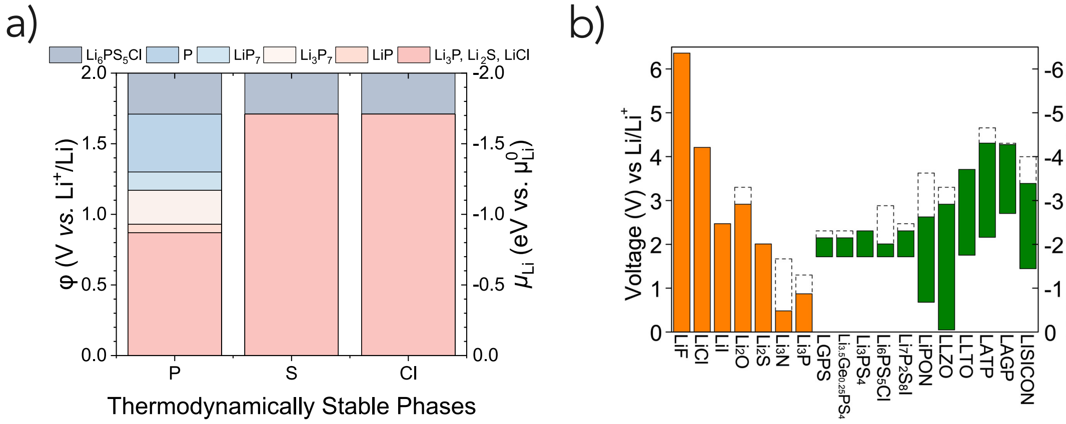

Figure 4.4: a) Illustration of stable phases in different reductive regions. Reprinted from [247] based on data reported in [136]; b) Electrochemical stability window of various SSEs and selected lithium binary compounds. Reprinted with permission from [136], Copyright 2015 American Chemical Society.

However, due to its thermodynamic instability against lithium metal, the P phase undergoes further lithiation, leading to the formation of partially reduced Li_xP phases. The stability window of different P-containing phases is shown in Figure 4.4a[247]. These intermediate Li_xP species continue to evolve through successive reduction steps until ultimately forming Li_3P. This progressive lithiation introduces compositional and volumetric changes within the SEI, which can significantly influence its structural integrity, conductivity, and overall passivation behaviour. Consequently, understanding the kinetics and thermodynamics of these transitions is crucial for predicting the long-term interfacial stability of Li_6PS_5Cl|Li systems.

It is also important to note that the theoretical oxidation potential of Li_3P and partially reduced Li_xP species is lower than the theoretical reduction potential of

Li_6PS_5Cl. This means that Li_3P and Li_xP phases are thermodynamically unstable when in contact with Li_6PS_5Cl SSE and suggests that, in principle, the SEI will continue to grow as long as a lithium source is available on the anode side to sustain lithium transport through these P-containing phases. Additionally, the Li^+ diffusivity in partially reduced Li_xP phases has been reported to be comparable to or even higher than that in Li_3P as shown in Figure 4.5[255].

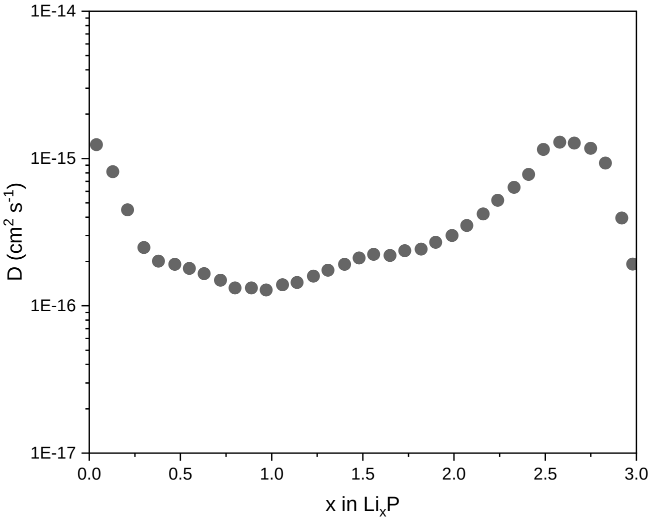

Figure 4.5: Diffusivity of Li^+ in red phosphorus as it undergoes lithiation calculated from galvanostatic intermittent titration technique (GITT) measurements, Replotted based on data reported in [255], Copyright 2020 Elsevier

Since both Li_2S and LiCl are stable in contact with both Li_6PS_5Cl and lithium metal and exhibit low ionic and electronic conductivities, it is reasonable to infer that the SEI growth in the $Li_6PS_5Cl|Li$ system is primarily governed by the reaction between lithiated phosphorus species and Li_6PS_5Cl, followed by lithium diffusion through the SEI layer[256–259]. These effects are expected to deviate from the conventional diffusion-limited SEI growth model, which predicts a linear relationship between SEI thickness and the square root of time.

4.3.3 The evolution of Li_6PS_5Cl-lithium metal SEI by *in situ* XPS

Early in Narayanan *et al.*'s study, the temporal stability of reduced phosphorus species formed on top of Li_6PS_5Cl by VEP method was investigated. As shown

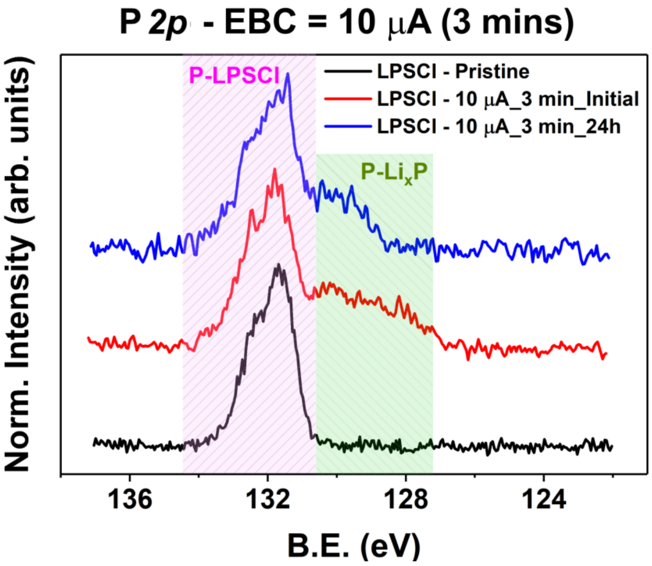

Figure 4.6: Temporal stability of partially reduced Li_xP induced by VEP lithium plating. P 2p core-level spectra on the LPSCl pellet after exposing to the electron beam of 10 μA ($\sim$ 0.05 mA cm^{-2}) for 3 minutes and its change over time without any further treatment. Reprinted with permission from [174], Copyright 2022 Springer Nature

in the P 2p core-level spectra in Figure 4.6, partially reduced Li_xP species were detected after exposing the Li_6PS_5Cl pellet to a 10 μA electron beam ($\sim$0.05 mA cm^{-2}) for 3 minutes (plotted in red), while the remaining phosphorus species retained their original PS_4 structure. In this case, the fully reduced Li_3P phase was absent, as additional lithium is required to fully lithiate the P-containing SEI species. Notably, after 24 hours of resting under OCV condition inside the XPS chamber, significant changes in both peak shape and BE position were observed, indicating that the chemical composition of the interphase evolved over time. These findings suggest that the initially formed Li_xP species underwent further transformations, likely due to continued interactions with the other SEI components or the underlying SSE. This contrasts with the conclusion drawn by Narayanan *et al.*, who reported that the formed Li_xP exhibits reasonable stability, as Li_xP species remained detectable after 24 hours of resting. Notably, this phenomenon has been observed for the first time but has not yet been investigated in depth[174].

To gain a deeper understanding of the evolution of P-containing species within the SEI formed between Li_6PS_5Cl and lithium, an *in situ* XPS experiment was conducted using a current density comparable to that employed in Aktekin *et al.*'s study. To begin, the stability of Li_6PS_5Cl under electron beam exposure was assessed by applying a 30 μA beam current—more than ten times the 2.5 μA beam current used for SEI investigations. During this experiment, the Li_6PS_5Cl pellet was grounded to the sample stage using carbon tape, with no lithium source provided underneath. As shown in Figure 4.7, no noticeable changes in peak position or shape were observed, indicating that the Li_6PS_5Cl SSE remains stable under the applied 30 μA electron beam. Therefore, the variations in spectral features observed during the VEP experiment, where a lithium source was provided, should be attributed to reactions with the deposited lithium rather than beam-induced degradation of the SSE. It is important to note that the applied electron beam current during the VEP-XPS experiment in this study was 2.5 μA, significantly lower than the beam current used in the beam damage test. Therefore, the Li_6PS_5Cl SSE should also remain stable under these lower electron beam conditions.

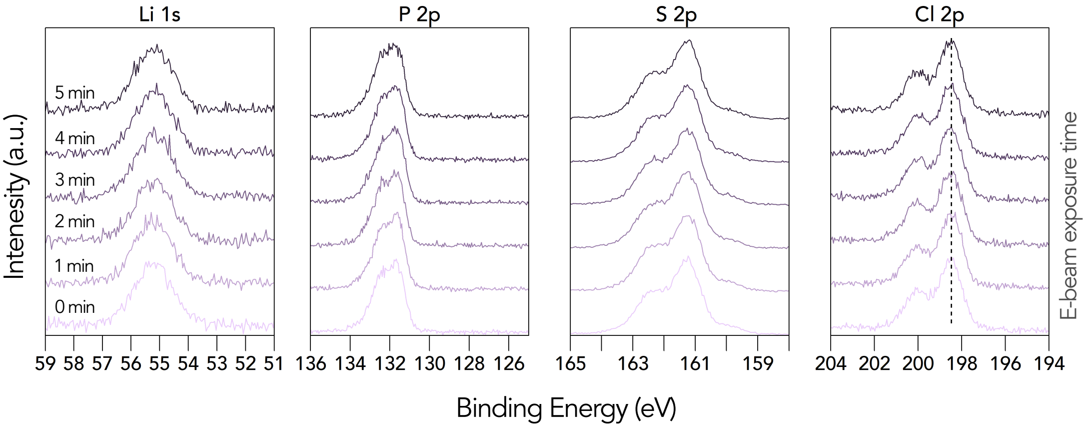

Figure 4.7: XPS spectra for VEP-XPS experiment of Li_6PS_5Cl surface without lithium source underneath the pellet. The applied beam current is 30 μA. The electron beam exposure time is labelled in the first column. Peak intensities are presented without normalisation, and charge calibration was performed using the Cl $2p_{3/2}$ peak at 198.5 eV.

As discussed earlier, Li_xP species are thermodynamically unstable in contact with Li_6PS_5Cl, suggesting that further interfacial reactions and SEI growth are expected to occur. Mentioned earlier in Chapter 3, *in situ* XPS techniques hold the potential of probing the SEI evolution kinetics. To further explore this phenomenon and gain deeper insights into the SEI growth mechanism of Li_6PS_5Cl electrolytes, VEP-XPS experiment was performed on the Li_6PS_5Cl pellet with lithium source (the lithium foil) provided. In this case, the applied electron beam was 2.5 μA so

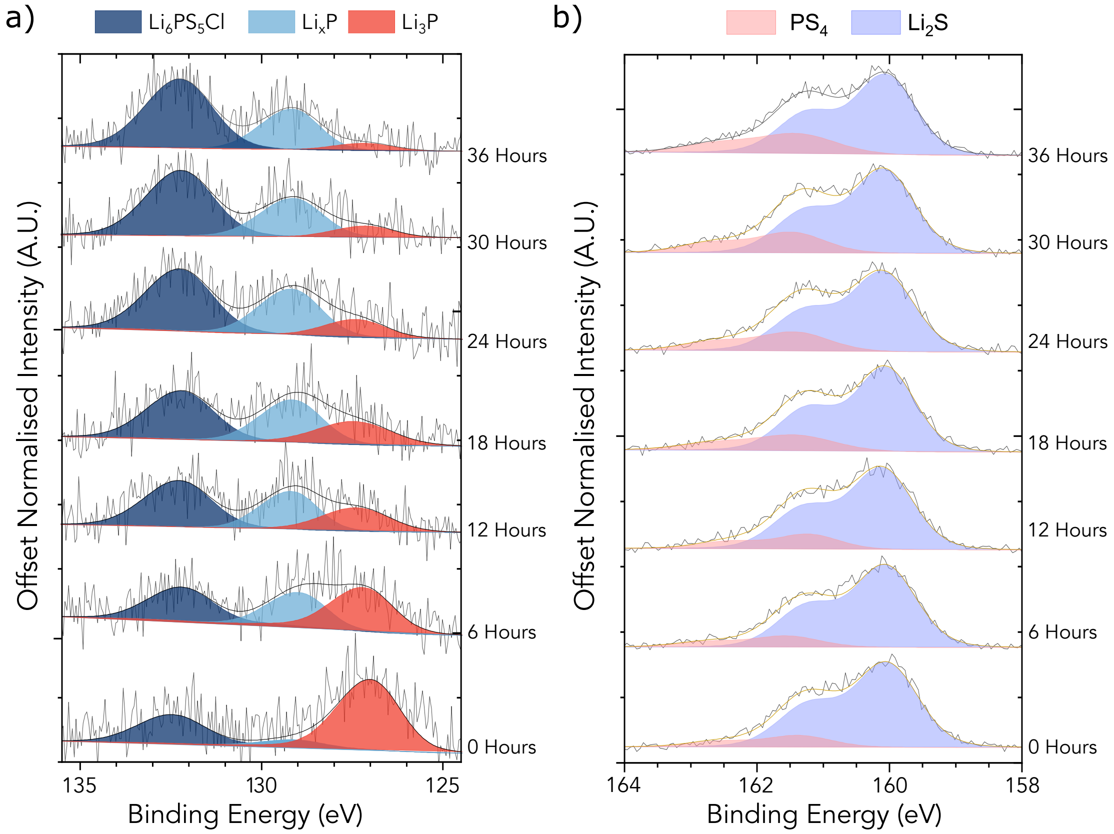

Figure 4.8: XPS spectra of the Li_6PS_5Cl pellet surface after ∼0.01 mAh cm^2 of lithium was VEP through the Li_6PS_5Cl pellet over 1 hour using an electron beam current of 2.5 μA (∼0.01 mA cm^{-2}): a) P 2p spectra and b) S 2p spectra. The resting time, labelled in hours, is indicated on the right side of the corresponding spectra. Reproduced from [247]

that the applied current density through the 5 mm pellet was ∼12.73 μA cm^2, which is close to the current density during the CTTA test (15.6 μA cm^{-2}). After 1 hour of electron beam plating, the P 2p spectra initially consists of two peaks corresponding to residual Li_6PS_5Cl and Li_3P immediately after the lithium plating step (labelled as 0 hours). The peak corresponding to Li_xP is low in intensity as shown in Figure 4.8a (labelled in light blue colour). The signal-to-noise ratio is comparatively low, most likely because other specimens loaded in the analysis chamber were outgassing and temporarily degrading the vacuum. Despite this limitation, the measurement remains reliable: a gradual attenuation of Li_3P signal and an increase in the Li_xP signal remain clearly discernible over time. The formation of Li_2S is evidenced by the S 2p peak at ~160 eV, as shown in Figure 4.8b. Similarly, the formation of LiCl is also expected, although the Cl 2p-LiCl peak overlaps with the Cl 2p-Li_6PS_5Cl peak due to their similar binding environments and the Cl 2p spectra is included in Figure A.3[174, 198, 234]. This indicates that the top surface of the formed SEI, which is in close contact with lithium metal, is primarily composed of fully lithiated lithium binary components, including Li_2S, LiCl, and Li_3P, consistent with previous reports[174, 176].

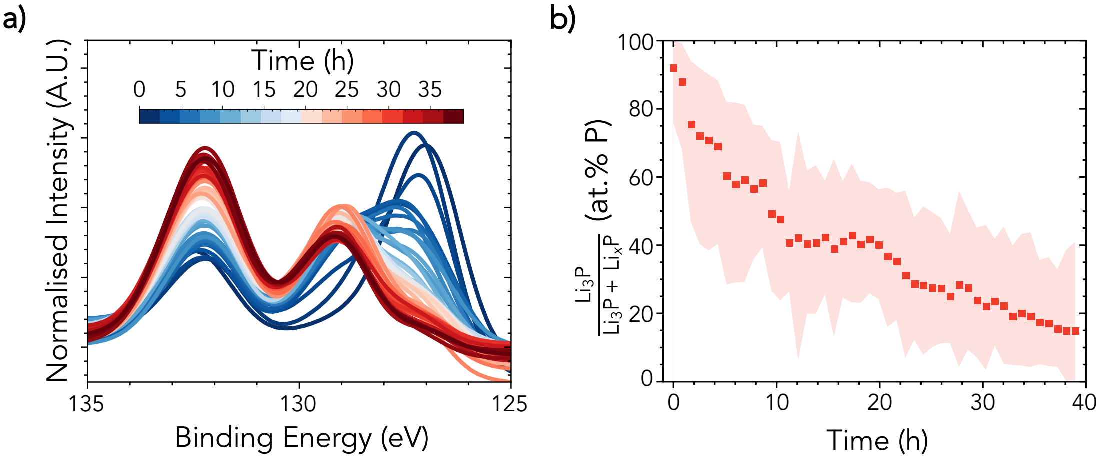

Figure 4.9: a) Mean normalised P 2p fitted spectra over time; b) Fraction of the Li_3P component among P-containing SEI species. Reproduced from [247].

The sample was then left under OCV conditions inside the XPS chamber, with continuous XPS measurements taken at 53 minute intervals. After the lithium metal was consumed, the intensity of peaks corresponding to Li_xP gradually increased over time, while the Li_3P peak decreased. Additionally, the peak associated with P 2p-Li_6PS_5Cl also exhibited a progressive increase in intensity, as more clearly illustrated in Figure 4.9a. Although the presence of lithium metal should, in principle, be detectable, its identification is challenging due to possible reactions with P-containing species or oxidation by residual gases in the XPS chamber. This issue will be discussed in detail later. The fraction of Li_3P over the P-containing SEI species continuous to decrease over time as shown in Figure 4.9b. These findings indicate that the SEI formed between Li_6PS_5Cl and lithium metal undergoes continuous growth via the delithiation of P-containing species[247].

4.3.4 Evolution of phosphorus during its lithiation and its stability against lithium metal

To further investigate whether P-containing species continue to evolve in contact with Li_6PS_5Cl electrolyte, the interfacial reactions between Li_6PS_5Cl and phosphorus, the subsequent lithiation of phosphorus, and the stability of the resulting species were examined using a combination of *in situ* sputtering and VEP techniques as shown in Figure 4.10. While previous studies have primarily employed *in situ* sputtering of lithium metal onto SSEs to probe SEI formation at the lithium|electrolyte interface, this work instead utilises *in situ* phosphorus sputtering within the XPS chamber to investigate its reactivity and interaction with Li_6PS_5Cl.

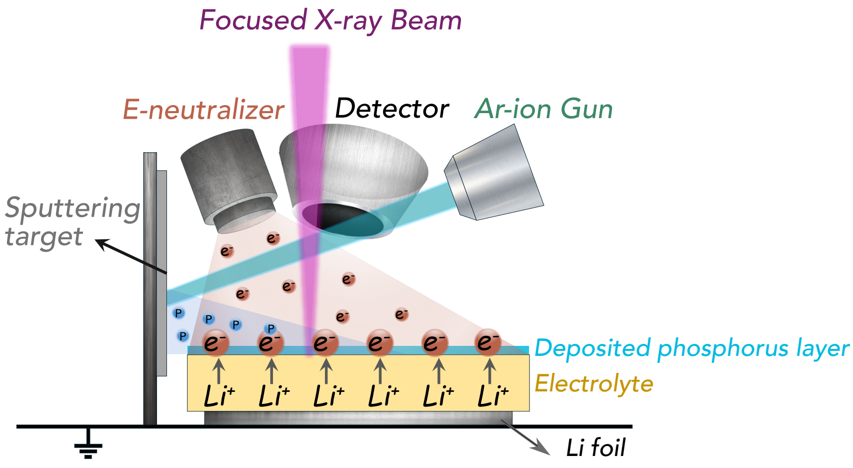

Figure 4.10: Schematic of the experimental setup: phosphorus sputtering is carried out first, followed by a VEP step that lithiated the deposited phosphorus layer.

As shown in Figure 4.11, the bonding environments for S and Cl remain stable throughout the phosphorus sputtering process. However, the P 2p spectra reveal the emergence of an additional component corresponding to P_{uc}, likely introduced by reactions between the incoming phosphorus and the Li_6PS_5Cl surface—a similar phenomenon was also observed in Chapter 5. The P^0 peak appears at a binding energy of approximately 129.7 eV, consistent with previous XPS measurements of

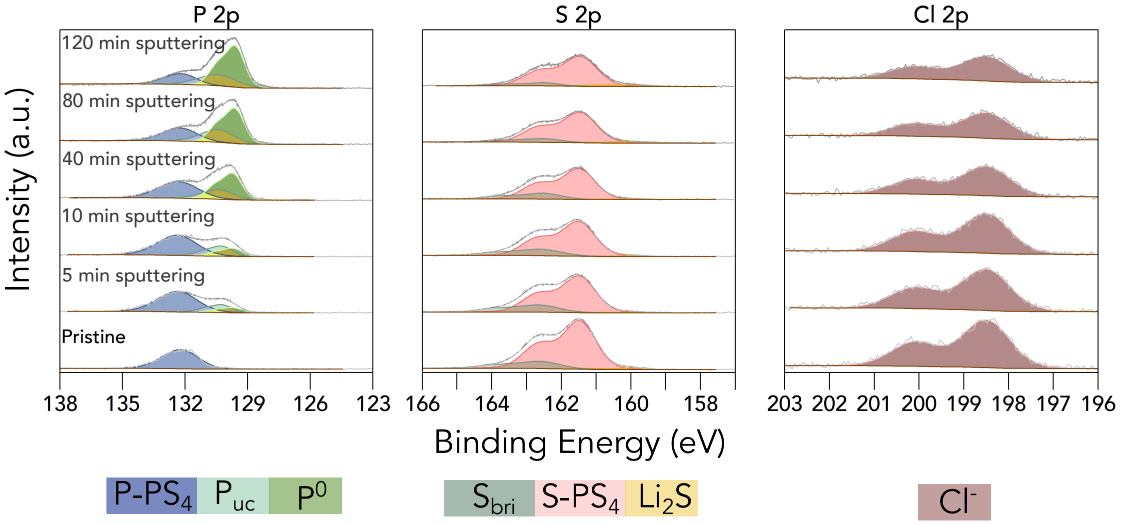

Figure 4.11: XPS spectra of the Li_6PS_5Cl pellet surface after phosphorus sputtering process. The sputtering time is indicated in the first column. The BE was calibrated based on Cl $2p_{3/2}$ to 198.5 eV.

red phosphorus[260]. Despite the presence of the P_{uc} peak, the sputtered phosphorus exhibits good chemical stability against Li_6PS_5Cl, as indicated by the increasing intensity of the P^0 peak and the lack of significant changes in the S 2p and Cl 2p spectra. Additionally, there were no changes observed for C 1s, O 1s and Li 1s spectra during the sputtering process as shown in Figure A.6.

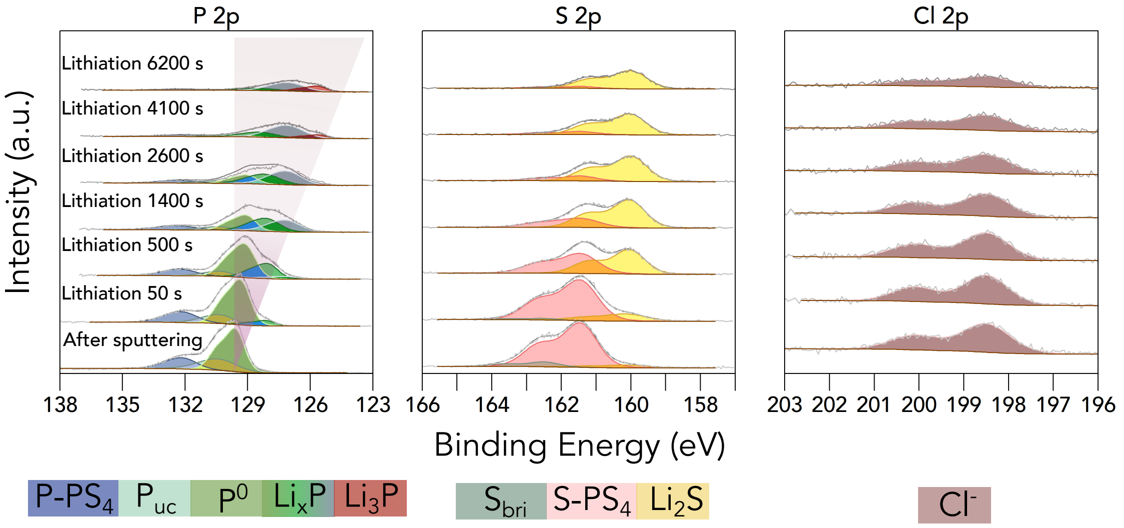

Figure 4.12: XPS spectra of the Li_6PS_5Cl pellet surface (with phosphorus sputtered on top) during VEP lithiation process. The electron beam exposure time is labelled in the first column and the applied beam current was 30 μA. The BE was calibrated based on Cl $2p_{3/2}$ to 198.5 eV.

After the sputtering process, a phosphorus layer was deposited on the surface of the Li_6PS_5Cl pellet. Subsequently, a 30 μA electron beam was directed onto the surface to gradually lithiate the phosphorus layer. As shown in Figure 4.12, reactions occurred during the lithiation of the sputtered phosphorus, as evidenced by the emergence of P 2p peaks corresponding to Li_xP species and the formation of Li_2S, indicating decomposition of the underlying Li_6PS_5Cl. Multiple components were fitted within the P 2p spectra across the BE range of approximately 129.3 to 125.7 eV. Accurate identification of specific Li_xP phases is challenging due to their similar BEs and potential overlap. The P $2p_{3/2}$ peak at $\sim$125.7 eV likely corresponds to fully reduced Li_3P, consistent with previous reports[174, 183], assuming charge calibration relative to Cl $2p_{3/2}$ at 198.5 eV. As lithiation progresses and the valence state of phosphorus decreases (indicating higher electron density), the BEs of the P-containing species shift downward, culminating in the formation of fully reduced Li_3P, highlighted in red. Additionally, the Li 1s peak shifts toward lower BE, consistent with the formation of SEI species, which exhibit lower BE values compared to Li 1s in Li_6PS_5Cl. The emergence of a Li_2O signal becomes evident after approximately 1400 s of electron beam plating as shown in Figure A.6, which may result from interactions between Li_2S and residual gases in the XPS chamber, or from reactions between the plated lithium metal and trace environmental contaminants.

After the phosphorus was fully reduced to Li_3P, lithium metal was expected to begin plating on the surface. The evolution of the Li 1s spectra is shown in Figure A.5, where a small peak at approximately 52 eV (if charge calibrated based on Cl $2p_{3/2}$ to 198.5 eV) appears after 4100 seconds of lithium plating, confirming the presence of metallic lithium on the surface. It is important to note, however, that due to the ongoing lithiation of P-containing species and the oxidation of deposited lithium, detecting metallic lithium is particularly challenging. The lithium continuously reacts either with surrounding SEI components or with residual gases in the chamber, complicating its observation.

The stability of the lithiated phosphorus species and other decomposition products was subsequently evaluated through continuous XPS measurements on

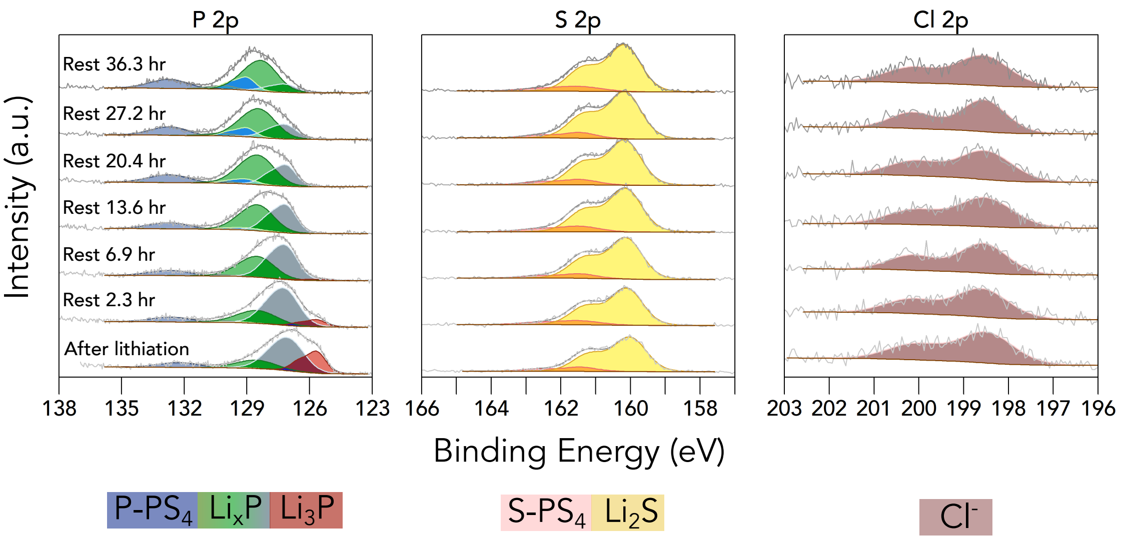

Figure 4.13: XPS spectra evolution of the Li_6PS_5Cl pellet surface (with phosphorus sputtered on top) after the VEP lithiation process. The resting time is labelled in the first column. The BE was calibrated based on Cl $2p_{3/2}$ to 198.5 eV.

the surface. During the OCV resting period, no significant changes were observed in the S 2p and Cl 2p spectra as shown in Figure 4.13, which proves the stability of Li_2S and LiCl against both lithium metal and Li_6PS_5Cl. As previously discussed, P-containing species are expected to undergo gradual delithiation over time. During the resting time, the P 2p spectra exhibited clear evolution, characterised by a decrease in the Li_3P peak and a corresponding increase in the relative intensity of partially reduced Li_xP species. This further proves that the SEI formed between Li_6PS_5Cl and lithium metal undergoes continuous growth via the delithiation of P-containing species as schematically shown in Figure 4.14.

In summary, the P-containing SEI species continuously evolve, leading to ongoing changes in both the composition and microstructure of the SEI. As a result, the SEI properties dynamically shift over time. This contradicts the observations in Figure 4.3, where the SEI growth appears to follow a linear relationship with the square root of time. Given that the Li^+ diffusivities of different Li_xP phases vary, the SEI growth should, in principle, deviate from this expected linear trend. To further validate this observation, a modified CTTA experiment was conducted to characterise the SEI growth, as discussed in the following section.

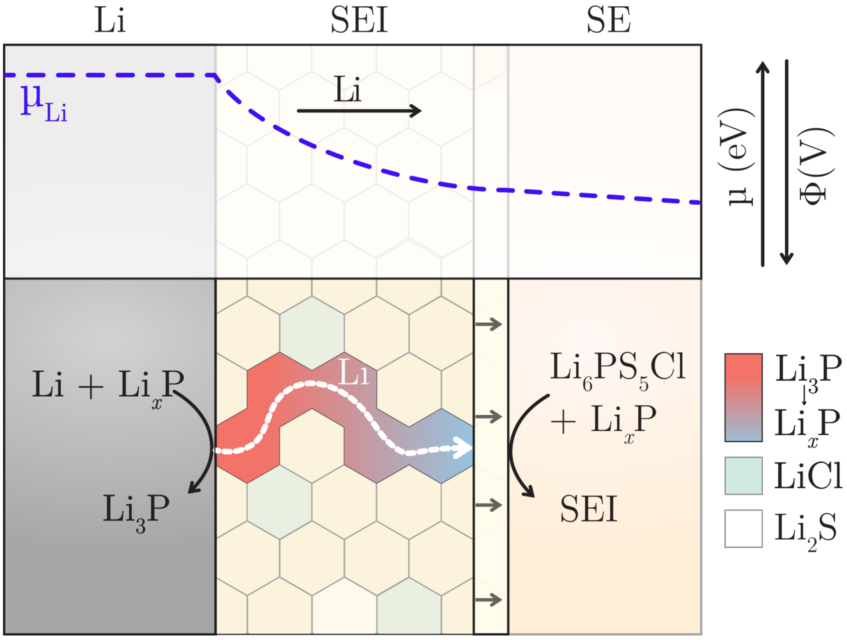

Figure 4.14: Illustration of the chemical potential gradient over the SEI, and the lithium pathway through the P-containing species with the SEI. Reproduced from [247]

4.3.5 Li_6PS_5Cl-lithium SEI characterised by a modified CTTA method

To verify the continuous evolution of the SEI between Li_6PS_5Cl and lithium metal, a modified CTTA method was employed to monitor SEI growth and its corresponding changes in impedance as shown in Figure 4.2. A three-electrode setup was employed, incorporating a In-InLi alloy ring as the reference electrode to minimise artifacts during EIS measurements.

As shown in Figure 4.15a, the OCV duration progressively increases after each lithium titration step, indicating that the SEI becomes more passivating as it thickens. The relationship between the accumulated charge and the square root of the OCV duration is plotted in Figure 4.15b. Unlike the trend observed in Figure 4.3d, the first 15 hours do not appear to follow a linear relationship. This suggests that, during the initial phase, SEI growth may not be solely diffusion-limited, and reactions involving P-containing SEI species may contribute to the observed deviations.

As shown in Figure 4.16, impedance measurements were conducted after the titrated lithium had been fully consumed. The impedance data were fitted using a Randles circuit incorporating a finite Warburg element with a reflective boundary

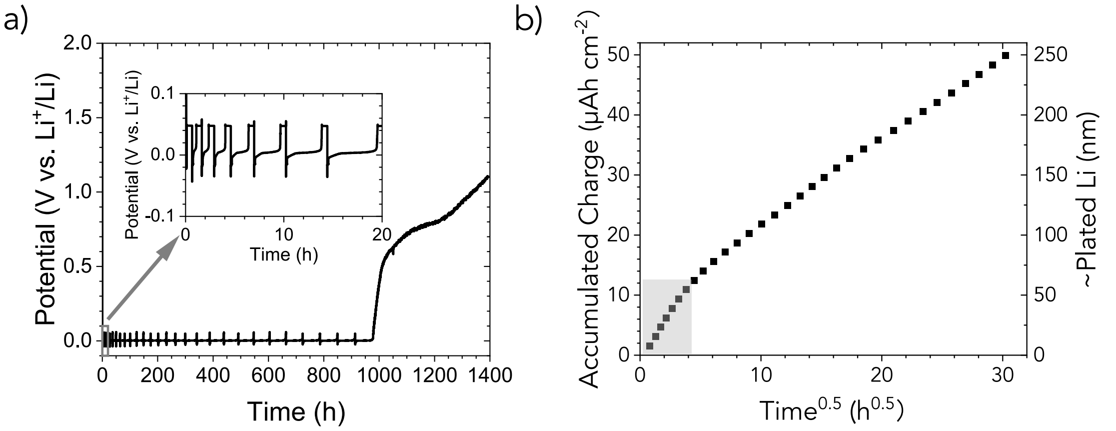

Figure 4.15: a) Variation of potential during the CTTA experiment; b) Relationship between the accumulated charge and the square root of the OCV duration, representing the time required to consume the deposited lithium. Reproduced from [247]

($M_{a(SEI)}$), with CPEs used in place of ideal capacitors, as illustrated in Figure A.4. This enabled the monitoring of SEI resistance variation over time. Figure 4.16b illustrates that R_{SEI} progressively increases over time but does not follow the linear relationship described in Equation 4.5. Instead, the resistance curve deviates towards lower values, which could be attributed to the presence of partially reduced Li_xP phases. These phases exhibit higher lithium diffusivity compared to the fully reduced Li_3P phase, thereby influencing the overall impedance response.

Following approximately 1000 hours of the CTTA experiment, with a total lithium titration of around 50 μAh cm^{-2}, the cell was left under OCV conditions while PEIS measurements were performed hourly for 400 hours. As depicted in Figure 4.16d, R_{SEI} continues to increase over time, indicating either a compositional change in the SEI, continued SEI growth, or a combination of both processes. Additionally, the OCV gradually increases over time, exhibiting a trend similar to the delithiation profile of red phosphorus[255]. This observation is also consistent with the findings from the XPS measurements, where the fraction of Li_3P over (Li_xP and Li_3P) is decreasing over time.

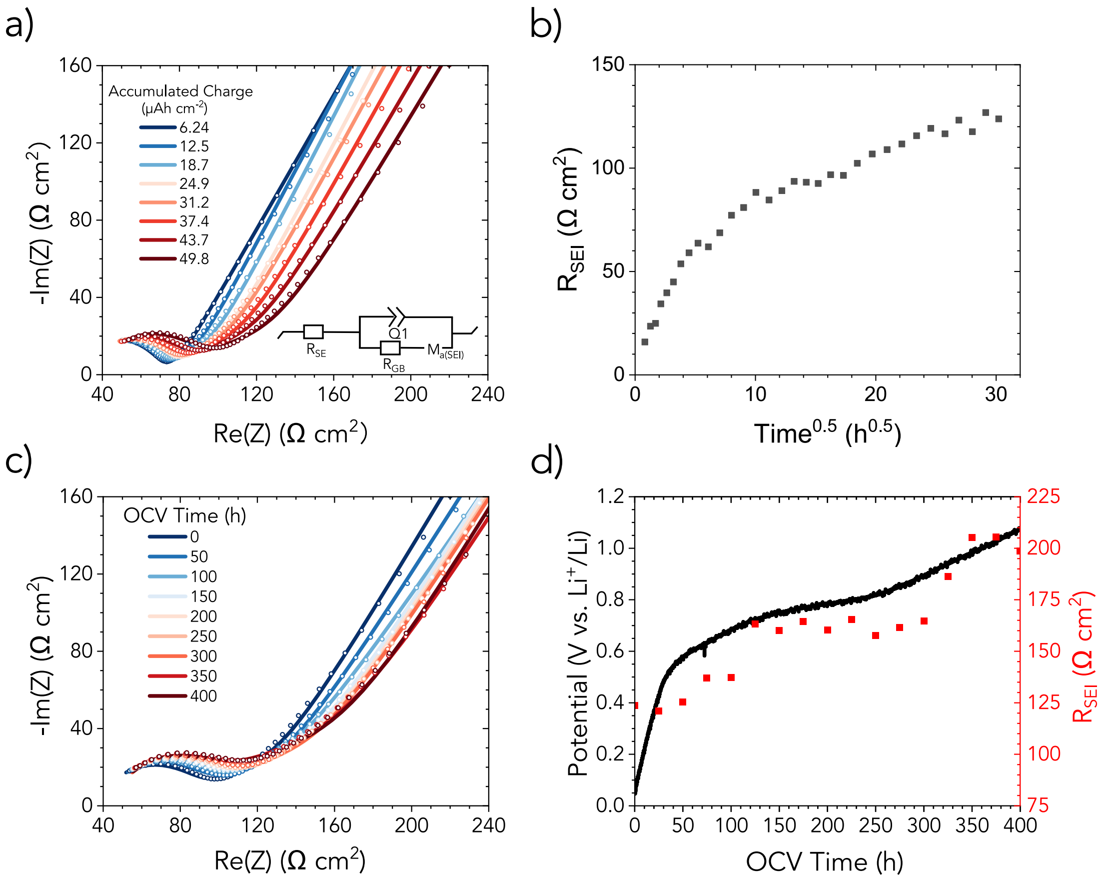

Figure 4.16: Evolution of SEI impedance: (a) SEI impedance evolution (circles represent data points, lines indicate fitted results) following the titration step, with accumulated charge values labelled in the inset. The equivalent circuit used for fitting the impedance is included in the inset (with $M_{a(SEI)}$ illustrated in Figure A.4; (b) evolution of R_{SEI} as a function of square root of time; (c) SEI impedance evolution under lithium-free conditions (after completing all lithium titration steps, monitored under OCV resting conditions), with EIS measurements conducted every hour; (d) evolution of OCV potential and SEI resistance in lithium-free conditions as a function of OCV time. Reproduced from [247].

4.4 Summary

Despite ongoing research, the mechanisms governing SEI formation and growth between Li_6PS_5Cl and lithium metal remain unclear. This study employs both *in situ* XPS and a modified CTTA measurement to provide a deeper understanding of SEI evolution.

In the VEP-XPS experiment, ~0.01 mAh cm^2 of lithium metal was deposited onto the Li_6PS_5Cl surface, where both the residual Li_6PS_5Cl phase and Li_3P were detected in the P 2p spectra. By continuously monitoring the surface after lithium deposition, the results reveal that the Li_3P phase within the SEI is not stable and undergoes progressive delithiation to Li_xP, while the SEI continues to grow. Additionally, the phosphorus sputtering and subsequent lithiation experiment further confirms the continuous evolution of P-containing species on the surface of the Li_6PS_5Cl pellet. As a result, SEI formation cannot be attributed solely to diffusion-limited growth. This suggests that the SEI thickness should deviate from the expected linear relationship with the square root of time. This hypothesis is supported by the modified CTTA measurement, where SEI growth during the initial 15 hours does not follow the linear relationship when the accumulated charge is plotted against the square root of time. And the relationship between R_{SEI} and square root of time also deviated from linear relationship towards lower values as the Li_xP species may have higher lithium diffusivities compared to fully lithiated Li_3P phase.

These findings indicate that a phosphorus-free interphase is essential for establishing a passivating layer between Li_6PS_5Cl and lithium metal. Otherwise, the SEI will continue to grow due to ongoing reactions between lithiated phosphorus species and Li_6PS_5Cl, along with the subsequent diffusion of lithium through the SEI. The stability of the SEI could potentially be further enhanced by introducing a phosphorus-free artificial interlayer that exhibits good stability with both Li_6PS_5Cl and lithium metal. However, this approach requires further investigation in future studies.

5

In situ XPS investigation of the SEI formed between lithium metal anode and lithium phosphorus oxynitride

Contents

The major part of the work in this chapter was reported in the following published research article: Turrell, Stephen J; Liang, Yi; Cai, Tiancheng; Jagger, Ben; Pasta. Origin of Stability in the Solid Electrolyte Interphase formed between Lithium and Lithium Phosphorus Oxynitride. Chemistry of Materials 2025 [261]. (joint first authorship: Stephen prepared the LiPON samples, whereas Yi performed the XPS experiments and data analysis)

This chapter will mainly focus on the XPS characterisation of the SEI formed between LiPON and lithium metal as it evolves during *in situ* experiments.

5.1 Introduction

In Chapter 3, the stability and SEI composition of LGPS and LAGP SSEs against lithium metal were investigated using *in situ* XPS techniques. While the LAGP SSE exhibited improved stability against lithium metal compared to LGPS, achieving consistent cycling stability in systems incorporating an LMA remains challenging. The stability of the SEI formed between Li_6PS_5Cl and lithium metal is investigated in Chapter 4, which demonstrates that the SEI can continue to grow via the delithiation of P-containing species, which necessitating further investigation on solutions to improve the interface stability.

While SSEs that combine both high Li^+ conductivity and stability in contact with lithium metal remain elusive, one glassy SSE—lithium phosphorus oxynitride (LiPON)—has been studied extensively for over 30 years due to its exceptional stability against lithium metal, despite its relatively low Li^+ conductivity. This glassy material was first reported by Marchand in 1983 and later identified as a promising solid electrolyte by Bates *et al.* in 1992[106, 262]. Bates *et al.* deposited LiPON via reactive RF magnetron sputtering of Li_3PO_4 in a nitrogen atmosphere, producing LiPON thin films approximately 1 μm thick. The term “LiPON” is now broadly used to describe a family of materials with the general formula $Li_xPO_yN_z$. Since then, LiPON with varying stoichiometries and properties have been synthesised using a range of deposition techniques, including RF magnetron sputtering, chemical vapour deposition (CVD) and atomic layer deposition (ALD), and others[263, 264].

A simulated amorphous LiPON structure with the composition $Li_{2.94}PO_{3.50}N_{0.31}$ is shown in Figure 5.1a. Within the LiPON structure, nitrogen (N) can adopt

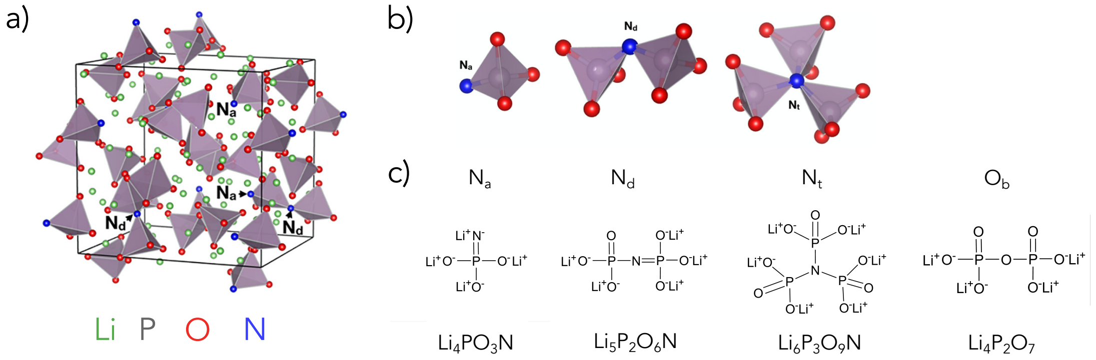

Figure 5.1: (a) Schematic of simulated amorphous LiPON structure with a composition of $Li_{2.94}PO_{3.50}N_{0.31}$; (b) phosphate units with nitrogen (N) exist in different environments: apical nitrogen (N_a), double-bridging nitrogen (N_d) and triple-bridging nitrogen (N_t) and (c) structural formulae of the phosphate units. (a) and (b) reprinted with permission from [93], Copyright 2018 American Chemical Society

three distinct spatial configurations: apical nitrogen (N_a), double-bridging nitrogen (N_d), and triple-bridging nitrogen (N_t), as illustrated in Figure 5.1b, with their corresponding structural formulae provided in Figure 5.1c. The incorporation of nitrogen into the structure reduces local interactions between Li^+ and the matrix, thereby improving ionic conductivity compared to pure Li_3PO_4. In addition to nitrogen content, other factors such as the degree of amorphousness, lithium concentration, and structural configuration, also influence the ionic conductivity of LiPON[93, 263, 265].

Although the ionic conductivity of LiPON is relatively low ($\sim 10^{-6}$ S cm^{-1}) compared to many powder-processed SSEs, LiPON is typically fabricated as thin films to ensure that its overall impedance remains comparable to that of pressed "bulk" electrolytes. More importantly, LiPON exhibits excellent electrochemical stability in contact with lithium metal and has demonstrated remarkable resistance to lithium dendrite penetration in thin-film cells[266–268]. Notably, Neudecker *et al.* reported that a "lithium-free" cell, employing a 2 μm thick LiPON electrolyte and a 2.7 μm thick $LiCoO_2$ cathode, exhibited stable cycling over 500 cycles between 3.0 and 4.2 V vs. Li^+/Li at a current density of 5 mA cm^{-2}[269]. While LiPON is primarily suitable as a solid electrolyte for low-capacity thin-film batteries, understanding the origins of its exceptional electrochemical and mechanical stability is crucial for guiding the development of bulk SSEs with similarly robust performance.

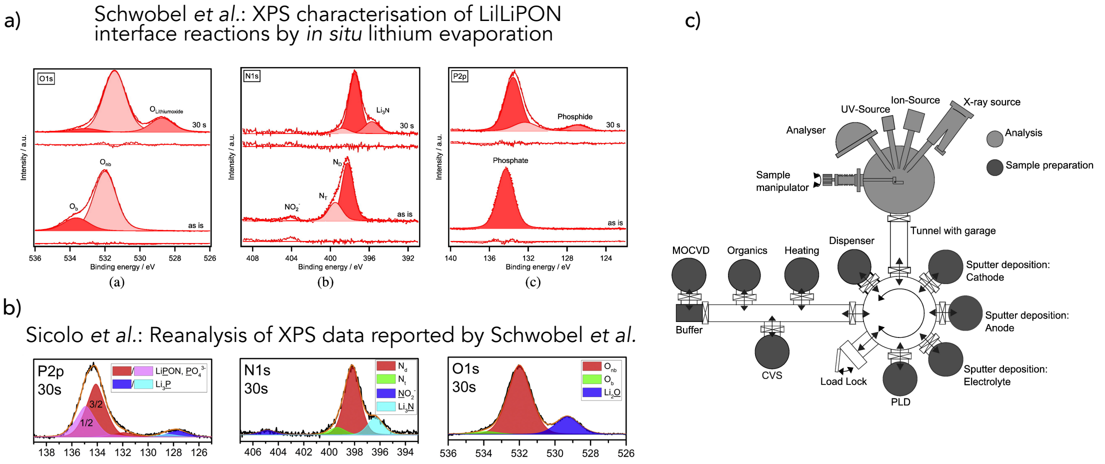

Figure 5.2: Previous XPS investigations on the Li|LiPON interfacial reactions: a) Fitted XPS spectra of O 1s, N 1s, and P 2p emissions before and after lithium deposition. Reprinted with permission from [270], Copyright 2015 Elsevier; b) Reanalysed XPS data by Sicolo *et al.*, based on the work of Schwöbel *et al.* shown in (a). Reproduced with permission from [271], Copyright 2017 Elsevier; c) Schematic illustration of the experimental setup used for *in situ* lithium evaporation and subsequent XPS analysis, Reprinted with permission from [270], Copyright 2015 Elsevier.

Some earlier investigations into the SEI formed between LiPON and lithium metal provided initial insights into its composition. In 2015, Schwöbel *et al.* employed XPS to demonstrate that an SEI comprising Li_2O, Li_3N, and Li_3P formed when lithium metal was evaporated onto a LiPON film as shown in Figure 5.2a [270]. In a subsequent study, Sicolo *et al.* reanalysed the XPS spectra and identified additional evidence for the presence of Li_3PO_4 within the SEI shown in Figure 5.2b[271].

The theoretical electrochemical stability window of LiPON, reported as 0.68-2.63 V vs. Li^+/Li based on first-principles calculations by Zhu *et al.*, indicates its thermodynamic instability in contact with lithium metal. Consequently, decomposition is expected at the Li|LiPON interface. Combining these experimental and computational findings suggests that the apparent electrochemical stability of LiPON is not due to intrinsic chemical stability but rather the formation of a passivating interphase that effectively suppresses further degradation.

a) Cheng *et al.* cryogenic characterisation of Li|LiPON interface.

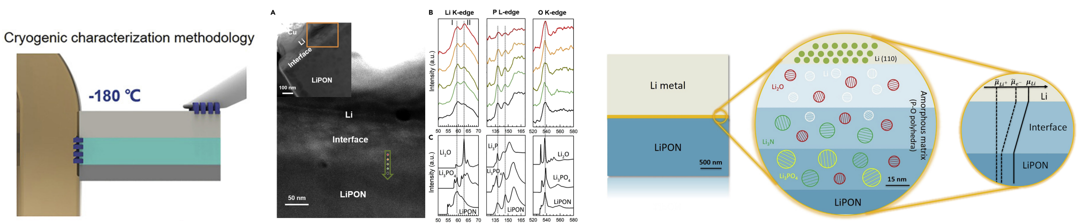

b) Hood *et al.* *in situ* TEM characterisation of Li|LiPON interface.

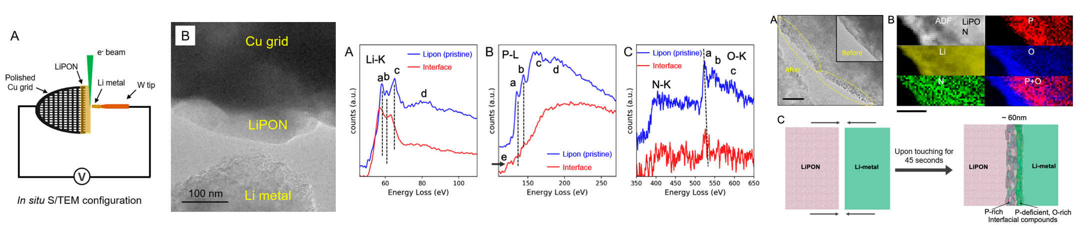

Figure 5.3: a) Cryogenic TEM investigation of the Li|LiPON interphase. Reproduced with permission from [272], Copyright 2020 Elsevier; b) *In situ* TEM investigation of the Li|LiPON interphase, showing the differences before and after contact between the LiPON sample and lithium metal. Reproduced with permission from [273], Copyright 2020 American Chemical Society.

Two TEM studies have reported that a 60-80 nm thick SEI layer comprising Li_2O and Li_3N forms at the Li|LiPON interface[272, 273]. However, these studies disagreed on the nature of the P-containing phases. A cryogenic high-resolution TEM investigation by Cheng *et al.*, conducted on a lift-out sample from a Li|LiPON interface, identified the presence of Li_3PO_4, as shown in Figure 5.3a. In contrast, Hood *et al.* performed *in situ* EELS analysis on a similarly formed interface and observed P^{3-} features (Figure 5.3b), suggesting the presence of Li_3P. Despite this discrepancy, both studies reported a consistent spatial distribution of SEI components: the P-rich phase (Li_3PO_4 or Li_3P) was localised near the LiPON side, while the O-rich phase (Li_2O) was predominantly located adjacent to the lithium metal. These experimental findings were later supported by first-principles calculations by Wang *et al.*, who evaluated the relative interfacial stabilities of SEI components in contact with lithium metal[274]. Their results indicated that the Li|Li_2O interface is the most stable, followed by Li|Li_3N and Li|Li_3P, whereas the

Li|Li_3PO_4 interface exhibits the lowest stability. This gradient in interfacial stability provides a rational explanation for the observed distribution of SEI species.

Electroanalytical and neutron reflectometry techniques have also been employed to investigate the SEI formed at the interface between lithium metal and LiPON[275, 276]. By quantifying the capacity loss during lithium plating—attributed to SEI formation, assuming a known SEI composition—the thickness of the interphase was estimated to be less than 7 nm. This is significantly thinner than values reported by TEM studies, likely due to differences in sample preparation and measurement conditions.

This investigation focused on the chemical and structural changes associated with SEI formation on the LiPON surface using the *in situ* XPS technique, wherein lithium metal is plated under conditions simulating the first charge of an "anode-free" cell[277]. As described in Section 2.1.2, these conditions were achieved using the VEP-XPS (*in situ* lithium plating) technique, which enables the electrochemical plating of lithium metal onto the LiPON surface. Notably, this is the first time that this technique has been applied to study SEI formation on LiPON. Additionally, the effects of the LiPON processing route, composition, and thickness on SEI formation were investigated, providing insight into the variability that may arise between different studies and practical implementations of LiPON electrolytes.

5.2 Experimental

5.2.1 Preparation of substrates

Discs of 304 stainless steel (SST) (15.8 mm diameter coin cell spacers) were used as substrates for thin film deposition. The stainless steel spacers were ground and polished to a mirror-like finish free from visible scratches with the final polishing step performed using a 1 μm grade diamond suspension. All substrates were cleaned by sonication in isopropanol and distilled water, followed by drying. During deposition, the spacers were mounted on glass slides using double-sided Kapton tape.

5.2.2 Deposition of lithium metal

As the sample for *in situ* lithium plating experiments needs a lithium source underneath the SSE layer, a thin layer of lithium film was deposited by thermal evaporation of lithium granules (Glentham Life Sciences Ltd, purity 99.4%) from a molybdenum boat under vacuum ($<5\times10^{-5}$ mbar). The deposition of lithium thin films was performed using a PVD system (MB EVAP, MBraun) integrated into an argon-filled glovebox ([H_2O] and [O_2]$<$ 0.1 ppm).

For thin-film LiPON samples, the lithium source was first deposited onto polished stainless-steel spacers prior to the LiPON deposition process. In contrast, for bulk-processed LiPON samples, the lithium source was directly deposited onto the LiPON sample. The deposition process produced lithium films approximately 1-2 μm thick, as measured using the quartz crystal monitor of the PVD system.

5.2.3 Synthesis of thin film LiPON

The well-polished stainless steel spacers were used as the substrates for LiPON deposition, as good electrical contact with the XPS sample stage is required when performing *in situ* lithium plating experiments. For the *in situ* plating experiment sample, a $\sim$1 μm layer of lithium metal was first evaporated onto the spacers using the method described in section 5.2.2. The sample used for the *in situ* lithium sputtering experiment was directly sputtered onto a polished SST spacer.

The deposition of thin film LiPON was carried out using the same PVD system mentioned above. LiPON films were deposited by RF magnetron sputtering using a circular magnetron source with a target-to-substrate distance of $\sim$12 cm. Sputtering targets were prepared within the glovebox by lightly pressing dried lithium orthophosphate (Li_3PO_4) powder (Merck, batch number MKCT2638) into a 2” diameter, $\sim$2 mm deep circular copper holder using a glass microscope slide. The base vacuum pressure for the deposition processes was maintained below 5×10^{-5} mbar. Nitrogen gas was injected at a flow rate of 20 sccm, and in combination with vacuum system baffling, this established a process pressure of approximately 1×10^{-2} mbar. The applied RF power was set to 50 W, and the deposition time for the *in situ* lithium plating sample was 6 hours, which resulted in a ~0.6 μm thin film LiPON sample. One additional ultra-thin LiPON sample of ~0.01 μm thickness was prepared by deposition for 40 minutes under the same conditions. The resulting sample structure is schematically shown in Figure 5.4a.

5.2.4 Synthesis of bulk-processed LiPON

1.5 g of lithium metaphosphate ($LiPO_3$) powder (Stanford Advanced Materials, purity 99.9% metals basis) was placed into an alumina boat that had been aerosol coated with a boron nitride suspension and allowed to dry. The boat was then placed in the centre of a quartz glass tube (22 mm inner diameter, 1.2 m length) enclosed in a split tube furnace (Carbolite Ltd). In order to remove the moisture from the powder and melt the powder (the melting temperature of $LiPO_3$ is 656 °C), the tube was heated to 750 °C at a rate of 10 °C per minute, during which the nitrogen gas flowed through the tube at a rate of ~300 sccm.

Shortly before the end of the heating ramp, the nitrogen supply was turned off and the remaining nitrogen in the system was allowed to flow through the furnace tube until the pressure equalised with the atmosphere, which took several minutes. Once the nitrogen flow had ceased, a supply of anhydrous ammonia (BOC Ltd) was turned on and the flow rate was set to ~200 sccm; the transition of the atmosphere inside the tube from nitrogen to ammonia occurred gradually, taking several minutes for the residual nitrogen to be fully displaced.

The furnace temperature was maintained at 750 °C for 3 hours and 15 minutes, with the ammonia flow sustained throughout the dwell period except for the final 15 minutes. During this stage, ammonolysis of $LiPO_3$ proceeded according to Equation 5.1.

$$LiPO_3 + xNH_3 \rightarrow LiPO_{3-(3x/2)}N_x + (3x/2)H_2O \tag{5.1}$$

After turning off the ammonia flow, the residual gas was allowed to purge through the furnace tube before reintroducing nitrogen flow. The sample was then annealed for about 5 to 10 minutes under a pure nitrogen atmosphere at 750 °C, which helps to reduce water vapour bubbles trapped within the solidified glass. It is worth noting that longer annealing times did not lead to significant further reductions in bubble volume but resulted in nitrogen loss, and this should be avoided to maximise the electrochemical stability and ionic conductivity of the resulting LiPON glass sample.

At the end of the 750 °C dwell, nitrogen flow was maintained as the furnace cooled naturally over several hours. Once the temperature dropped below approximately 200 °C, the boat containing the sample was safely removed from the tube. Then the glass casting was broken into pieces to create a series of individual samples for subsequent treatments. Each sample was alternately sonicated in isopropanol and ground on successively finer silicon carbide papers to remove residual boron nitride residue and produce parallel-sided samples with thicknesses below 1 mm. Final polishing was carried out inside a glovebox using a 1 μm grade diamond lapping film, resulting in a reflective surface finish free of visible scratches.

A 2 μm layer of lithium metal (to act as the lithium source) was evaporated onto one side of the bulk-processed LiPON sample followed by the sputter deposition of ~350 nm of nickel, which was to protect the lithium layer and ensure good electrical contact with the XPS sample holder. The sample is shown schematically in Figure 5.4b.

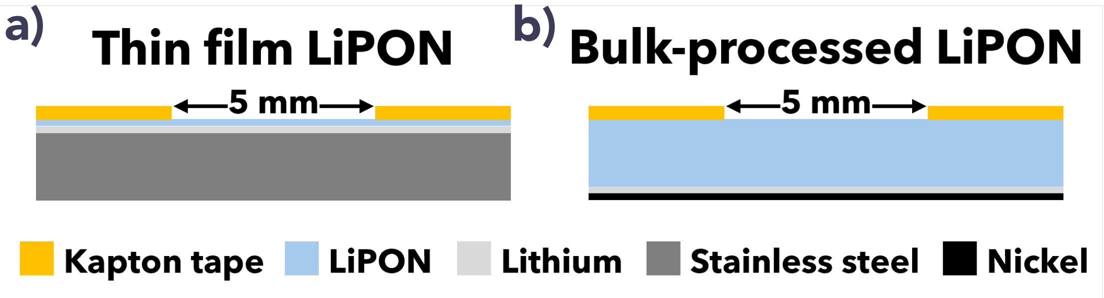

Figure 5.4: Schematic diagrams showing cross-sections of the samples fabricated for *in situ* lithium plating XPS experiments: a) thin film LiPON; b) bulk-processed sample. A thermally evaporated film of lithium beneath the LiPON acted as the source for lithium plating. Punched Kapton tape was placed on top of the samples to define a 5 mm diameter circular current path. Reprinted from [261]

5.2.5 Chemical characterisation and the study of SEI formation by XPS

XPS characterisation of thin film and bulk-processed LiPON samples was performed in a Physical Electronics (PHI) VersaProbe III instrument with an Al K-alpha ($h\upsilon = 1486.6$ eV) source and a chamber maintained at a pressure below 10^{-8} mbar.

Each sample to be characterised was attached to the XPS sample holder within an Ar-filled glovebox ($[H_2O]$ and $[O_2] < 1$ ppm) using electrically conductive carbon tape and transferred to the XPS instrument in an airtight PHI transfer vessel. SXI was employed to locate the centre of the sample, and the probing area for the XPS measurements was set to 500 μm × 500 μm about this point. Prior to conducting XPS measurements, the surface of each LiPON sample was etched for 1 minute using the built-in Ar-ion gun operated at 2 kV. This brief step was intended to remove surface contamination without significantly altering the LiPON structure.

The pass energy for the survey scan was 224 eV and 55 eV for the high-resolution XPS scans, and the duration of each high-resolution scan was approximately 33 minutes. Collected XPS data was processed using CasaXPS software (Casa Software Ltd): a Shirley-type background was applied to each core-level spectrum, peak components were fitted using a Gaussian-Lorentzian line shape. The charge calibration was performed using the adventitious C 1s spectral component at 284.8eV, ensuring consistency across all XPS measurements[223]. Chemical compositions were determined using relative sensitivity factors calculated for the same instrument at the same pass energy (Table 5.1).

Table 5.1: RSF×T(E) values (the products of the relative sensitivity factor and transmission function) calculated for the elements in LiPON by performing XPS measurements on reference samples in the same instrument at a pass energy of 55 eV.

Li 1s	O 1s	P 2p	N 1 s
1.0±0.0	33.5±2.6	25.3±1.8	17.3±3.5

After characterising the LiPON surfaces, *in situ* lithium plating XPS was performed to study the development of the SEI between LiPON and lithium metal.

The electron flood gun was directed to the sample surface and was used to apply a current of 30 μA. A piece of Kapton tape containing a 5 mm diameter hole was used as a mask on the sample; therefore, the applied current density can be calculated as ~0.15 mA cm^{-2}, which is typical of values used previously for cycling all-thin-film cells with LiPON electrolytes[266–269]. As electrons accumulated on the LiPON surface, the resulting potential difference initiated oxidation of the underlying lithium to Li$^+$. This was drawn to the sample surface and reduced back to lithium metal. The deposited lithium metal reacted with the LiPON to form an SEI. By alternating between XPS measurements and lithium plating, it was possible to track chemical changes in the near-surface region. The electron flood gun was kept off during the XPS measurement.

5.3 Results and discussion

Molecular properties of pristine LiPON sample

XPS has been utilised to elucidate the binding environment within the LiPON structure as well as its SEI composition against lithium metal.

The series of core-level spectra shown in Figure 5.5 were collected after Ar-ion etching of the pristine samples for the purpose of surface cleaning. Notably, the spectra presented in Figure 5.5a and 5.5b exhibit similarities, indicating that the molecular structures of the thin-film and bulk-processed LiPON samples share comparable characteristics. This can, to some extent, be attributed to their similar chemical compositions in terms of Li, P, and O content, as summarised in Table 5.2. Although the N/P ratio of the thin-film sample was nearly double that of the bulk-processed sample, this difference narrowed slightly when the contribution from an emission feature at 403.3 eV in the N 1s spectrum of the bulk-processed sample was included in the calculation (this will be discussed later).

Previous XPS studies on both thin-film and bulk-processed LiPON have consistently fitted the principal emissions in the O 1s and N 1s spectra with two components to account for the presence of asymmetric shoulder peaks[270, 271, 278–283]. Similar fittings were adopted in the present study, as shown in Figure

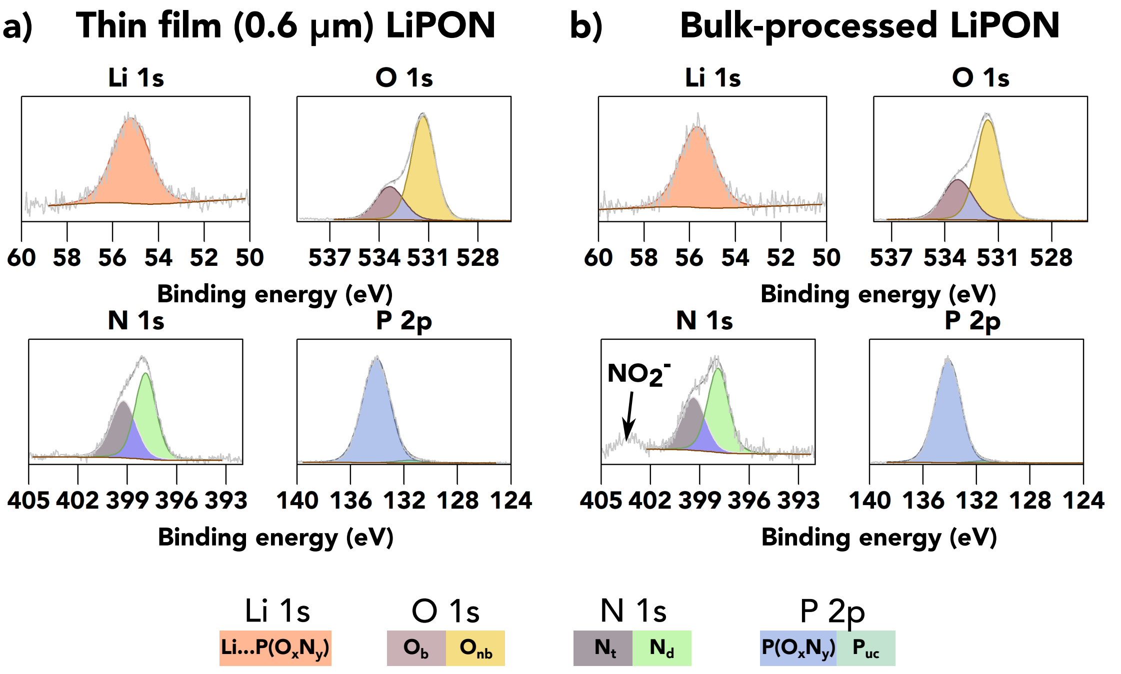

Figure 5.5: High-resolution core-level spectra after Ar-ion etching for (a) the ~0.6 μm thick LiPON film sample and (b) the ~800 μm thick bulk-processed LiPON sample. Reprinted from [261]

5.5. The spectral components were assigned to specific chemical environments within the LiPON structure, guided by the attributions made in these previous studies. Examples of these environments are illustrated on the structural formula of a hypothetical LiPON fragment in Figure 5.6.

The Li 1s spectra exhibit a single peak at 55.2-55.7 eV, which was fitted with a component labelled "Li...P(O_xN_y)". This designation reflects the chemically similar environments of Li^+ in LiPON, where each lithium ion is coordinated to a non-bridging oxygen or nitrogen atom within a P(O_xN_y) tetrahedral unit. Two components were fitted in the O 1s spectra. The peak at higher binding energy (~533 eV) is attributed to oxygen in P-O-P linkages, commonly referred to as bridging oxygen (O_b), which is shared between two P(O_xN_y) units. The more intense peak at lower binding energy (531-532 eV) corresponds to non-bridging oxygen (O_{nb}), which is bonded to phosphorus but not shared among multiple tetrahedral units.

The identification and assignment of N 1s peaks can be complex, involving potentially N_t, N_d and N_a[265, 285]. As reported by Lacivita *et al.*, the nitrogen

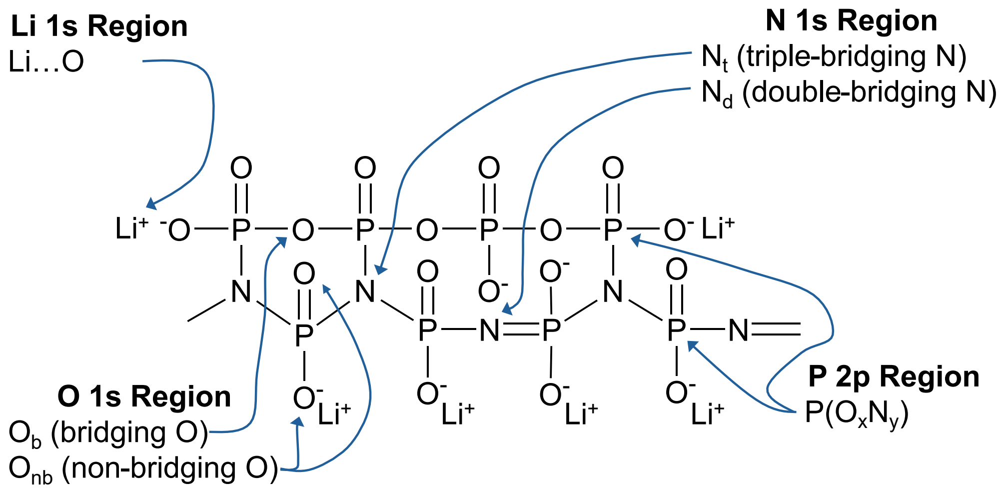

Figure 5.6: Structural formula of a hypothetical LiPON fragment, with examples of the different chemical environments distinguishable in XPS spectra highlighted. The relative proportions of the different chemical environments in this fragment are not necessarily representative of the LiPON compositions reported in this study. Reprinted from [261]. Drawn with reference to [284]

bonding environments within LiPON are closely related to the composition, especially the lithium concentration. When the Li:P ratio is below 2 the N atoms should be present in N_t and N_d environments. With the increase in Li:P ratio, N_a configuration starts to form to accommodate more lithium in the structure[265]. An additional peak in the N 1s spectrum, centred at approximately 404 eV, has been observed in previous studies and attributed to O-N=O (NO_2^-) species[270, 286, 287]. In this work, a peak at 403.3 eV was detected in the N 1s spectrum of the bulk-processed sample but was absent in the corresponding spectrum of the thin-film sample. Notably, this peak was not present before Ar-ion etching and did not appear in the N 1s spectra of the thin-film sample, either before or after etching, as shown in Figure 5.7. The corresponding N 1s spectra for the ultra-thin LiPON sample are presented in Figure A.9.

The Ar-ion etching may have cleaved P-O and P-N bonds on the surface of the bulk-processed sample, leading to the formation of NO_2^- through subsequent reactions involving liberated oxygen and nitrogen species. It remains unclear why a similar process was not observed on thin film samples, unless subtle differences in surface properties between these samples played a role. Previous studies suggest

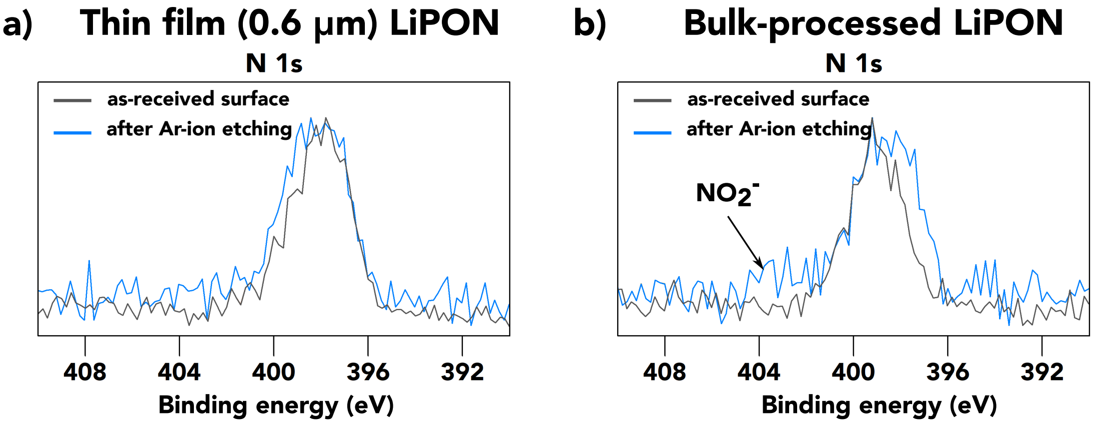

Figure 5.7: Normalised N 1s XPS spectra in the binding energy range of 409 eV to 391 eV extracted from survey scans for (a) the ~0.6 μm thick LiPON film sample and (b) the ~800 μm thick bulk-processed LiPON sample before and after Ar-ion etching. Reprinted from [261]

that NO_2^- is a surface phase rather than an intrinsic component of the LiPON structure[288, 289]. Therefore, it has been excluded from the spectra shown in Figure 5.8 and from subsequent analyses, including the chemical composition calculations (Table 5.2) and the N 1s component fractions (Figure 5.9b)[288, 289].

However, the removal of nitrogen from the LiPON surface during the formation of this phase results in a slight nitrogen deficiency in the bulk-processed LiPON composition calculated from the XPS data (Table 5.2), which may not accurately represent the overall sample. When the contribution from the NO_2^- peak is included, the adjusted composition of the bulk-processed sample is determined to be $Li_{1.30}PO_{2.65}N_{0.29}$.

Table 5.2: Chemical compositions and ratios of bridging to non-bridging oxygen (O_b/O_{nb}) and triple-bridging to double-bridging nitrogen (N_t/N_d) calculated for the thin film and bulk-processed LiPON samples from the XPS spectra acquired prior to lithium plating in Figure 5.5. The bulk-processed LiPON composition neglects an emission in the N 1s spectrum from NO_2^-, which is not part of the LiPON structure.

	Thin film LiPON	Bulk-processed LiPON
Chemical composition	$Li_{1.60}PO_{2.72}N_{0.46}$	$Li_{1.30}PO_{2.66}N_{0.25}$
O_b/O_{nb}	0.37	0.49
N_t/N_d	0.80	0.72

According to Table 5.2, the Li:P ratio for both thin-film and bulk-processed samples is less than 2, so the component at higher binding energy (~399 eV) is attributed to N_t, while the component at lower binding energy (~398 eV) is attributed to N_d[265, 285]. The most primitive molecules containing N_t, N_d, N_a and O_b are illustrated by the structural formulae in Figure 5.1 to aid the comparison of these bonding arrangements.

The ratios of N_t to N_d and O_b to O_{nb} presented in Table 5.2 are calculated from the component area ratios of the fitted XPS spectra. As expected from the similar appearance of the spectra, the values of these ratios are comparable for the two samples. Both N_t and O_b form linkages between neighbouring molecular chains, so the higher nitrogen and lithium concentrations observed in the thin-film sample may account for its slightly higher N_t/O_b ratio.

In the case of the P 2p spectra, the overall emission between 133 and 134 eV is collectively assigned to '$P(O_xN_y)$'. Although phosphorus exists in multiple distinct chemical environments due to the variable composition of $P(O_xN_y)$, the binding energy differences of among these environments are too small to be resolved by XPS.

It is worth noting that Lacivita *et al.* have questioned the assignment of the N 1s spectral components to N_d and N_t in LiPON thin films[265]. Using *ab initio* molecular dynamics simulations, they found that LiPON with a Li/P ratio comparable to that of the Li_3PO_4 sputtering target contained nitrogen predominantly in N_d and N_a environments, with no evidence of N_t. This contrasts with an earlier study by Sicolo *et al.*, in which a simulated melt-quench process applied to crystalline $Li_{1.25}PO_2N_{0.75}$ yielded an amorphous structure containing both N_d and N_t[290]. Notably, their LiPON composition was deficient in Li and O, making it closer to the $LiPO_3$ precursor used for bulk-processed LiPON. These computational studies suggest that N_a formation is favoured over N_t at higher Li/P ratios, aligning with the structural requirement that $P(O_xN_y)$ units containing N_a accommodate more Li^+ than those containing N_t (Figure 5.1). Lacivita *et al.* proposed that the N 1s spectral components at ~398 eV and ~399 eV of LiPON thin films sputtered from Li_3PO_4 are better assigned to N_a and N_d, respectively, rather than N_d and N_t.

However, this interpretation assumes close compositional congruence between the sputtering target and the resulting thin films, which may not always hold true.

In practice, lithium loss inevitably occurs to some extent during the sputtering of lithium compounds. This loss depends not only on the sputter deposition conditions but also on the specific characteristics of the deposition system used[291]. Consequently, the chemical compositions of LiPON films can vary across different studies. In this work, as well as in several previous reports, the LiPON films exhibited compositions comparable to those of $LiPO_3$-derived bulk-processed LiPON. This compositional similarity accounts for the comparable molecular structures observed in these samples, despite their fundamentally different processing routes[109, 270, 292–294].

5.3.1 Lithiation and structural evolution of the LiPON

Following the structural analysis of the pristine samples, this section focuses on the changes that occurred in the surface regions of the two LiPON samples upon lithium plating. As shown in Figure 5.8, the spectral evolution indicates the formation of new chemical environments corresponding to SEI species after a certain amount of lithium metal had been plated. The changes observed in both the thin film and bulk-processed LiPON samples followed similar patterns, as expected due to their comparable chemical compositions and initial molecular structures. However, these changes occurred over a longer cumulative lithium plating time in the bulk-processed sample, primarily due to its greater thickness, as discussed later in Section 5.3.4. Figure 5.9 presents the evolution of the component fractions for each core-level spectrum in Figure 5.8 as a function of cumulative plating time, while the associated binding energy shifts are plotted in Figure A.10.

The structural evolutions within the LiPON samples during the lithiation process are most clearly reflected in the O 1s and N 1s spectra shown in Figure 5.8, as well as in the corresponding component fraction plots presented in Figure 5.9. With increasing cumulative lithium plating time, the fraction of O_{nb} increased, while that of O_b decreased. Simultaneously, the fractions of both N_t and N_d declined,

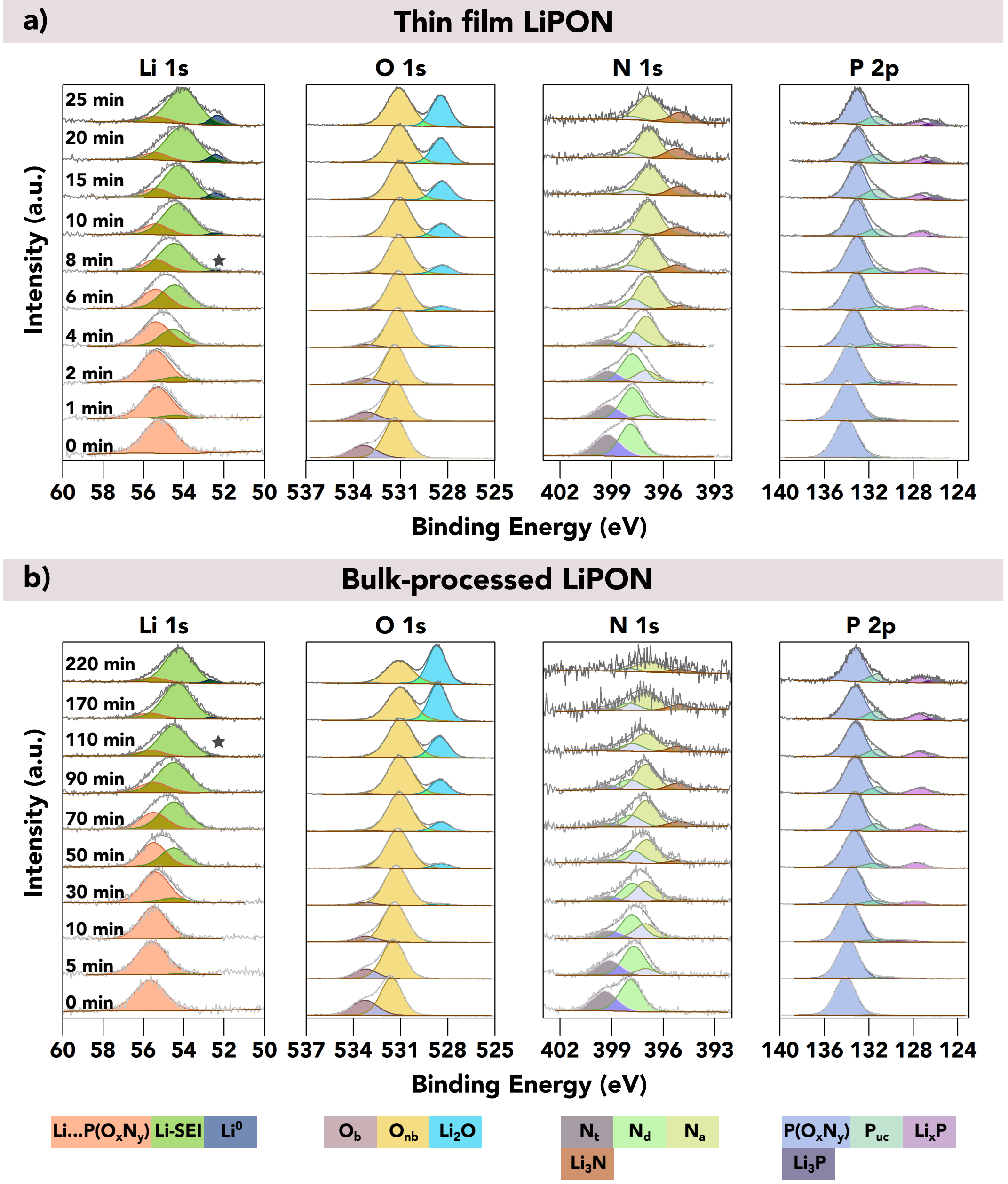

Figure 5.8: Time series of XPS core-level spectra acquired during the *in situ* lithium plating experiments performed on a) a ~0.6 μm thick LiPON film sample and b) an ~800 μm bulk-processed LiPON sample. Acquired spectra (grey) are shown along with linear combination fitting results. The cumulative lithium plating time (electron beam exposure time) is indicated in the first column. The peak intensities of each acquired core-level spectrum have been normalised to improve the visibility of minor spectral contributions. Individual spectral components are coloured, and a key is provided below each group of spectra. O$_b$, O$_{nb}$, N$_t$, N$_d$, N$_a$ and P$_{uc}$ are bridging oxygen, non-bridging oxygen, triple-bridging nitrogen, double-bridging nitrogen, apical (non-bridging) nitrogen and undercoordinated phosphorus, respectively. The appearance of the Li^0 (lithium metal) peak is highlighted with a star. Reprinted from [261]

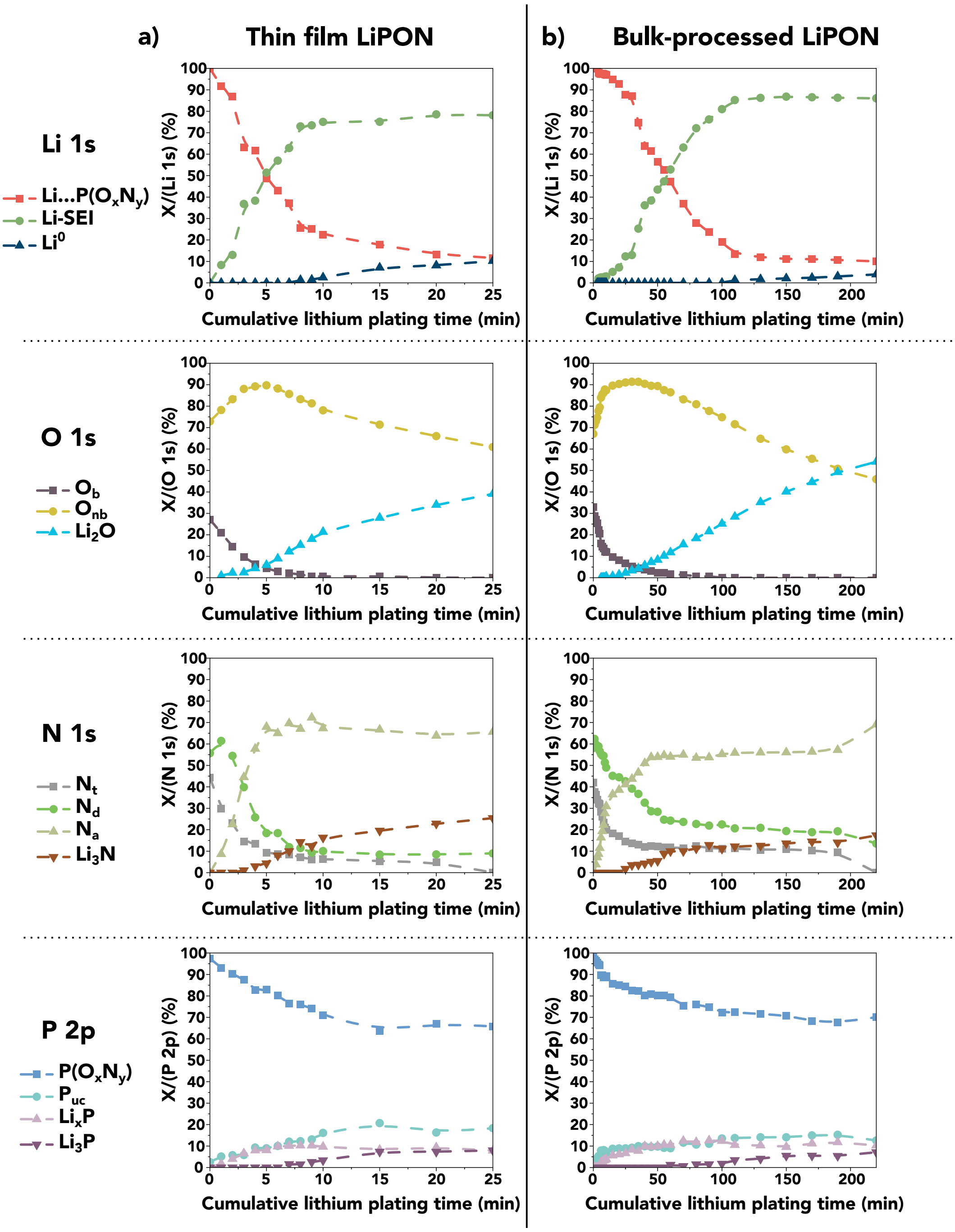

Figure 5.9: Changes in component (X) fractions for each of the core-level spectra in Figure 5.8 over cumulative lithium plating time, calculated from the component peak areas. The plots in a) and b) correspond to the thin film and bulk-processed LiPON samples, respectively. Reprinted from [261]

although a brief increase of over 5 at% in the N_d fraction was observed during the initial plating step in the thin film sample. A new N 1s component, marked in brown, appeared at a lower binding energy, consistent with N_a, and its fraction grew rapidly before stabilising as the fractions of N_d and N_t reached their baselines[265].

These observations—the reduction in bridging environments (O_b, N_t, N_d) alongside the increase in non-bridging environments (O_{nb}, N_a)—suggest that the extended phosphate chain structures of the LiPON samples were progressively cleaved upon lithiation. This structural evolution can be described as a transition from metaphosphate towards orthophosphate character, which aligns with the earlier discussion on the influence of Li/P ratio on molecular configuration. Consequently, LiPON compositions exhibiting a more orthophosphate-like character, with a Li/P ratio approaching that of the Li_3PO_4 precursor, are expected to have a lower lithiation capacity and undergo less pronounced structural changes when lithium is plated onto their surface.

5.3.2 Formation and chemical evolution of the SEI

The onset of SEI formation was indicated by the emergence of a secondary component, labelled as 'Li-SEI', in the Li 1s spectra at 54.0-54.6 eV, appearing after cumulative plating times of one minute for the thin film sample and four minutes for the bulk-processed LiPON sample. This Li-SEI component corresponds to Li^+ in species including Li_2O, Li_3N, and Li_3P—the binary SEI compounds commonly observed in previous studies[270–272, 274]. Since these compounds exhibit similar binding energies in the Li 1s region, their identities were further confirmed through the appearance of new components in other core-level spectra, with assignments made based on previously reported literature.

As shown in Figure 5.9, the first binary SEI compound detected was Li_xP, which appeared in the P 2p spectra at approximately 128.5 eV after 1 and 5 minutes of lithium plating for the thin film and bulk-processed samples, respectively. Li_xP represents a lithium phosphide phase in which phosphorus exhibits a higher oxidation state compared to Li_3P (P^{3-}), resulting in a higher binding energy. While Li_xP has previously been reported as a component of the SEI formed on certain sulphide electrolytes—such as the SEI between LGPS and lithium metal (discussed in Chapter 3) and between Li_6PS_5Cl and lithium metal (Chapter 4)—this represents the first identification of its presence at the Li|LiPON interface[174, 185].

Li_2O also formed within the first minute of plating on the thin film sample, as evidenced by the emergence of a peak at approximately 528.4 eV in the O 1s spectrum. In contrast, this peak was not observed in the bulk-processed sample until a cumulative plating time of 8 minutes. The next binary compound to emerge was Li_3N, identifiable in the N 1s spectra at approximately 395 eV, appearing after cumulative plating times of 3 minutes for the thin film sample and 25 minutes for the bulk-processed sample. Following this, emissions corresponding to Li_3P emerged in the P 2p spectra after cumulative plating times of 7 and 60 minutes for the thin film and bulk-processed samples, respectively. This peak was centred at a binding energy of approximately 126 eV. The delayed appearance of Li_3P suggests that it formed as a result of the progressive lithiation of Li_xP into Li_3P. Further evidence for this transition is provided by the gradual decrease in the binding energy of P in Li_xP, approaching the characteristic value of Li_3P, as shown in Figure A.10. Once Li_3P had formed, all the expected binary SEI compounds were present.

Another component in the P 2p spectra, labelled as 'P_{uc}' (undercoordinated P), has not been discussed thus far, as it does not correspond to a well-defined LiPON structural unit or a specific SEI compound. Sicolo *et al.* conducted a computational study on the Li|LiPON interface, which revealed that undercoordinated P atoms, generated through the breaking of P-N and P-O bonds, could be reduced to oxidation states of +3, +2, or -2 upon reacting with lithium metal[271]. The observed increase in the P_{uc} fraction from the beginning of lithium plating can be attributed to the cleavage of P-N and P-O bonds associated with N_t, N_d, and O_b units as lithiation progressed. Subsequent reactions between lithium and P-O_{nb} or -N_a likely contributed to the formation of Li_xP, Li_2O, and Li_3N. It is also important to highlight that some P_{uc} was already present before lithium plating commenced. This is likely a result of bond cleavage during the Ar-ion etching process, as evidenced by the absence of P_{uc} emissions in the pre-etching P 2p spectra shown in Figure 5.10.

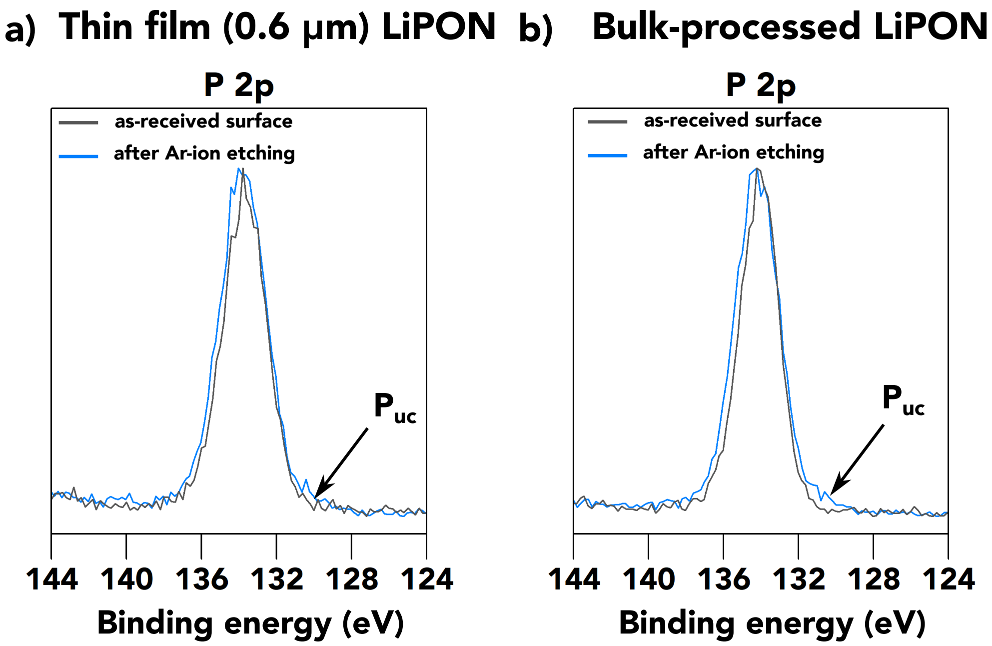

Figure 5.10: P 2p XPS spectra in the binding energy range of 144 eV to 124 eV extracted from survey scans for (a) the ~0.6 μm thick LiPON film sample and (b) the ~800 μm thick bulk-processed LiPON sample before and after Ar-ion etching. The peak intensities have been normalised to improve the visibility of minor spectral contributions. Reprinted from [261]

The XPS results in Figure 5.8 reveal the presence of Li_2O, Li_3N, and Li_3P in the SEIs formed on both LiPON samples, which is broadly consistent with previous studies of the Li|LiPON interface. However, two earlier investigations also reported Li_3PO_4 as an SEI phase, either as a replacement for or in coexistence with Li_3P[270, 272]. Identifying Li_3PO_4 from core-level XPS spectra is challenging, as it lacks distinct spectral features and its emissions overlap with those from LiPON. Specifically, it contributes to the emission of Li 1s-Li...$P(O_xN_y)$, O 1s-O_{nb}, and P 2p-$P(O_xN_y)$ components. However, the fraction of the $P(O_xN_y)$ signal attributable to Li_3PO_4 can be estimated by subtracting the contributions from LiPON, namely those associated with phosphorus bonded to N_t, N_d, N_a, and O_b.

The maximum possible contribution of P from LiPON can be estimated by assuming the simplest structural units containing N_t, N_d, N_a, and O_b, as illustrated in Figure 5.1. Although the precise molecular structures of the LiPON samples remain unknown, these simplest structural units provide a useful framework for approximation. The chemical formulae of these units were used to convert the measured atomic fractions of N_t, N_d, N_a, and O_b into the corresponding atomic fraction of P. This calculated P fraction was then subtracted from the total measured atomic fraction of P in the $P(O_xN_y)$ component to estimate the minimum possible fraction of P attributable to Li_3PO_4. Table 5.3 provides an illustrative example of this calculation, with the complete results shown in Figure 5.11.

Table 5.3: Calculation of the minimum atomic fraction of P associated with Li_3PO_4 for the ~0.6 μm LiPON film sample at a cumulative plating time of 10 minutes.

X	Concentration in sample (at%)	P/X ratio in structural unit	Concentration of P (at%)
O_b	0.21	2	0.42
N_t	0.24	3	0.72
N_d	0.38	2	0.76
N_a	2.57	1	2.57
Sum [P]			4.47
$P(O_xN_y)$	5.66	1	5.66
Difference			1.19

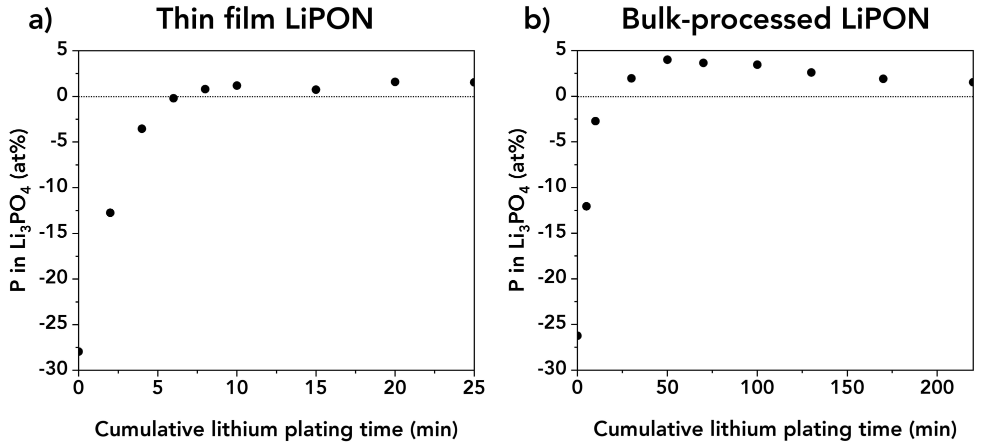

Figure 5.11: Evolution of the minimum (mathematically) possible concentration of P associated with Li_3PO_4 in (a) the ~0.6 μm thick LiPON film sample and (b) the ~800 μm thick bulk-processed LiPON sample with cumulative lithium plating time. Negative values are non-physical. Reprinted from [261]

At the early stages of lithium plating, the concentrations of Li_3PO_4 in both LiPON samples were expected to be negligible, which accounts for the initially negative P concentrations calculated using the method described above. However, the calculated values became positive after approximately 7 and 20 minutes of lithium plating for the thin film and bulk-processed samples, respectively, before stabilising at around 1.2 at% and 4 at%. This corresponds to at least 15% and 50% of the detected P being present in the form of $\mathrm{Li_3PO_4}$. These results demonstrate that $\mathrm{Li_3PO_4}$ was a significant constituent of the SEI formed on both LiPON samples in this study.

Based on the spectral results and the preceding discussion, the degradation process of the LiPON samples during lithium plating is proposed in Equations 5.2 to 5.5. These reactions were formulated using the hypothetical chemical compositions of the individual structural units illustrated in Figure 5.1, as the precise molecular properties of the fabricated LiPON samples remain unknown. It is worth noting that intermediate reaction steps involving $\mathrm{P_{uc}}$ species are likely, as suggested by the XPS spectra in Figure 5.8. However, incorporating such intermediates would require additional assumptions, as $\mathrm{P_{uc}}$ lacks a well-defined stoichiometry; its composition depends on several variables and is therefore difficult to predict. Since these assumptions are not necessary to explain the key features of the lithiation and SEI formation processes, they have been omitted for clarity.

$$Li_6P_3O_9N + (5+x)Li \rightarrow Li_5P_2O_6N + Li_xP + 3Li_2O \tag{5.2}$$

$$Li_5P_2O_6N + (5+x)Li \rightarrow Li_4PO_3N + Li_xP + 3Li_2O \tag{5.3}$$

$$Li_4PO_3N + (5+x)Li \rightarrow Li_xP + 3Li_2O + Li_3N \tag{5.4}$$

$$Li_4P_2O_7 + (5+x)Li \rightarrow Li_3PO_4 + Li_xP + 3Li_2O \tag{5.5}$$

Equation 5.2 proposes a decomposition pathway of $\mathrm{N_t}$ units ($\mathrm{Li_6P_3O_9N}$) into $\mathrm{N_d}$ units ($\mathrm{Li_5P_2O_6N}$), which aligns with the observed decrease in the $\mathrm{N_t}$ fraction during lithium plating (Figure 5.9). Moreover, the brief increase in the $\mathrm{N_d/N_t}$ ratio at the onset of lithium plating in the thin film sample supports this decomposition pathway, and the SEI products predicted by this reaction—$\mathrm{Li_xP}$ and $\mathrm{Li_2O}$—were indeed the first to form during the experiments.

In both samples, the decline in $\mathrm{N_t}$ was subsequently followed by a decrease in $\mathrm{N_d}$ and a corresponding increase in $\mathrm{N_a}$, consistent with the reaction proposed in Equation 5.3. This reaction yields additional Li_xP and Li_2O—aligning with the observation that these were the only SEI components present at the onset of N_a formation. According to a previous report, $P(O_xN_y)$ units containing N_a are unstable in contact with lithium metal and are prone to decomposition. This instability suggests that the $P(O_xN_y)$ units containing N_a are expected to decompose via a reaction such as that described in Equation 5.4[272]. This reaction yields Li_3N and Li_xP, consistent with the experimentally observed sequence of binary SEI compound formation. Continued lithiation of Li_xP ultimately leads to the formation of Li_3P. Equation 5.5, adapted from a decomposition reaction proposed by Schwöbel *et al.*, accounts for the sharp decrease in O_b ($Li_4P_2O_7$) and the concurrent increase in O_{nb} (Li_3PO_4) shown in Figure 5.9[270]. Importantly, this reaction provides a mechanistic pathway for the formation of Li_3PO_4, supporting its identification as a major SEI component.

This analysis of the decomposition pathways indicates that the initial lithiation of LiPON, followed by the progressive lithiation of its decomposition products, leads to the formation of SEI compounds as co-products. Although the same binary SEI phases are expected to form irrespective of whether the LiPON exhibits metaphosphate or orthophosphate character, the initial concentrations of N_t, N_d, N_a, and O_b are expected to influence both the resulting SEI composition and its overall thickness. For instance, Li_3N is expected to form earlier during the decomposition of orthophosphate-type LiPON due to its higher initial fraction of N_a. Conversely, the decomposition of metaphosphate-type LiPON, characterised by a greater initial O_b fraction, would likely yield a higher concentration of Li_3PO_4 in the SEI[265]. This aligns with the observation that the bulk-processed LiPON, which exhibited a higher initial O_b/O_{nb} ratio, formed an SEI with a greater fraction of Li_3PO_4 compared to the thin film sample. Depending on the specific passivating roles of Li_3N and Li_3PO_4, such compositional differences could influence the time required to establish a sufficiently protective SEI, and therefore, the final SEI thickness necessary for passivation.

5.3.3 Passivation of the Li/LiPON interface and final structure of the SEI

The Li-LiPON interphase eventually developed into a passivating layer, effectively impeding further decomposition of the underlying LiPON. This transition was evidenced by the accumulation of unreacted lithium metal on the sample surfaces as lithium plating continued. The Li 1s-Li^0 emission appeared after 8 minutes of plating on the thin film sample and after 110 minutes on the bulk-processed sample. The intensity of this Li 1s-Li^0 peak increased with further plating, as shown in Figure 5.12. Additional evidence for the formation of a passivating interphase is provided by the core-level binding energy plots in Figure A.10, which show that the binding energies of most spectral components stabilised following the appearance of the Li^0 signal. This stabilisation indicates that the major chemical and structural changes within the SEI had largely ceased, consistent with the formation of a passivating SEI that inhibits further reaction.

An exception to this stabilisation was observed in the binding energy of the Li-SEI component, which began to decrease for both samples as plating continued. This shift was attributed to the increasing O 1s emission from Li_2O and the diminishing contributions from other SEI compounds, resulting from the thickening lithium metal layer, as shown in Figure 5.12. However, the apparent increase in Li_2O was likely an artefact produced by the reaction of freshly deposited lithium metal on the exposed sample surface with residual O_2 in the XPS chamber, as discussed in Section 3.3.4. This interpretation aligns with observations reported in previous studies[130, 162, 174, 185, 271, 295].

Since LiPON spans a broad range of Li^+ concentrations and decomposes through a series of lithiation reactions, inward lithium diffusion from the surface is expected to result in SEIs with spatially non-uniform chemical compositions and structures. In terms of the characteristics of the fully formed SEI, this implies that the most lithiated species would be concentrated near the lithium metal side, while the least lithiated species would be located closer to the LiPON side of the interphase. This

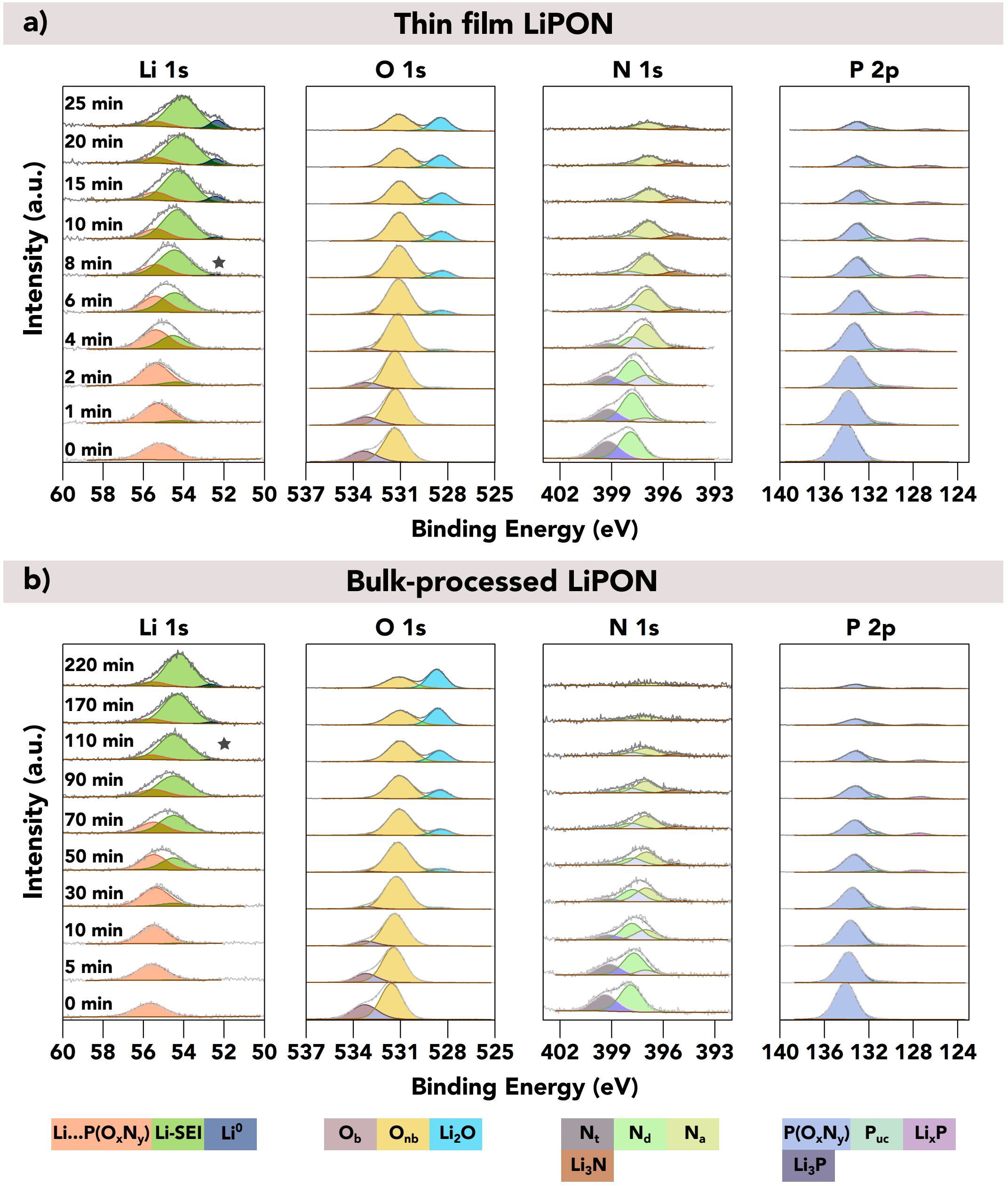

Figure 5.12: Time series of XPS core-level spectra acquired during the *in situ* lithium plating experiments performed on a) a ~0.6 μm thick LiPON film sample and b) an ~800 μm thick bulk-processed LiPON sample. Acquired spectra (grey) are shown along with linear combination fitting results. The cumulative lithium plating time (electron beam exposure time) is indicated in the first column. Individual spectral components are coloured, and a key is provided below each group of spectra. O_b, O_{nb}, N_t, N_d, N_a and P_{uc} are bridging oxygen, non-bridging oxygen, triple-bridging nitrogen, double-bridging nitrogen, apical (non-bridging) nitrogen and undercoordinated phosphorus, respectively. The appearance of the Li^0 (lithium metal) peak is highlighted with a star. This is an non-normalised version of figure 5.8. Reprinted from [261]

distribution creates a lithiation gradient and, consequently, a lithium chemical potential gradient across the SEI.

The reactions described in Equations 5.2 to 5.5 correlate the evolution of the XPS spectra with the degree of lithiation as lithium plating progresses. Accordingly, the compositional variations within the SEI may represent a spatial manifestation of the temporal sequence of reactions observed during the *in situ* lithium plating experiment. In this framework, $\mathrm{O_b}$, $\mathrm{N_t}$, and $\mathrm{N_d}$ are expected to be most concentrated near the LiPON side of the interphase, while partially (intermediate) lithiated species such as $\mathrm{P_{uc}}$, $\mathrm{Li_xP}$, $\mathrm{N_a}$, and $\mathrm{Li_3PO_4}$ are likely localised toward the central region. Fully lithiated products, including $\mathrm{Li_2O}$, $\mathrm{Li_3N}$, and $\mathrm{Li_3P}$, are expected to be predominant near the lithium metal side.

While the XPS technique is limited in providing a complete depiction of the final SEI structure, several key properties can be inferred from the core-level spectra acquired after passivation. This analysis is enabled by the interplay of three key factors:

(1) the stabilisation of both the SEI and LiPON structures following passivation,

(2) the subsequent accumulation of lithium metal during continued plating

(3) the limited probing depth characteristic of XPS

After passivation, chemical changes within the LiPON samples and their SEIs were minimal. As a result, the ongoing evolution of the core-level spectra primarily reflected the changing sampling depth as the lithium metal layer thickened. Following passivation, the fractions of most core-level components corresponding to SEI species either stabilised or increased slightly (Figure 5.9), indicating that the SEI progressively occupied a larger proportion of the XPS probing volume relative to the underlying LiPON.

The decreases in the $\mathrm{Li...P(O_xN_y)}$ and $\mathrm{O_{nb}}$ fractions as shown in Figure 3.3.4 were primarily driven by the strong growth in the Li 1s and O 1s emissions from $\mathrm{Li^0}$ and $\mathrm{Li_2O}$, respectively. The fractions of $\mathrm{O_b}$ and $\mathrm{N_t}$ were the only other components to exhibit a notable decline in both samples after passivation. There remains some uncertainty as to whether these components should be classified as part of the SEI, as their bonding configurations are characteristic of the early stages of lithiation and reflect the structural transition of LiPON from metaphosphate to orthophosphate character. Notably, these were the only components to diminish entirely with continued lithium plating beyond passivation, indicating that the species from which they originated were primarily concentrated near the interface with the underlying LiPON.

As the O 1s emissions from O_b became negligible around the point at which SEI growth ceased, it is reasonable to infer that the SEI thicknesses were on the order of the XPS probing depth. For the elements in LiPON, the kinetic energies of the ejected photoelectrons exceed 950 eV, corresponding to an inelastic mean free path (λ_{IMFP}) of approximately 38-55 Å in lithium metal[171]. Given that the effective XPS probing depth is approximately $3\lambda_{\mathrm{IMFP}}$, this yields an estimated probing depth of 11-17 nm in lithium metal. This value should be considered an upper limit for the SEI thickness, as phosphorus, oxygen, and nitrogen are heavier than lithium, and thus the corresponding λ_{IMFP} values in LiPON and its SEI are likely to be lower.

Previously studies based on TEM characterisation have reported the thickness of the Li-LiPON SEI of about 76 and approximately 60 nm by Cheng *et al.* and Hood *et al.*, respectively[272, 273]. In the work by Cheng *et al.*, the nanostructured interphase was investigated using cryo-TEM, where a multilayer-mosaic SEI morphology was observed. The identified decomposition products included Li_3N, Li_2O, Li_3PO_4, and an amorphous matrix[272]. Hood *et al.* employed an *in situ* TEM approach, in which LiPON and Li metal were brought into contact inside the TEM column using a piezo-controlled scanning tunnelling microscope (STM) tip. In their study, a P-rich layer was found to concentrate on the LiPON side, whereas a P-deficient and O-rich layer formed on the Li metal side[273]. In contrast, the SEIs formed in this investigation appear to be thinner than those reported in TEM studies, but are in good agreement with the values obtained from electroanalytical and neutron reflectometry measurements[275, 276]. This discrepancy may arise from the more rapid passivation facilitated by the *in situ* XPS technique, in which lithium was electrochemically deposited—similar to the processes used in electroanalytical and neutron reflectometry measurements. However, it is important to note that SEI thickness estimates derived from XPS carry greater uncertainty compared to direct imaging methods such as TEM. Notably, the O_b emission from the bulk-processed sample diminished slightly earlier relative to the appearance of the Li^0 peak when compared to the thin film sample. This observation suggests that the SEI formed on the bulk-processed sample may have been comparatively thicker than that on the thin film sample. Such a difference would be consistent with the lower lithium content of the bulk-processed sample (Table 5.2), which implies a greater capacity for lithiation.

Then it is important to consider the N 1s spectral components associated with the primary decomposition products of LiPON, specifically N_d and N_a. Although these bonding configurations have not previously been linked to the Li-LiPON SEI, Figure 5.9 suggests their presence, as both components remained detectable even after O_b and N_t had disappeared. A sharp decline in the N_d fraction was observed in the bulk-processed LiPON sample between cumulative plating times of 190 and 220 minutes. This implies that species containing N_d bonding configurations were predominantly located near the LiPON interface, in agreement with the earlier analysis. In contrast, the N_a fraction remained stable in the thin film sample but increased sharply in the bulk-processed sample toward the end of lithium plating. Moreover, as shown in Figure 5.12, distinct N 1s emissions from N_a remained visible in both samples after passivation. These observations suggest that N_a-containing species were situated further from the LiPON side of the interphase than those containing N_d, consistent with the spatial decomposition profile inferred from the LiPON degradation analysis.

The presence of both N_a and Li_3PO_4 within the bulk of each SEI is further evidenced by the plateauing of the P 2p emission from $P(O_xN_y)$ structures, although their precise spatial distribution relative to one another remains uncertain. The fractions of the core-level components associated with P_{uc} and Li_xP initially increased and then stabilised after passivation, suggesting that these species were also concentrated away from the LiPON side of each SEI. In contrast, the core-level emission fractions of Li_3P and Li_3N continued to increase during lithium accumulation after passivation, consistent with their expected predominance near the lithium metal side of the SEI.

The morphology of the accumulated lithium metal must also be considered, as electrodeposited lithium rarely forms a uniform layer[295, 296]. Based on the applied current density of 0.15 mA cm^{-2} (calculated by dividing the applied beam current by the sample area), the amount of lithium plated at the point when the Li 1s-Li^0 peak first appeared corresponds to areal capacities of 0.04 and 0.28 mAh cm^{-2} for the thin film and bulk-processed samples, respectively. These capacities translate to estimated lithium layer thicknesses of approximately 0.21 μm and 1.33 μm. Given that the XPS probing depth in lithium metal is about 17 nm, emissions from the Li-LiPON SEI should have been completely attenuated within roughly one minute of additional lithium plating after passivation. The fact that SEI signals persisted indicates that certain regions of the electrodeposited lithium layer were thinner than the XPS probing depth, while other regions were substantially thicker. Only towards the end of each experiment did the thinnest regions approach the probing depth, leading to significant attenuation of SEI-related emissions. Nevertheless, aside from the delay in complete attenuation, the overall evolution of the core-level spectral component fractions in Figure 5.9 is expected to be largely unaffected by the non-uniformity of the lithium metal layer, because deposition of lithium metal on the surface occurs only after the SEI has become passivated.

Figure 5.13 illustrates the proposed spatial distribution of different species within the Li-LiPON SEI. This structure broadly aligns with the graded SEI model reported by Sicolo *et al.* based on their XPS analysis, but this work identifies additional SEI components, including P_{uc}, Li_xP, and N_a, as well as an N_d-rich layer near the LiPON side of the SEI[271]. However, this proposed structure contrasts with the findings from TEM studies by Cheng *et al.* and Hood *et al.*, as well as the computational work by Wang *et al.*, which suggest that Li_2O is the dominant SEI phase in direct

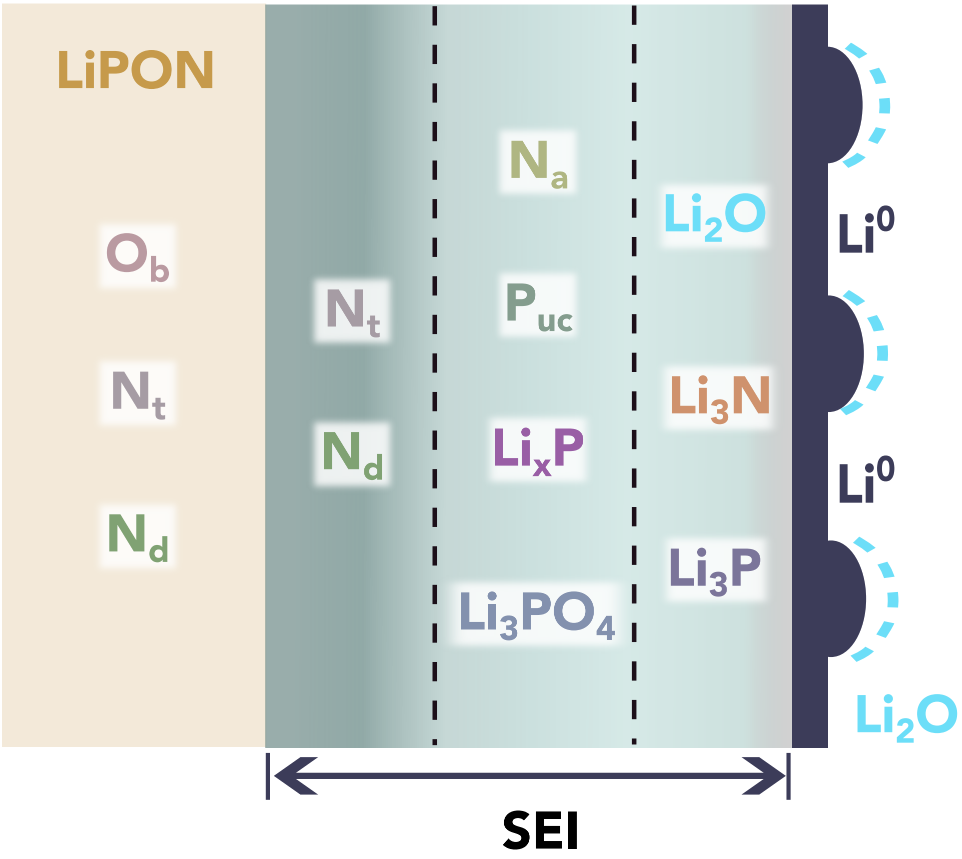

Figure 5.13: Schematic diagram of the Li-LiPON SEI structure determined from the results of the *in situ* lithium XPS plating experiments. The dashed lines between the layers of the SEI structure indicate that these are not “hard” boundaries and some degree of intermixing is expected. The layer thicknesses are not drawn to scale. Reprinted from [261]

contact with lithium metal[272–274]. This raises a potential discrepancy, as the present XPS analysis indicates that Li_3P was the final SEI component to form prior to passivation, implying that it was the phase in contact with lithium metal. Additionally, both Li_3N and Li_2O were also in contact with the lithium metal surface. The order of SEI formation may be influenced, at least in part, by differences in lithium deposition methods—whether electrochemical plating or physical sputtering. Nevertheless, the depth resolution of the *in situ* XPS technique used in this study is insufficient to definitively resolve the precise arrangement of the binary SEI phases, leaving some uncertainty regarding their exact spatial distribution.

As discussed in Chapter 3, the Li|LGPS interface forms a MCI due to the continuous electron-conducting pathway established by the decomposition products Li_3P and Ge, both of which exhibit ionic conductivities exceeding 10^{-4} S cm^{-1}. Similarly, Li_xP and Li_3P have been identified as SEI components at the Li|Li_6PS_5Cl interface[174, 183]. Notably, the low oxidation potential of Li_3P to Li_xP (0.87 V vs Li^+/Li) lies below the theoretical reduction potential of Li_6PS_5Cl (1.71 V vs Li^+/Li)[136]. This allows the oxidation of Li_xP to proceed at a potential lower than the SSE's reduction potential, meaning that, as long as lithium metal is present to feed the redox process, the SEI can continue to grow in a diffusion-limited manner as discussed in Chapter 4.

In contrast, two key factors prevent continuous SEI growth at the Li|LiPON interface. First, the reduction potential of LiPON, calculated by Zhu *et al.* as 0.68 V vs Li^+/Li, is lower than the oxidation potentials of most lithiated binary lithium compounds[136]. Second, the graded SEI structure formed at the Li|LiPON interface spatially separates the most reduced species from the LiPON layer, thereby preventing the establishment of a continuous electron-conductive pathway. Together, these factors contribute to the superior stability of LiPON against lithium metal.

5.3.4 Discussion about the differences for LiPON samples with different thicknesses

As discussed above, SEI formation on both samples followed a similar pattern, with the primary difference being the cumulative plating time required for SEI formation and the achievement of passivation. This is unexpected given the comparable SEI compositions, which should, in principle, require similar amounts of plated lithium to form. Since the applied beam current was the same for both samples, it is therefore essential to evaluate whether the actual current densities were indeed equivalent, as determined by the current path area and the electron flood gun current.

According to Ohm's law, when a constant current (I) is applied to the sample, the voltage difference (V) across the sample can be calculated as V=IR. However, it is important to note that the system does not instantly reach this voltage due to the presence of the geometric capacitance (CPE_{geom}) in the circuit. Initially, a portion of the applied current is diverted into the capacitive branch of the circuit, causing a transient response. As the potential difference builds up, the fraction of current flowing through the capacitive branch gradually decreases. The current flow into the capacitive component ceases once the voltage reaches its steady-state maximum, at which point all of the applied current flows through the resistive component. In this investigation, the physical manifestation of this process is the accumulation of electrons on the LiPON surface until the potential difference required to drive the applied current (30 μA) through R_i is reached. Once this condition is satisfied, the sample current (I_{sample}) should equal the electron flood gun current (I_{gun}).

EIS measurements were performed to characterise the resistance and capacitance properties of both thin film and bulk-processed samples. The experimental setup and results are detailed in Section A.3. The collected data are presented as Nyquist plots, with the corresponding ECM diagrams included as insets. Although the interfaces with the "electrode" were essentially non-blocking, the applied ECM model remains valid for representing the electrical responses of the samples during the *in situ* lithium plating experiment. For simplification in the subsequent analysis, interfacial capacitances are neglected, and the interfacial resistance, R, is incorporated into the overall ionic resistance of the sample, denoted as R_i.

As previously discussed, the capacitance of the bulk-processed sample could have contributed to its seemingly lower average value of I_{sample} during each plating step as the SEI evolutions takes much more time. A portion of the applied current could have initially been diverted into charging the interfacial capacitance, rather than directly contributing to lithium plating. However, the CPE_{geom} capacitances obtained from fitting the data included in Figures A.12 and A.13 were approximately 1×10^{-9} for the thin film and 5×10^{-10} F for the bulk-processed sample. It is worth noting that the capacitance values for both samples are very small, and and the thin film LiPON sample exhibited a higher capacitance than the bulk-processed one. This implies that, for the same applied current, more charge would have accumulated on the thin film sample. In practice, the capacitance value for the bulk-processed LiPON sample used in the *in situ* plating experiment would likely have been even lower due to its greater thickness.

Another possibility is that the true steady-state value of sample current $\mathrm{I_{sample}}$, was lower for the bulk-processed sample than for the thin film sample. To investigate this, $\mathrm{V_{sample}}$ was calculated assuming $\mathrm{I_{sample}}$=30 μA. The ionic resistance, $\mathrm{R_i}$, at room temperature was measured by EIS, yielding approximately 5000 Ω for the thin film sample and 7×10^7 Ω for the bulk-processed sample, with a top electrical contact diameter of 2 mm. Given that the current path in the *in situ* experiment was 5 mm in diameter and the bulk-processed sample was twice as thick, the corrected values of $\mathrm{R_i}$ were calculated as approximately 800 Ω for thin film sample and 2×10^7 Ω for bulk-processed sample. Based on these values, the $\mathrm{V_{sample}}$ was estimated to be ~0.024 V for thin film sample and ~600 V for bulk-processed sample. This significant difference suggests that the high resistance of the bulk-processed sample could have resulted in a substantial electrical field build-up, which might have affected the $\mathrm{I_{sample}}$ by repelling the incoming electrons from the flood gun. In this case, the actual $\mathrm{I_{sample}}$ for the bulk-processed sample is supposed to be lower than $\mathrm{I_{gun}}$=30 μA, resulting a lower lithium plating rate.

Moreover, the accelerating voltage of the electron flood gun ($\mathrm{V_{gun}}$) was only about 1 V, as it is designed to provide a low-energy electron beam for charge neutralisation. This means that $\mathrm{V_{gun}}$= 1 V represents the maximum potential drop that could be achieved by each sample. Since the calculated $\mathrm{V_{sample}}$= 600 V for the bulk-processed sample far exceeds this limit, it could not have been reached in practice. Instead, the actual current passing through the sample should have been no more than $\frac{I_{gun}}{600} = 0.05\ \mu A$. This suggests that the extra current provided by the electron flood gun must have been deflected to ground due the accumulated surface charge. In contrast, the calculated $\mathrm{V_{sample}}$ for the thin film sample, which is 0.024 eV, was significantly lower than 1 V, meaning that its $\mathrm{I_{sample}}$ should have been close to $\mathrm{I_{gun}}$, although some degree of electron deflection could still have occurred. The significant discrepancy in V_{sample} also highlights the influence of sample geometry and resistance on the electrochemical conditions of the plating experiment, reinforcing the need to consider these factors when comparing results between samples with different dimensions and conductivities. As in previous chapters, the SEI formation was examined on three SSEs—LAGP, LGPS, and Li_6PS_5Cl—using VEP method. The calculated voltage difference across each pellet, V_{sample} is small: ~6 mV for LAGP (diameter=8.38 mm, thickness=~850 μm, I= 20 μA, ionic conductivity σ=~0.5 mS cm^{-1}); ~3.4 mV for LGPS (diameter=8.0 mm, thickness=~850 μm, I= 20 μA, ionic conductivity σ=~1.0 mS cm^{-1}); and ~0.53 mV for Li_6PS_5Cl (diameter=5.0 mm, thickness=~750 μm, I= 2.5 μA, ionic conductivity σ=~1.8 mS cm^{-1}). Because the calculated voltage differences are on millivolt scale, I_{sample} can be regarded as very close to the gun current I_{gun}.

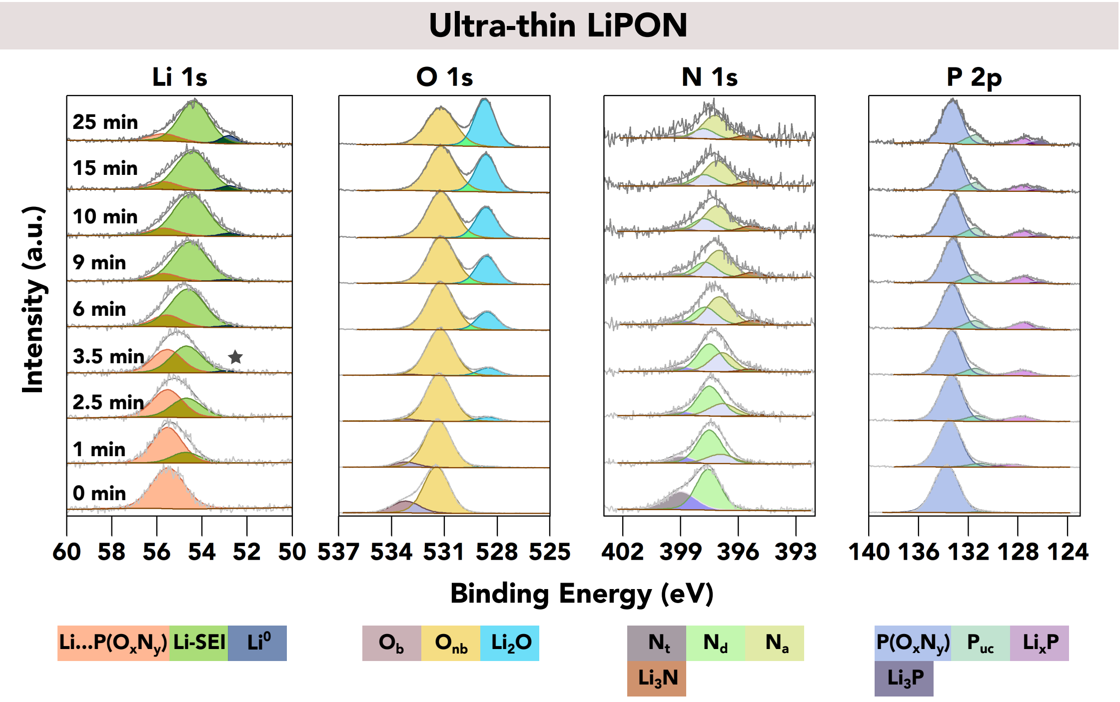

Figure 5.14: Time series of XPS core-level spectra acquired during the *in situ* lithium plating experiments performed on a ~0.01 μm thick LiPON film sample. Acquired spectra (grey) are shown along with linear combination fitting results; the intensities were normalised to the strongest peak in each spectrum. The cumulative lithium plating time (electron beam exposure time) is indicated in the first column. Individual spectral components are coloured, and a key is provided below each group of spectra. O_b, O_{nb}, N_t, N_d, N_a and P_{uc} are bridging oxygen, non-bridging oxygen, triple-bridging nitrogen, double-bridging nitrogen, apical (non-bridging) nitrogen and undercoordinated phosphorus, respectively. The appearance of the Li^0 (lithium metal) peak is highlighted with a star. Reprinted from [261]

To investigate whether the deflection of the incident electron beam can occur when V_{sample} is well below 1 V, an additional *in situ* lithium plating experiment was conducted on an "ultra-thin" LiPON film with a thickness of $\sim$0.01 μm. The core-level spectra acquired from this sample, shown in Figure 5.14, closely resemble those of the thin film and bulk-processed samples presented in Figure 5.8. This suggests that the SEI composition, structure and the formation process were consistent in all three samples.

Furthermore, the SEI thickness formed on the ultra-thin sample was also on the order of the XPS probing depth, as indicated by the negligible O_{b} emission upon the appearance of Li 1s-Li^0 peak. The detection of Li^0 at a cumulative plating time of 3.5 minutes indicates that SEI formation occurred in approximately half the time required for the $\sim$0.6 μm film. Assuming that the ionic conductivity of the ultra-thin sample was comparable to that of the $\sim$0.6 μm film, its resistance can be estimated as $\sim$10 Ω, yielding a V_{sample} of approximately 3×10^{-4} V for I_{sample}=30 μA. This demonstrates that the lithium plating rate is dependent on the sample thickness even when V_{sample} is lower than $\frac{V_{\text{gun}}}{40}$. Based on above discussion, for the condition $I_{sample} = I_{gun}$ to be satisfied, V_{sample} must be less than V_{gun}. thereby necessitating the use of thin film LiPON. There is an effect even going from 600 nm thick LiPON to 10 nm thick LiPON, so the results suggest that very thin LiPON films are required.

The result suggests that the properties of the fully-formed Li-LiPON SEI do not depend strongly on the applied current density, at least at levels below 0.15 mA cm^{-2}. The influence of current density on SEI formation could be investigated further by varying the beam current of the neutraliser gun. Despite the broad range of effective current densities across different samples, the formed SEIs exhibit comparable chemical and structural properties and reached similar thicknesses. This also indicates that, during the *in situ* lithium plating experiment, the condition $I_{sample} = I_{gun}$ is not necessarily met. This represents a clear limitation that must be considered in future studies, particularly when the influence of applied current density is of interest.

5.3.5 Li-LiPON SEI evolution by *in situ* sputtering

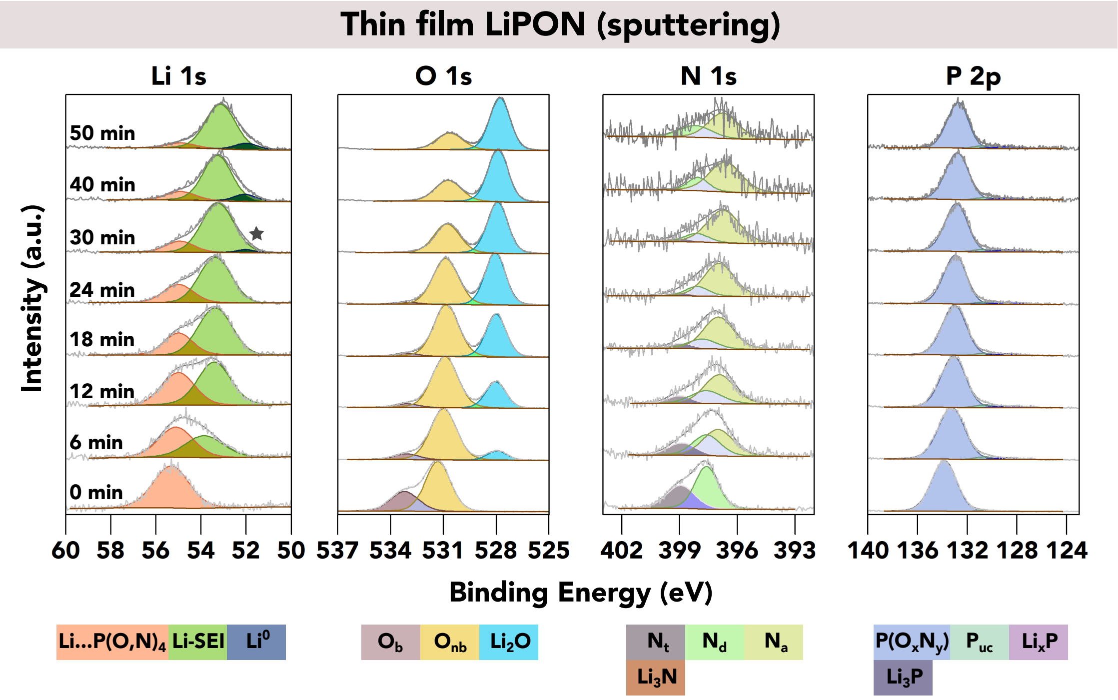

Figure 5.15: Time series of XPS core-level spectra acquired during the *in situ* lithium sputtering experiment performed on a thin film LiPON sample. Acquired spectra (grey) are shown along with linear combination fitting results; the intensities were normalised to the strongest peak in each spectrum. The cumulative lithium sputtering time is indicated in the first column. Individual spectral components are coloured, and a key is provided below each group of spectra. O_b, O_{nb}, N_t, N_d, N_a and P_{uc} are bridging oxygen, non-bridging oxygen, triple-bridging nitrogen, double-bridging nitrogen, apical (non-bridging) nitrogen and undercoordinated phosphorus, respectively. The appearance of the Li^0 (lithium metal) peak is highlighted with a star.

Building upon previous XPS investigations of the Li-LiPON interface, the results vary depending on the method used to construct the interface, such as lithium evaporation or physically attaching a lithium film to the LiPON sample[270, 272]. The *in situ* lithium plating technique, however, more accurately simulates the first charging process of a LiPON-based system, providing insights into the actual electrochemical reactions occurring at the interface between LiPON and lithium metal. To evaluate SEI formation under different lithium deposition techniques, another *in situ* lithium sputtering XPS experiment, as introduced in Section 2.1.2, was conducted. Unlike *in situ* lithium plating, where lithium is electrochemically deposited onto the LiPON surface, the *in situ* sputtering technique relies on physical deposition, in which lithium atoms are sputtered from a lithium metal target and subsequently deposited onto the LiPON sample. This technique introduces lithium without electrochemical driving forces, enabling an alternative perspective on SEI formation.

As shown in Figure 5.15, the bridging structures, including O_b, N_t, and N_d, decrease as the sputtering process progresses, which aligns with the previous discussion in Section 5.3.2. This trend suggests that LiPON undergoes structural decomposition during lithium deposition, consistent with the observations made during *in situ* lithium plating. However, a notable difference is the absence of Li_3N and Li_3P formation in this case. This contrast suggests that the mechanism of SEI formation differs between electrochemical and physical lithium deposition methods. This observation is consistent with previous findings for SEI formation on LAGP and LGPS SSEs, where variations in SEI composition and evolution were observed depending on the lithium deposition technique employed. Three possible reasons have been discussed in Section 3.3.5, reinforcing the importance of studying SEI formation under conditions that closely mimic the actual working environment of a practical cell.

5.4 Summary

In this work, the formation and properties of the SEI between LiPON and lithium metal was firstly studied by *in situ* lithium plating XPS. XPS spectra collected from the pristine LiPON surfaces revealed that both the thin film and bulk-processed samples exhibited similar metaphosphate glass structures, despite being prepared using different precursors and fabrication routes. The structural similarities are attributed to the comparable [Li]/[P] ratios in the thin film and bulk-processed samples, which likely result from lithium loss during the sputter deposition process.

During the *in situ* lithium plating, the results indicate that SEI formation on both samples proceeded in a similar manner. LiPON underwent lithiation through a series of reactions, resulting in a graded SEI structure: the most lithiated species (Li_2O, Li_3N, and Li_3P) were concentrated near the lithium metal side, intermediate lithiation products (P_{uc}, Li_xP and N_a) were concentrated towards the central region, and the least lithiated species (N_t and N_d) were located near the LiPON interface. And the intermediate lithiation species are reported here for the first time as constituents of the Li-LiPON SEI. Additionally, the presence of Li_3PO_4 in the SEI was confirmed, and its concentration relative to Li_3P appears to be influenced by the LiPON composition. The analysis suggests that a less amount of Li_3PO_4 would form if the LiPON exhibited orthophosphate character, as significant Li_3PO_4 formation is expected to result from the breakdown of O_b structural units. Thus, while the formation mechanisms and final structures of the SEI should be similar for metaphosphate and orthophosphate LiPON compositions, the relative concentrations of species and final thicknesses may differ.

The timescale over which changes occurred during the *in situ* plating experiment differed significantly—particularly between the thin film and bulk-processed LiPON samples—as the cumulative plating time required for passivation increased with sample thickness under a constant electron flood gun current. This underscores an important limitation of the *in situ* lithium plating technique: the low accelerating voltage of the electron flood gun, combined with the high impedance of the investigated sample, can result in an actual applied current density that is significantly lower than the nominal value. In the case of the LiPON sample, the actual current decreases with increasing sample thickness, as a greater portion of the electron beam current is deflected to ground by surface charge accumulation. This also suggests that the properties of the Li-LiPON SEI are not strongly dependent on the applied current density, at least up to 0.15 mA cm^2. When applying this technique to investigate SEI formation on other SSEs, it is advisable to perform calculations beforehand to assess the likelihood of electron beam deflection. The use of electron flood guns with higher accelerating voltages may effectively mitigate this issue. Based on the results, the thicknesses of the formed SEIs after passivation were both on the order of the XPS probing depth (i.e., <17 nm), which is significantly thinner than previously reported values (60-80 nm from TEM studies). However, this thickness is in reasonable agreement with the values obtained from electroanalytical and neutron reflectometry measurements. This discrepancy may be attributed to the stronger electrochemical driving force in the *in situ* plating experiment, which could promote faster passivation, or to the metaphosphate character of the LiPON samples investigated in this study.

The graded structure of the Li-LiPON SEI underpins its high electrochemical stability since it contains a layer of thermodynamically stable compounds in contact with the lithium metal and phases with very low electronic conductivities that provide kinetic stability. Glassy material systems are generally capable of accommodating a broader range of Li^+ concentrations than crystalline compounds, which must meet stringent requirements related to lattice symmetry, strain, and local charge distribution. Another expected benefit of glassy solid electrolytes is their enhanced resistance to lithium dendrite formation and growth, owing to the absence of crystallographic defects. Accordingly, the findings of this investigation support renewed interest in glassy solid electrolytes. Moreover, sputter deposition may accelerate the discovery of new glassy electrolyte materials, as the development of bulk synthesis routes is often complex and challenging.

6
Conclusion and future work

All-solid-state batteries are regarded as one of the most promising next-generation energy storage systems. Replacing the liquid electrolytes in conventional LIBs with SSEs enables direct lithium metal plating, thereby enhancing capacity, facilitating faster charging and discharging (as Li^+ is the sole mobile ion within the SSE), and improving thermal stability and safety. Additionally, the increased mechanical strength of SSEs can, in principle, suppress lithium dendrite penetration, further enhancing performance. However, further modifications and optimisations of SSEs are required to develop materials that exhibit long-term stability against both anodes and cathodes during cycling while maintaining high ionic conductivity. Given the low potential of lithium metal anodes and the limited electrochemical stability of most SSEs, the formation of a interphase is inevitable due to interfacial reactions. This interphase layer plays a crucial role in determining battery performance, making the investigation of its composition, formation mechanism, and evolution essential for the advancement of all-solid-state battery technology.

The development of *in situ* XPS techniques offers significant advantages for investigating the chemical and electrochemical interactions occurring at electrode-electrolyte interfaces. Due to its high surface sensitivity, XPS is particularly well-suited for interphase analysis, as these layers typically range from a few tens to hundreds of nanometres in thickness. This study focuses on the interphase formation at the interfaces between lithium metal and several promising SSE candidates, aiming to provide a deeper understanding of their degradation mechanisms and the stability of the resulting interphase.

In Chapter 3, two SSEs, LGPS and LAGP, with limited stability against lithium metal, were investigated. The results indicate that both SSEs form conductive phases within the interphase; however, LAGP exhibits greater stability, as evidenced by the emergence of a metallic lithium peak. This finding highlights that the stability of the interphase is influenced not only by its composition but also by the fraction and spatial distribution of conductive phases within its structure. The interphase formed between LGPS and lithium metal contains more than 20 vol% of conductive phases (Li_3P and Ge), resulting in a continuous conduction pathway. Consequently, the potential of the interphase aligns with that of the lithium metal anode, leading to continuous interphase growth. In contrast, the SEI formed on LAGP contains less than 11 vol% of conductive phases (Ge), which is insufficient to form a continuous conduction network, thereby enhancing its stability against lithium metal.

As an attempt to probe the SEI evolution kinetics on LAGP, continuous XPS measurements were performed on the LAGP pellet surface following the emergence of the metallic lithium peak by VEP. In principle, the kinetics of SEI evolution can be estimated by analysing the rate of decrease in the peak intensity of the metallic lithium signal, along with the corresponding increase in the intensities of peaks associated with SEI decomposition products. However, accurate quantification of SEI evolution is hindered by the oxidation of lithium metal in the XPS chamber, leading to peak overlap, particularly for oxide-based SSEs. Ideally, a higher vacuum level is preferred to minimise the reaction between lithium metal and other products with the chamber environment. Nonetheless, this approach provides a novel method for assessing the stability of the formed SEI, offering valuable insights into its long-term interfacial behaviour.

Argyrodite SSEs with compositions of Li_6PS_5Cl or close to it have been regarded as some of the most promising sulphide-based SSEs due to their improved stability against lithium metal. However, recent developments in the CTTA technique have shown that SEI growth between Li_6PS_5Cl and lithium metal follows a linear relationship with the square root of time, raising questions about the true stability of the formed SEI. To investigate this further, *in situ* XPS was employed to form the SEI within the XPS chamber, allowing continuous monitoring after the VEP step. The results indicate that the SEI evolves over time through P-containing SEI species, which aligns with first-principles calculations suggesting that both fully lithiated Li_3P and partially lithiated Li_xP phases are thermodynamically unstable in contact with Li_6PS_5Cl. The instability of P-containing species was further demonstrated by *in situ* sputtering of a phosphorus layer, which was subsequently lithiated. XPS results revealed that the lithiated phosphorus layer underwent continuous delithiation when left under open-circuit conditions. Additionally, modified CTTA measurements reveal that SEI growth deviates from the expected linear relationship with the square root of time, further confirming that its evolution is not solely diffusion-limited. This indicates that a artificial layer is necessary to establish a stable SEI, preventing continuous growth driven by reactions between lithiated phosphorus species and Li_6PS_5Cl.

Subsequently, another SSE, LiPON, was investigated using the *in situ* XPS technique for the first time. While LiPON has been widely recognised for its excellent stability against lithium metal, the characteristics of its SEI remain poorly understood. The *in situ* XPS characterisation provides direct observation of the LiPON SEI evolution as lithium deposition progresses. The results was a graded SEI structure, where the most lithiated species (Li_2O, Li_3N, and Li_3P) species are more concentrated near the lithium metal side, the least lithiated species (triple-bridging N and double-bridging N) are close to the LiPON side, and the intermediate lithiated species (apical N, Li_xP, undercoordinated P, and Li_3PO_4) are concentrated in the central region of the SEI. This graded SEI structure ensures that the most lithiated species do not directly interact with the LiPON layer, while the low reduction potential of the LiPON SSE further prevents additional interfacial reactions. This spatial separation plays a crucial role in preventing continuous SEI growth, thereby contributing to the remarkable stability of LiPON against lithium metal. Additionally, a limitation of the *in situ* XPS technique was identified when probing SEI formation on bulk-processed LiPON samples, which exhibit significant resistance. Since the electron neutraliser is specifically designed for charge neutralisation, the energy of the electron beam is limited to approximately 1 eV. Consequently, the maximum achievable ohmic drop across the sample is also restricted. When the sample resistance is substantial, the actual current density deviates from the nominal value calculated as the applied current divided by the sample area. This deviation may affect the SEI formation process and estimation of the SEI thickness. Therefore, careful consideration must be given when comparing the result form different samples, especially for highly resistive samples.

This work provides a thorough understanding of the interfacial phenomena at the anode side in SSB systems, particularly regarding the factors that govern interphase formation, evolution, and stability. Through the combined application of advanced characterisation techniques and systematic investigation, this study successfully deconvoluted complex interfacial chemistries and proposes more accurate reaction mechanisms. The findings highlight the critical roles of interphase composition and spatial distribution in determining the electrochemical performance of SSBs. Moreover, the insights gained offer valuable guidance for the rational design and engineering of next-generation SSEs and SSE|electrode interfaces.

Appendices

A

Appendix

Contents

A.1 Additional figure and information about Chapter 3

A.1.1 Density values of different SEI components obtained from Materials Project

Table A.1: Density values of different SEI component

Sample	Density (g cm^{-3})	Reference
$LiAlO_2$	2.64	[297]
$Li_4P_2O_7$	2.38	[298]
Li_3PO_4	2.54	[299]
Ge	5.28	[300]
Li_3P	1.48	[301]
Li_2S	1.67	[302]

A.1.2 Calculation of lithium deposition rates

Passed charge per minute: $q = It = 20\ \mu A * 1\ min = 3.3 \times 10^{-4}\ mAh$

Mole number of deposited Li:

$n_{Li} = n_{e^-} = \frac{q}{F} = \frac{3.3 \times 10^{-4}\ mAh}{96485\ C\ mol^{-1}} = \frac{3.3 \times 10^{-4} \times 10^{-3} \times 3600\ C}{96485\ C\ mol^{-1}} = 1.24 \times 10^{-8}\ mol$

Mass of deposited lithium metal:

$m_{Li} = M_{Li} \times n_{Li} = 6.941\ g\ mol^{-1} \times 1.23 \times 10^{-8}\ mol = 8.63 \times 10^{-8}\ g$

Volume of deposited lithium: $V_{Li} = \frac{m_{Li}}{\rho_{Li}} = \frac{8.55 \times 10^{-8}\ g}{0.53\ g\ cm^{-3}} = 1.63 \times 10^{-7}\ cm^3$

Lithium deposition thickness per minute:

For LAGP sample: $t_{Li} = \frac{V_{Li}}{A} = \frac{1.63 \times 10^{-7}\ cm^3}{\pi \times (\frac{0.84}{2})^2\ cm^2} = 2.94 \times 10^{-7}\ cm = 2.94\ nm$

For LGPS sample: $t_{Li} = \frac{V_{Li}}{A} = \frac{1.61 \times 10^{-7}\ cm^3}{\pi \times (\frac{0.80}{2})^2\ cm^2} = 3.24 \times 10^{-7}\ cm = 3.24\ nm$

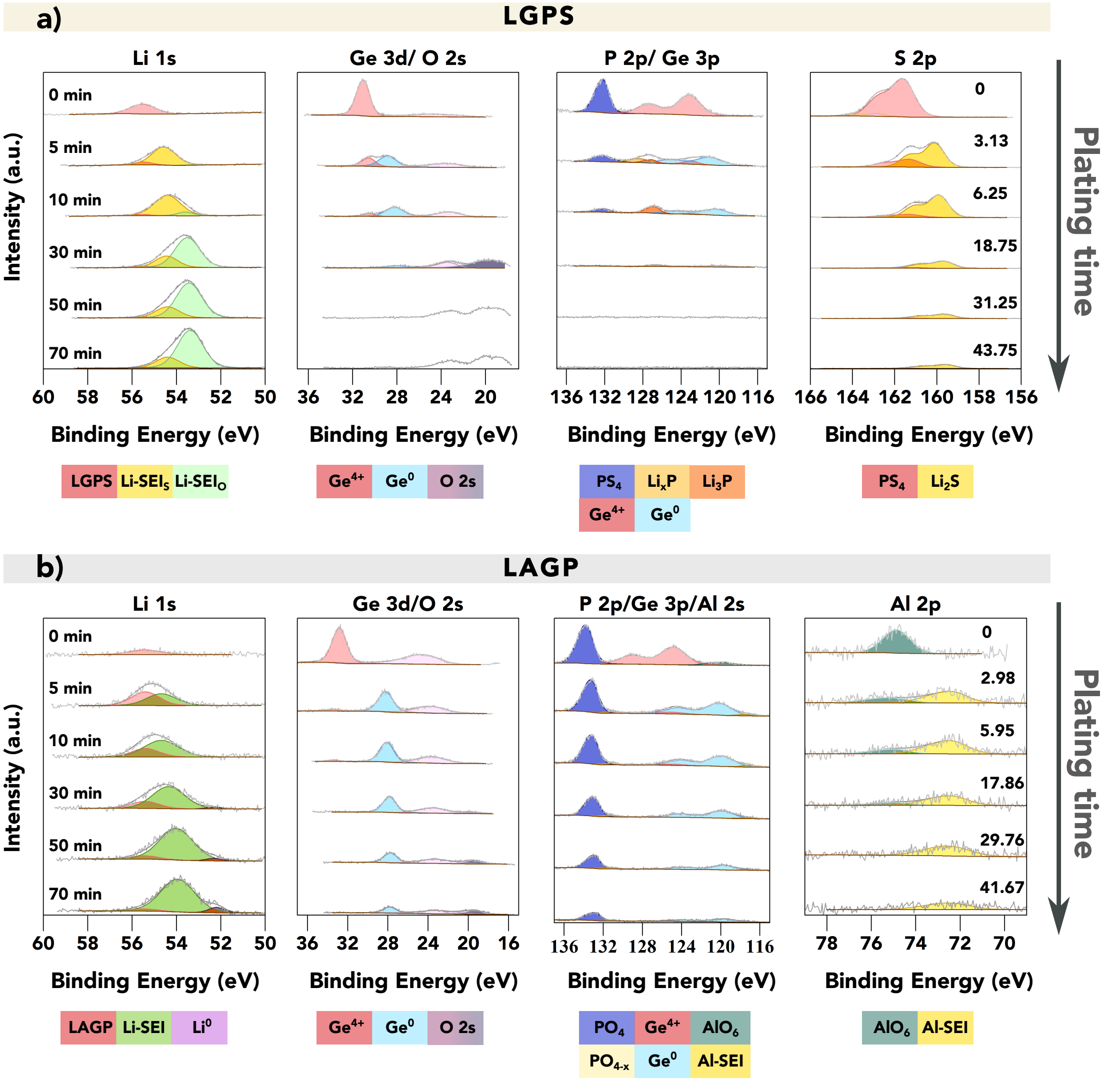

Figure A.1: VEP-XPS investigations of LGPS and LAGP. The plots show a time series of XPS core spectra acquired during VEP-XPS experiments examining the SEI formation on top of (a) LGPS and (b) LAGP. The total Li plating time (electron beam exposure time) is given in the first column, and the passed charge q_A (μAh cm^{-2}), normalised by area, is labelled in the last column. Acquired spectra (grey) are shown along with linear combination fitting results. The individual spectral components are coloured; a key is provided below each group of spectra. For LGPS SE, two Li 1s SEI peaks are labelled in two colours with the subscripts denoting the main non-Li contributing element, as their close BE values make it difficult to deconvolute the peaks accurately. The peak intensities were not normalised. The applied beam current was 20 μA for both samples. Reprinted from Liang *et al.* [162]

Table A.2: Structure information of possible Al-containing SEI decomposition phases, Data retrieved from the Materials Project from database version v2024.12.18[303]

Materials	Structure	Al-O bond length(Å)	Materials project ID
LAGP	AlO_6		
$LiAlO_3$	AlO_6	1.85	mp-1185313
$LiAlO_2$ (trigonal)	AlO_6	1.91	mp-8001
$LiAlO_2$ (tetragonal)	AlO_4	1.75*2; 1.77*2	mp-3427
Li_5AlO_4	AlO_4	1.76-1.78	mp-15960
$LiAl_5O_8$	AlO_6 AlO_4	1.85-1.94 1.78-1.82	mp-530399
$AlPO_4$	AlO_4	1.73; 1.74	mp-5331

Table A.3: Electrical and ionic conductivities of different SEI components at 298 K

Component	Electronic conductivity (S/cm)	Ionic conductivity (S/cm)
Li_2O [304]	10^{-14}	10^{-12}
$AlPO_4$ [305–309]	10^{-8}	low
$LiAlO_2$[231, 310]	insulating	10^{-9}
Li_3PO_4 [106, 311]	10^{-9}	10^{-8}
$Li_4P_2O_7$[312]	10^{-9}(80 °C)	insulating
Li_2S [258, 259]	10^{-9}	10^{-8}
Li_3P [222, 234]	10^{-4}	10^{-4}
Ge[313, 314]	10^{-2}	10^{-2}

Table A.4: Binding energy and full width at half maximum (FWHM) information for the fitted results in Figure 3.1.

	LGPS SSE					
	P 2p3/2		Ge 3p3/2		Al 2s	
E-beam exposure time (min)	Peak position (eV)	FWHM (eV)	Peak position (eV)	FWHM (eV)	Peak position (eV)	FWHM (eV)
0	131.99	1.32	123.07	2.83		
10	131.87	1.31	122.96	2.9		
30	131.79	1.27	122.86	2.81		
60	131.77	1.27	122.82	2.8		
90	131.74	1.31	122.82	2.8		
	LAGP SSE					
0	134.55	1.9	125.16	3.4	120.4	2.83
10	134.48	1.93	125.04	3.4	120.32	2.9
30	134.42	1.91	124.94	3.4	120.29	2.79
60	134.4	1.86	124.9	3.45	120.32	2.76
90	134.42	1.86	124.9	3.41	120.28	2.74

Table A.5: Binding energy and full width at half maximum (FWHM) information for the fitted results in Figure 3.3a

E-beam exposure time (min)	Li 1s-LGPS		Li 1s-SEI$_S$		Li 1s-SEI$_O$	
	Peak position (eV)	FWHM (eV)	Peak position (eV)	FWHM (eV)	Peak position (eV)	FWHM (eV)
0	55.52	1.2				
5	55.5	1	54.57	1.29	53.3	1.44
10	55.5	1	54.4	1.3	53.6	1.3
30	55.52	0.95	54.45	1.19	53.51	1.32
50	55.5	1.02	54.4	1.26	53.43	1.35
70	55.5	1	54.4	1.26	53.38	1.35
	Ge 3d5/2-Ge^{4+}		Ge 3d5/2-Ge^0			
	Peak position (eV)	FWHM (eV)	Peak position (eV)	FWHM (eV)		
0	30.85	1.19				
5	30.35	1.23	28.63	1.72		
10	30.3	1.26	28	1.77		
30			27.86	1.8		
50						
70						
	P 2p3/2-PS$_4^{3-}$		P 2p3/2-Li$_x$P		P 2p3/2-Li$_3$P	
	Peak position (eV)	FWHM (eV)	Peak position (eV)	FWHM (eV)	Peak position (eV)	FWHM (eV)
0	132.05	1.46				
5	132	1.9	128.16	2.31	127	1.14
10	131.99	1.86			126.71	1.34
30	132	1.9			126.53	1.50
50						
70						
	S 2p3/2-PS$_4^{3-}$		S 2p3/2-Li$_2$S			
	Peak position (eV)	FWHM (eV)	Peak position (eV)	FWHM (eV)		
0	161.59	1.24				
5	161.3	1.26	160.1	1.06		
10	161.3	1.32	159.9	1.07		
30	161.3	1.41	159.69	1.14		
50	161.3	1.4	159.65	1.16		
70	161.42	1.4	159.61	1.16		

Table A.6: Binding energy and full width at half maximum (FWHM) information for the fitted results in Figure 3.3b

E-beam exposure time (min)	Li 1s-LAGP		Li 1s-SEI		Li 1s-Li^0	
	Peak position (eV)	FWHM (eV)	Peak position (eV)	FWHM (eV)	Peak position (eV)	FWHM (eV)
0	55.43	1.2				
5	55.4	1	54.68	1.6	52.33	
10	55.4	1	54.68	1.83	52.31	
30	55.4	0.95	54.31	1.83	52.33	0.91
50	55.41	1.02	54.01	1.81	52.31	0.85
70	55.43	1	53.94	1.81	52.2	0.85
	Ge 3d5/2-Ge^{4+}		Ge 3d5/2-Ge^0			
	Peak position (eV)	FWHM (eV)	Peak position (eV)	FWHM (eV)		
0	32.61	1.5				
5	33.29	1.53	28.01	1.5		
10	33.24	1.5	27.9	1.45		
30			27.63	1.35		
50			27.53	1.34		
70			27.6	1.32		
	P 2p3/2-PO$_4^{3-}$		P 2p3/2-Li$_x$P			
	Peak position (eV)	FWHM (eV)	Peak position (eV)	FWHM (eV)		
0	133.62	1.64				
5	133.09	1.5				
10	133.04	1.47				
30	132.92	1.4				
50	132.84	1.4				
70	132.79	1.45				
	Al 2p3/2-AlO$_6$		Al 2p3/2-AlO$_4$			
	Peak position (eV)	FWHM (eV)	Peak position (eV)	FWHM (eV)		
0	74.73	1.6				
5	75	1.6	72.31	1.57		
10	74.85	1.64	72.32	1.67		
30	74.87	1.64	72.3	1.7		
50			72.3	2		
70			72.3	2		

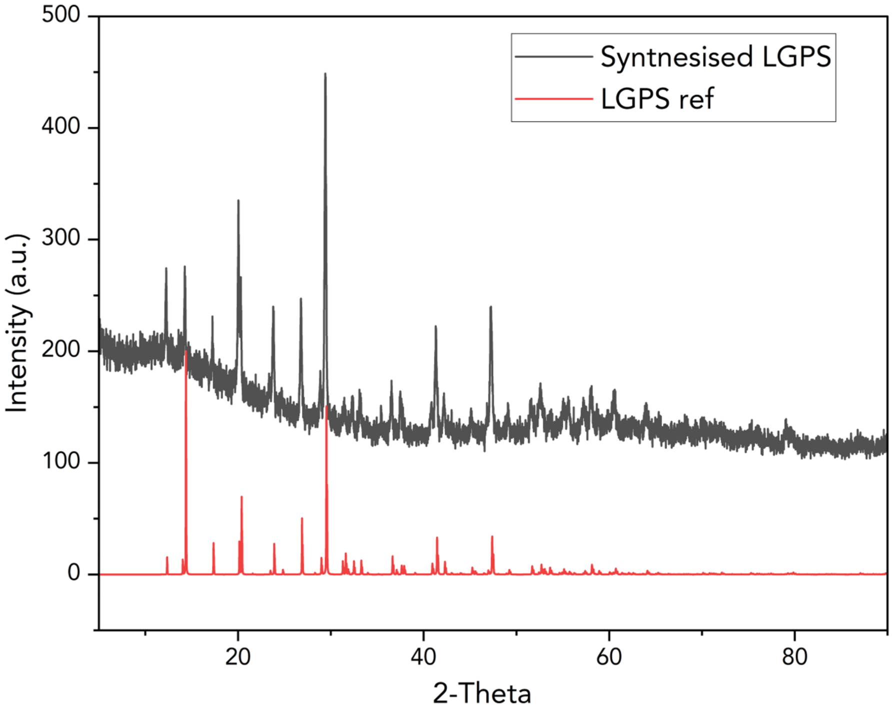

Figure A.2: XRD spectra of the synthesised LGPS powder with ref spectra [315] shown in red colour. Reprinted from Liang *et al.* [162]

A.2 Additional figure and information about Chapter 4

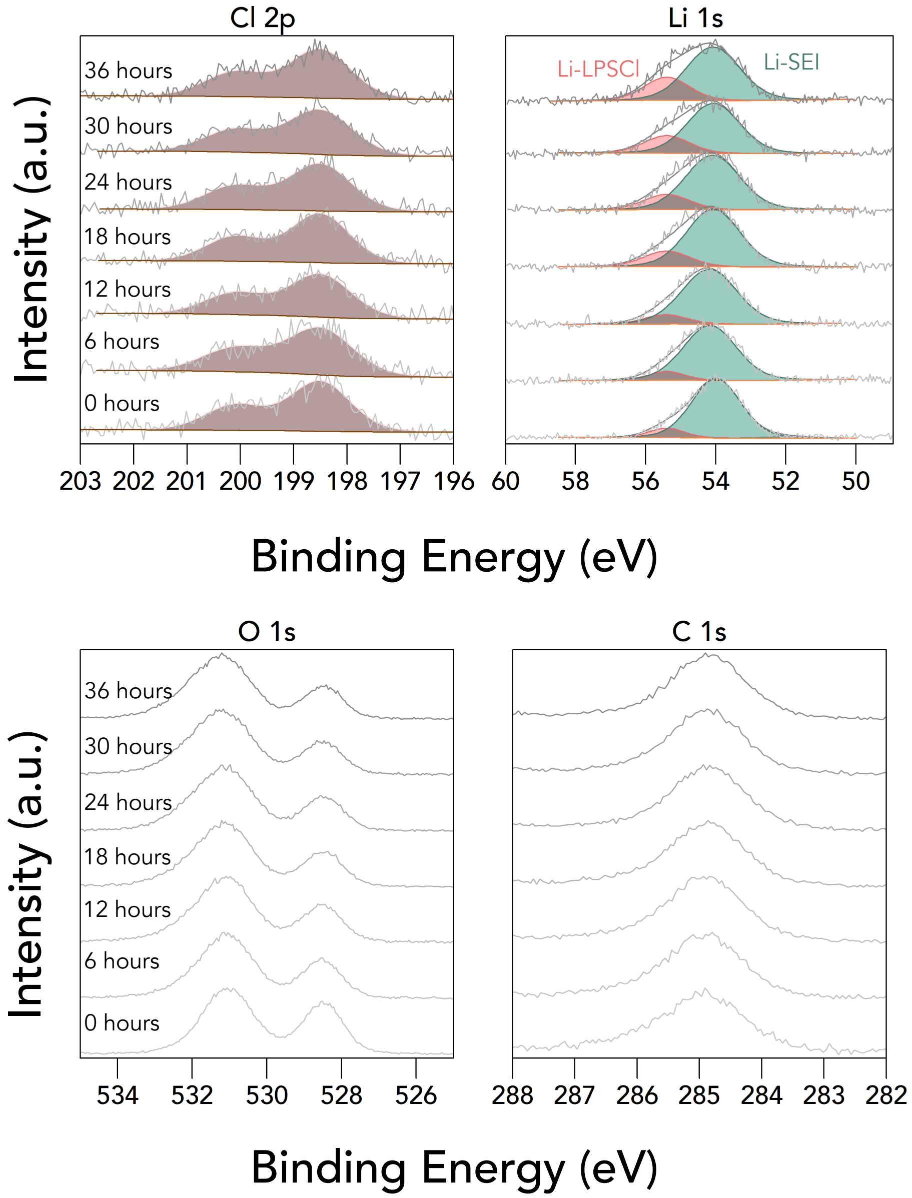

Figure A.3: Supplementary XPS spectra—Cl 2p, Li 1s, O 1s, C 1s—of the Li_6PS_5Cl pellet surface after ∼0.01 mAh cm^2 of lithium was VEP through the Li_6PS_5Cl pellet over 1 hour using an electron beam current of 2.5 μA (∼0.01 mA cm^{-2})

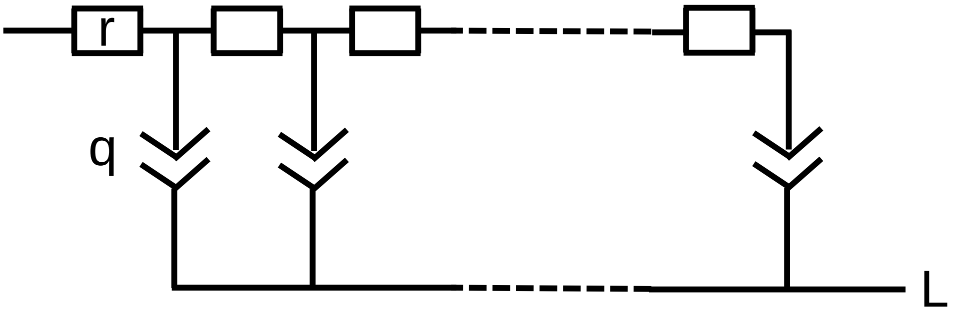

Figure A.4: Equivalent circuit of M_a transmission line element in Figure 4.16. Note: This model more accurately reflects the multi-component nature of the formed SEI.

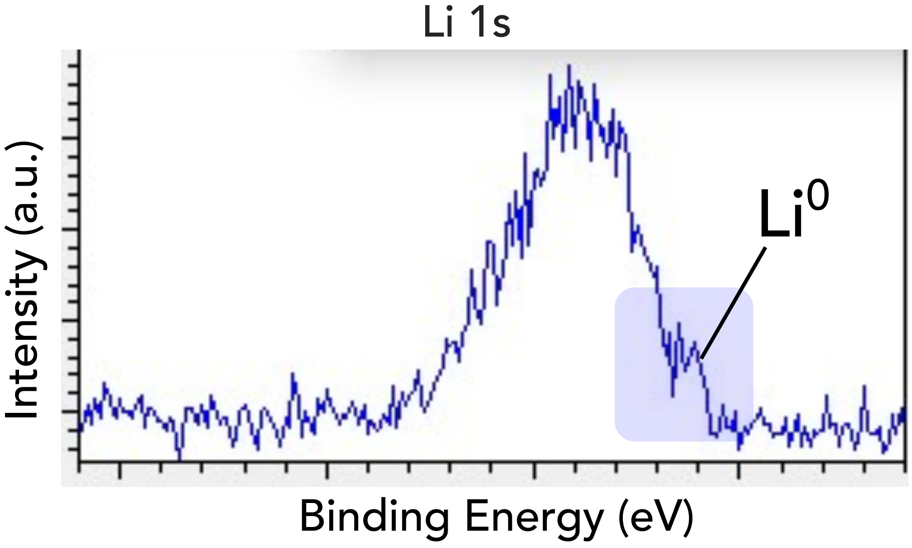

Figure A.5: Li 1s spectra copied from a screenshot after the 4 sweep of Li 1s spectrum after 4100 s of electron beam exposure of the Li_6PS_5Cl with sputtered phosphorus. The set sweep number for Li 1s measurement was 16. Note: The x-axis is intentionally left unlabelled due to the absence of charge calibration.

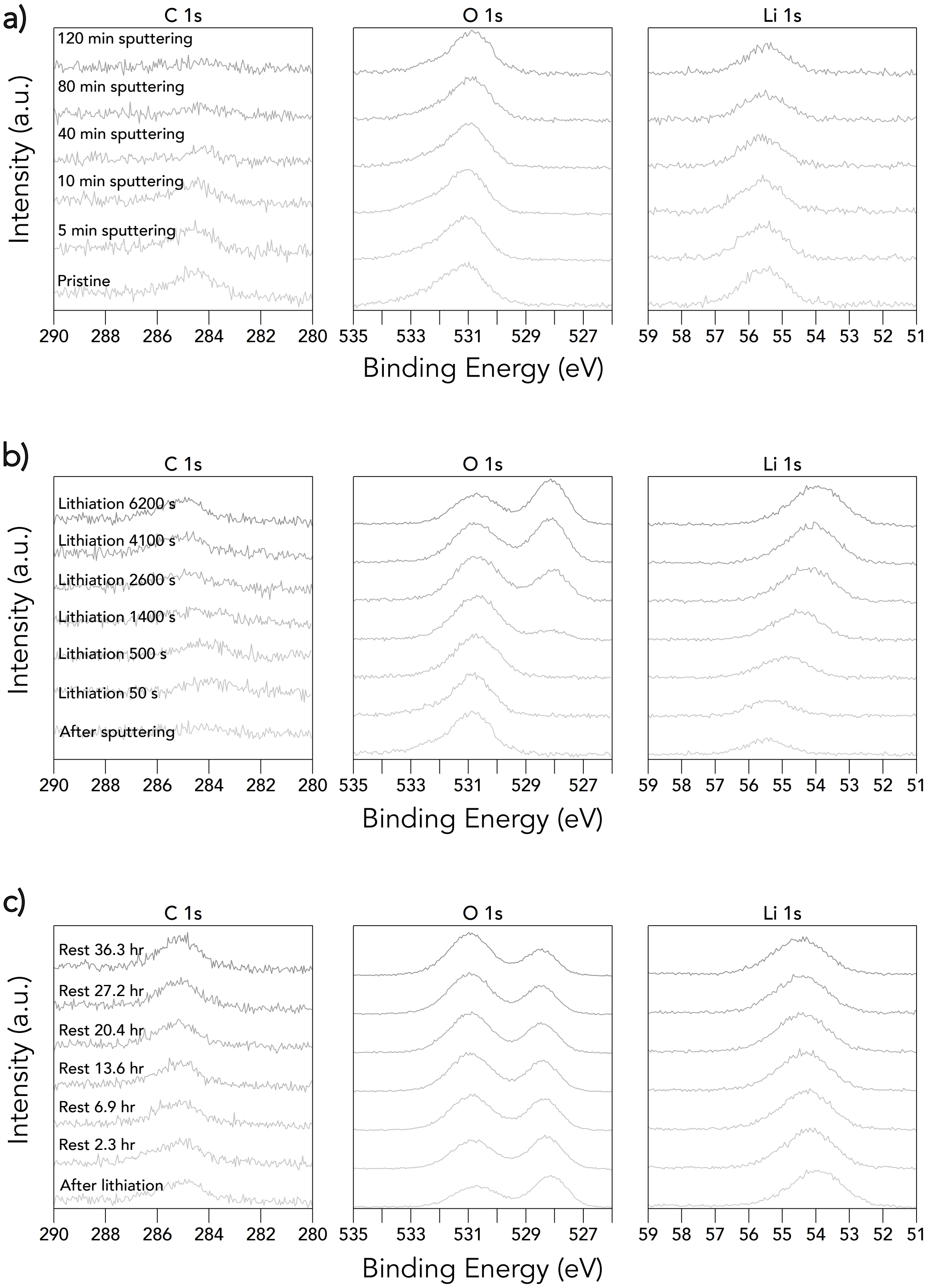

Figure A.6: C 1s, O 1s, and Li 1s XPS spectra of the Li_6PS_5Cl surface during: (a) phosphorus sputtering, (b) subsequent lithiation of the phosphorus layer, and (c) the following resting period.

A.3 Additional figure and information about Chapter 5

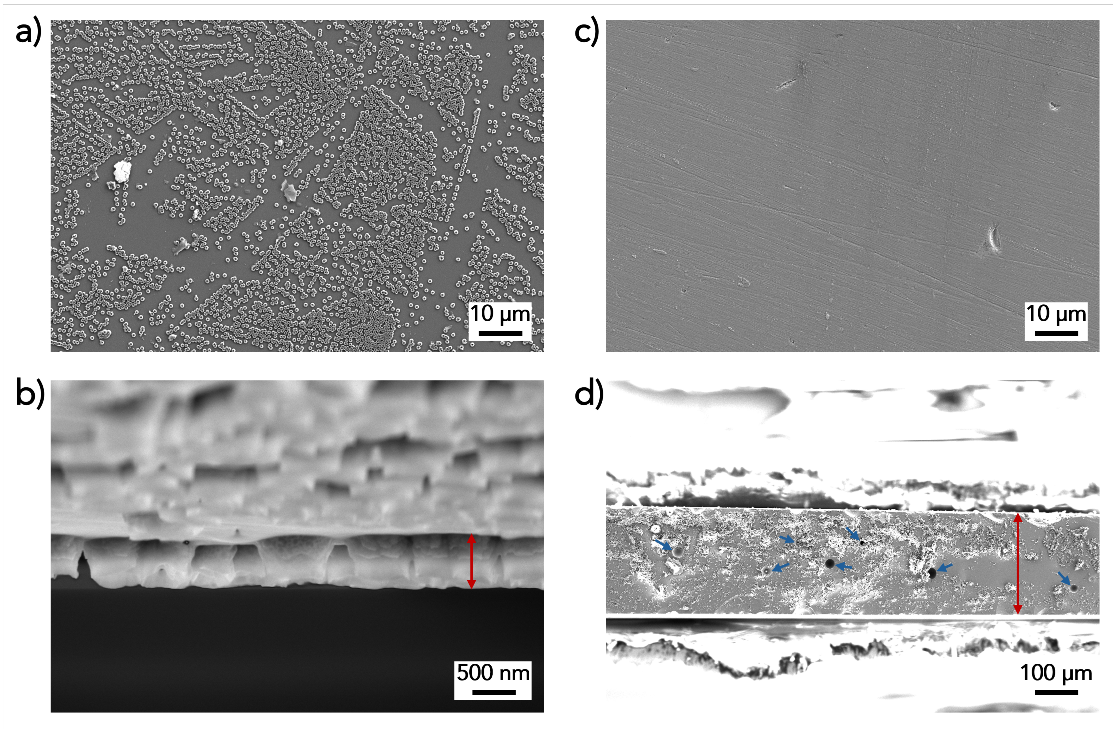

Figure A.7: SEM images of: a) and b) a LiPON film sputter-deposited on undoped silicon at 50 W for 6 hours; and c) and d) a bulk-processed LiPON sample. The cross-sectional views in b) and d) are taken from fracture surfaces. Red arrows indicate the thickness of the LiPON layers, while blue arrows mark the positions of distinct bubbles intersecting the fracture surface. Reprinted from [261]

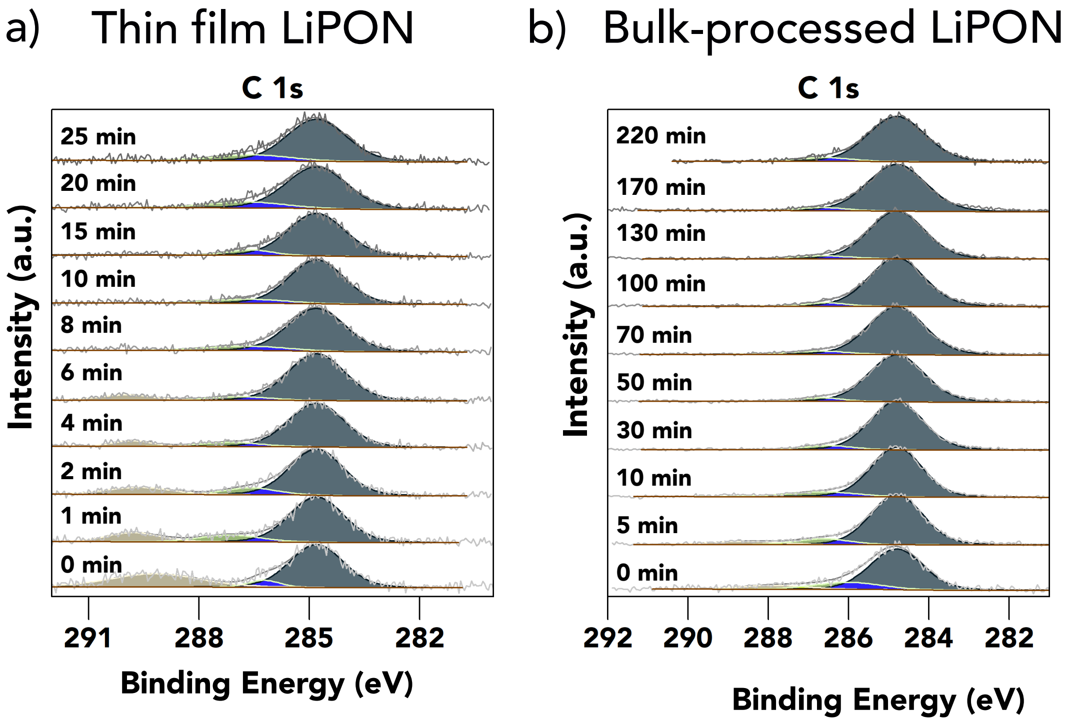

Figure A.8: Time series of C 1s core-level spectra acquired during the *in situ* lithium plating experiments performed on a) a ∼0.6 μm thick LiPON film sample and b) an ∼800 μm bulk-processed LiPON sample

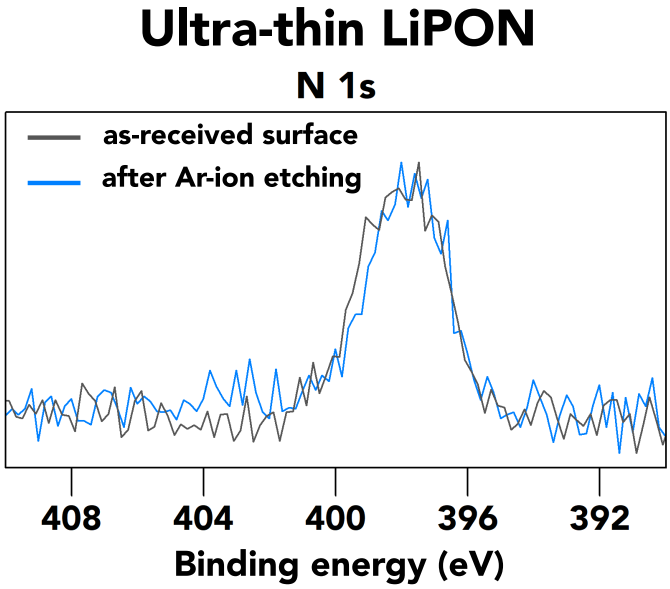

Figure A.9: Normalised N 1s XPS spectra in the binding energy range of 409 eV to 391 eV extracted from survey scans for ultra-thin LiPON film sample before and after Ar-ion etching.

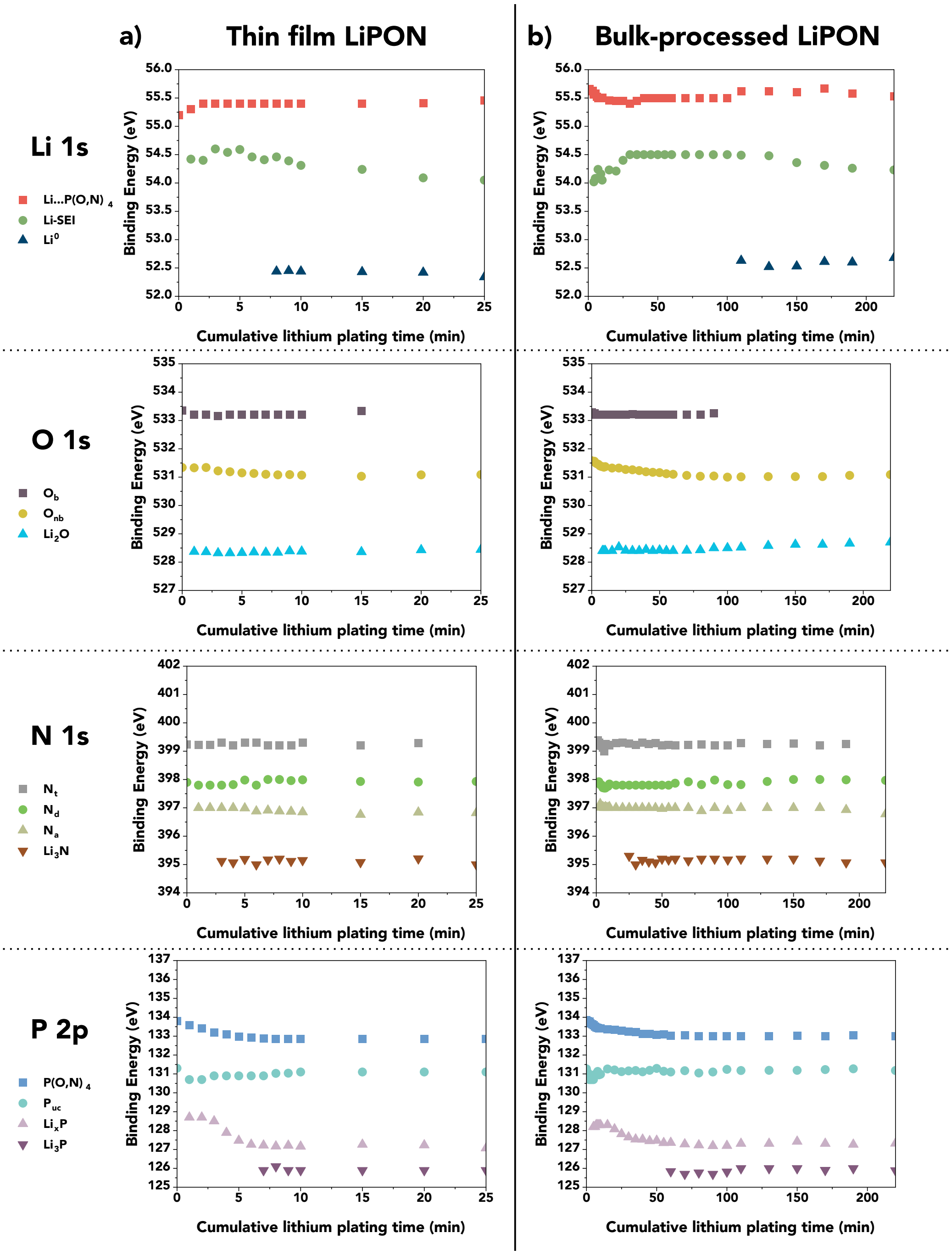

Figure A.10: Evolution of the core-level XPS spectral component binding energies for (a) the ~0.6 μm thick LiPON film sample and (b) the ~800 μm thick bulk-processed LiPON sample during the in situ lithium plating experiments. Reprinted from [261]

Ionic conductivity measurements

Experimental methods

Electrochemical impedance spectroscopy (EIS) was performed on a LiPON film deposited for 6 hours on a stainless steel substrate and a sample of bulk-processed LiPON. Prior to these measurements, pieces of Kapton tape containing a punched 2 mm diameter hole were attached to the top surface of the thin film sample and the parallel surfaces of the bulk-processed sample (aligned to coincide). Nickel electrical contacts were then sputter deposited; the Kapton tape provided the required shadow masking and was subsequently removed. To prevent air exposure during the EIS measurements, each sample was inserted into a laminated aluminium pouch, connected to copper foil electrodes using Kapton tape and sealed under vacuum within an Ar-filled glovebox ([H_2O] and [O_2] $<$ 1 ppm). Standard materials and methods for laboratory-scale pouch cell construction were used.

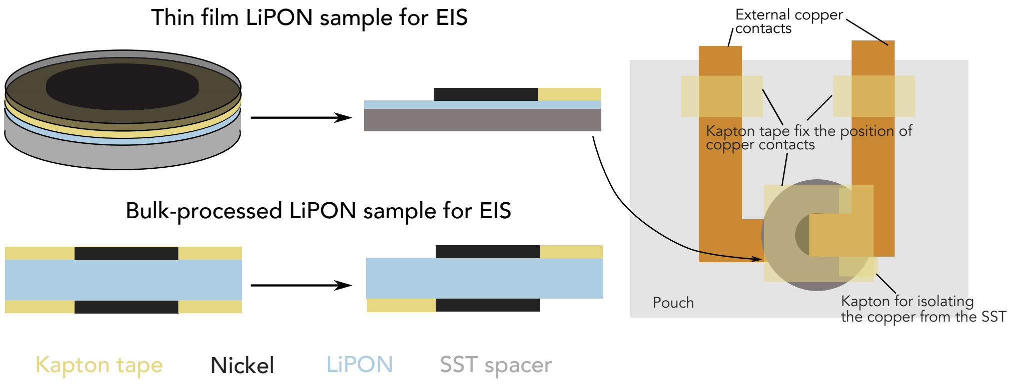

Figure A.11: Schematic diagrams showing the samples fabricated for EIS measurements.

The pouches were removed from the glovebox and connected to an MTZ-35 impedance analyser (BioLogic Science Instruments). Impedance measurements were performed from 35 MHz to 0.1 Hz at an amplitude of 10 mV. On account of its novelty, additional impedance measurements were performed on the bulk-processed LiPON sample at a series of temperatures between 25 and 100 °C for determination of the activation energy. A temperature-controlled climatic chamber (ITS, BioLogic Science Instruments) was used to bring the sample to the required temperatures.

Equivalent circuit models were fitted to the impedance data using ZView software (Scribner Associates Inc.) to determine the ionic resistance of each LiPON sample, thereby enabling calculations of ionic conductivity.

Electrochemical impedance spectroscopy (EIS)

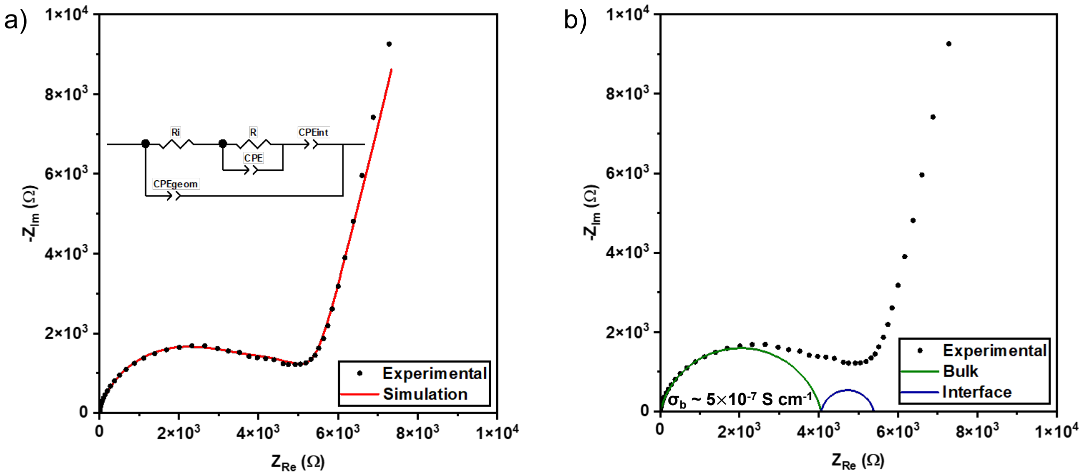

Figure A.12: Nyquist plots from EIS measurements on a ~0.6 μm thick LiPON film at room temperature. For clarity, measurements at frequencies below 16.3 Hz have not been plotted. The equivalent circuit used to simulate the Nyquist plot consists of resistances (R) and constant phase elements (CPE) and is shown in (a) along with the simulation result. 'R_i' corresponds to the ionic resistance of the LiPON electrolyte, 'R' to the resistance of an interfacial layer, 'CPE_{geom}' to the geometric capacitance, 'CPE' to the interfacial layer capacitance and 'CPE_{int}' to the blocking electrode interfacial capacitance. The contributions to the sample impedance are plotted as two semicircles in (b) to enable the magnitudes of the bulk and interfacial layer impedances to be compared. The ionic conductivity of the LiPON (σ_b, calculated from R_i) was ~ 5×10^{-7} S cm^{-1}. Reprinted from [261]

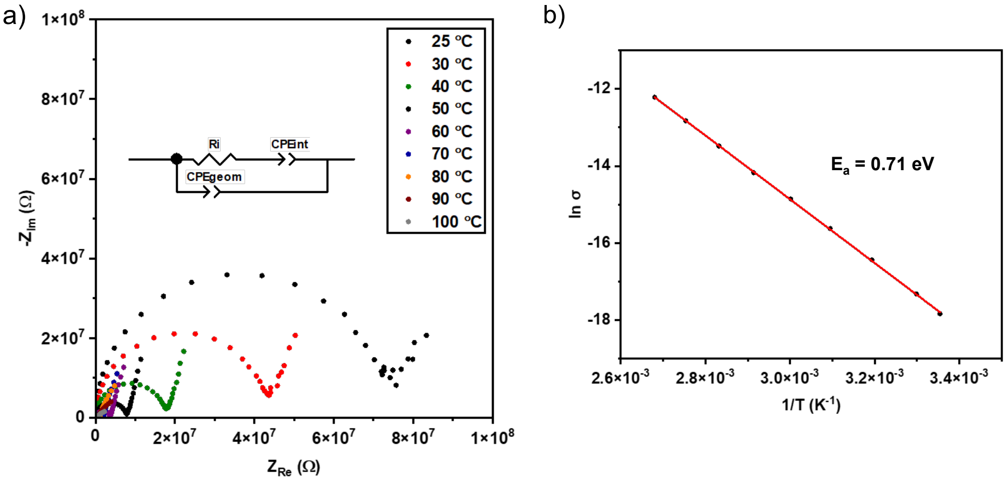

Figure A.13: Results of EIS measurements on a ~400 μm thick bulk-processed LiPON sample at temperatures between 25 °C and 100 °C. The Nyquist plots recorded at each temperature are shown in (a) along with the equivalent circuit used for simulation, which consists of a resistance (R) and constant phase elements (CPE). '$\mathrm{R_i}$' corresponds to the ionic resistance of the LiPON electrolyte, '$\mathrm{CPE_{geom}}$' to the geometric capacitance and '$\mathrm{CPE_{int}}$' to the blocking electrode interfacial capacitance. The values of $\mathrm{R_i}$ determined from simulations of the Nyquist plots were used to calculate the ionic conductivity of the LiPON at each temperature, and these values were used to construct the Arrhenius plot in (b). Least squares fitting was used to fit a linear trendline to the data, and the activation energy for $\mathrm{Li^+}$ conduction was calculated from the gradient. Reprinted from [261]

References

[1] *Energy consumption in the UK 2023 - GOV.UK.* URL: `https://www.gov.uk/government/statistics/energy-consumption-in-the-uk-2023`.

[2] Eelco T C Vogt and Bert M Weckhuysen. “The refinery of the future”. In: *Nature* / 629 (2024).

[3] Sadnan Sakib et al. “Role of battery energy storage systems: A comprehensive review on renewable energy zones integration in weak transmission networks”. In: *Journal of Energy Storage* 128 (Aug. 2025), p. 117223.

[4] Saeed Rahimpour Golroudbary et al. “Global environmental cost of using rare earth elements in green energy technologies”. In: *Science of The Total Environment* 832 (Aug. 2022), p. 155022.

[5] Hernández-López Daniela-Abigail et al. “Life cycle assessment of photovoltaic panels including transportation and two end-of-life scenarios: Shaping a sustainable future for renewable energy”. In: *Renewable Energy Focus* 51 (Oct. 2024), p. 100649.

[6] Belay Teffera, Berhanu Assefa, and Getachew Assefa. “Assessing the life cycle environmental impacts of hydroelectric generation in Ethiopia”. In: *Sustainable Energy Technologies and Assessments* 41 (Oct. 2020), p. 100795.

[7] A.G. Olabi and M.A. Abdelkareem. “Energy storage systems towards 2050”. In: *Energy* 219 (Mar. 2021), p. 119634.

[8] Canan Acar. “A comprehensive evaluation of energy storage options for better sustainability”. In: *International Journal of Energy Research* 42.12 (Oct. 2018), pp. 3732–3746.

[9] Maxwell Woody, Gregory A. Keoleian, and Parth Vaishnav. “Decarbonization potential of electrifying 50% of U.S. light-duty vehicle sales by 2030”. In: *Nature Communications 2023 14:1* 14.1 (Nov. 2023), pp. 1–12.

[10] Zachary P. Cano et al. “Batteries and fuel cells for emerging electric vehicle markets”. In: *Nature Energy 2018 3:4* 3.4 (Apr. 2018), pp. 279–289.

[11] *Energy Technology Perspectives 2023.* Energy Technology Perspectives. OECD, Jan. 2023.

[12] Robert C. Pietzcker et al. “Long-term transport energy demand and climate policy: Alternative visions on transport decarbonization in energy-economy models”. In: *Energy* 64 (Jan. 2014), pp. 95–108.

[13] Lin Chen et al. “Strategies to achieve a carbon neutral society: a review”. In: *Environmental Chemistry Letters* 20.4 (Aug. 2022), pp. 2277–2310.

[14] Jie Deng et al. “Electric Vehicles Batteries: Requirements and Challenges”. In: *Joule* 4.3 (Mar. 2020), pp. 511–515.

[15] Gracia Brückmann, Fabian Willibald, and Victor Blanco. “Battery Electric Vehicle adoption in regions without strong policies”. In: *Transportation Research Part D: Transport and Environment* 90 (Jan. 2021), p. 102615.

[16] Michael Woodward and Hamilton Jamie. *New market. New entrants. New challenges. Battery Electric Vehicles Contents*. Tech. rep. 2017.

[17] Ghassan Zubi et al. “The lithium-ion battery: State of the art and future perspectives”. In: *Renewable and Sustainable Energy Reviews* 89 (June 2018), pp. 292–308.

[18] Fazel Mohammadi and Mehrdad Saif. “A comprehensive overview of electric vehicle batteries market”. In: *e-Prime - Advances in Electrical Engineering, Electronics and Energy* 3 (Mar. 2023), p. 100127.

[19] Yuqing Chen et al. “A review of lithium-ion battery safety concerns: The issues, strategies, and testing standards”. In: *Journal of Energy Chemistry* 59 (Aug. 2021), pp. 83–99.

[20] Zvonimir imi et al. “Battery energy storage technologies overview”. In: *International journal of electrical and computer engineering systems* 12.1 (Apr. 2021), pp. 53–65.

[21] Yang-Kook Sun. “Promising All-Solid-State Batteries for Future Electric Vehicles”. In: *ACS Energy Letters* 5.10 (Oct. 2020), pp. 3221–3223.

[22] Mohamed Houache et al. “On the Current and Future Outlook of Battery Chemistries for Electric VehiclesMini Review”. In: *Batteries* 8.7 (July 2022), p. 70.

[23] J.-M. Tarascon and M. Armand. “Issues and challenges facing rechargeable lithium batteries”. In: *Nature* 414.6861 (Nov. 2001), pp. 359–367.

[24] Mingi Choi, Junepyo Cha, and Jingeun Song. “Impact of lightweighting and driving conditions on electric vehicle energy consumption: In-depth analysis using real-world testing and simulation”. In: *Energy* 323 (May 2025), p. 135746.

[25] Martin Winter, Brian Barnett, and Kang Xu. “Before Li Ion Batteries”. In: *Chemical Reviews* 118.23 (Dec. 2018), pp. 11433–11456.

[26] Valadoula Deimede and Costas Elmasides. “Separators for Lithium-Ion Batteries: A Review on the Production Processes and Recent Developments”. In: *Energy Technology* 3.5 (May 2015), pp. 453–468.

[27] Salvatore Luiso and Peter Fedkiw. “Lithium-ion battery separators: Recent developments and state of art”. In: *Current Opinion in Electrochemistry* 20 (Apr. 2020), pp. 99–107.

[28] James T. Frith, Matthew J. Lacey, and Ulderico Ulissi. “A non-academic perspective on the future of lithium-based batteries”. In: *Nature Communications* 14.1 (Jan. 2023), p. 420.

[29] Akira Yoshino. “The Birth of the Lithium-Ion Battery”. In: *Angewandte Chemie International Edition* 51.24 (June 2012), pp. 5798–5800.

[30] Y. Nishi. “The Dawn of Lithium-Ion Batteries”. In: *Interface magazine* 25 (3 Jan. 2016), pp. 71–74.

[31] Gregory Tzermias et al. “Methodology for the Optimisation of Battery Hybrid Energy Storage Systems for Mass and Volume Using a Power-To-Energy Ratio Analysis”. In: *Batteries* 7 (2 June 2021), p. 37.

[32] *Energy density: Active materials & electrode loading.* URL: `https://www.quantumscape.com/resources/blog/energy-density-active-materials-electrode-loading/`.

[33] *Innolith introduces battery cell for high-power EV applications | Automotive Powertrain Technology International.* URL: `https://www.automotivepowertraintechnologyinternational.com/news/battery-technology/innolith-introduces-battery-cell-for-high-power-ev-applications.html`.

[34] F.M. Nizam Uddin Khan et al. “Maximizing energy density of lithium-ion batteries for electric vehicles: A critical review”. In: *Energy Reports* 9 (Oct. 2023), pp. 11–21.

[35] Thomas Waldmann et al. “18650 vs. 21700 Li-ion cells A direct comparison of electrochemical, thermal, and geometrical properties”. In: *Journal of Power Sources* 472 (Oct. 2020), p. 228614.

[36] F M Nizam Uddin Khan et al. “Design and optimization of lithium-ion battery as an efficient energy storage device for electric vehicles: A comprehensive review”. In: *Journal of Energy Storage* 71 (Nov. 2023), p. 108033.

[37] V.K Bupesh Raja, Ignatius Raja, and Rahul Kavvampally. “Advancements in Battery Technologies of Electric Vehicle”. In: *Journal of Physics: Conference Series* 2129.1 (Dec. 2021), p. 012011.

[38] *FOTW# 1167, January 4, 2021: Median Driving Range of All-Electric Vehicles Tops 250 Miles for Model Year 2020 | Department of Energy.*

[39] International Energy Agency. “Global EV Outlook 2024 Moving towards increased affordability”. In: (2024).

[40] Julio A. Sanguesa et al. “A Review on Electric Vehicles: Technologies and Challenges”. In: *Smart Cities* 4.1 (Mar. 2021), pp. 372–404.

[41] Manuel Weiss et al. “Fast Charging of Lithium-Ion Batteries: A Review of Materials Aspects”. In: *Advanced Energy Materials* 11.33 (Sept. 2021).

[42] Asad A. Naqvi et al. “Aprotic lithium air batteries with oxygen-selective membranes”. In: *Materials for Renewable and Sustainable Energy* 11.1 (Apr. 2022), pp. 33–46.

[43] Matthew Burton et al. “Thin Lithium Metal Anodes for Solid State Batteries: The Case for Scalable Evaporation”. In: *ChemRxiv.* (Sept. 2024).

[44] Matthew Burton et al. “Techno-economic assessment of thin lithium metal anodes for solid-state batteries”. In: *Nature Energy* 10.1 (Dec. 2024), pp. 135–147.

[45] Yongteng Dong et al. “Challenges and Strategies of Fast-Charging Li-Ion Batteries with a Focus on Li Plating”. In: *Energy Material Advances* 5 (Jan. 2024).

[46] Shichang Ma et al. “Investigation of the Optimal Fast Charging Strategy without Lithium Plating for Lithium-Ion Batteries”. In: *Space: Science & Technology* 5 (Jan. 2025).

[47] Logan Pierce and Peter Slowik. *Assessment of U.S. electric vehicle charging needs and announced deployments through 2032.* ICCT Report ID 89. Accessed 14 July 2025. Washington, DC: International Council on Clean Transportation, Mar. 2024.

[48] *Charger Types and Speeds | US Department of Transportation.* URL: `https://www.transportation.gov/rural/ev/toolkit/ev-basics/charging-speeds?utm_source=chatgpt.com`.

[49] Jianhui He, Jingke Meng, and Yunhui Huang. “Challenges and recent progress in fast-charging lithium-ion battery materials”. In: *Journal of Power Sources* 570 (June 2023), p. 232965.

[50] Suting Weng et al. “Kinetic Limits of Graphite Anode for Fast-Charging Lithium-Ion Batteries”. In: *Nano-Micro Letters* 15.1 (Dec. 2023), p. 215.

[51] Jürgen Janek and Wolfgang G. Zeier. “A solid future for battery development”. In: *Nature Energy* 1.9 (Sept. 2016), p. 16141.

[52] Xiqian Yu et al. “Battery Safety: From Lithium-Ion to Solid-State Batteries”. In: *Engineering* 21 (Feb. 2023), pp. 9–14.

[53] Yuejiu Zheng et al. “Study on the correlation between state of charge and coulombic efficiency for commercial lithium ion batteries”. In: *Journal of Power Sources* 289 (Sept. 2015), pp. 81–90.

[54] Albert W. Xiao et al. “Understanding the conversion mechanism and performance of monodisperse FeF2 nanocrystal cathodes”. In: *Nature Materials* 19.6 (2020), pp. 644–654.

[55] Chengcheng Fang et al. “Quantifying inactive lithium in lithium metal batteries”. In: *Nature* 572.7770 (Aug. 2019), pp. 511–515.

[56] Dongping Lu et al. “Failure Mechanism for Fast-Charged Lithium Metal Batteries with Liquid Electrolytes”. In: *Advanced Energy Materials* 5.3 (Feb. 2015), p. 1400993.

[57] Pekka Peljo and Hubert H. Girault. “Electrochemical potential window of battery electrolytes: the HOMOLUMO misconception”. In: *Energy & Environmental Science* 11.9 (2018), pp. 2306–2309.

[58] John S. Newman. *Electrochemical systems.* eng. Ed. by Karen E. Thomas-Alyea. 3rd edition. Hoboken, N.J. ; Wiley, 2004.

[59] John B. Goodenough and Youngsik Kim. “Challenges for rechargeable Li batteries”. In: *Chemistry of Materials* 22.3 (Feb. 2010), pp. 587–603.

[60] Surya Sekhar Manna, Preeti Bhauriyal, and Biswarup Pathak. “Identifying suitable ionic liquid electrolytes for Al dual-ion batteries: role of electrochemical window, conductivity and voltage”. In: *Materials Advances* 1.5 (Aug. 2020), pp. 1354–1363.

[61] E. Peled, D. Golodnitsky, and G. Ardel. “Advanced Model for Solid Electrolyte Interphase Electrodes in Liquid and Polymer Electrolytes”. In: *Journal of The Electrochemical Society* 144.8 (Aug. 1997), pp. L208–L210.

[62] Arie Zaban, Ella Zinigrad, and Doron Aurbach. “Impedance Spectroscopy of Li Electrodes. 4. A General Simple Model of the LiSolution Interphase in Polar Aprotic Systems”. In: *The Journal of Physical Chemistry* 100.8 (Jan. 1996), pp. 3089–3101.

[63] Peng Bai et al. “Transition of lithium growth mechanisms in liquid electrolytes”. In: *Energy & Environmental Science* 9.10 (Oct. 2016), pp. 3221–3229.

[64] E. Peled. “The Electrochemical Behavior of Alkali and Alkaline Earth Metals in Nonaqueous Battery SystemsThe Solid Electrolyte Interphase Model”. In: *Journal of The Electrochemical Society* 126.12 (Dec. 1979), pp. 2047–2051.

[65] Henry Adenusi et al. “Lithium Batteries and the Solid Electrolyte Interphase (SEI)Progress and Outlook”. In: *Advanced Energy Materials* 13.10 (Mar. 2023).

[66] Xiao-Ru Chen et al. “A Coaxial-Interweaved Hybrid Lithium Metal Anode for Long-Lifespan Lithium Metal Batteries”. In: *Advanced Energy Materials* 9.39 (Oct. 2019), p. 1901932.

[67] Qingyu Wang et al. “Confronting the Challenges in Lithium Anodes for Lithium Metal Batteries”. In: *Advanced Science* 8.17 (Sept. 2021).

[68] Charles Monroe and John Newman. “The Impact of Elastic Deformation on Deposition Kinetics at Lithium/Polymer Interfaces”. In: *Journal of The Electrochemical Society* 152.2 (2005), A396.

[69] F. Croce et al. “Nanocomposite polymer electrolytes for lithium batteries”. In: *Nature* 394.6692 (July 1998), pp. 456–458.

[70] Jun Huang et al. “Solid-State Electrolytes for Lithium Metal Batteries: State-of-the-Art and Perspectives”. In: *Advanced Functional Materials* 35 (1 Jan. 2025), p. 2411171.

[71] Tao Yu et al. “Ductile Inorganic Solid Electrolytes for All-Solid-State Lithium Batteries”. In: *Chemical Reviews* 125 (6 Mar. 2025), pp. 3595–3662.

[72] Shuixin Xia et al. “Practical Challenges and Future Perspectives of All-Solid-State Lithium-Metal Batteries”. In: *Chem* 5.4 (Apr. 2019), pp. 753–785.

[73] Rusong Chen et al. “Approaching Practically Accessible Solid-State Batteries: Stability Issues Related to Solid Electrolytes and Interfaces”. In: *Chemical Reviews* 120.14 (July 2020), pp. 6820–6877.

[74] Noriaki Kamaya et al. “A lithium superionic conductor”. In: *Nature Materials* 10.9 (Sept. 2011), pp. 682–686.

[75] Yoshikatsu Seino et al. “A sulphide lithium super ion conductor is superior to liquid ion conductors for use in rechargeable batteries”. In: *Energy and Environmental Science* 7.2 (Jan. 2014), pp. 627–631.

[76] Yuki Kato et al. “High-power all-solid-state batteries using sulfide superionic conductors”. In: *Nature Energy* 1.4 (Mar. 2016), p. 16030.

[77] Teyeb Ould Ely, Dana Kamzabek, and Dhritiman Chakraborty. “Batteries Safety: Recent Progress and Current Challenges”. In: *Frontiers in Energy Research* 7 (Sept. 2019), p. 452480.

[78] Akitoshi Hayashi et al. “Preparation of $Li_2SP_2S_5$ Amorphous Solid Electrolytes by Mechanical Milling”. In: *Journal of the American Ceramic Society* 84.2 (Feb. 2001), pp. 477–79.

[79] Yaxiang Lu et al. “Research and development of advanced battery materials in China”. In: *Energy Storage Materials* 23 (Dec. 2019), pp. 144–153.

[80] Jürgen Janek and Wolfgang G. Zeier. “Challenges in speeding up solid-state battery development”. In: *Nature Energy* 8.3 (Feb. 2023), pp. 230–240.

[81] Wenjia Zhao et al. “Solid-State Electrolytes for Lithium-Ion Batteries: Fundamentals, Challenges and Perspectives”. In: *Electrochemical Energy Reviews* 2.4 (Dec. 2019), pp. 574–605.

[82] Rachna Khurana et al. “Suppression of lithium dendrite growth using cross-linked polyethylene/poly(ethylene oxide) electrolytes: A new approach for practical lithium-metal polymer batteries”. In: *Journal of the American Chemical Society* 136.20 (May 2014), pp. 7395–7402.

[83] Anantha Iyenger Gopalan et al. “Development of electrospun PVdFPAN membrane-based polymer electrolytes for lithium batteries”. In: *Journal of Membrane Science* 325.2 (Dec. 2008), pp. 683–690.

[84] Yoichi Tominaga and Kenta Yamazaki. “Fast Li-ion conduction in poly(ethylene carbonate)-based electrolytes and composites filled with TiO 2 nanoparticles”. In: *Chemical Communications* 50.34 (Apr. 2014), pp. 4448–4450.

[85] Shobhna Choudhary and R. J. Sengwa. “Effect of different anions of lithium salt and MMT nanofiller on ion conduction in melt-compounded PEO-LiX-MMT electrolytes”. In: *Ionics* 18.4 (Apr. 2012), pp. 379–384.

[86] Qian Zhou et al. “Intermolecular Chemistry in Solid Polymer Electrolytes for High-Energy-Density Lithium Batteries”. In: *Advanced Materials* 31.50 (Dec. 2019), p. 1902029.

[87] Yi Zhang et al. “Effects of lithium salts on PEO-based solid polymer electrolytes and their all-solid-state lithium-ion batteries”. In: *Ionics* 28.6 (June 2022), pp. 2751–2758.

[88] Yoshiyuki Inaguma. “Perovskite-Type Lithium-Ion Solid Electrolytes”. In: *Next Generation Batteries.* Singapore: Springer Singapore, Jan. 2021, pp. 187–199.

[89] Yonggang Wang et al. “Antiperovskites with Exceptional Functionalities”. In: *Advanced Materials* 32.7 (Feb. 2020), p. 1905007.

[90] Wei Xia et al. “Antiperovskite Electrolytes for Solid-State Batteries”. In: *Chemical Reviews* 122.3 (Feb. 2022), pp. 3763–3819.

[91] Weike Ye et al. “Deep neural networks for accurate predictions of crystal stability”. In: *Nature Communications 2018 9:1* 9.1 (Sept. 2018), pp. 1–6.

[92] Andreas Rossbach, Frank Tietz, and Steffen Grieshammer. “Structural and transport properties of lithium-conducting NASICON materials”. In: *Journal of Power Sources* 391 (July 2018), pp. 1–9.

[93] Valentina Lacivita, Nongnuch Artrith, and Gerbrand Ceder. “Structural and Compositional Factors That Control the Li-Ion Conductivity in LiPON Electrolytes”. In: *Chemistry of Materials* 30.20 (Oct. 2018), pp. 7077–7090.

[94] M ITOH et al. “High lithium ion conductivity in the perovskite-type compounds”. In: *Solid State Ionics* 70-71.PART 1 (May 1994), pp. 203–207.

[95] Hiroo Kawai and Jun Kuwano. “Lithium Ion Conductivity of A-Site Deficient Perovskite Solid Solution La0.67x Li3x TiO3”. In: *Journal of The Electrochemical Society* 141.7 (July 1994), pp. L78–L79.

[96] Jiayao Lu and Ying Li. “Perovskite-type Li-ion solid electrolytes: a review”. In: *Journal of Materials Science: Materials in Electronics* 32.8 (Apr. 2021), pp. 9736–9754.

[97] A.G. Belous et al. “Investigation into complex oxides of $La_{2/3\text{-}x}Li_{3x}TiO_3$ composition”. In: *Izv. Akad. Nauk SSSR, Neorg. Mater* 23.3 (1987), pp. 470–472.

[98] Zhi Deng et al. “Anti-perovskite materials for energy storage batteries”. In: *InfoMat* 4.2 (Feb. 2022).

[99] Minjie Hou et al. “Challenges and perspectives of NASICON-type solid electrolytes for all-solid-state lithium batteries”. In: *Nanotechnology* 31.13 (Mar. 2020), p. 132003.

[100] Rachel DeWees and Hui Wang. “Synthesis and Properties of NaSICONtype LATP and LAGP Solid Electrolytes”. In: *ChemSusChem* 12.16 (Aug. 2019), pp. 3713–3725.

[101] J. Kuwano and A.R. West. “New Li+ ion conductors in the system, Li4GeO4-Li3VO4”. In: *Materials Research Bulletin* 15.11 (Nov. 1980), pp. 1661–1667.

[102] Y -W. Hu, I. D. Raistrick, and R. A. Huggins. “Ionic Conductivity of Lithium OrthosilicateLithium Phosphate Solid Solutions”. In: *Journal of The Electrochemical Society* 124.8 (Aug. 1977), pp. 1240–1242.

[103] Chongyang Shao et al. “Structure and ionic conductivity of cubic Li7La3Zr2O12 solid electrolyte prepared by chemical co-precipitation method”. In: *Solid State Ionics* 287 (Apr. 2016), pp. 13–16.

[104] Minjea Kim, Hyun Gyu Park, and Kwangjin Park. “A strategy of enhancing the ionic conductivity of Li7La3Zr2O12 under accurate sintering conditions”. In: *Physical Chemistry Chemical Physics* 24.47 (Dec. 2022), pp. 29159–29164.

[105] Muhammad Umair et al. “Oxide Solid Electrolytes in Solid-State Batteries”. In: *Batteries & Supercaps* 2024 (2024), e202400667.

[106] J BATES. “Electrical properties of amorphous lithium electrolyte thin films”. In: *Solid State Ionics* 53-56.PART 1 (July 1992), pp. 647–654.

[107] J B Bates et al. *Fabrication and characterization of amorphous lithium electrolyte thin films and rechargeable thin-film batteries.* Tech. rep. 1993, p. 103.

[108] N DUDNEY. “Sputtering of lithium compounds for preparation of electrolyte thin films”. In: *Solid State Ionics* 53-56 (July 1992), pp. 655–661.

[109] Naoki Suzuki et al. “A lithium phosphorous oxynitride (LiPON) film sputtered from unsintered Li3PO4 powder target”. In: *Solid State Ionics* 191.1 (June 2011), pp. 49–54.

[110] Hong Liu et al. “Priority and Prospect of Sulfide-Based Solid-Electrolyte Membrane”. In: *Advanced Materials* 35.50 (Dec. 2023), p. 2206013.

[111] Prashun Gorai et al. “Defect chemistry of disordered solid-state electrolyte $Li_{10}GeP_2S_{12}$”. In: *Journal of Materials Chemistry A* 8.7 (Feb. 2020), pp. 3851–3858.

[112] A. Gallo-Bueno et al. “Unsupervised machine learning to classify crystal structures according to their structural distortion: A case study on Li-argyrodite solid-state electrolytes”. In: *Energy and AI* 9 (Aug. 2022), p. 100159.

[113] Fuminori Mizuno et al. “New, highly ion-conductive crystals precipitated from Li 2S-P2S5 glasses”. In: *Advanced Materials* 17.7 (Apr. 2005), pp. 918–921.

[114] Yoshitaka Matsushita and Mercouri G. Kanatzidis. “Synthesis and structure of Li4GeS4”. In: *Zeitschrift fur Naturforschung - Section B Journal of Chemical Sciences* 53.1 (Jan. 1998), pp. 23–30.

[115] Philipp Bron et al. “Li10SnP2S12: An affordable lithium superionic conductor”. In: *Journal of the American Chemical Society* 135.42 (Oct. 2013), pp. 15694–15697.

[116] Philipp Bron, Stefanie Dehnen, and Bernhard Roling. “Li10Si0.3Sn0.7P2S12 A low-cost and low-grain-boundary-resistance lithium superionic conductor”. In: *Journal of Power Sources* 329 (Oct. 2016), pp. 530–535.

[117] Yuki Kato et al. “Synthesis, structure and lithium ionic conductivity of solid solutions of Li10(Ge1-xMx)P2S12 (M =Si, Sn)”. In: *Journal of Power Sources* 271 (Dec. 2014), pp. 60–64.

[118] Hans Jörg Deiseroth et al. “Li6PS5X: A Class of Crystalline Li-Rich Solids With an Unusually High Li+ Mobility”. In: *Angewandte Chemie International Edition* 47.4 (Jan. 2008), pp. 755–758.

[119] Parvin Adeli et al. “Boosting Solid-State Diffusivity and Conductivity in Lithium Superionic Argyrodites by Halide Substitution”. In: *Angewandte Chemie - International Edition* 58.26 (June 2019), pp. 8681–8686.

[120] Yinghui Cai et al. “Air Stability and Interfacial Compatibility of Sulfide Solid Electrolytes for Solid-State Lithium Batteries: Advances and Perspectives”. In: *ChemElectroChem* 9.5 (Mar. 2022), e202101479.

[121] Xiaona Li et al. “Progress and perspectives on halide lithium conductors for all-solid-state lithium batteries”. In: *Energy & Environmental Science* 13.5 (2020), pp. 1429–1461.

[122] Tetsuya Asano et al. “Solid Halide Electrolytes with High Lithium-Ion Conductivity for Application in 4 V Class Bulk-Type All-Solid-State Batteries”. In: *Advanced Materials* 30.44 (Nov. 2018).

[123] Xiaona Li et al. “Air-stable Li_3InCl_6 electrolyte with high voltage compatibility for all-solid-state batteries”. In: *Energy & Environmental Science* 12.9 (2019), pp. 2665–2671.

[124] Xiaona Li et al. “Water-Mediated Synthesis of a Superionic Halide Solid Electrolyte”. In: *Angewandte Chemie International Edition* 58.46 (Nov. 2019), pp. 16427–16432.

[125] Luise M. Riegger et al. “Lithium-Metal Anode Instability of the Superionic Halide Solid Electrolytes and the Implications for Solid-State Batteries”. In: *Angewandte Chemie International Edition* 60.12 (Mar. 2021), pp. 6718–6723.

[126] Changhong Wang et al. “A universal wet-chemistry synthesis of solid-state halide electrolytes for all-solid-state lithium-metal batteries”. In: *Science Advances* 7.37 (Sept. 2021).

[127] Yongheum Lee et al. “Lithium Argyrodite Sulfide Electrolytes with High Ionic Conductivity and Air Stability for All-Solid-State Li-Ion Batteries”. In: *ACS Energy Letters* (Dec. 2021), pp. 171–179.

[128] Partha P. Paul et al. “Interfaces in all solid state Li-metal batteries: A review on instabilities, stabilization strategies, and scalability”. In: *Energy Storage Materials* 45 (Mar. 2022), pp. 969–1001.

[129] William D. Richards et al. “Interface Stability in Solid-State Batteries”. In: *Chemistry of Materials* 28.1 (Jan. 2016), pp. 266–273.

[130] Sebastian Wenzel et al. “Interphase formation on lithium solid electrolytesAn in situ approach to study interfacial reactions by photoelectron spectroscopy”. In: *Solid State Ionics* 278 (Oct. 2015), pp. 98–105.

[131] Theodosios Famprikis et al. “Fundamentals of inorganic solid-state electrolytes for batteries”. In: *Nature Materials 2019 18:12* 18.12 (Aug. 2019), pp. 1278–1291.

[132] Claire Villevieille. “Interfaces and Interphases in Batteries: How to Identify and Monitor Them Properly Using Surface Sensitive Characterization Techniques”. In: *Advanced Materials Interfaces* 9.8 (Mar. 2022).

[133] Masahiro Tatsumisago, Motohiro Nagao, and Akitoshi Hayashi. “Recent development of sulfide solid electrolytes and interfacial modification for all-solid-state rechargeable lithium batteries”. In: 1.1 (2013), pp. 17–25.

[134] Zhipeng Zhang et al. “Matching strategy between sulfide solid electrolyte and various anodes: electrolyte modification, interface engineering and electrode structure design”. In: *Energy Storage Materials* 69 (May 2024), p. 103422.

[135] Linan Jia et al. “LiSolid Electrolyte Interfaces/Interphases in All-Solid-State Li Batteries”. In: *Electrochemical Energy Reviews 2024 7:1* 7.1 (Mar. 2024), pp. 1–48.

[136] Yizhou Zhu, Xingfeng He, and Yifei Mo. “Origin of Outstanding Stability in the Lithium Solid Electrolyte Materials: Insights from Thermodynamic Analyses Based on First-Principles Calculations”. In: *ACS Applied Materials & Interfaces* 7.42 (Oct. 2015), pp. 23685–23693.

[137] Yang Lu et al. “Critical Current Density in Solid-State Lithium Metal Batteries: Mechanism, Influences, and Strategies”. In: *Advanced Functional Materials* 31.18 (May 2021).

[138] William S. LePage et al. “Lithium Mechanics: Roles of Strain Rate and Temperature and Implications for Lithium Metal Batteries”. In: *Journal of The Electrochemical Society* 166.2 (Jan. 2019), A89–A97.

[139] Sudarshan Narayanan et al. “In situ and operando characterisation of Li metal Solid electrolyte interfaces”. In: *Current Opinion in Solid State and Materials Science* 26.2 (Apr. 2022), p. 100978.

[140] Xia Hu et al. “External-pressureelectrochemistry coupling in solid-state lithium metal batteries”. In: *Nature Reviews Materials* 9.5 (Apr. 2024), pp. 305–320.

[141] Xin Zhang et al. “Pressure-Driven Interface Evolution in Solid-State Lithium Metal Batteries”. In: *Cell Reports Physical Science* 1.2 (Feb. 2020), p. 100012.

[142] Changhong Wang et al. “Progress and Prospects of Inorganic Solid-State Electrolyte-Based All-Solid-State Pouch Cells”. In: *Advanced Materials* 35.19 (May 2023), p. 2209074.

[143] Chengcheng Fang et al. “Pressure-tailored lithium deposition and dissolution in lithium metal batteries”. In: *Nature Energy* 6.10 (Oct. 2021), pp. 987–994.

[144] Eric Jianfeng Cheng, Asma Sharafi, and Jeff Sakamoto. “Intergranular Li metal propagation through polycrystalline Li6.25Al0.25La3Zr2O12 ceramic electrolyte”. In: *Electrochimica Acta* 223 (Jan. 2017), pp. 85–91.

[145] Yaoyu Ren et al. “Direct observation of lithium dendrites inside garnet-type lithium-ion solid electrolyte”. In: *Electrochemistry Communications* 57 (Aug. 2015), pp. 27–30.

[146] Lauryn L. Baranowski et al. “Multi-Scale Mechanical Behavior of the Li3PS4 Solid-Phase Electrolyte”. In: *ACS Applied Materials and Interfaces* 8.43 (Nov. 2016), pp. 29573–29579.

[147] Thorben Krauskopf et al. “Physicochemical Concepts of the Lithium Metal Anode in Solid-State Batteries”. In: *Chemical Reviews* 120.15 (Aug. 2020), pp. 7745–7794.

[148] Martin Winter. “The Solid Electrolyte Interphase The Most Important and the Least Understood Solid Electrolyte in Rechargeable Li Batteries”. In: *Zeitschrift für Physikalische Chemie* 223.10-11 (Dec. 2009), pp. 1395–1406.

[149] Aiping Wang et al. “Review on modeling of the anode solid electrolyte interphase (SEI) for lithium-ion batteries”. In: 4.1 (Mar. 2018), pp. 1–26.

[150] Gerald Gourdin and Vicky Doan-Nguyen. “In situ, operando characterization of materials for electrochemical devices”. In: *Cell Reports Physical Science* 2.12 (Dec. 2021).

[151] Marm B. Dixit et al. “Status and prospect of *in situ* and *operando* characterization of solid-state batteries”. In: *Energy & Environmental Science* 14.9 (Sept. 2021), pp. 4672–4711.

[152] Yihang Liu, Qiuyun Li, and Ziqiang Wang. “Recent progress about transmission electron microscopy characterizations on lithium-ion batteries”. In: *Journal of Energy Chemistry* 95 (Aug. 2024), pp. 39–56.

[153] Lei Zhang et al. “Recent advances in *in situ* and *operando* characterization techniques for $Li_7La_3Zr_2O_{12}$-based solid-state lithium batteries”. In: *Materials Horizons* 10.5 (May 2023), pp. 1479–1538.

[154] Runze Zhang et al. “The value of in situ/operando Raman spectroscopy in all-solid-state Li batteries”. In: (2023).

[155] Jun Zhao et al. “Size-Dependent Chemomechanical Failure of Sulfide Solid Electrolyte Particles during Electrochemical Reaction with Lithium”. In: *Nano Letters* 22.1 (Jan. 2022), pp. 411–418.

[156] Thorben Krauskopf et al. “The Fast Charge Transfer Kinetics of the Lithium Metal Anode on the Garnet-Type Solid Electrolyte $Li_{6.25}Al_{0.25}La_3Zr_2O_{12}$”. In: *Advanced Energy Materials* 10.27 (July 2020), p. 2000945.

[157] Ziying Wang et al. “In situ STEM-EELS observation of nanoscale interfacial phenomena in all-solid-state batteries”. In: *Nano Letters* 16.6 (2016), pp. 3760–3767.

[158] Chenfei Shen et al. “In Situ and Ex Situ TEM Study of Lithiation Behaviours of Porous Silicon Nanostructures”. In: *Scientific Reports* 6.1 (Aug. 2016), p. 31334.

[159] Hideki Masuda et al. “Dynamically visualizing battery reactions by operando Kelvin probe force microscopy”. In: *Communications Chemistry* 2.1 (Dec. 2019), p. 140.

[160] Natalia Andrea Cañas et al. “Operando X-ray diffraction during battery cycling at elevated temperatures: A quantitative analysis of lithium-graphite intercalationăcompounds”. In: *Carbon* 116 (May 2017), pp. 255–263.

[161] Lingzi Sang et al. “Evolution at the Solid Electrolyte/Gold Electrode Interface during Lithium Deposition and Stripping”. In: *Chemistry of Materials* 29.7 (Apr. 2017), pp. 3029–3037.

[162] Yi Liang et al. “*In situ* XPS investigation of the SEI formed on LGPS and LAGP with metallic lithium”. In: *Chemical Communications* 60.86 (2024), pp. 12597–12600.

[163] Sebastian Wenzel et al. “Direct Observation of the Interfacial Instability of the Fast Ionic Conductor $Li_{10}GeP_2S_{12}$ at the Lithium Metal Anode”. In: *Chemistry of Materials* 28.7 (Apr. 2016), pp. 2400–2407.

[164] Pascal Hartmann et al. “Degradation of NASICON-Type Materials in Contact with Lithium Metal: Formation of Mixed Conducting Interphases (MCI) on Solid Electrolytes”. In: *The Journal of Physical Chemistry C* 117.41 (Oct. 2013), pp. 21064–21074.

[165] Sebastian Wenzel et al. “Interphase formation and degradation of charge transfer kinetics between a lithium metal anode and highly crystalline Li7P3S11 solid electrolyte”. In: *Solid State Ionics* 286.August 2017 (Mar. 2016), pp. 24–33.

[166] Fred A. Stevie and Carrie L. Donley. “Introduction to x-ray photoelectron spectroscopy”. In: *Journal of Vacuum Science & Technology A: Vacuum, Surfaces, and Films* 38.6 (Dec. 2020).

[167] Christopher D. Easton et al. “Practical guides for x-ray photoelectron spectroscopy: Analysis of polymers”. In: *Journal of Vacuum Science & Technology A: Vacuum, Surfaces, and Films* 38.2 (Mar. 2020).

[168] B. Vincent Crist. “XPS guide for insulators: Electron flood gun operation and optimization, surface charging, controlled charging, differential charging, useful FWHMs, problems and solutions, and advice”. In: *Journal of Vacuum Science & Technology A* 42.3 (May 2024), p. 32803.

[169] Justin G Connell. “X-ray photoelectron spectroscopy for batteries”. In: *Batteries*. 2053-2563. IOP Publishing, Dec. 2021, pp. 8–1.

[170] M. P. Seah and W. A. Dench. “Quantitative electron spectroscopy of surfaces: A standard data base for electron inelastic mean free paths in solids”. In: *Surface and Interface Analysis* 1.1 (1979), pp. 2–11.

[171] S. Tanuma, C. J. Powell, and D. R. Penn. “Calculations of electron inelastic mean free paths. IX. Data for 41 elemental solids over the 50 eV to 30 keV range”. In: *Surface and Interface Analysis* 43.3 (Mar. 2011), pp. 689–713.

[172] D. Nanda Gopala Krishna and John Philip. “Review on surface-characterization applications of X-ray photoelectron spectroscopy (XPS): Recent developments and challenges”. In: *Applied Surface Science Advances* 12 (Dec. 2022), p. 100332.

[173] Donald R Baer, Kateryna Artyushkova, and Hagai Cohen. "XPS guide: Charge neutralization and binding energy referencing for insulating samples". In: *J. Vac. Sci. Technol. A* 38 (2020), p. 31204.

[174] Sudarshan Narayanan et al. "Effect of current density on the solid electrolyte interphase formation at the lithiumLi6PS5Cl interface". In: *Nature Communications* 13.1 (Nov. 2022), p. 7237.

[175] Joshua S. Gibson et al. "Gently does it!: *in situ* preparation of alkali metalsolid electrolyte interfaces for photoelectron spectroscopy". In: *Faraday Discussions* 236 (2022), pp. 267–287.

[176] Sebastian Wenzel et al. "Interfacial reactivity and interphase growth of argyrodite solid electrolytes at lithium metal electrodes". In: *Solid State Ionics* 318 (May 2018), pp. 102–112.

[177] George H Major et al. "Practical guide for curve fitting in x-ray photoelectron spectroscopy". In: *Journal of Vacuum Science & Technology A* 38.6 (2020), p. 061203.

[178] Alexander G. Shard. "Practical guides for x-ray photoelectron spectroscopy: Quantitative XPS". In: *Journal of Vacuum Science & Technology A* 38.4 (July 2020), p. 41201.

[179] Paul Van der Heide. *X-ray photoelectron spectroscopy : an introduction to principles and practices.* Wiley, 2012.

[180] J. C. Vickerman and Ian S. Gilmore. *Surface analysis : the principal techniques.* Ed. by J. C. Vickerman and Ian S. Gilmore. 2nd ed. John Wiley & Sons Ltd., 2009.

[181] Edouard Quérel et al. "Operando Characterization and Theoretical Modeling of Metal|Electrolyte Interphase Growth Kinetics in Solid-State Batteries. Part I: Experiments". In: *Chemistry of Materials* 35.3 (Feb. 2023), pp. 853–862.

[182] Soochan Kim et al. "Thin Solid Electrolyte Separators for Solid-State Lithium-Sulfur Batteries". In: *Nano Letters* 22.24 (Dec. 2022), pp. 10176–10183.

[183] Andrew L. Davis et al. "Operando Analysis of Interphase Dynamics in Anode-Free Solid-State Batteries with Sulfide Electrolytes". In: *Journal of The Electrochemical Society* 168.7 (July 2021), p. 070557.

[184] Justin G. Connell et al. "Kinetic versus Thermodynamic Stability of LLZO in Contact with Lithium Metal". In: *Chemistry of Materials* 32.23 (Dec. 2020), pp. 10207–10215.

[185] Kevin N. Wood et al. "Operando X-ray photoelectron spectroscopy of solid electrolyte interphase formation and evolution in Li2S-P2S5 solid-state electrolytes". In: *Nature Communications* 9.1 (June 2018), p. 2490.

[186] Chenfeng Ding et al. "Photoemission spectroscopy of battery materials". In: *Applied Physics Reviews* 11.4 (Dec. 2024), p. 41331.

[187] Fengquan She et al. "Exploring the stability of lithium metal surface by X-ray photoelectron spectroscopy". In: *Vacuum* 211 (May 2023), p. 111893.

[188] Vaithiyalingam Shutthanandan et al. "Applications of XPS in the characterization of Battery materials". In: *Journal of Electron Spectroscopy and Related Phenomena* 231 (Feb. 2019), pp. 2–10.

[189] Brian R. Strohmeier. “An ESCA method for determining the oxide thickness on aluminum alloys”. In: *Surface and Interface Analysis* 15.1 (1990), pp. 51–56.

[190] Alice J. Merryweather et al. “Operando optical tracking of single-particle ion dynamics in batteries”. In: *Nature* 594.7864 (June 2021), pp. 522–528.

[191] Paul E Larson and Michael A. Kelly. “Europäisches Patentamt European Patent Office *EP000848247B1*”. 1997.

[192] N. Fleck et al. “Characterization techniques in energy generation and storage”. In: *Emerging Nanotechnologies for Renewable Energy*. Elsevier, Jan. 2021, pp. 259–285.

[193] *File:Electron-matter interaction volume and various types of signal generated - v2.svg - Wikimedia Commons*.

[194] *EDX Analysis - SEM - EDS Analysis - Advancing Materials*. URL: `https://www.thermofisher.com/blog/materials/edx-analysis-with-sem-how-does-it-work/`.

[195] *X-ray diffraction | Definition, Diagram, Equation, & Facts | Britannica*. URL: `https://www.britannica.com/science/X-ray-diffraction`.

[196] Andrei A. Bunaciu, Elena gabriela Udritioiu, and Hassan Y. Aboul-Enein. “X-Ray Diffraction: Instrumentation and Applications”. In: *Critical Reviews in Analytical Chemistry* 45.4 (Oct. 2015), pp. 289–299.

[197] Martin Trunec and Karel Maca. “Advanced Ceramic Processes”. In: *Advanced Ceramics for Dentistry*. Elsevier, Jan. 2014, pp. 123–150.

[198] Burak Aktekin et al. “SEI growth on Lithium metal anodes in solid-state batteries quantified with coulometric titration time analysis”. In: *Nature Communications* 14.1 (Oct. 2023), p. 6946.

[199] Shangshang Wang et al. “Electrochemical impedance spectroscopy”. In: *Nature Reviews Methods Primers* 1.1 (June 2021), p. 41.

[200] Xin-Bing Cheng et al. “Toward Safe Lithium Metal Anode in Rechargeable Batteries: A Review.” In: *Chemical reviews* 117.15 (Aug. 2017), pp. 10403–10473.

[201] Dingchang Lin, Yayuan Liu, and Yi Cui. “Reviving the lithium metal anode for high-energy batteries”. In: *Nature Nanotechnology* 12.3 (Mar. 2017), pp. 194–206.

[202] Jun Lu et al. “High-Performance Anode Materials for Rechargeable Lithium-Ion Batteries”. In: *Electrochemical Energy Reviews* 1.1 (Mar. 2018), pp. 35–53.

[203] Abhik Banerjee et al. “Interfaces and Interphases in All-Solid-State Batteries with Inorganic Solid Electrolytes”. In: *Chemical Reviews* 120.14 (July 2020), pp. 6878–6933.

[204] Syed Atif Pervez et al. “Interface in Solid-State Lithium Battery: Challenges, Progress, and Outlook”. In: *ACS Applied Materials & Interfaces* 11.25 (June 2019), pp. 22029–22050.

[205] Yan-Yun Sun, Feng Li, and Pei-Yu Hou. “Research progress on the interfaces of solid-state lithium metal batteries”. In: *Journal of Materials Chemistry A* 9.15 (Apr. 2021), pp. 9481–9505.

[206] Hee-Dae Lim et al. “A review of challenges and issues concerning interfaces for all-solid-state batteries”. In: *Energy Storage Materials* 25 (Mar. 2020), pp. 224–250.

[207] Marlena Uitz et al. “Ion dynamics in solid electrolytes for lithium batteries”. In: *Journal of Electroceramics* 38.2-4 (June 2017), pp. 142–156.

[208] John Christopher Bachman et al. “Inorganic Solid-State Electrolytes for Lithium Batteries: Mechanisms and Properties Governing Ion Conduction”. In: *Chemical Reviews* 116.1 (Jan. 2016), pp. 140–162.

[209] P. P.R.M.L. Harks, F. M. Mulder, and P. H.L. Notten. “In situ methods for Li-ion battery research: A review of recent developments”. In: *Journal of Power Sources* 288 (Aug. 2015), pp. 92–105.

[210] Dongqing Liu et al. “Review of Recent Development of In Situ/Operando Characterization Techniques for Lithium Battery Research”. In: *Advanced Materials* 31.28 (2019), pp. 1–57.

[211] Felix Walther et al. “Visualization of the Interfacial Decomposition of Composite Cathodes in Argyrodite-Based All-Solid-State Batteries Using Time-of-Flight Secondary-Ion Mass Spectrometry”. In: *Chemistry of Materials* 31.10 (May 2019), pp. 3745–3755.

[212] Svenja K. Otto et al. “In Situ Investigation of Lithium MetalSolid Electrolyte Anode Interfaces with ToF-SIMS”. In: *Advanced Materials Interfaces* 9.13 (May 2022), p. 2102387.

[213] Cheng Ma et al. “Interfacial Stability of Li MetalSolid Electrolyte Elucidated via in Situ Electron Microscopy”. In: *Nano Letters* 16.11 (Nov. 2016), pp. 7030–7036.

[214] Feng Liang et al. “Designing inorganic electrolytes for solid-state Li-ion batteries: A perspective of LGPS and garnet”. In: *Materials Today* 50 (Nov. 2021), pp. 418–441.

[215] Andrea Paolella et al. “Understanding the Reactivity of a Thin Li1.5Al0.5Ge1.5(PO4)3 Solid-State Electrolyte toward Metallic Lithium Anode”. In: *Advanced Energy Materials* 10.32 (Aug. 2020), p. 2001497.

[216] Linchun He et al. “Failure Mechanism and Interface Engineering for NASICON-Structured All-Solid-State Lithium Metal Batteries”. In: *ACS Applied Materials & Interfaces* 11.23 (June 2019), pp. 20895–20904.

[217] Jared Tippens et al. “Visualizing Chemomechanical Degradation of a Solid-State Battery Electrolyte”. In: *ACS Energy Letters* 4.6 (June 2019), pp. 1475–1483.

[218] Zizheng Tong et al. “Degradation of a $Li_{1.5}Al_{0.5}Ge_{1.5}(PO_4)_3$ -Based Solid-State Li-Metal Battery: Corrosion of $Li_{1.5}Al_{0.5}Ge_{1.5}(PO_4)_3$ against the Li-Metal Anode”. In: *ACS Applied Energy Materials* 5.9 (Sept. 2022), pp. 11694–11704.

[219] Rui Iwasaki et al. “Weak Anisotropic Lithium-Ion Conductivity in Single Crystals of $Li_{10}GeP_2S_{12}$”. In: *Chemistry of Materials* 31.10 (May 2019), pp. 3694–3699.

[220] John A. Lewis et al. “Interphase Morphology between a Solid-State Electrolyte and Lithium Controls Cell Failure”. In: *ACS Energy Letters* 4.2 (Feb. 2019), pp. 591–599.

[221] Qipeng Yu et al. “Constructing Effective Interfaces for $Li_{1.5}Al_{0.5}Ge_{1.5}(PO_4)_3$ Pellets To Achieve Room-Temperature Hybrid Solid-State Lithium Metal Batteries”. In: *ACS Applied Materials & Interfaces* 11.10 (Mar. 2019), pp. 9911–9918.

[222] Jing Li et al. “Mixed ion-electron conducting Li_3P for efficient cathode prelithiation of all-solid-state Li-ion batteries”. In: *SmartMat* 4.5 (Oct. 2023), e1200.

[223] Neal Fairley et al. “Systematic and collaborative approach to problem solving using X-ray photoelectron spectroscopy”. In: *Applied Surface Science Advances* 5 (Sept. 2021), p. 100112.

[224] R. F. Egerton. “Choice of operating voltage for a transmission electron microscope”. In: *Ultramicroscopy* 145 (Oct. 2014), pp. 85–93.

[225] R. F. Egerton. “Radiation damage to organic and inorganic specimens in the TEM”. In: *Micron* 119 (Apr. 2019), pp. 72–87.

[226] Linchun He et al. “Electromechanical Failure of NASICON-Type Solid-State Electrolyte-Based All-Solid-State Li-Ion Batteries”. In: *Cite This: Chem. Mater* 33 (2021), pp. 6841–6852.

[227] Habin Chung and Byoungwoo Kang. “Mechanical and Thermal Failure Induced by Contact between a $Li_{1.5}Al_{0.5}Ge_{1.5}(PO_4)_3$ Solid Electrolyte and Li Metal in an All Solid-State Li Cell”. In: *Chemistry of Materials* 29.20 (Oct. 2017), pp. 8611–8619.

[228] Qiang Zhao et al. “A facile, scalable, high stability Lithium metal anode”. In: *SusMat* 2.1 (Feb. 2022), pp. 104–112.

[229] Yan Wu et al. “Enhancing the Li-ion storage performance of graphite anode material modified by LiAlO2”. In: *Electrochimica Acta* 235 (May 2017), pp. 463–470.

[230] Jin Li et al. “Stabilizing the LAGP/Li interface and in situ visualizing the interfacial structure evolution for high-performance solid-state lithium metal batteries”. In: *Energy & Environmental Science* 17 (15 July 2024), pp. 5521–5531.

[231] Sylvio Indris et al. “Li ion dynamics in a LiAlO 2 single crystal studied by 7Li NMR spectroscopy and conductivity measurements”. In: *Journal of Physical Chemistry C* 116.27 (July 2012), pp. 14243–14247.

[232] Qiwei Hu et al. “Li ion diffusion in LiAlO2 investigated by Raman spectroscopy”. In: *Solid State Sciences* 37 (Nov. 2014), pp. 103–107.

[233] Manuel Weiss et al. “Correlating Transport and Structural Properties in $Li_{1+x}Al_xGe_{2\text{-}x}(PO_4)_3$ (LAGP) Prepared from Aqueous Solution”. In: *ACS Applied Materials & Interfaces* 10.13 (Apr. 2018), pp. 10935–10944.

[234] Christoph D. Alt et al. “Quantifying multiphase SEI growth in sulfide solid electrolytes”. In: *Joule* 8.10 (Oct. 2024), pp. 2755–2776.

[235] Harvey Scher and Richard Zallen. “Critical Density in Percolation Processes”. In: *The Journal of Chemical Physics* 53.9 (Nov. 1970), pp. 3759–3761.

[236] Bertan Ozdogru et al. “Coupling between Voltage Profiles and Mechanical Deformations in LAGP Solid Electrolyte during Li Plating and Stripping”. In: *ACS Applied Energy Materials* 5.3 (Mar. 2022), pp. 2655–2662.

[237] Zhen Liu et al. “Temporal Evolution of Surface Contamination under Ultra-high Vacuum”. In: *Langmuir* 38.3 (Jan. 2022), pp. 1252–1258.

[238] *ESCALAB 250Xi XPS Microprobe.* URL: `https://www.jp.xpssimplified.com/escalab_250xi.php?utm_source=chatgpt.com`.

[239] *XPS System with UHV and High Pressure Prepration | SPECS.* URL: `https://www.specs-group.com/specs/products/detail/xps-system-with-uhv-and-high-pressure-prepration/`.

[240] *Standard PES systems.* URL: `https://prevac.eu/product/standard-pes-systems/`.

[241] *PHI 5600 XPS system Bakeout procedure to improve base vacuum | RBD TechSpot.* URL: `https://www.rbdinstruments.com/blog/bake-out-procedure-to-improve-base-vacuum/`.

[242] *Vacuum bake out: its importance and implementation - Leybold USA.* URL: `https://www.leybold.com/en-us/knowledge/blog/vacuum-bake-out?utm_source=chatgpt.com`.

[243] Yijie Liu et al. “Germanium Thin Film Protected Lithium Aluminum Germanium Phosphate for Solid-State Li Batteries”. In: *Advanced Energy Materials* 8.16 (June 2018), p. 1702374.

[244] Yue Zhang et al. “Progress and Perspectives of Lithium Aluminum Germanium Phosphate-Based Solid Electrolytes for Lithium Batteries”. In: *Advanced Functional Materials* 33.32 (Aug. 2023), p. 2300973.

[245] Shuo Wang et al. “High-Conductivity Argyrodite Li 6 PS 5 Cl Solid Electrolytes Prepared via Optimized Sintering Processes for All-Solid-State Lithium-Sulfur Batteries”. In: *ACS Applied Materials and Interfaces* 10.49 (Dec. 2018), pp. 42279–42285.

[246] Svenja-K. Otto et al. “In-Depth Characterization of Lithium-Metal Surfaces with XPS and ToF-SIMS: Toward Better Understanding of the Passivation Layer”. In: *Chemistry of Materials* 33.3 (Feb. 2021), pp. 859–867.

[247] Matthew Burton et al. “The Role of Phosphorous in the Solid Electrolyte Interphase of Argyrodite Solid Electrolytes”. In: *ChemRxiv.* (Jan. 2025).

[248] Sebastian Wenzel. “Thermodynamic and kinetic instability of inorganic solid electrolytes at lithium and sodium metal electrodes”. PhD thesis. Dissertation, GieSSen, Justus-Liebig-Universität, 2016.

[249] Hermann. Schmalzried. *Chemical kinetics of solids.* Weinheim ; VCH, 1995.

[250] G NAZRI. “Preparation, structure and ionic conductivity of lithium phosphide”. In: *Solid State Ionics* 34.1-2 (Apr. 1989), pp. 97–102.

[251] Alexey P. Maltsev et al. “Ionic Conductivity of Lithium Phosphides”. In: *Crystals 2023, Vol. 13, Page 756* 13.5 (May 2023), p. 756.

[252] Windhu Griyasti Suci et al. “Review of various sulfide electrolyte types for solid-state lithium-ion batteries”. In: *Open Engineering* 12.1 (Jan. 2022), pp. 409–423.

[253] Rui Wang et al. “Influence of Conductive additives on the stability of red phosphorus-carbon anodes for sodium-ion batteries”. In: *Scientific Reports 2019 9:1* 9.1 (Jan. 2019), pp. 1–6.

[254] Jiangxuan Song et al. “Chemically bonded phosphorus/graphene hybrid as a high performance anode for sodium-ion batteries”. In: *Nano Letters* 14.11 (Nov. 2014), pp. 6329–6335.

[255] Isaac Capone et al. “Electrochemo-Mechanical Properties of Red Phosphorus Anodes in Lithium, Sodium, and Potassium Ion Batteries”. In: *Matter* (2020), pp. 1–17.

[256] Maheshwar Sharon and R. R. Pradhananga. “Ionic conductivity of pure and Ca2+- and Sr2+-doped single crystals of LiCl”. In: *Journal of Solid State Chemistry* 40.1 (Nov. 1981), pp. 20–27.

[257] R. D. Armstrong and K. Landles. “Lithium ion conducting solids for ambient applications”. In: *Journal of Applied Electrochemistry* 12.5 (Sept. 1982), pp. 533–535.

[258] Sunho Choi et al. “Carbon-coated Li2S cathode for improving the electrochemical properties of an all-solid-state lithium-sulfur battery using Li2S-P2S5 solid electrolyte”. In: *Ceramics International* 44.7 (May 2018), pp. 7450–7453.

[259] Takashi Hakari, Akitoshi Hayashi, and Masahiro Tatsumisago. “Highly Utilized Lithium Sulfide Active Material by Enhancing Conductivity in All-solid-state Batteries”. In: *Chem. Lett* 44 (2015), pp. 1664–1666.

[260] Ye Hu et al. “Stable Cycling of Phosphorus Anode for Sodium-Ion Batteries through Chemical Bonding with Sulfurized Polyacrylonitrile”. In: *Advanced Functional Materials* 28.23 (June 2018).

[261] Stephen J. Turrell et al. “Origin of Stability in the Solid Electrolyte Interphase formed between Lithium and Lithium Phosphorus Oxynitride”. In: *Chemistry of Materials* (Apr. 2025).

[262] Roger Marchand. “Nitrogen-containing phosphate glasses”. In: *Journal of Non-Crystalline Solids* 56.1-3 (July 1983), pp. 173–178.

[263] Jed D. LaCoste, Andriy Zakutayev, and Ling Fei. “A Review on Lithium Phosphorus Oxynitride”. In: *The Journal of Physical Chemistry C* 125.7 (Feb. 2021), pp. 3651–3667.

[264] Zane A. Grady et al. “Emerging Role of Non-crystalline Electrolytes in Solid-State Battery Research”. In: *Frontiers in Energy Research* 8 (Sept. 2020), p. 557870.

[265] Valentina Lacivita et al. “Resolving the Amorphous Structure of Lithium Phosphorus Oxynitride (Lipon)”. In: *Journal of the American Chemical Society* 140.35 (Sept. 2018), pp. 11029–11038.

[266] B. Wang et al. “Characterization of Thin-Film Rechargeable Lithium Batteries with Lithium Cobalt Oxide Cathodes”. In: *Journal of The Electrochemical Society* 143.10 (Oct. 1996), pp. 3203–3213.

[267] Abdessalem Aribia et al. “Unlocking Stable Multi-Electron Cycling in NMC811 Thin-Films between 1.5 4.7 V”. In: *Advanced Energy Materials* 12.40 (Oct. 2022), p. 2201750.

[268] Juchuan Li et al. “Solid Electrolyte: the Key for High-Voltage Lithium Batteries”. In: *Advanced Energy Materials* 5.4 (Feb. 2015), p. 1401408.

[269] B. J. Neudecker, N. J. Dudney, and J. B. Bates. “Lithium-Free Thin-Film Battery with In Situ Plated Li Anode”. In: *Journal of The Electrochemical Society* 147.2 (Feb. 2000), p. 517.

[270] André Schwöbel, René Hausbrand, and Wolfram Jaegermann. “Interface reactions between LiPON and lithium studied by in-situ X-ray photoemission”. In: *Solid State Ionics* 273 (May 2015), pp. 51–54.

[271] Sabrina Sicolo et al. “Interfacial instability of amorphous LiPON against lithium: A combined Density Functional Theory and spectroscopic study”. In: *Journal of Power Sources* 354 (June 2017), pp. 124–133.

[272] Diyi Cheng et al. “Unveiling the Stable Nature of the Solid Electrolyte Interphase between Lithium Metal and LiPON via Cryogenic Electron Microscopy”. In: *Joule* 4.11 (Nov. 2020), pp. 2484–2500.

[273] Zachary D Hood et al. “Elucidating Interfacial Stability between Lithium Metal Anode and Li Phosphorus Oxynitride via in Situ Electron Microscopy”. In: *Nano Letters* 21.1 (2021), pp. 151–157.

[274] Kangli Wang, Jürgen Janek, and Doreen Mollenhauer. “Insight into the Li/LiPON Interface at the Molecular Level: Interfacial Decomposition and Reconfiguration”. In: *Chemistry of Materials* 36.10 (May 2024), pp. 5133–5141.

[275] Andrew S. Westover, Robert L. Sacci, and Nancy Dudney. “Electroanalytical Measurement of Interphase Formation at a Li Metal-Solid Electrolyte Interface”. In: *ACS Energy Letters* 5.12 (Dec. 2020), pp. 3860–3867.

[276] Katie L. Browning et al. “In Situ Measurement of Buried Electrolyte-Electrode Interfaces for Solid State Batteries with Nanometer Level Precision”. In: *ACS Energy Letters* 8.4 (Apr. 2023), pp. 1985–1991.

[277] Ceren Zor et al. “Lithium Plating and Stripping: Toward Anode-Free Solid-State Batteries”. In: *Advanced Energy and Sustainability Research* 5.8 (Aug. 2024), p. 2300001.

[278] Guozhen Li et al. “The influence of change in structural characteristics induced by beam current on mechanical properties of LiPON solid-state electrolyte films”. In: *International Journal of Hydrogen Energy* 39.28 (Sept. 2014), pp. 16103–16109.

[279] R Marchand et al. “Characterization of nitrogen containing phosphate glasses by X-ray photoelectron spectroscopy”. In: *Journal of Non-Crystalline Solids* 103.1 (June 1988), pp. 35–44.

[280] Nerea Mascaraque et al. “An interpretation for the increase of ionic conductivity by nitrogen incorporation in LiPON oxynitride glasses”. In: *Solid State Ionics* 233 (Feb. 2013), pp. 73–79.

[281] B. Wang et al. “Ionic conductivities and structure of lithium phosphorus oxynitride glasses”. In: *Journal of Non-Crystalline Solids* 183.3 (Apr. 1995), pp. 297–306.

[282] B. Fleutot et al. “Thorough study of the local structure of LiPON thin films to better understand the influence of a solder-reflow type thermal treatment on their performances”. In: *Solid State Ionics* 206 (Jan. 2012), pp. 72–77.

[283] B. Fleutot et al. “Investigation of the local structure of LiPON thin films to better understand the role of nitrogen on their performance”. In: *Solid State Ionics* 186.1 (Mar. 2011), pp. 29–36.

[284] Shingo KANEKO et al. “Influence of N_2 Concentration in the Induction Gases on the Ionic Conductivity of Lithium Phosphorus Oxynitride Solid Electrolyte Thin Film Prepared by Magnetron Sputtering”. In: *Journal of the Surface Finishing Society of Japan* 66.11 (Nov. 2015), pp. 540–543.

[285] Junchao Li and Wei Lai. “Structure and ionic conduction study on Li3PO4 and LiPON (Lithium phosphorous oxynitride) with the Density-Functional Tight-Binding (DFTB) method”. In: *Solid State Ionics* 351 (Aug. 2020), p. 115329.

[286] Diyi Cheng et al. “A free-standing lithium phosphorus oxynitride thin film electrolyte promotes uniformly dense lithium metal deposition with no external pressure”. In: *Nature Nanotechnology 2023 18:12* 18.12 (Aug. 2023), pp. 1448–1455.

[287] Yurong Su et al. “LiPON thin films with high nitrogen content for application in lithium batteries and electrochromic devices prepared by RF magnetron sputtering”. In: *Solid State Ionics* 282 (Dec. 2015), pp. 63–69.

[288] Annie Kim Landry et al. “Unveiling the Origins of High Ionic Conductivity in Lithium Phosphorus Oxynitride Amorphous Electrolytes”. In: *Chemistry of Materials* 35.21 (Nov. 2023), pp. 9313–9324.

[289] Gennady Cherkashinin et al. “The Effect of Interfacial Charge Distribution on Chemical Compatibility and Stability of the High Voltage Electrodes (LiCoPO4, LiNiPO4)/Solid Electrolyte (LiPON) Interface”. In: *Advanced Materials Interfaces* 7.12 (June 2020), p. 2000276.

[290] Sabrina Sicolo and Karsten Albe. “First-principles calculations on structure and properties of amorphous Li5P4O8N3 (LiPON)”. In: *Journal of Power Sources* 331 (Nov. 2016), pp. 382–390.

[291] Adam J. Lovett, Ahmed Kursumovic, and Judith L. MacManus-Driscoll. “Lithium Loss in Vacuum Deposited Thin Films”. In: *ACS Energy Letters* 9.4 (Apr. 2024), pp. 1753–1758.

[292] Naoki Suzuki, Tadashi Inaba, and Tohru Shiga. “Electrochemical properties of LiPON films made from a mixed powder target of Li3PO4 and Li2O”. In: *Thin Solid Films* 520.6 (Jan. 2012), pp. 1821–1825.

[293] Prabhu Doss Mani et al. “Ionic conductivity of bias sputtered lithium phosphorus oxy-nitride thin films”. In: *Solid State Ionics* 287 (Apr. 2016), pp. 48–59.

[294] Yaser Hamedi Jouybari et al. “The influence of sputter conditions on the properties of LiPON and its interfaces”. In: *Journal of Power Sources* 394 (Aug. 2018), pp. 160–169.

[295] Julien Morey et al. “*Operando* Auger/XPS using an electron beam to reveal the dynamics/morphology of Li plating and interphase formation in solid-state batteries”. In: *Journal of Materials Chemistry A* 11.17 (May 2023), pp. 9512–9520.

[296] Allen Pei et al. “Nanoscale Nucleation and Growth of Electrodeposited Lithium Metal”. In: *Nano Letters* 17.2 (Feb. 2017), pp. 1132–1139.

[297] The Materials Project. “Materials Data on LiAlO2 by Materials Project”. In: (July 2020).

[298] The Materials Project. “Materials Data on Li4P2O7 by Materials Project”. In: (July 2020).

[299] The Materials Project. “Materials Data on Li3PO4 by Materials Project”. In: (July 2020).

[300] The Materials Project. “Materials Data on Ge by Materials Project”. In: (July 2020).

[301] The Materials Project. “Materials Data on Li3P by Materials Project”. In: (July 2020).

[302] The Materials Project. “Materials Data on Li2S by Materials Project”. In: (July 2020).

[303] Anubhav Jain et al. “Commentary: The materials project: A materials genome approach to accelerating materials innovation”. In: *APL Materials* 1.1 (2013).

[304] Simon Lorger, Robert Usiskin, and Joachim Maier. “Transport and Charge Carrier Chemistry in Lithium Oxide”. In: *Journal of The Electrochemical Society* 166.10 (June 2019), A2215–A2220.

[305] M.I Youssif, F.Sh Mohamed, and M.S Aziz. “Chemical and physical properties of $Al_{1-x}Fe_xPO_4$ alloys”. In: *Materials Chemistry and Physics* 83.2-3 (Feb. 2004), pp. 250–254.

[306] Daniele Campanella et al. “Influence of $AlPO_4$ Impurity on the Electrochemical Properties of NASICON-Type $Li_{1.5}Al_{0.5}Ti_{1.5}(PO_4)_3$ Solid Electrolyte”. In: *ChemElectroChem* 9.24 (Dec. 2022).

[307] Chinnasamy R. Mariappan et al. “Correlation between micro-structural properties and ionic conductivity of Li1.5Al0.5Ge1.5(PO4)3 ceramics”. In: *Journal of Power Sources* 196.15 (Aug. 2011), pp. 6456–6464.

[308] Masashi Kotobuki and Masaki Koishi. “Preparation of Li1.5Al0.5Ti1.5(PO4)3 solid electrolyte via a solgel route using various Al sources”. In: *Ceramics International* 39.4 (May 2013), pp. 4645–4649.

[309] MOHAMED Sh. KHALIL, ADLY A. HANNA, and MARWA A. EL-SAYED. “SYNTHESIS OF mono-or di-VALENT CATIONS SUBSTITUTED Al-or Fe-PHOSPHATES AND THEIR ELECTRICAL CONDUCTIVITY”. In: *Phosphorus Research Bulletin* 14.0 (2002), pp. 77–87.

[310] D. Wohlmuth et al. “Order vs. disordera huge increase in ionic conductivity of nanocrystalline LiAlO2 embedded in an amorphous-like matrix of lithium aluminate”. In: *Journal of Materials Chemistry A* 2.47 (Nov. 2014), pp. 20295–20306.

[311] Heri Jodi et al. “SYNTHESIS AND ELECTROCHEMICAL CHARACTERIZATION OF Li3PO4 FORSOLID STATE ELECTROLYTES”. In: *Jurnal Sains Materi Indonesia* 18.1 (Mar. 2018), p. 1.

[312] Hany El-Shinawi, Edmund J. Cussen, and Serena A. Cussen. “Morphology-controlled synthesis of novel nanostructured Li4P2O7 with enhanced Li-ion conductivity for all-solid-state battery applications”. In: *Dalton Transactions* 53.9 (Feb. 2024), pp. 4139–4146.

[313] Xin Liu et al. “Recent progress on germanium-based anodes for lithium ion batteries: Efficient lithiation strategies and mechanisms”. In: *Energy Storage Materials* 30 (Sept. 2020), pp. 146–169.

[314] Anastasiia V. Iosimovska et al. “Thermodynamic stability and ionic conductivity in lithium-germanium binary system”. In: *Applied Physics Letters* 124.16 (Apr. 2024), p. 163904.

[315] Alexander Kuhn, Jürgen Köhler, and Bettina V. Lotsch. “Single-crystal X-ray structure analysis of the superionic conductor Li10GeP2S12”. In: *Physical Chemistry Chemical Physics* 15.28 (July 2013), pp. 11620–11622.